Electric Moments of Osmium, Platinum and Mercury Nuclei

Cheryl Su-Lean Lim

March 1990

A thesis submitted for the degree of Doctor of Philosophy of the Australian National University.

"Of making many books there is no end, and much study is a weariness of the flesh. The end of the matter; all has been heard. Fear God, and keep his commandments; for this is the whole duty of man."

Ecclesiastes 12:12-13

Preface

This thesis describes particle singles and particle-gamma coincidence measurements of E2, E3 and E4 matrix elements in ^{192}Os, ^{194,196,198}Pt and ^{198,200,202,204}Hg. The experiments were carried out at the Department of Nuclear Physics, Australian National University, under the supervision of Dr R.H. Spear and, for the first eighteen months, Dr M.P. Fewell.

The experimental work for ^{192}Os and ^{194,196,198}Pt was performed primarily by Drs M.P. Fewell, G.J. Gyapong, R.H. Spear and W.J. Vermeer, and myself. Occasional assistance was provided by Drs A.M. Baxter and S.M. Burnett. The ^{194,196}Pt experiment was initiated by Dr M.P. Fewell. Apart from some of the particle singles data for this experiment, which were obtained prior to my arrival, I analysed all the data presented in this thesis. The ^{198,200,202,204}Hg data were collected by Drs W.N. Catford and R.H. Spear, as well as by myself; Dr Catford provided invaluable advice and assistance in the analysis of these data.

Dr Fewell and I designed the target chamber described in chapter 4 on the basis of advice proferred by Dr D.C. Weisser, Mr G.P. Clarkson and Mr M. Jagla. The targets were made by Mr A.H.F. Muggleton and Dr M.T. Esat. The spectrum analysis, Coulomb excitation and least-squares fitting programs were already in existence before my arrival; I modified the Winther-de Boer Coulomb excitation program and incorporated it into a fitting program (MINUIT) from CERN for the analysis of particle-gamma coincidence data.

The interpretation of the data presented has involved discussions with Drs W.N. Catford, M.P. Fewell, G.J. Gyapong, B.A. Robson, R.H. Spear, A.E. Stuchbery and W.J. Vermeer. Their suggestions are gratefully acknowledged.

Some of the work described in this thesis, as well as related experiments, has appeared in the following publications :

1. C.S. Lim, M.D. Rebgetz, R.H. Spear, W.J. Vermeer, M.P. Fewell, B.A. Robson and R. Smith,
   "Energy dependence of the ^{16}O-^{208}Pb effective interaction"
   Phys. Lett. **B200** (1988) 263-265

2. C.S. Lim, R.H. Spear, W.J. Vermeer, M.P. Fewell and G.J. Gyapong,
   "Electric quadrupole moments of the first excited state of ^{192}Os"
   Nucl. Phys. **A485** (1988) 399-412

3. C.S. Lim, R.H. Spear, W.J. Vermeer and M.P. Fewell,
   "Possible discontinuity in octupole behaviour in the Pt-Hg region"
   Phys. Rev. **C39** (1989) 1142-1144

4. W.J. Vermeer, C.S. Lim and R.H. Spear,
   "Mixed symmetry in the vibrational nucleus ^{142}Ce"
   Phys. Rev. **C38** (1988) 2982-2984

5. R.H. Spear, W.J. Vermeer, S.M. Burnett, G.J. Gyapong and C.S. Lim,
   "Coulomb Excitation of ^{142}Ce and ^{144}Nd"
   Aust. J. Phys. **42** (1989) 345

No part of this thesis has been submitted for a degree at any other institution.

C.S. Lim

Australian National University, Canberra

March 1990.

Acknowledgments

I would like to express my gratitude to all the people who contributed in some way to the work involved in this thesis. I am indebted to both of my supervisors, Matthew Fewell, who continued to provide a great deal of assistance even after moving to Armidale, and Ray Spear, who put much effort into reading and commenting on my thesis. Special thanks go to my advisors, Andrew Stuchbery and Brian Robson, for the time that they spent in helping me with various aspects of my work. I would also like to thank Wilton Catford, Godfrey Gyapong and John Vermeer for their suggestions and assistance.

My thanks also go to the two chairmen of the Department of Nuclear Physics during the past four years, John Newton and Trevor Ophel, for allowing me to be a student here, as well as to all the members of the department for creating a stimulating and friendly environment. The skill and dedication of all the technical staff in the Department enabled the experiments to be run with the minimum of difficulty; of the many people who were involved in this way, I would like to make specific mention of Andy Rawlinson for his help with the vacuum systems, David Weisser for lessons in fiddling with the accelerator, Gavin Gilmour for photographic work and other pictures, Michael Jagla for creating a work of art from a near-impossible target chamber design, and Albert Muggleton for not only producing a large number of targets on demand but also for preserving my sanity with many conversations on canine topics.

My friends and family have extended a great deal of personal support over the last few years; this thesis would never have been completed without their encouragement. The Shaw, Minto and Allison families provided constant friendship and hospitality for which I am deeply grateful. I would like to acknowledge my fellow sufferers and nutritional advisors, Anna and Guna, for raising my vegetable intake in the last few months to heights which hopefully will never be surpassed. Many thanks to Bernhard for his never-failing and patient suggestions for a desperate MultiFig user and, finally, to Diana for faithfully sending me cheering and challenging letters every fortnight.

Abstract

Various E2, E3 and E4 moments in ^{192}Os, ^{194,196,198}Pt and ^{198,200,202,204}Hg have been measured using Coulomb excitation with ^{4}He, ^{7}Li, ^{12}C and ^{58}Ni projectiles, in conjunction with the particle singles and particle-γ coincidence techniques.

Values of $B(E2;0_1^+ \rightarrow 2_1^+)$ and $Q(2_1^+)$ were measured for ^{192}Os in response to the observation of a discrepancy between values of $Q(2_1^+)$ obtained from Coulomb excitation and muonic X-ray data. The present determination of $Q(2_1^+)$ was found to be in good agreement with that given by a muonic X-ray experiment, and consistent with a well-deformed prolate shape for this nucleus. It was shown that the earlier discrepancy may have been due to an inadequate treatment of corrections to and/or uncertainties in the earlier Coulomb excitation data.

Excitation probabilities for positive-parity states up to and including the 6_1^+ state in ^{196}Pt and the 4_2^+ state in ^{194}Pt were obtained from particle-singles and particle-γ coincidence data. E2 and E4 transition matrix elements were extracted; the static E2 moments for the 2_1^+, 2_2^+, 4_1^+ and 6_1^+ states in ^{196}Pt and the 2_1^+ and 4_1^+ states in ^{194}Pt were also derived. All of these static quadrupole moments except $Q(6_1^+)$ of ^{196}Pt were found to have relatively large magnitudes between 0.5 and 1.0 e b. Comparison with model predictions indicates that a better overall description of both diagonal and off-diagonal E2 matrix elements in these nuclei is given by the Boson Expansion Theory than by the Interacting Boson Model.

Measurements of $B(E3;0_1^+ \rightarrow 3_1^-)$ for ^{194,196,198}Pt and ^{198,200,202,204}Hg were performed to investigate a proposed discontinuity in octupole behaviour between ^{198}Pt and ^{198}Hg. The excitation energies of the 3_1^- states in the Hg isotopes were confirmed; E3 transition strengths were found to lie between 5 and 11 W.u. for Pt and in the range 22 to 27 W.u. for Hg. No evidence was found to support a suggestion that the 3_1^- states in Pt are of a non-collective nature. Examination of the various explanations of octupole behaviour in the Pt and Hg nuclei shows that as yet no hypothesis has been formulated to adequately describe the data.

Contents

List of Figures

List of Tables

Chapter 1

Introduction

The electric moments of nuclei are a rich source of information on nuclear structure. The static electric quadrupole moment of the nucleus indicates the shape of its charge distribution while collective features can be deduced from measurements of E2, E3 and E4 transition strengths.

In this thesis, three experiments are reported in which various electric moments were measured for nuclei in the Os-Pt-Hg transitional region between the well-deformed rare earth nuclei and the doubly closed-shell nucleus ^{208}Pb, in order to examine some aspects of collective quadrupole and octupole behaviour. These studies concern :

(a) measurements of the static electric quadrupole moments of the first 2^+ states in ^{192}Os and ^{194,196}Pt, which were carried out to investigate the location and mass-dependent rate of change of a predicted transition from prolate to oblate deformation in the Os-Pt nuclei,

(b) the evaluation of a proposal that ^{196}Pt is a prototype of the O(6) dynamical symmetry of the Interacting Boson Model (IBM) on the basis of measurements of B(E2) and quadrupole moment values for that nucleus, and

(c) determinations of $B(E3;0_1^+ \rightarrow 3_1^-)$ for ^{194,196,198}Pt and ^{198,200,202,204}Hg, which were made to examine the cause and nature of an apparent change in collective octupole behaviour between ^{198}Pt and ^{198}Hg.

The three experiments described in the present work all utilize Coulomb excitation,

which is accepted to be a model-independent technique for the determination of electric moments. As the literature extant on Coulomb excitation theory is vast, only those fundamental features deemed to be essential to the understanding of the three Coulomb excitation experiments in this thesis are included in chapter 2. It has been noted recently that measurements of static electric quadrupole moments from Coulomb excitation experiments sometimes show a significant difference to those obtained for the same nuclei from muonic X-ray data (Ho81); it has been suggested that the cause of this discrepancy might be the different techniques used. The greatest deviation between muonic X-ray and Coulomb excitation data was observed in the static electric quadrupole moment of the first 2^+ state, $Q(2_1^+)$, of ^{192}Os. Chapter 3 describes a new determination of $Q(2_1^+)$ for ^{192}Os, by means of particle singles spectroscopy, to test the degree of agreement of Coulomb excitation data with the results of muonic X-ray experiments.

The increasing sophistication of experimental techniques and Coulomb excitation theory have made simultaneous model-independent determinations of the electromagnetic matrix elements for a number of collective states more accurate and precise. In chapter 4, particle singles and particle-gamma coincidence measurements of E2 and E4 moments for states up to and including the 4_1^+ state in ^{194}Pt and the 6_1^+ state in ^{196}Pt are compared with the predictions of the IBM as well as those of other models. These results, together with the ^{192}Os measurements, are discussed in the context of the prolate-to-oblate transition predicted to occur in the Os and Pt nuclei.

An investigation of the evolution in collective octupole behaviour in the Pt, Hg and Pb nuclei is presented in chapter 5. Experimental determinations of $B(E3;0_1^+ \rightarrow 3_1^-)$ for ^{194,196,198}Pt and ^{198,200,202,204}Hg are used to examine a proposal that the 3_1^- states in the even-mass Pt isotopes are of a different nature to those in the even-mass Hg isotopes.

Chapter 2

Coulomb Excitation Theory

2.1 Introduction

The term 'Coulomb excitation' means the excitation of a nucleus by the time-dependent electromagnetic field of another nucleus during collision. The importance of this process in the elucidation of nuclear structure rests primarily on the fact that the Coulomb interaction is very well-understood, thus minimizing uncertainties due to the use of model parameters. However, this is not the case when the distance of closest approach of the colliding nuclei is small enough for nuclear forces to become significant; for this reason it is imperative that the energy of the collision is well below the Coulomb barrier to ensure that the electromagnetic force dominates all other effects. If this condition is satisfied, the only nuclear properties of significance are the electromagnetic matrix elements. Since Coulomb excitation results in the selective excitation of low-lying collective bands, the excitation probabilities of the observed states can be used to give a direct measure of, say, E2 and E3 matrix elements and hence, information about quadrupole and octupole collective motion. Further selectivity can be exercised by the variation of experimental conditions; in particular, choice of projectile mass is crucial in determining which matrix elements are measured. For instance, the use of light-ion projectiles (e.g. ^{4}He) results primarily in single-step excitation, giving information about matrix elements connecting the ground state and the lower-lying states. The excitation probabilities obtained thus are relatively insensitive to second- and higher-order effects, such as the reorientation

effect, multiple excitation, virtual excitation of the giant dipole resonance (GDR), and interference from higher states. The size of these effects can be determined by using heavier projectiles like ^{12}C or ^{58}Ni to increase the component of multiple excitation, i.e. excitation of a final state via the excitation of intermediate states. This flexibility makes Coulomb excitation an important tool for elucidating nuclear structure.

2.2 Non-relativistic Semi-classical Theory

The semi-classical approximation is the assumption that the projectile can be considered to be a point charge travelling along an hyperbolic trajectory defined by the repulsive electric field of the target nucleus. Consideration of the projectile as a point charge is equivalent to specifying that its dimensions as a localized wave packet are small compared with the distance of closest approach, i.e.,

$$\eta = \frac{2\pi a}{\lambda} = \frac{Z_p Z_t e^2}{\hbar v} \gg 1 \tag{2.1}$$

where the Sommerfeld parameter, η, is the ratio of a, half the distance of closest approach of the centres of the nuclei, to $\lambda/2\pi$, the de Broglie wavelength of the projectile and v is the velocity of the projectile before the collision. The subscripts p and t refer to the projectile and target respectively. For the projectile trajectory to be hyperbolic, the energy loss of the projectile must be negligible compared to its initial energy E_p, i.e.,

$$\Delta E_p \ll E_p \, . \tag{2.2}$$

In addition, the interaction is assumed to be purely electromagnetic and the charge distributions of the two particles are assumed not to overlap. These conditions are met by ensuring that bombarding energies are low enough to avoid nuclear interference; this is known as ensuring that the energies used are 'safe'. From equation (2.1) it can be seen that for constant v and Z_t, the semi-classical approximation becomes more valid as Z_p increases; as a consequence, quantum-mechanical effects will be most important for light projectiles like ^{4}He and ^{1}H. Partial corrections can be made for this by using

symmetrization, as explained in § 2.5.1.

For relativistic effects to be negligible, the condition,

$$(\frac{v}{c})^2 \ll \Delta P \tag{2.3}$$

where ΔP is the uncertainty in the excitation probability or other quantities being measured, must be met.

The most common approach (Al75, Fe78t) to evaluating the Coulomb excitation process is to derive coupled differential equations for the excitation amplitudes $a_n(t)$ of the state $|n>$ with energy E_n from the Schrödinger time-dependent equation

$$i\hbar\frac{\partial\psi(t)}{\partial t} = [H_0 + V(t)]\psi(t) \ , \tag{2.4}$$

where $V(t)$ is the time-dependent electromagnetic interaction and ψ(t) is the wave function of the target nucleus which can be written in terms of the eigenstates ϕ_n of the unperturbed nucleus :

$$\psi(t) = \sum_n a_n(t)\phi_n \ . \tag{2.5}$$

Equation (2.4) can be written in terms of the time-dependent excitation amplitudes a_n(t) :

$$i\hbar\frac{\partial a_n(t)}{\partial t} = \sum_m <n|\ V(t)|\ m>\ \exp\ [i(E_n - E_m)t/\hbar]a_m(t) \ . \tag{2.6}$$

Certain limiting conditions and assumptions can be imposed to solve these coupled differential equations :

(a) both nuclei are in their ground states at $t = -\infty$,

(b) only one nucleus is excited, and

(c) the ground state of that nucleus is unpolarized.

The second condition restricts the electromagnetic interaction to monopole-monopole and monopole-multipole interactions only. The monopole-monopole interaction is responsible for the classical hyperbolic trajectory of the projectile while the monopole-multipole interaction results in excitation of the nucleus.

For the sake of simplicity, the summation in equation (2.6) is restricted to low-lying states. Since the adiabaticity parameter ξ_{fi} for a transition from initial state $|i>$ to final state $|f>$ is defined (Al75) by

$$\xi_{fi} = \eta_f - \eta_i = \frac{\Delta E_{fi} a}{v\hbar} , \tag{2.7}$$

population of states at high excitation energy requires ξ to be large, i.e. $\xi \gg 1$. Consequently, the restriction to low-lying states implies that, for the transition from the ground state $|0>$ to the final state $|f>$,

$$\xi_{f0} = \frac{E_f a}{v\hbar} \lesssim 1 . \tag{2.8}$$

(Significant excitation occurs when $\xi \sim 1$. The condition $\xi \gg 1$ corresponds to an adiabatic process.) Restricting the summation to a finite number of states means (Al75) that

$$\sum_k a^*_{n,k}(t) a_{m,k}(t) = \delta_{nm} \tag{2.9}$$

and

$$\sum_n a^*_{n,k}(t) a_{n,k'}(t) = \delta_{kk'}. \tag{2.10}$$

Hence

$$\bar{a}_{l,n}(\infty) = \sum_k a^{0*}_{n,k}(\infty) a^0_{l,k}(\infty) = \delta_{nl} \tag{2.11}$$

can be used as an initial condition. If the assumption that

$$a_m(t) = a_{IM}(t) = \delta_{II_0}\delta_{MM_0}, \tag{2.12}$$

is made, equation (2.6) becomes

$$a_{I_f M_f I_i M_i} = \frac{1}{i\hbar}\int_{-\infty}^{\infty} <I_f M_f|V(t)|I_i M_i> \exp\,[i(E_f - E_i)t/\hbar]dt \tag{2.13}$$

for $a_{I_f M_f I_i M_i}$, the excitation amplitude to a state $|f>$ for a nucleus in initial state $|i>$. I_n and M_n are the spin and magnetic quantum number of the state $|n>$. Classically, the

time-dependent electromagnetic interaction $V(t)$ can be written in terms of current and charge densities $\vec{j}(\vec{r})$ and $\rho(\vec{r})$:

$$V(t) = \frac{1}{4\pi} \int \int \frac{\rho(\vec{r}_p)\rho(\vec{r}_t)/\epsilon_0 - \mu_0 \vec{j}(\vec{r}_p).\vec{j}(\vec{r}_t)}{\mid \vec{r}_p - \vec{r}_t \mid} d\vec{r}_p d\vec{r}_t \tag{2.14}$$

where $\vec{r}_p$ and $\vec{r}_t$ are measured with respect to the centre-of-mass of the two nuclei. Since the assumption that $\rho(\vec{r}_p)$ and $\rho(\vec{r}_t)$ do not overlap has been made, $V(t)$ can be written in terms of three contributing parts :

$$V(t) = \mathcal{V}_{EE}(t) + \mathcal{V}_{EM}(t) + \mathcal{V}_{MM}(t) \tag{2.15}$$

with E and M denoting the electric and magnetic multipole moments respectively. Several previously mentioned constraints (the 'safe energy' criterion, negligible relativistic effects) ensure that $(v/c)^2$ is small, hence $\mathcal{V}_{MM}(t)$, which can be shown to be equal to $(v/c)^2 \mathcal{V}_{EE}(t)$ (Appendix A of Al75), can be ignored. If the assumption that the excited nucleus is a point charge with no magnetic moment is made, and the case of target excitation is considered, $\mathcal{V}_{EE}$ and $\mathcal{V}_{EM}$ will have the forms

$$\mathcal{V}_{EE} = 16\pi Z_p e \sum_{\lambda\mu} (-1)^{\mu} (2\lambda+1)^{-1} \mathcal{M}(E\lambda, -\mu) r^{-\lambda-1} Y_{\lambda\mu}(\hat{r}) \tag{2.16}$$

$$\mathcal{V}_{EM} = Z_p e \mu_0 \sum_{\lambda\mu} (-1)^{\mu} (2\lambda^2+\lambda)^{-1} \mathcal{M}(M\lambda, -\mu) r^{-\lambda-1} \frac{d\vec{r}}{dt} (\vec{r} \times \vec{\nabla}) Y_{\lambda\mu}(\hat{r}) \tag{2.17}$$

where $Y_{\lambda\mu}(\hat{r})$ are the spherical harmonics defined by Condon and Shortley. The multipole moment $\mathcal{M}(\sigma\lambda, \mu)$ of the electric (E) or magnetic (M) transition with multipolarity λ is defined as

$$\mathcal{M}(E\lambda, \mu) = \int \rho(\vec{r}) \vec{r}^{\lambda} Y_{\lambda\mu}(\hat{r}) d\vec{r} \tag{2.18}$$

$$\mathcal{M}(M\lambda, \mu) = \frac{1}{c(1+\lambda)} \int \vec{r}^{\lambda} \vec{j}(\vec{r}).(\vec{r} \times \vec{\nabla}) Y_{\lambda\mu}(\hat{r}) d\vec{r} \tag{2.19}$$

where $\vec{r}$ is the distance between the colliding nuclei. From the Wigner-Eckart theorem, the reduced electromagnetic matrix element connecting the initial and final states $\mid i >$

and $|f>$ is defined by

$$<I_f M_f|\mathcal{M}(E\lambda,\mu)|I_i M_i>=(-1)^{I_f-M_f}\begin{pmatrix} I_i & \lambda & I_f \\ -M_i & \mu & M_f \end{pmatrix}<f\|\mathcal{M}(\sigma\lambda)\|i> \quad . \quad (2.20)$$

The probability of excitation from ground state $|0>$ to state $|n>$, P_n, is related to the differential cross-section for inelastic scattering by the equation

$$\frac{d\sigma(n)}{d\Omega} = P_n \frac{d\sigma(R)}{d\Omega} \quad (2.21)$$

where $d\sigma(R)/d\Omega$ denotes the Rutherford differential cross-section. This relation assumes a negligible effect on the projectile trajectory by the collision [equation (2.2)]. In terms of excitation amplitudes the excitation probability and the differential cross-section are written

$$\frac{d\sigma(n)}{d\Omega} = P_n \frac{a^2}{4}\sin^{-4}(\frac{\theta}{2}) \quad (2.22)$$

$$P_n = \frac{1}{2I_0+1}\sum_{M_0 M_n} |\, a_{I_n M_n I_0 M_0}\,|^2 \quad (2.23)$$

assuming an unpolarized ground state. Thus, the above two equations can be combined with equation (2.13) to determine the reduced transition probability, which is defined as

$$\begin{aligned} B(\sigma\lambda;0\rightarrow n) &= \sum_{\mu M_n} |<I_n M_n|\mathcal{M}(\sigma\lambda,\mu)|I_0 M_0>|^2 \\ &= \frac{1}{2I_0+1}\,|<I_n\|\mathcal{M}(\sigma\lambda)\|I_0>|^2, \end{aligned} \quad (2.24)$$

from measured excitation probabilities or differential cross-sections. It has been shown (Bi65) that as $\xi\rightarrow\infty$ (i.e. the energy of the transition increases), the excitation probability P_n takes on an $e^{-2\pi\xi}$ dependence, indicating the rapid fall-off of excitation due to the repulsive Coulomb field.

It is worth noting that in semi-classical theory, the coordinate system used is that in which the z-axis is aligned with the projectile angular momentum vector $\vec{L}$, whereas in quantum-mechanical treatment, the z-axis is aligned with the momentum of incoming

particles $\hbar\vec{k_i}$ to exploit the azimuthal symmetry of that system.

2.3 Perturbation Theory

2.3.1 Introduction

In their classic work on Coulomb excitation (Al56), Alder *et al.* used perturbation theory to derive expressions for the excitation amplitudes and excitation probabilities in terms of reduced nuclear matrix elements. Whilst the first-order treatment commonly employed in the past is only accurate for cases where excitation probabilities for all states other than the ground state are small, it is of fundamental importance as a basis for understanding more complex situations and for developing a rigorous treatment of higher order processes. A brief summary of the basic steps, results and their practical significance is given below; full details can be found in Al56 and Al75.

Since all the cases considered in the present work involve significant excitation of the target nucleus and negligible excitation of the projectile, the assumption of target excitation alone is made in the rest of this chapter. This implies that the projectile is treated as a structureless point charge.

2.3.2 First-Order Perturbation Theory

First-order perturbation theory is valid only when P_0, the excitation probability of the ground state, is of order 1 and P_n, the excitation probability for any state $|n>$ above the ground state $|0>$, is much smaller than 1. In this approximation the following expression for the excitation amplitudes can be derived from equations (2.13), (2.16) and (2.17) :

$$a_{I_f M_f I_i M_i} = \frac{4\pi Z_p e}{i\hbar} \sum_{\lambda\mu} \frac{(-1)^\mu}{2\lambda+1} < I_f M_f \,|\mathcal{M}(\sigma\lambda,\mu)\,| I_i M_i > S_{\sigma\lambda,\mu} \qquad (2.25)$$

where the integrals

$$S_{E\lambda,\mu} = \int_{-\infty}^{\infty} Y_{\lambda\mu}[\theta(t),\phi(t)][r(t)]^{-\lambda-1} \exp\,[\frac{i}{\hbar}(E_f - E_i)t]dt \qquad (2.26)$$

and

$$S_{M\lambda,\mu} = \frac{1}{\lambda c}\int_{-\infty}^{\infty}(\vec{r}\times\vec{\nabla}[r(t)]^{-\lambda-1}Y_{\lambda\mu}[\theta(t),\phi(t)]\ \exp\ [\frac{i}{\hbar}(E_f - E_i)t]dt \qquad (2.27)$$

are introduced to separate the dependence on nuclear properties from the dependence on the collision parameters, r, θ and ϕ, which describe the motion of the projectile with respect to the target. From the Wigner-Eckart theorem, equation (2.25) is equivalent to

$$a_{I_fM_fI_iM_i} = \frac{4\pi Z_p e}{i\hbar}\sum_{\lambda\mu}\frac{1}{2\lambda+1}(-1)^{I_i-M_i}\begin{pmatrix} I_i & \lambda & I_f \\ -M_i & \mu & M_f\end{pmatrix} < I_f\|\mathcal{M}(\sigma\lambda)\|I_i > S_{\sigma\lambda,\mu} \qquad (2.28)$$

where σ denotes either an electric or magnetic transition. By rewriting the orbit in terms of the eccentricity of the orbit, ϵ, and a parameter w which is defined by

$$r(t) = a(\epsilon\ \cosh\ w + 1)\ , \qquad (2.29)$$

and by introducing the orbital integrals $R_{\sigma\lambda,\mu}(\theta,\xi)$ and the collision functions $Q_{\sigma\lambda,\mu}(\epsilon,w)$,

$$Q_{\sigma\lambda,\mu}(\epsilon,w) = a^{\lambda}\frac{(2\lambda-1)!!}{(\lambda-1)!}\sqrt{\frac{\pi}{2\lambda+1}}r(w)[r(t)]^{-\lambda-1}Y_{\lambda\mu}[\theta(t),\phi(t)] \qquad (2.30)$$

$$R_{\sigma\lambda,\mu}(\theta,\xi) = \int_{-\infty}^{\infty}Q_{\sigma\lambda,\mu}(\epsilon,w)\ \exp\ [i\xi(\epsilon\ \sinh\ w + w)]dw\ , \qquad (2.31)$$

the dependence on r can be separated from the other parameters :

$$a_{I_fM_fI_iM_i} = \frac{4\sqrt{\pi}Z_p e}{iv\hbar}\sum_{\lambda\mu}\sqrt{2\lambda+1}\frac{(\lambda-1)!}{a^{\lambda}(2\lambda+1)!!}(-1)^{I_i-M_i}\begin{pmatrix} I_i & \lambda & I_f \\ -M_i & \mu & M_f\end{pmatrix}$$
$$\times < I_f\|\mathcal{M}(\sigma\lambda)\|I_i > R_{\sigma\lambda,\mu}\ . \qquad (2.32)$$

From the above, equations (2.22) and (2.23) can be written in the forms

$$\frac{d\sigma(f)}{d\Omega} = 4\pi(\frac{Z_p e a}{v\hbar})^2\ \sin^{-4}(\frac{\theta}{2})\frac{(\lambda-1)!}{a^{2\lambda}(2\lambda-1)!!}B(\sigma\lambda;i\rightarrow f)R^2_{\sigma\lambda}(\theta,\xi) \qquad (2.33)$$

$$P_f = \sum_{\lambda}\mid\chi^{\sigma\lambda}_{i\rightarrow f}\mid^2 R^2_{\sigma\lambda}(\theta,\xi) \qquad (2.34)$$

where $R^2_{\sigma\lambda}(\theta,\xi) = \sum_\mu \mid R_{\sigma\lambda,\mu}(\theta,\xi) \mid^2$ and $\chi^{\sigma\lambda}_{i\mapsto f}$, the strength function, is defined by the equations

$$\chi^{M\lambda}_{i\mapsto f} = \frac{16\pi Z_p e(\lambda-1)! < f\|\mathcal{M}(M\lambda)\|i>}{c\hbar(2\lambda+1)!!a^\lambda(2I_i+1)^{1/2}} \tag{2.35}$$

$$\chi^{E\lambda}_{i\mapsto f} = \frac{\sqrt{16\pi} Z_p e(\lambda-1)! < f\|\mathcal{M}(E\lambda)\|i>}{v\hbar(2\lambda+1)!!a^\lambda(2I_i+1)^{1/2}} . \tag{2.36}$$

$R^2_{\sigma\lambda}$ is normalized so that $R^2_{\sigma\lambda}(\pi,0) = 1$.

The following properties of the function $R^2_{\sigma\lambda}$ are worth noting :

(a) $R^2_{E\lambda}(\theta,\xi) \leq R^2_{E\lambda}(\pi,0) = 1$

(b) $R^2_{M\lambda}(\pi,0) = 0$

(c) $R^2_{\sigma\lambda}(0,\xi) = 0$

(d) as $\xi \to 0$ and $\theta \to \pi, R^2_{EL} \sim R^2_{El}$ for all values of l and L.

(e) as $\theta \to 0$, $R^2_{E\lambda} \propto \exp\,[-2\xi/\sin\frac{\theta}{2}]\sin\frac{\theta}{2}$ and $R^2_{M\lambda} \propto \exp\,[-2\xi/\sin\frac{\theta}{2}]$;

(f) as $\theta \to \pi$, $R^2_{M\lambda} \to \cot^2\frac{\theta}{2}(\lambda+1)/[2(2\lambda+1)^2]$

(g) if $\xi \gg \sin(\frac{\theta}{2})$, $R^2_{\sigma\lambda} \propto \exp\,[-\xi(2\ \mathrm{cosec}(\frac{\theta}{2}) + \pi)]$

(h) $\frac{d\sigma}{d\Omega} \propto R^2_{\sigma\lambda}$.

It is also important to notice that the strength function $\chi^{\sigma\lambda}_{i\mapsto f}$ has the following characteristics :

(a) $\chi^{\sigma\lambda}_{i\mapsto f} \propto (\lambda-1)!(2\lambda+1)!!$

(b) $\chi^{\sigma\lambda}_{i\mapsto f} \propto Z_p a^{-\lambda} \propto Z_p(Z_pZ_t)^{-\lambda}$

(c) $\chi^{M\lambda}_{i\mapsto f} \sim \chi^{E\lambda}_{i\mapsto f} v/c$

(d) $\chi^{E\lambda}_{i\mapsto f} \propto E^{\lambda-\frac{1}{2}}$ but $\chi^{M\lambda}_{i\mapsto f} \propto E^\lambda$

(e) $|\chi^{\sigma\lambda}|^2 \propto B(\sigma\lambda; i \to f)$.

The most important consequences of these properties are that :

(a) Coulomb excitation probabilities are larger for low multipolarity transitions, high bombarding energies, electric transitions and high mass projectiles,

(b) the Coulomb excitation functions, which are directly proportional to the orbital integrals $R_{\lambda\mu}(\theta,\xi)$, decrease exponentially as $\theta \rightarrow 0°$ and vary rapidly at forward angles so that experimenters using forward angles must take special care in defining the scattering angle, and

(c) electric transitions are favoured over magnetic ones as $\theta \rightarrow 180°$.

2.3.3 Higher Order Perturbation Theory

Second-order effects are important in most Coulomb excitation experiments, necessitating the inclusion of higher-order terms in calculations. The excitation amplitude can be written as a sum of terms to kth order :

$$a_{i\mapsto f} = a^1_{i\mapsto f} + a^2_{i\mapsto f} + \ldots + a^k_{i\mapsto f} \tag{2.37}$$

where $a^1_{i\mapsto f}$ is $a_{I_f M_f I_i M_f}$ as defined in equation (2.13) and

$$\begin{aligned} a^k_{i\mapsto f} \;=\; & \sum (\frac{-i}{\hbar})^k \int_{-\infty}^{\infty} dt < f|V_\sigma(t)|z^{k-2}> \exp\,[i(E_f - E_{z^{k-2}})t/\hbar] \\ & \times \int_{-\infty}^{t} dt' < z^{k-2}|V_\sigma(t')|z^{k-3}> \exp\,[i(E_{z^{k-2}} - E_{z^{k-3}})t'/\hbar] \\ & \times \ldots \\ & \times \int_{-\infty}^{t^{k-2}} dt^{k-1} < z|V_\sigma(t^{k-1})|i> \exp\,[i(E_z - E_i)t^{k-1}/\hbar] \end{aligned} \tag{2.38}$$

is the kth order excitation amplitude for excitation of state $|f>$ via $(k-1)$ intermediate states $|z>$, $|z'>$, etc., where $V_\sigma(t)$ denotes the monopole-multipole interaction $\mathcal{V}_{E\sigma}$. Similarly, the excitation probability can be written as

$$P_{i\mapsto f} = P^1_{i\mapsto f} + P^2_{i\mapsto f} + P^{1,2}_{i\mapsto f} + P^3_{i\mapsto f} + P^{1,3}_{i\mapsto f} + P^{2,3}_{i\mapsto f} + \ldots + P^k_{i\mapsto f}\ . \tag{2.39}$$

In a treatment analogous to that outlined in the previous section, a multipole expansion can be performed on $a^k_{i\rightarrow f}$. The second-order excitation amplitude, for example, becomes

$$\begin{aligned} a^2_{I_f M_f I_i M_i} &= -\frac{1}{2}\sum_{\lambda\lambda' k\kappa I_z}(2k+1)\sqrt{(2I_i+1)(2I_z+1)(2\lambda+1)(2\lambda'+1)} \\ &\times (-1)^{I_i+I_f+k+\lambda+\lambda'+I_i-M_i}\begin{Bmatrix} I_i & I_f & k \\ \lambda' & \lambda & I_f \end{Bmatrix}\begin{pmatrix} I_i & k & I_f \\ -M_i & \kappa & M_f \end{pmatrix} \\ &\times \chi^{\lambda}_{i\rightarrow z}\chi^{\lambda'}_{z\rightarrow f}[R_{\lambda\lambda' k\kappa}(\theta,\xi_{zi},\xi_{fz}) + iG_{\lambda\lambda' k\kappa}(\theta,\xi_{zi},\xi_{fz})] \end{aligned} \tag{2.40}$$

where $R_{\lambda\lambda' k\kappa}$ and $G_{\lambda\lambda' k\kappa}$ are double integrals involving $R_{\sigma\lambda,\mu}R_{\sigma\lambda',\mu'}$ with the properties that if $\xi_{zi} \sim -\xi_{fz}$ (i.e. excitation of a low-lying final state $|f>$ via a high-lying intermediate state $|z>$), $R_{\lambda\lambda' k\kappa} \propto \exp[-2\pi\xi_{zi}]$ and $G_{\lambda\lambda' k\kappa} \propto \xi_{zi}^{-1}$; if both ξ_{zi} and ξ_{fz} are large and positive (corresponding to two-step excitation to a state at high excitation energy), $a^2_{i\rightarrow f}$ tends to zero.

It is also instructive to consider the second-order excitation probability

$$P_{i\rightarrow f} = P^1_{i\rightarrow f} + P^{1,2}_{i\rightarrow f} + P^2_{i\rightarrow f} \quad . \tag{2.41}$$

where the first order excitation probability can be written as

$$P^1_{i\rightarrow f} = \sum_{\lambda} |\, \chi^{\lambda}_{i\rightarrow f}\,|^2\, R^2_{\sigma\lambda}(\theta,\xi_{fi}) \; . \tag{2.42}$$

The other terms in equation (2.41) are

$$\begin{aligned} P^{1,2}_{i\rightarrow f} &\propto \chi^{\lambda}_{i\rightarrow f}\chi^{\lambda'}_{i\rightarrow z}\chi^{\lambda''}_{z\rightarrow f} \\ &\propto a_{if}a_{iz}a_{zf} \\ &\propto <I_f\|\mathcal{M}(\sigma\lambda)\|I_i><I_z\|\mathcal{M}(\sigma\lambda')\|I_i><I_f\|\mathcal{M}(\sigma\lambda'')\|I_z> \end{aligned} \tag{2.43}$$

and

$$P^2_{i\rightarrow f} \propto \chi^{\lambda_1}_{i\rightarrow z}\chi^{\lambda_2}_{z\rightarrow f}\chi^{\lambda'_1}_{i\rightarrow z}\chi^{\lambda'_2}_{z\rightarrow f} \; . \tag{2.44}$$

The term $P^{1,2}_{i\rightarrow f}$ includes what is known as the reorientation effect where the intermediate

state in a two-step excitation process is also the final state. For this case, equation (2.43) becomes

$$P_{i\rightarrow f}^{1,2} \propto |<I_f||\mathcal{M}(\sigma\lambda)||I_i>|^2 <I_f||\mathcal{M}(\sigma\lambda)||I_f> \tag{2.45}$$

which is proportional to the product $B(E2; I_i \rightarrow I_f)\,Q(I_f)$ for an even-even nucleus. $Q(I_f)$ is the quadrupole moment of the state $|f>$. The term $P_{i\rightarrow f}^{2}$ corresponds to double excitation in which the role of most high-lying states as intermediate states, apart from the giant dipole resonance, can be ignored. Thus, in second-order perturbation theory, the excitation probability can be written as

$$P_{i\rightarrow f} = B(E2; i \rightarrow f) f(\theta, \xi)[1 + \rho(\theta, \xi) Q(J_f^{\pi})] \tag{2.46}$$

for situations in which $P_{i\rightarrow f}^{2}$ is negligible.

Besides the reorientation effect (which is discussed further in § 3.2) other important higher-order processes are multiple excitation, virtual excitation of the giant dipole resonance and interference effects of low-lying states. Schematic drawings of these processes are shown in fig. 2.1; their treatment is discussed below.

2.4 Multiple Excitation

2.4.1 General Treatment of Multiple Coulomb-Excitation Data

Multiple excitation, that is, excitation via one or more intermediate lower states, occurs with increasing probability as the mass of the projectile increases. This is valuable for the study of states with excitation energies or spins that are too high to be excited by the single-step excitation produced by protons or alpha particles, and has been of particular importance in understanding collective bands with enhanced B(E2)'s, which are strongly populated by multiple-step excitation.

In such experiments, the excitation probabilities for the lowest-lying excited states are relatively large; consequently, the rather simplistic perturbation theory approach is no longer valid. However, the Sommerfeld parameter η is large (≥ 25) for most experimental configurations where $Z_p \geq 2$; in addition, the orbit of heavier projectiles is less affected

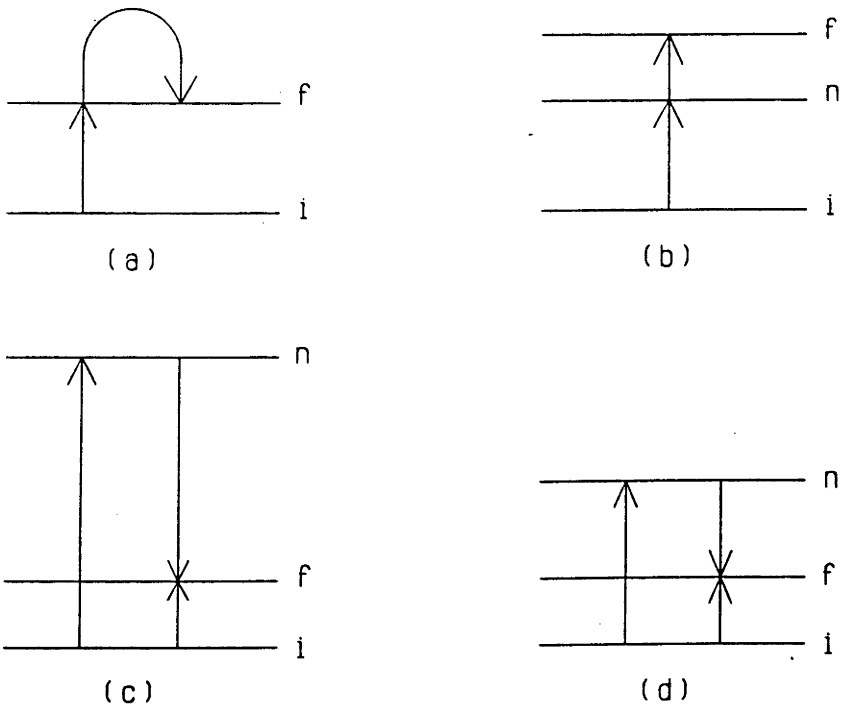

Figure 2.1: Schematic drawings of some higher-order excitation processes, illustrating (a) the reorientation effect, (b) multiple excitation, (c) virtual excitation of the GDR and (d) interference effects from low-lying states. Initial, final and intermediate states are denoted by i, f and n, respectively.

by collisions, i.e., the energy loss, typically less than 1 or 2 MeV, is much smaller than the bombarding energy, which can be of the order of 200 MeV or more. Hence, use of the semi-classical approximation can still be justified and these collisions can be treated as an interaction between a quantized nuclear system and a strong external classical field. Since the energy loss is relatively small, the so-called 'sudden approximation', which assumes that ξ is zero, can also be used.[1]

The main difficulty with analysis of data from multiple-excitation experiments is the high degree of correlation between the various electromagnetic matrix elements of the excited nucleus. This occurs because each state can be excited directly from the ground state as well as by multiple-step excitation via one or more intermediate states. Consequently, the strengths of the transitions involving all the intermediate states will contribute to the total excitation probability; in principle, therefore, a very large number of matrix elements may have to be considered. Clearly, this is not always practical. There

[1]The adiabaticity ξ is a measure of the suddenness of a head-on collision. As mentioned earlier, large values of ξ correspond to an adiabatic process.

are two approaches to this problem : one can either use a nuclear model like the harmonic vibrator or rigid rotor as a basis for calculating cross-sections for the intermediate states or only consider matrix elements for a finite number of states. The former procedure is useful for comparison of model predictions with experimental values. The latter is more common in experimental physics as it is not model-dependent; the Winther-de Boer multiple Coulomb-excitation code (Wi66) employs this method. This program uses values given by the user for the reduced nuclear matrix elements to generate coupled differential equations in a similar manner to that outlined in § 2.2. These equations are solved by using numerical integration techniques to obtain excitation probabilities which depend on the spin, parity and excitation energy of the nuclear states involved and on the magnitude and phase of the matrix elements used. Limits to the number of states and matrix elements can be set by determining which states are of sufficiently high excitation energy that they have little or no effect on the predicted excitation probabilities. In addition, it is possible to insist that the maximum number of intermediate steps in a transition is of the order of $\chi^{E\lambda}_{i\mapsto f}$ because the time for any given single-step transition to occur is $\tau_{coll}/\chi^{E\lambda}_{i\mapsto f}$ and so the maximum number of steps in the collision time τ_{coll} is $\chi^{E\lambda}_{i\mapsto f}$. Classically, this is reflected in the maximum value for the angular momentum transfer $\Delta l_{max} \leq \hbar\lambda(\chi^{E\lambda}_{i\mapsto f})^{\lambda}$ for any given multipolarity λ.

Alternatively, one can diagonalize the so-called χ matrix. This method is explained in Al60 and Al75. The basic idea is to write the matrix elements in the form

$$< I_m M_m \mid \frac{1}{\hbar}\int_{-\infty}^{\infty} V_E(t)dt \mid I_n M_n > \simeq \chi_{\rm eff}\rho^{\lambda\mu}_{mn}\delta_{M_m M_n} \qquad (2.47)$$

where the elements of the symmetric matrix ρ are defined in terms of the reduced matrix elements connecting the ground state and first excited state :

$$\rho^{M_m M_n}_{mn} = (-1)^{I_m - M_m + 1}\sqrt{(2I_0+1)(2\lambda+1)}\begin{pmatrix} I_m & \lambda & I_n \\ -M_m & \mu & M_n \end{pmatrix}\frac{< I_m \| \mathcal{M}(E\lambda) \| I_n >}{< I_0 \| \mathcal{M}(E\lambda) \| I_1 >} \qquad (2.48)$$

and the parameter $\chi_{\rm eff}$ is defined by

$$\chi_{\rm eff} = \frac{3}{4\pi} J_{2,0}(\theta_{lab}) \chi^{\lambda}_{0\to 1} \tag{2.49}$$

where $J_{2,0}(\theta_{lab})$ is a Bessel function. The elements of χ are then grouped so that all strong transitions ($\chi_{mn} > 1$) are in one group, and the other groups contain elements which are strongly coupled to other elements within the group but weakly coupled to elements in other groups. Each group is diagonalized separately. The advantage of the diagonalization method is that the expansion can usually be terminated after the first or second term. The rapidity of convergence is determined by ξ and χ; for example, if ξ=0 then the first term alone is significant. Thus, in the limit $\xi \to 0$, the dependence on bombarding energy can be extracted, provided only one multipolarity is important; similarly, the dependence on scattering angle can be removed if the approximation that μ=0 is made. This approximation is quite accurate at backward scattering angles since, in the coordinate system where the z-axis is aligned with the symmetry axis, the rotational invariance of the Hamiltonian with respect to the z-axis gives conservation of magnetic quantum number. Two of the major consequences of this are that $R_{E\lambda,\mu}$ vanishes for $\mu = \pm 1$, and, for $\mu = \pm 2$, $R_{E\lambda,\mu}$ vanishes at $\pi = 0$ and is small everywhere else. For back angles, $R_{E\lambda,0} \to 1$ as $\theta \to \pi$. At forward angles, it is more convenient to use perturbation theory since the excitation probability $P \simeq |\chi|^2$.

Until recently the simultaneous determination of matrix elements from many states was not feasible, due to the large amount of CPU time needed to solve the coupled differential equations numerically. In the last ten years, developments in computer technology have now made this type of work possible. Two of the better-known programs which have been employed in this way are GOSIA and ALADIN. GOSIA (Cz83) makes use of a so-called "fast approximation" to calculate the excitation amplitudes; the approximation is pictorially described by Wu (Wu83t) as approximating the sine wave shape of the collision wave function by a square wave. ALADIN is a package developed at GSI which reduces the computation time by taking the correlation between the many matrix elements into account (Gr84). These programs are discussed in more detail in § 4.3.

2.4.2 Particle-Gamma Coincidence Measurements

Many Coulomb-excitation experiments involve the measurement of angular correlations of γ-rays which have been emitted from excited target nuclei. These angular correlations can be used to determine the multipolarity of the transition, the spins of the states involved, mixing and branching ratios and, of course, electromagnetic matrix elements.

The γ-ray angular correlation of a transition of multipolarity λ from state $|f>$ to ground state $|0>$ can be written (Al75)

$$W(\theta_p,\theta_\gamma) = \sum_{k=0,2,4} F_k(\lambda\lambda I_0 I_f) a_k^{E\lambda}(\theta_p,\xi) \frac{1}{\gamma_{n\to f}} [\sum_{LL'} F_k(LL' I_n I_f)\delta_L \delta_{L'}^*] P_k(cos\theta_\gamma) \quad (2.50)$$

where $\gamma_{n\to f}$ is the decay rate for a transition to state $|f>$ from $|n>$ and the geometrical coefficient is defined as

$$F_k(LL'I_2I_1) = (-1)^{I_1+I_2-1}\sqrt{(2k+1)(2I_1+1)(2L+1)(2L'+1)} \begin{pmatrix} L & L' & k \\ 1 & -1 & 0 \end{pmatrix} \times \begin{Bmatrix} L & L' & k \\ I_1 & I_1 & I_2 \end{Bmatrix} . \quad (2.51)$$

The particle parameter $a_k^{E\lambda}(\theta,\xi)$ is the ratio of $b_{k0}^{\lambda\lambda}(\theta,\xi)$ to $b_{00}^{\lambda\lambda}(\theta,\xi)$ where

$$b_{k\kappa}^{\lambda\lambda'} = \frac{-1}{\sqrt{2k+1}} \begin{pmatrix} \lambda & \lambda' & k \\ 1 & -1 & 0 \end{pmatrix}^{-1} \sum_{\mu,\mu',\kappa} (-1)^{\mu'} \begin{pmatrix} \lambda & \lambda' & k \\ \mu & -\mu' & \kappa' \end{pmatrix} R_{E\lambda,\mu} R_{E\lambda',\mu'} D_{\kappa'\kappa}^k (\frac{\pi}{2}, \frac{\pi+\theta}{2}, \pi) \quad (2.52)$$

where $R_{E\lambda,\mu}, R_{E\lambda',\mu'}$ are the orbital integrals defined earlier and $D_{\kappa'\kappa}^k$ is the rotation matrix as defined by Bohr and Mottelson (Bo69). The summation includes even values of μ,μ' and κ only. Equation (2.50) is derived using a coordinate system in which the z axis is along the direction of the incoming projectile. To obtain equation (2.50) several assumptions have been made (Bo84) :

(a) the system has axial symmetry (e.g. using an annular particle detector),

(b) the observed angular correlation is integrated over time,

(c) there is no deorientation (perturbation of the angular correlation by the hyperfine electromagnetic fields at the nucleus),

(d) none of the states involved are linearly or circularly polarized,

(e) parity is conserved,

(f) there are no coincidences between two or more γ-ray detectors, and

(g) the highest multipole moment considered is quadrupole.

The consequences of these assumptions are to make $a_k^{E\lambda}$ independent of time and to make only k=0,2,4 terms non-zero.

In the situation where a γ-ray comes from a state that is not fed by de-exciting γ-rays, equation (2.50) can be simplified to the form

$$W(\theta) = \sum_{k=0,2,4} F_k(\lambda\lambda I_i I_f) a_k^{E\lambda}(\xi) P_k(cos\theta) \ . \tag{2.53}$$

The geometrical coefficients are normalized so that $F_0(\lambda\lambda I_i I_f) = 1$; values of F_k can be calculated easily or found in tables such as those of Yamazaki (Ya67).

In most coincidence experiments thick targets have to be used to compensate for the low counting rates. As the projectiles pass through the target, they lose finite amounts of energy, thus changing the effective bombarding energy and hence the cross-section. This energy loss is described in terms of the stopping cross-section $S(E)$, which is in units of energy divided by target thickness, and is a property of the target and projectile combination. Semi-empirical formulae for calculating $S(E)$ can be found in many references, including Northcliffe and Schilling (No70) and Ziegler (Zi80). Many tables and graphs of predictions of these formulae are also included in the references. The uncertainty in the extrapolation of $S(E)$ for heavy ions from proton or alpha data is usually estimated to be about 10% (Zi80). In the present work the formulae given by Ziegler (Zi80) were used; the values obtained for the stopping cross-sections were employed to calculate γ-ray yields as described in § 4.4.4.

2.5 Deviations And Corrections

2.5.1 Symmetrization and Quantal Corrections

One of the assumptions made in the semi-classical theory of Coulomb excitation is that the kinetic energy of the projectile after the collision is the same as its initial kinetic energy. This assumption becomes less justifiable for lighter mass projectiles which will tend to lose more kinetic energy in a collision. It is more accurate to use some sort of mean velocity to make the derived expression symmetric with respect to the interchange of initial and final velocities. The WKB approximation has been used by Alder and Winther to derive the following symmetrized equations (Al75) :

$$\xi_{fi} = \frac{Z_p Z_t e^2}{\hbar}[v_f^{-1} - v_i^{-1}] \tag{2.54}$$

$$a_{fi} = \frac{Z_p Z_t e^2}{m_0 v_f v_i} \tag{2.55}$$

$$\chi_{fi}^{E\lambda} = \frac{\sqrt{16\pi} Z_p e(\lambda-1)! < f\|\mathcal{M}(E\lambda)\|i>}{\sqrt{v_i v_f}\hbar(2\lambda+1)!! a_{fi}^{\lambda}\sqrt{2I_f+1}} \tag{2.56}$$

$$\chi_{fi}^{M\lambda} = \frac{\sqrt{16\pi} Z_p e(\lambda-1)! < f\|\mathcal{M}(M\lambda)\|i>}{\sqrt{v_i v_f}\hbar(2\lambda+1)!! a_{fi}^{\lambda}\sqrt{2I_f+1}} \tag{2.57}$$

$$d\sigma(i\rightarrow f) = \frac{v_f}{4v_i} P(i\rightarrow f) a_{fi}^2 \csc^4(\frac{\theta_{CM}}{2}) d\Omega \tag{2.58}$$

where v_i and v_f are the asymptotic relative velocities corresponding to states $|i>$ and $|f>$ and m_0 is the reduced mass. Qualitatively, equation (2.58) can also be arrived at by considering the consequences of the principle of detailed balance (time-reflection invariance) from which one would expect to be able to write the cross-section for inelastic scattering as

$$d\sigma/d\Omega = f(v_i, v_f)\frac{v_f}{v_i} , \tag{2.59}$$

where $f(v_i, v_f)$ is some function which is symmetric with respect to the interchange of v_i and v_f. The above equations are valid for multiple excitation in which two conditions

$$(2I_i+1)v_i^2 d\sigma(i\rightarrow f) = (2I_f+1)v_f^2 d\sigma(f\rightarrow i) \tag{2.60}$$

$$\sum_f P(i\rightarrow f) = 1 \tag{2.61}$$

need to be fulfilled. However, the symmetrized expression for a_{fi} results in slightly different projectile orbits for each state. Consequently, when excitation probabilities are calculated for a number of states, the calculations should be carried out using only one of those states as the final state $\mid f >$ to prevent violation of the unitarity condition [equation (2.61)].

Although most of the effect of the finite energy loss of the projectile can be accounted for by the symmetrization procedure, the WKB calculations are not exact for finite values of η. They differ from the quantum-mechanical results by terms of the order of η^{-1} in some cases and η^{-2} in others. Quantal corrections to the differential cross-section are of the order of η^{-2}; in the case of the reorientation effect, the corrections to $\rho(\theta,\xi)$ [cf. equation (2.46)] are of the order of η^{-1}. Figs. 2.2a and b are plots of $dc_{E2}/d\Omega$ and e, the correction coefficients for the differential E2 cross-sections and for the reorientation effect respectively (i.e. the coefficients of the η^{-2} and η^{-1} terms), vs. ξ for varying values of θ. Note that in general, the magnitude of the corrections decreases as the scattering angle approaches 180°; this is another advantage of using backward scattering angles. Values

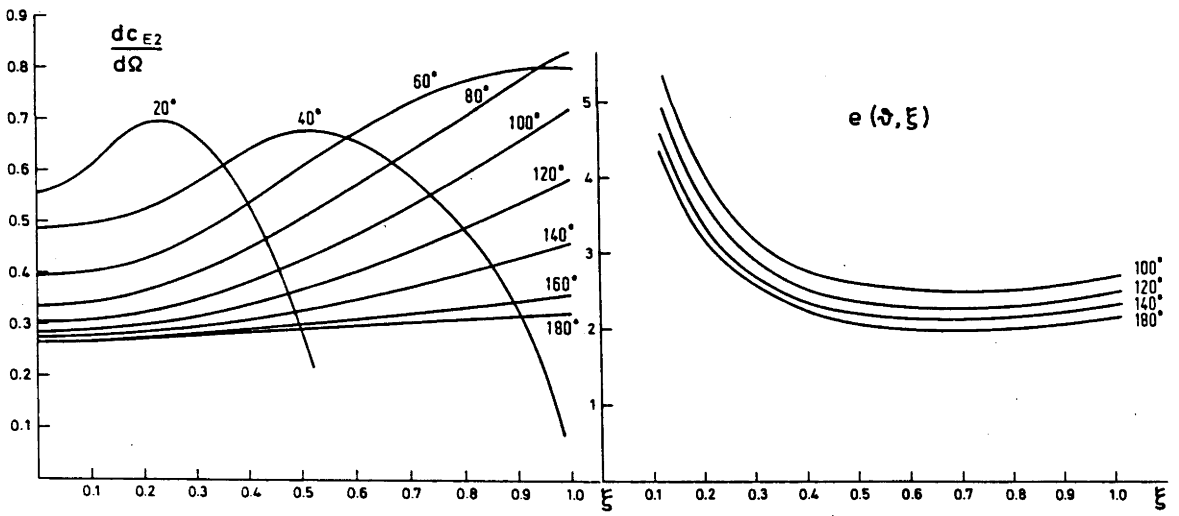

Figure 2.2: The quantum mechanical corrections $dc_{E2}/d\Omega(\theta,\xi)$ and $e(\theta,\xi)$ for (a) the differential quadrupole cross-section coefficient and (b) the reorientation coefficient as a function of ξ for a range of values of θ (taken from Al75).

of η and ξ for the various experimental configurations used in the present work are listed in table 2.1. The tabulated values of η^{-1} and η^{-2} indicate that corrections to extracted transition probabilities will be significant for data obtained with ^{4}He and ^{7}Li projectiles

Table 2.1: Values of η and ξ for the experiments in the present work.

Target	Proj	E_p[a] (MeV)	θ_{lab}[b]	η	η^{-1} ($\times 10^{-2}$)	η^{-2} ($\times 10^{-3}$)	ξ[c]
^{192}Os	^{4}He	14.2–16.5	171°	12–13	8	6.4	0.08–0.09
^{192}Os	^{12}C	44–47	155°	36–38	3	0.9	0.08–0.09
^{192}Os	^{12}C	40–55	175°	34–39	3	0.9	0.07–0.10
^{194}Pt	^{4}He	14–16	175°	12–13	8	6.4	0.13–0.40
^{194}Pt	^{12}C	42–46	170–175°	38–39	3	0.9	0.14–0.39
^{196}Pt	^{4}He	14.2–15.8	169–175°	12–13	8	6.4	0.14–0.29
^{196}Pt	^{7}Li	22.0–22.5	164–170°	21	5	2.5	0.17–0.30
^{196}Pt	^{12}C	42–46	170–175°	38–39	3	0.9	0.15–0.31
^{196}Pt	^{58}Ni	214–226	168°	175–179	0.6	0.036	0.14–0.35
^{198}Pt	^{4}He	15.6	175°	12.4	8	6.4	0.17
^{198}Hg	^{12}C	54	90°	36	3	0.9	0.95
^{200}Hg	^{12}C	54–55	90°	35–36	3	0.9	0.92–0.95
^{202}Hg	^{12}C	54–55	90°	35–36	3	0.9	0.92–0.95
^{204}Hg	^{12}C	54–55	90°	35–36	3	0.9	0.92–0.94

[a]) range of bombarding energies used
[b]) scattering angle in the laboratory system (to nearest degree)
[c]) calculated for the transitions considered in present work; the minimum value is that for the $0_1^+ \rightarrow 2_1^+$ transition in the case of the Os and Pt nuclei.

only, while quantum-mechanical corrections to quadrupole moments must be considered for all the projectiles used except ^{58}Ni.

Quantal corrections to the angular correlation of emitted γ-rays from an excited target nucleus are of the order of η^{-1}, as in the case of the reorientation effect. The particle parameters $a_k^{E\lambda}(\xi)$ in equation (2.53) are changed by quantum-mechanical corrections to

$$a_k^{E\lambda}(\xi)' = a_k^{E\lambda}(\xi) - d_k^{E\lambda}(\xi)\eta^{-1}. \tag{2.62}$$

The variation of the correction coefficient $d_k^{E\lambda}(\xi)$ with ξ is shown in fig. 2.3 for the case of $E2$ excitation. Values of ξ for the angular correlation measurements with ^{58}Ni projectiles

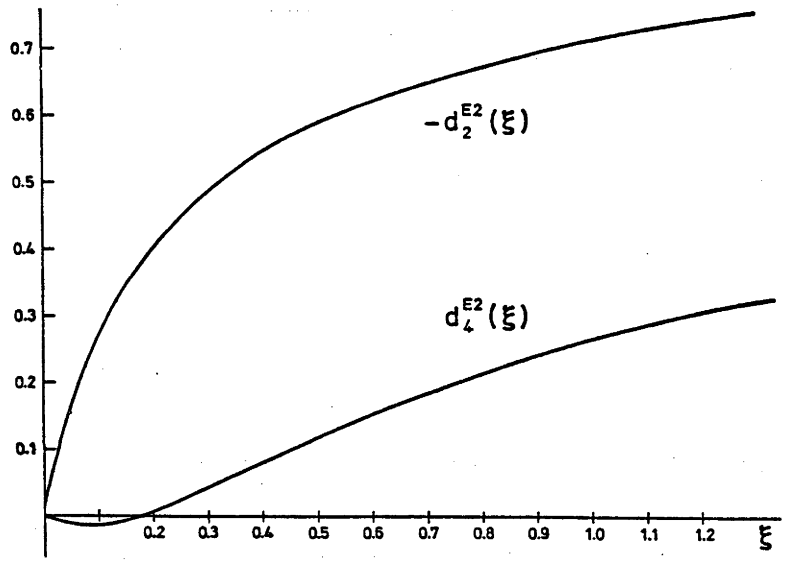

Figure 2.3: The quantum mechanical corrections $d_k^{E2}(\xi)$ for the particle parameters as a function of ξ for a range of values of θ (taken from Al75).

(described in chapter 4) range from 0.14 to 0.35, while η^{-1} is $\sim$ 0.006 (cf. table 2.1); this results in a correction of 0.5% for a_2^{E2}. The values of d_4^{E2} are less than 0.1 for these values of ξ, corresponding to a correction of less than 0.05% for a_4^{E2}.

An example of a code which incorporates quantum-mechanical calculations for Coulomb excitation is AROSA (Ro74). This program is limited to cases with J $\leq$ 8 and $\eta \leq$ 30. More recent work has produced a number of iterative procedures which could extend the feasibility of such calculations beyond their former limits. The majority (To79, Al77, Ic77) follow an 'inward-outward' method in which the second-order coupled differential equations are re-written as two sets of coupled first-order differential equations which

are solved exactly for boundary conditions at r = ∞ and approximately for conditions at r = 0. Alder *et al.* also propose a second method which gives an exact solution for the excitation amplitudes $a_n^{\pm}(r)$ (Al77) and improves the fit to the boundary conditions during successive iterations. Both methods are claimed to produce excellent agreement within two iterations; Alder *et al.* recommend the second as it requires less computing effort but stress that it is not suitable for situations in which a nuclear force must be incorporated into the calculations.

A simpler way of implementing these quantal corrections in the case of the 2_1^+, 2_2^+ and 4_1^+ states of an even-even nucleus is to use the expressions derived by Alder *et al.* (Al72) for corrections to the excitation probabilities :

$$P(2_1^+) = (\chi^{(2)}_{0\to 2})^2 p_2(\theta,\xi)[1 + x_2(0,2,2)c(\xi,0,\theta) + x_2(0,2',2)c(\xi_{0\to 2'},\xi_{2'\to 2},\theta)] \tag{2.63}$$

$$P(2_2^+) = (\chi^{(2)}_{0\to 2})^2(\chi^{(2)}_{2\to 2'})^2 \Pi_2(\xi_{0\to 2},\xi_{2\to 2'},\theta) \tag{2.64}$$

$$P(4_1^+) = (\chi^{(2)}_{0\to 2})^2(\chi^{(2)}_{2\to 4})^2 \Pi_4(\xi_{0\to 2},\xi_{2\to 4},\theta)[1 + d(\xi_{0\to 2},\xi_{2\to 4},\theta)/x_4(0,2,4) + (x_4(0,2,4))^{-2} a(\xi_{0\to 2},\xi_{2\to 4},\theta)] \tag{2.65}$$

where

$$x_2(i,n,f) = \chi^{(2)}_{i\to n}\chi^{(2)}_{n\to f}/\chi^{(2)}_{i\to f} \tag{2.66}$$

$$x_4(i,n,f) = \chi^{(2)}_{i\to n}\chi^{(2)}_{n\to f}/\chi^{(4)}_{i\to f} \tag{2.67}$$

and the functions $\Pi_2, \Pi_4, c, \tilde{c}, d, a$ and p_2 are tabulated in Al72 for different values of ξ, θ and η. Higher-order terms are neglected. This method was used in the analysis of the data described in chapters 3 and 4. Quantal corrections were not included in the extraction of the E3 transition probabilities obtained for Pt and Hg (chapter 5) as the statistical uncertainties were large enough to make this unnecessary.

2.5.2 Relativistic Effects

Relativistic effects are expected to be of the order of $(v/c)^2$. Bombarding energies in Coulomb excitation are typically about 4 MeV/amu, and this corresponds to a value of $(v/c)^2$ of about 0.8%. Since excitation probabilities are now commonly measured with precision of the order of 1%, the consideration of relativistic corrections is important. At the moment there is no theory that is generally accepted as applicable to all Coulomb-excitation experiments.

Alder and Winther (Al75) suggested that in general, relativistic effects can be accounted for by a change in projectile energy

$$\Delta E_p = \frac{-E_p^2[1 - \sin(\theta/2)]}{2m_0c^2[1 + \sin(\theta/2)]}[1 + 2\sin(\theta/2)] \; . \tag{2.68}$$

They pointed out that this is rather smaller than the off-the-cuff estimate of $(v/c)^2$ and that the reason for this difference is not apparent.

Fewell (Fe84) considered the case where $\theta = 180°$, i.e. backward scattering. He calculated the orbit of the projectile in the rest frame of the centre of inertia of the two particles, assuming that both nuclei are classical point charges. Next, the scalar (electric) potential of the exciting nucleus was expanded in multipole moments about the centre of mass of the nucleus. Only the scalar potential was considered as there is effectively no magnetic excitation in backscattering. Finally, the potential was used as a perturbation in time-dependent perturbation theory. Fewell expressed some doubt about the validity of this latter step due to the uncertainty in the form of a term describing the strong interaction between the nuclei but asserted that this term will probably have no significant effect provided only states of one parity are considered. This theory has not yet been tested experimentally. It should be applicable to many Coulomb excitation studies, for instance, those of collective states in even-even nuclei. Fewell calculated the corrections to the Coulomb excitation probabilities of the ground state band of ^{194}Pt for three different mass and charge distributions; he carried out these calculations for 63 MeV ^{16}O, 230 MeV ^{58}Ni and 550 MeV ^{136}Xe projectiles. He found that variation of the mass and charge distributions had little effect for states below the 8^+. The average

Table 2.2: Relativistic corrections as a percentage of calculated Coulomb excitation probabilities for the ground state band of ^{194}Pt, assuming $\theta = 180°$ (from Fe84); statistical uncertainties for measured excitation probabilities for the ground state band of ^{196}Pt, obtained with 220 MeV ^{58}Ni projectiles in the present work.

	63 MeV ^{16}O	230 MeV ^{58}Ni	550 MeV ^{136}Xe	220 MeV ^{58}Ni
J^π	% correction[a])	% correction[a])	% correction[a])	% statistical uncertainty
2^+	−0.7	−1.7	−0.5	5.2
4^+	+0.1	+3.1	−3.9	7.3
6^+	+1.9	+7.2	+3.4	12.2
8^+	–	+11.4	+9.8	–
10^+	–	+15.6	+14.4	–

[a]) mean of the three values given in Fe84

of his results for the different mass and charge distributions are given in table 2.2. The size of the corrections is expected to be proportional to the number of intermediate states in a transition, and this is reflected by the tabulated results. Fewell also calculated the effect of relativistic corrections on $B(E2;0_1^+ \rightarrow 2_1^+)$ and $Q(2_1^+)$ for ^{198}Hg and found that while the correction to $Q(2_1^+)$ (+0.02 e b) was small compared to the uncertainty in the measured value (0.12 e b), the change in $B(E2;0_1^+ \rightarrow 2_1^+)$ (-0.024 e^2b^2 compared with an uncertainty of 0.006 e^2b^2) was significant.

The statistical uncertainties obtained for 220 MeV ^{58}Ni projectiles on a ^{196}Pt target in the present work, as listed in table 2.2, can be compared with the corrections calculated by Fewell for the case of 230 MeV ^{58}Ni projectiles on a ^{194}Pt target since the excitation energies of the ground state band in ^{194}Pt and ^{196}Pt are very similar. The statistical uncertainties quoted for the measured excitation probabilities in ^{196}Pt are significantly larger than the corrections calculated by Fewell for states with the same spins and sim-

ilar excitation energies in ^{194}Pt. In addition, the values of $(v/c)^2$ for the experiments described in this thesis are listed in table 2.3 together with the minimum uncertainty in the excitation probability ΔP_{min} measured for each projectile-target combination. It can be seen from comparison of the two columns in table 2.3 that ΔP_{min} is significantly larger than $(v/c)^2$ in all cases. These results indicate that relativistic effects are minor and probably negligible for the present work.

2.5.3 Deviations from the Coulomb Potential

There are several phenomena which affect the Coulomb potential by small but significant amounts. It is conventional to assume (Al75, Fe78t) that the predominant effect on the Coulomb potential $Z_p Z_t e^2/r$ is associated with a change in the distance of closest approach $2a$. Alder and Winther (Al75) estimated this change to be

$$\frac{\Delta(2a)}{2a} \simeq \frac{\Delta V}{E_p}[1 + \sin(\theta/2)]/2 \tag{2.69}$$

where ΔV is calculated at the distance of closest approach. In the laboratory frame this results in an effective decrease in the bombarding energy of

$$\Delta E_p = \frac{1}{2}\Delta V(1 + \frac{A_p}{A_t})[1 + \sin(\theta/2)] \, . \tag{2.70}$$

The three phenomena which are usually considered to be of significance are vacuum polarization, nuclear polarization and electron screening. The first of these occurs when virtual electron-positron pairs are created and annihilated. The term 'nuclear polarization' refers to the polarization of a colliding nucleus due to the Coulomb field of the other nucleus. Electron screening is caused by the reduction by atomic electrons of the repulsive Coulomb interaction between two nuclei. Contributions from these phenomena to the potential are described respectively by the following expressions (Fe78t) :

Table 2.3: Values of $(v/c)^2$ and ΔP_{min} for the various experimental configurations used in the present work.

Target	Projectile	E_p[a] (MeV)	θ_{lab}[b]	$(v/c)^2$	ΔP_{min}[c]
^{192}Os	^{4}He	14.2–16.5	171.3°	$1.59 - 1.85 \times 10^{-4}$	5×10^{-3}
^{192}Os	^{12}C	44–47	155.25°	$4.92 - 5.26 \times 10^{-4}$	1×10^{-2}
^{192}Os	^{12}C	40–55	174.8°	$4.47 - 6.15 \times 10^{-4}$	1×10^{-2}
^{194}Pt	^{4}He	14–16	174.8°	$1.55–1.77 \times 10^{-4}$	4×10^{-3}
^{194}Pt	^{12}C	42–46	170–175°	$4.65 - 5.09 \times 10^{-4}$	4.5×10^{-3}
^{196}Pt	^{4}He	14.2–15.8	168.7–174.8°	$1.56–1.73 \times 10^{-4}$	2.5×10^{-3}
^{196}Pt	^{7}Li	22.0–22.5	164.0–169.9°	$2.41 - 2.46 \times 10^{-4}$	5.3×10^{-3}
^{196}Pt	^{12}C	42–46	170–175°	$4.605.04 \times 10^{-4}$	2.5×10^{-3}
^{196}Pt	^{58}Ni	214–226	168°	$2.34–2.48 \times 10^{-3}$	5.3×10^{-2}
^{198}Pt	^{4}He	15.6	174.8°	1.69×10^{-4}	2.1×10^{-1}
^{198}Hg	^{12}C	54	90°	5.86×10^{-4}	2.8×10^{-1}
^{200}Hg	^{12}C	54–55	90°	$5.80 - 5.90 \times 10^{-4}$	9.6×10^{-2}
^{202}Hg	^{12}C	54–55	90°	$5.74 - 5.85 \times 10^{-4}$	8.3×10^{-2}
^{204}Hg	^{12}C	54–55	90°	$5.68–5.79 \times 10^{-4}$	1.3×10^{-1}

[a]) range of bombarding energies used
[b]) mean scattering angle in the laboratory system
[c]) $P(3_1^-)$ for Hg and ^{198}Pt; $P(2_1^+)$ for other nuclei

$$\Delta V_{vp} = 2.33\frac{Z_p Z_t}{r}[\ln\frac{386}{r} - 1.411] \text{ keV} \quad (2.71)$$

$$\Delta V_{np} = -2.52r^{-4}[A_p^{5/3}Z_t^2 + A_t^{5/3}Z_p^2] - r^{-6}[\frac{0.88(A_pA_t)^{5/3}}{A_p^{0.234} + A_t^{0.234}} + 1037(Z_t^2\alpha_p^{(2)} + Z_p^2\alpha_t^{(2)})] \text{ keV} \quad (2.72)$$

$$\Delta V_{es} = (-32.65Z_pZ_t^{7/5} + 22.85fZ_p^2Z_t^{2/5})10^{-3} \text{ keV} \quad (2.73)$$

where r, the distance between the centres of the two nuclei, is in femtometres, f is the fraction of orbital electrons of the target nucleus with velocities higher than that of the projectile (assumed to be 0.5) and the quadrupole polarizabilities of the target and projectile, $\alpha_t^{(2)}$ and $\alpha_p^{(2)}$, are

$$\alpha^{(2)} = 5.027[\frac{B(E2;2_1^+ \rightarrow 0_1^+)}{E_x(2_1^+)} + \frac{[0.0833ZA^{4/3} - B(E2;2_1^+ \rightarrow 0_1^+)]^2}{15.5ZA^{2/3} - E_x(2_1^+)B(E2;2_1^+ \rightarrow 0_1^+)}] \quad (2.74)$$

where the excitation energy of the first 2^+ state, $E_x(2_1^+)$, is in MeV and $B(E2;2_1^+ \rightarrow 0_1^+)$ is in e^2fm^4. The three effects will cancel to some extent; however, for nuclei with a low-lying 2_1^+ state and a large transition strength to that state, the value of $\alpha^{(2)}$ can be quite large, causing the r^{-6} term in equation (2.72) to equal or even dominate the r^{-4} term. When this occurs, as is the case in the even-mass Os and Pt nuclei, the effect of nuclear polarization becomes quite substantial.

2.5.4 Uncertainties due to Assumed Matrix Elements

An uncertainty which is time-consuming to calculate and thus often ignored, is that due to the effect of imprecisely-known matrix elements on the calculated excitation probabilities of observed transitions. The uncertainty in the values assumed for these matrix elements results in a corresponding uncertainty in those matrix elements which are deduced from the measured excitation probabilities. The simplest way of estimating the contribution to the final uncertainty is to vary the value of each assumed matrix element in turn and to add the resultant changes in the measurements in quadrature. However, it should be noted that this can give an overestimate of the total contribution because of the correlation between matrix element values mentioned earlier.

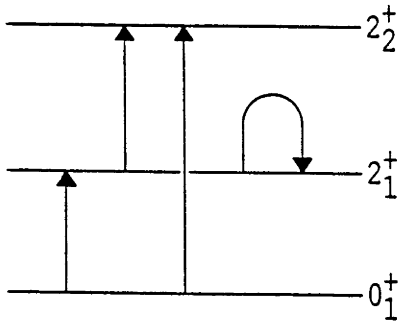

Figure 2.4: Level scheme of a nucleus in which $P_4(2_2^+)$ will affect values extracted for matrix elements involving the 2_1^+ state.

There are two special cases of this uncertainty which are particularly important; they are interference effects from low-lying states and virtual excitation of the giant dipole resonance. These cases are discussed below.

2.5.4.1 Interference effects of low-energy states

Calculated excitation probabilities are sensitive not only to the magnitudes of the matrix elements but also to their relative signs. This is particularly important for states which are connected by strong transitions. Hence, the values deduced for $<2_1^+||\mathcal{M}(E2)||0_1^+>$ and $<2_1^+||\mathcal{M}(E2)||2_1^+>$ in the example shown in fig. 2.4 will depend on the sign of the product $<2_1^+||\mathcal{M}(E2)||0_1^+><2_1^+||\mathcal{M}(E2)||2_1^+><2_2^+||\mathcal{M}(E2)||0_1^+><2_2^+||\mathcal{M}(E2)||2_1^+>$, as well as its magnitude. This product, which is known as $P_4(2_2^+)$, is independent of sign conventions and its sign has been measured experimentally for some nuclei. In the case of a nucleus for which the sign of $P_4(2_2^+)$ is not known, the measured excitation probabilities should be analysed for both situations $P_4(2_2^+) > 0$ and $P_4(2_2^+) < 0$, resulting in two alternative solutions. Similar precautions should be taken to account for the effects of interference from other low-lying states.

2.5.4.2 The effect of the giant dipole resonance

The giant dipole resonance (GDR) is a collection of 1^- states at high excitation energy which are strongly coupled to the ground state by relatively large electric dipole strengths.

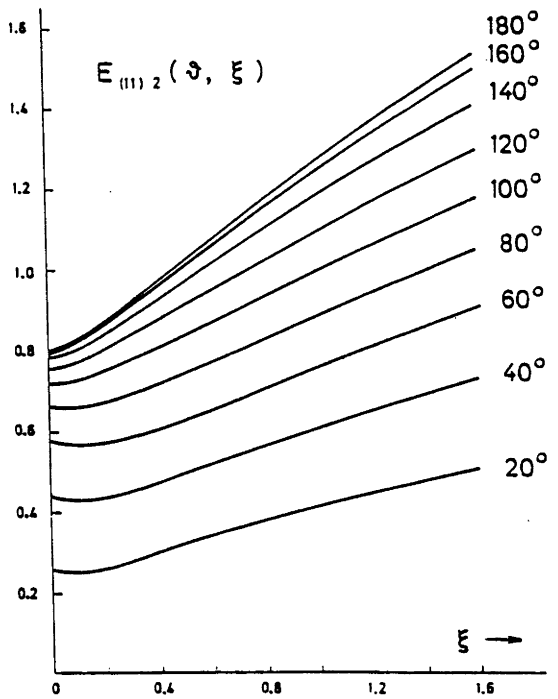

Figure 2.5: The function $E_{(11)2}(\theta,\xi)$, which describes the dipole polarization effect in quadrupole excitation, as a function of the adiabaticity ξ for various values of the scattering angle θ (taken from Al75).

Their major role in Coulomb excitation is to act as intermediate states in the excitation of low-lying states. Alder and Winther (Al75) treated the virtual excitation of the GDR as a polarization of the nucleus by the electric field of the exciting nucleus, resulting in an induced transient $E1$ moment in the former. Using first-order perturbation theory, they estimated the fractional decrease in excitation probability for the 2_1^+ state to be approximately equal to the product $\sum_{\lambda'\lambda''} z(\lambda',\lambda'',\lambda)E_{(\lambda'\lambda'')\lambda}(\theta,\xi)$. Their graph of the function $E_{(11)2}(\theta,\xi)$ vs. ξ for different values of θ is reproduced in fig. 2.5. For the case of virtual excitation to the GDR, when $\lambda' = \lambda'' = 1, \lambda$=2,

$$z_{(11)2} \simeq 0.5 \times 10^{-2} \frac{E_p A_t}{Z_t^2(1 + A_p/A_t)} \tag{2.75}$$

which gives values of z between 1.7×10^{-3} and 2.5×10^{-2} for the work covered in this thesis. The values of ξ for measurements of $B(E2;0_1^+ \rightarrow 2_1^+)$ described in the present work range from 0.07 to 0.17. From fig. 2.5, this corresponds to values of $E_{(11)2}(\theta,\xi)$ between 0.8 and 0.86, so the fractional change in excitation probability is less than 2.2×10^{-2}, which is relatively small.

Alternatively, the hydrodynamic estimate of the polarization potential (Ve84t)

$$V_{pol} = \frac{-hcZ_p^2e^2\sigma_{-2}}{16\pi^3\epsilon_0 r^4}[1 + \frac{8\pi}{3Z_teR_0}\sum_{\mu} M(E2,\mu)Y^*_{2\mu}(\vec{E})] \tag{2.76}$$

where r is the distance between the two nuclei, $\vec{E}$ is the Coulomb field, σ_{-2} is the minus-two moment of the photonuclear absorption cross-section and

$$M(E2,\mu) = 3Z_teR_0^2\alpha_{2\mu}/4\pi \ , \tag{2.77}$$

can be used. The excited nucleus is assumed to have a quadrupole deformation. The electric quadrupole potential V_{EQ} is changed to

$$V'_{EQ} = V_{EQ}[1 - \frac{0.0056akA_tE_p}{Z_t^2(1 + A_p/A_t)r(t)}] \tag{2.78}$$

assuming that the target is excited. Units of E_p and r, a are MeV and femtometres respectively. The parameter k is defined by

$$\sigma_{-2} = 3.5kA^{5/3}\mu\text{b/MeV} \tag{2.79}$$

where k=1.0 gives the semi-empirical hydrodynamic model estimate of σ_{-2} for heavy nuclei (Le57). This form of V_{EQ} is used in the Winther-de Boer program because of the ease with which it can be incorporated into the code.

The Winther-de Boer modification for the GDR does not include depopulation of the ground state due to virtual excitation of the GDR, which results in reduction of the ground state amplitude. A rough estimate of this effect can be obtained by introducing a 1^- state at the appropriate energy and including an E1 transition matrix element of reasonable strength (say, 1 Weisskopf unit) between this state and the ground state. Depopulation is not expected to be important for light projectiles but can result in significant changes to the excitation probability when the projectiles are of mass $\sim$ 50 or higher. Consequently, the effect of depopulation should be insignificant for all the data measured in the present work apart from that obtained with ^{58}Ni projectiles as

described in chapter 4. Calculations of excitation probabilities for the case of ^{58}Ni on ^{196}Pt, assuming a 1^- state at 14 MeV, resulted in a change of about 1.5% for the first excited state, increasing to about 10% for the 4_2^+ and 6_1^+ states (at 1.299 and 1.525 MeV respectively). However, these estimates are themselves uncertain as they depend strongly on the value assigned to the matrix element connecting the GDR to the ground state, which has not been measured in many nuclei.

2.5.5 Nuclear Forces and the 'Safe-Energy' Criterion

As explained in § 2.1, nuclear forces become increasingly important as the energy of the collision approaches the Coulomb barrier. This is manifested as an increasing deviation of experimentally-observed excitation probabilities from the values calculated by the Winther-de Boer code. In general, this deviation becomes significant when the two nuclear surfaces are less than about 5 fm apart. This observation has led to the wide-spread use of criteria such as that proposed by Cline (Cl78) (which states that to obtain reliable measurements of Coulomb-excitation probabilities, the minimum distance between the centres of the two nuclei must be $1.25[(A_p^{1/3} + A_t^{1/3}) + 5]$ fm and at least 1 fm greater than this for reorientation-effect measurements) as a basis for deciding what bombarding energies will be free of Coulomb-nuclear interference effects. However, this criterion is merely intended as a guideline to the choice of suitable energies and in cases where the measured excitation probabilities are quoted to 1% precision, the surest method of eliminating nuclear effects is to collect data over an energy range which is large enough for any significant deviation from calculated values to be noticeable, so that data taken at energies for which the deviation occurs can be omitted from the analysis. This deviation is due to the competition between the repulsive Coulomb potential and the attractive nuclear potential. Nuclear forces are negligible at large distances but predominate when two nuclei are very close together. Fig. 5.7 shows that the exact distance at which the nuclear contribution becomes significant is not always the same for different projectiles; there is also no intrinsic reason why this distance should be the same for different excited states of the target nucleus. In principle, this means that the maximum safe-energy should be determined for each excited state under investigation; however, this is not usu-

ally necessary as the choice of maximum safe energy will depend to some extent on the precision of the measurement of the excitation probability, and excitation probabilities for the higher states are often measured to very low precision. As part of an investigation into the dependence of Coulomb-nuclear interference on the nuclear potential, the excitation probabilities of the first excited state of ^{208}Pb under bombardment with ^{16}O projectiles were measured for a wide range of bombarding energies. Since this work is relevant to the general theory of Coulomb excitation, but not central to the main subject of this thesis, a reprint of the Physics Letters publication of this work is included as Appendix A.

2.5.6 The Effect of Finite Target Thickness

As a beam of projectiles traverses a target, it experiences a finite loss of energy. Thus, the bombarding energy of a projectile at the back of the target will be lower than at the front and consequently, the total excitation cross-section will be lower. If the energy loss is large enough to result in a significant change in cross-section, the observed excitation probability will be smaller than that calculated assuming the initial bombarding energy. This effect can be taken into account by calculating excitation probabilities $P_{calc}(J_n^\pi)$ as the ratio of the cross-section of excitation integrated over the range of projectile energies experienced by the target nuclei to the integrated Rutherford cross-section, i.e. :

$$P_{calc}(J_n^\pi) = \int_{E_i}^{E_f} [\frac{dE}{S(E)} \frac{d\sigma(J_n^\pi)}{d\Omega}] / \int_{E_i}^{E_f} [\frac{dE}{S(E)} \frac{d\sigma(R)}{d\Omega}] \tag{2.80}$$

where $[\frac{d\sigma(J_n^\pi)}{d\Omega}]$ and $[\frac{d\sigma(R)}{d\Omega}]$ are, respectively, the differential cross-sections for excitation to the state J_n^π and for Rutherford scattering at a bombarding energy E which lies in the range E_i, the projectile energy at the front of the target, to E_f, the projectile energy at the back of the target. $S(E)$ is the stopping cross-section calculated from the formulae given by Ziegler (Zi80) as mentioned in § 2.4.2; it is important to remember that $S(E)$ is a function of the bombarding energy.

If the target is sufficiently thin, the change in cross-section and stopping cross-section

may be negligible. In such a situation, the approximation

$$P_{calc}(J_n^\pi) = [\frac{d\sigma(J_n^\pi)}{d\Omega}]/[\frac{d\sigma(R)}{d\Omega}] \tag{2.81}$$

can be made and the effective bombarding energy taken to be the energy of the projectile at the centre of the target.

2.6 Summary

Despite the many corrections and uncertainties which should be included in its analysis, Coulomb excitation is a relatively simple technique and is valuable as a tool for the study of nuclear structure because of its independence from any model assumptions. In recent years, some doubts have been raised about the integrity of results obtained with this technique; one of these was the suggestion that an apparent discrepancy between the results for $Q(2_1^+)$ of ^{192}Os in Coulomb excitation experiments and that from muonic X-ray data (Ho81) could reflect an intrinsic dependence of electromagnetic moment measurements on the probe used (i.e. hadronic scattering as compared with a bound leptonic probe). This proposal of a probe-dependency is discussed in more detail in the next chapter. It will be seen that a discrepancy such as that noted by Hoehn *et al.* often arises from an inadequate treatment of the corrections and uncertainties described above, and that Coulomb excitation can still be considered a reliable and direct means of extracting information on nuclear electromagnetic properties.

Chapter 3

Coulomb Excitation Of ^{192}Os

3.1 Introduction

For many years now the Os and Pt nuclei have been known to lie in a region of nuclear shape transition. In particular, both experimental and theoretical work have provided support for the prediction made by Kumar and Baranger of a prolate-to-oblate transition in the vicinity of ^{192}Os. The results of their Pairing-Plus-Quadrupole (PPQ) calculations (Ku68) showed that a transition of nuclear shape was expected to occur between ^{190}Os and ^{192}Os, and between ^{188}Pt and ^{190}Pt, viz, that Os nuclei with A$\leq$190 would be prolate while those with A$\geq$192 would be oblate; similarly, the Pt nuclei were predicted to be prolate for A$\leq$188 and oblate for A$\geq$190.

Subsequent work has generally concluded that such a transition does indeed occur near ^{192}Os although opinions differ on details like the rate of this transition and the shape of that nucleus. There are also varying predictions on the extent of γ-softness or γ-instability in the Os isotopes. (A γ-unstable or γ-soft nucleus is one in which the potential is independent of γ, the parameter which describes the degree of triaxiality of the nucleus. By one convention, a value of γ=0° corresponds to an axially symmetric prolate nucleus and γ=60° to an axially symmetric oblate one; a triaxial nucleus is indicated by γ=30°. The quadrupole deformation parameter, β_2, is assumed to have positive values only, according to this convention.) For example, Kumar and Baranger have obtained $\gamma \sim 45°$ and $\beta_2 \sim 0.19$ (Ku68a) for ^{192}Os, indicating an oblate shape. The

General Collective Model (GCM) calculations of Sedlmayr *et al.* (Se74) suggest that the Os nuclei change from an axially symmetric deformation at ^{184}Os to a γ-unstable and slightly oblate shape at ^{192}Os. Later GCM calculations by Hess *et al.* (He81) predict that ^{192}Os, ^{192}Pt and ^{194}Pt are all γ-soft and nearly triaxial; however, ^{192}Os is predicted to tend to a prolate shape while the Pt nuclei are predicted to be oblate. Ansari (An88) has proposed on the basis of his Hartree-Fock-Bogoliubov calculations that a sudden transition occurs with a prolate shape for ^{192}Os and an oblate one for ^{194}Os.

Some of the characteristic features of such a transition are (Ku72) :

(a) a change of sign in the quadrupole moment of the first excited state $Q(2_1^+)$,

(b) the crossing of the 2_2^+ and 4_1^+ levels,

(c) a local minimum in the ratio of the excitation energies of the 2_2^+ state and the 2_1^+ state, $E_x(2_2^+)/E_x(2_1^+)$,

(d) a local maximum in the ratio $B(E2;0_1^+ \rightarrow 2_2^+)/E_x(2_2^+)$,

(e) a local maximum in the isotope shift $\Delta<r^2>$, and

(f) a local minimum in the two-neutron transfer cross-section.

The first of these features occurs because the intrinsic quadrupole moment of a nucleus, Q_0, which can be deduced from its observed (spectroscopic) quadrupole moment, is related to the nuclear charge distribution $\rho(r,\theta,\phi)$ by

$$Q_0 = \int \rho(r,\theta,\phi) r^2 Y_{20}(\theta,\phi) d\vec{r} \tag{3.1}$$

where Y_{20} is a spherical harmonic. Positive values of Q_0 correspond to prolate shapes and negative values indicate oblate ones; Q_0 is zero for a spherical nucleus. The spectroscopic quadrupole moment, which is often denoted by one of the symbols Q_s, Q^2 or $Q(J_n^\pi)$, is related to Q_0 in the rotational model by (Bo75)

$$Q^2 = -\sqrt{\frac{16\pi}{5}}\left[\frac{J(2J-1)}{(J+1)(2J+1)(2J+3)}\right]^{1/2} <J\|\mathcal{M}(E2)\|J> \tag{3.2}$$

$$= \frac{3K^2 - J(J+1)}{(J+1)(2J+3)} Q_0 \, . \tag{3.3}$$

Table 3.1: Experimental measurements of $Q(2_1^+)$ in e b for $^{186,188,190,192}Os$ from different techniques.

	Muonic X-rays[a])	Coulomb Excitation[b])	Mössbauer[c])
^{186}Os	−1.63(4)	−1.20(15)	−1.61(3)
^{188}Os	−1.46(4)	−1.33(9)	−1.46
^{190}Os	−1.18(3)	−0.99(7)	−1.26(7)
^{192}Os	−0.96(3)	−0.53(10)	

[a]) from Ho81
[b]) weighted average of Pr70, La72 and Ru78
[c]) from Wa72, normalized to value of $Q(2_1^+)$ for ^{188}Os measured by Ho81

For the ground state band of an even-even nucleus, K, the projection of the angular momentum J on the intrinsic z-axis of the nucleus, is zero; hence

$$Q^2 = \frac{-J}{(2J+3)} Q_0 \tag{3.4}$$

will have the opposite sign to Q_0 for those states.

Values for $Q(2_1^+)$ obtained using three different techniques are listed for each stable even-mass Os isotope in table 3.1. Prior to the present work several reorientation effect measurements of $Q(2_1^+)$ had been made for ^{192}Os, giving a weighted mean of −0.53(10) e b. The earlier of these were by members of the Pittsburgh group, Pryor and Saladin, (Pr70) and Lane and Saladin (La72). These were followed by an unpublished measurement by Russo *et al.* (Ru78) at Rochester. As $Q(2_1^+)$ for $^{186,188,190}Os$ had been measured to be between −1 and −2 e b, the smaller magnitude of $Q(2_1^+)$ for ^{192}Os was believed to reflect a trend towards increased sphericity and vibrational structure (Ca69) and hence towards the oblate shapes predicted by Kumar and Baranger for the heavier Os isotopes. However, in 1977 a significantly different preliminary value of −0.91(3) e b, which is similar in magnitude to that measured for ^{190}Os, was obtained by Hoehn and his collaborators who had completed a series of muonic X-ray measure-

ments of $Q(2_1^+)$ for the stable even-A osmium nuclei (Ho77) using a newly-developed model-independent approach (Wa77) to the analysis of muonic X-ray data. Comparison with reorientation-effect and Mössbauer measurements revealed that although the Mössbauer-effect measurements of quadrupole moment ratios (Wa72) agreed well with those of Hoehn *et al.*, the values of $Q(2_1^+)$ obtained from Coulomb-excitation experiments for the Os isotopes were smaller in magnitude than those obtained from muonic X-rays with the maximum discrepancy occurring at ^{192}Os : the final value obtained from the muonic X-ray experiment was $-0.96(3)$ e b (Ho81) whereas the weighted mean of the Coulomb excitation measurements was $-0.53(10)$ e b. No Mössbauer measurements had been made for ^{192}Os. This discrepancy prompted discussion of the possibility that there might be a fundamental difference between the results from the two techniques, perhaps arising from the difference in the distance of the probe from the excited nucleus. Examination of the uncertainties inherent in the analysis of the muonic X-ray data revealed that the most probable sources of discrepancy could not be responsible for the large differences observed (Ho81). Another reorientation measurement was carried out subsequently by the Pittsburgh group (Ch83) in which a value of $-0.80(18)$ e b, consistent with that from muonic X-ray data, was obtained. However, this apparent agreement may have been misleading as the matrix elements quoted by Chen *et al.* suggest that the sign used for $P_4(2_2^+)$, the interference term involving the 2_2^+ state, was opposite to that determined experimentally by Baker *et al.* (Ba76b). As explained in § 2.5.4.1, the sign of $P_4(2_2^+)$ can have a large effect on the values deduced for $Q(2_1^+)$ and $B(E2;0_1^+ \rightarrow 2_1^+)$. The above-mentioned measurements of $Q(2_1^+)$ for ^{192}Os are summarized in table 3.2.

As the reorientation effect has generally been accepted as providing model-independent and relatively direct measurements of electric moments (Bo68), any dependence of values extracted for $Q(2_1^+)$ on the technique used would be a matter of concern for workers in this field. This could lead one to question the dependability of the results of Coulomb excitation experiments. For example, one might ask if reorientation measurements of $Q(2_1^+)$ for a particular nucleus which have been carried out at different laboratories and analysed by different procedures will give results that agree with each other. It should be noted that experimental evidence of a prolate-to-oblate transition between ^{192}Os and

Table 3.2: Previous measurements of $Q(2_1^+)$ for ^{192}Os.

Authors	$Q(2_1^+)$ (e b)	Experimental procedure
Pryor and Saladin (Pr70)	−0.40(20)	Coulomb excitation
Lane and Saladin (La72)	−0.50(20)	Coulomb excitation
Russo *et al.* (Ru78)	−0.60(13)	Coulomb excitation
Hoehn *et al.* (Ho81)	−0.96(3)	Muonic X-rays
Chen *et al.* (Ch83)	−0.80(18)	Coulomb excitation

^{192}Pt (Gy87) is based largely on comparison of the value of $Q(2_1^+)$ for ^{192}Pt which was measured at ANU by Gyapong *et al.* with those measurements of $Q(2_1^+)$ for ^{192}Os listed in table 3.2. Thus, it was important to see whether a value for ^{192}Os opposite in sign to that of ^{192}Pt would be obtained when the same experimental and analytical procedures were used.

In summary, there was a twofold purpose in measuring $Q(2_1^+)$ for ^{192}Os : firstly, to examine the apparent conflict between the results of muonic X-ray and Coulomb excitation experiments and, secondly, to investigate the prolate-to-oblate transition in the Os and Pt nuclei.

3.2 The Reorientation Effect and the Study of Static Moments

There are four methods commonly in use for measurements of electric and magnetic moments (Hä74); these are Mössbauer and perturbed angular correlation measurements, inelastic scattering, muonic X-ray experiments and reorientation effect experiments. The reorientation effect was given its name by Breit *et al.* (Br56) because one of the observed effects of the interaction between the electric field gradient (EFG) and static electric

moments Q^λ of order λ in Coulomb excitation is the redistribution of magnetic substates of the final state of the nucleus after excitation, which affects the angular distribution of de-exciting γ-rays. The other result of the interaction is an increase in the effective excitation energy of the final state, which causes a decrease in the excitation cross-section. The interaction of the EFG with Q^2 is much larger than the interaction with higher-order moments, so that the reorientation effect provides a direct measure of the quadrupole moment of a state. A detailed discussion of this effect can be found in various references, such as Bo68.

As explained in § 2.3.3, the contribution of the reorientation effect to the excitation probability of a 2_1^+ state is given by the second term in the following equation (Al75) :

$$P(2_1^+) \simeq f(\theta,\xi)B(E2;0_1^+ \rightarrow 2_1^+)[1 + Q(2_1^+)\rho(\theta,\xi)]. \tag{3.5}$$

By introducing a function $K(\theta,\xi)$, this can also be written in the form (Bo68)

$$P(2_1^+) \simeq f(\theta,\xi)B(E2;0_1^+ \rightarrow 2^+)[1 + 1.32\frac{A_p\Delta E_p}{Z_t(1+A_p/A_t)}Q(2^+)K(\theta,\xi)] \tag{3.6}$$

where ΔE_p is the energy lost by the projectile during the collision. To determine $Q(2_1^+)$ using the reorientation effect, the excitation probability of the 2_1^+ state, $P(2_1^+)$, should be measured for at least two different sets of experimental parameters by varying the mass of the projectile, the scattering angle or the bombarding energy. As the function $K(\theta,\xi)$ depends only weakly on the bombarding energy, it is difficult to obtain a value for $Q(2_1^+)$ from measurements of $P(2_1^+)$ where the bombarding energy alone has been changed. However, $K(\theta,\xi)$ varies quite rapidly at forward angles while $\rho(\theta,\xi)$, the sensitivity parameter, is strongly dependent on the projectile mass. Consequently, most reorientation effect experiments use changes in projectile mass and/or scattering angle to obtain values for $Q(2_1^+)$.

It is important to note that equations (3.5) and (3.6) were derived in the context of perturbation theory, which assumes that $P(J_n^\pi)$ is small for all states J_n^π other than the ground state. Since the relatively large magnitudes of the measured excitation probabilities for ^{192}Os (and for all the nuclei considered in this thesis) invalidate this assumption,

the analysis in the present work was not based on these equations. Instead, matrix elements were derived from measured excitation probabilities using the Winther-de Boer multiple Coulomb excitation code (Wi66), which solves the coupled differential equations involving the Coulomb excitation amplitudes [equation (2.13)]. However, equations (3.5) and (3.6) are useful as a means of illustrating the way in which excitation probabilities depend on various experimental parameters and also as the basis for a convenient representation of $B(E2;0_1^+ \rightarrow 2_1^+)$ and $Q(2_1^+)$ (cf. fig. 3.8).

3.3 Experimental Procedures and Analysis

3.3.1 General Experimental and Analytical Procedures for Particle Singles Spectroscopy

The particle singles spectroscopy technique was used to measure the static electric quadrupole moment of the first excited state of ^{192}Os. This is generally seen as the simplest and most straightforward of all techniques in Coulomb excitation, its basic requirements being no more than a beam of suitable projectiles, a target and a particle detector from which a spectrum of the type shown in fig. 3.1 can be obtained. Absolute excitation probabilities $P_{exp}(J_n^\pi)$ are extracted directly from a spectrum by measuring the ratio of the peak areas corresponding to projectiles scattered from nuclei excited to the state of interest and those which have undergone elastic scattering. The excitation probability is sometimes defined as $A(J_n^\pi)/A(0_1^+)$ or $A(J_n^\pi)/[A(0_1^+)+A(J_n^\pi)]$, where $A(J_n^\pi)$ denotes the area of the J_n^π peak. In this thesis, $P_{exp}(J_n^\pi)$ is defined as

$$P_{exp}(J_n^\pi) = \frac{A(J_n^\pi)}{\Sigma_i A(J_i^\pi)} \tag{3.7}$$

where the summation is over all observed states i.

There are several types of detectors in common use in particle spectroscopy (En74). In the present work an annular silicon surface-barrier detector and an Enge split-pole magnetic spectrometer (Sp67) were used. A position-sensitive gas-filled detector oriented so that its surface was perpendicular to the particle trajectory (Op88) was employed

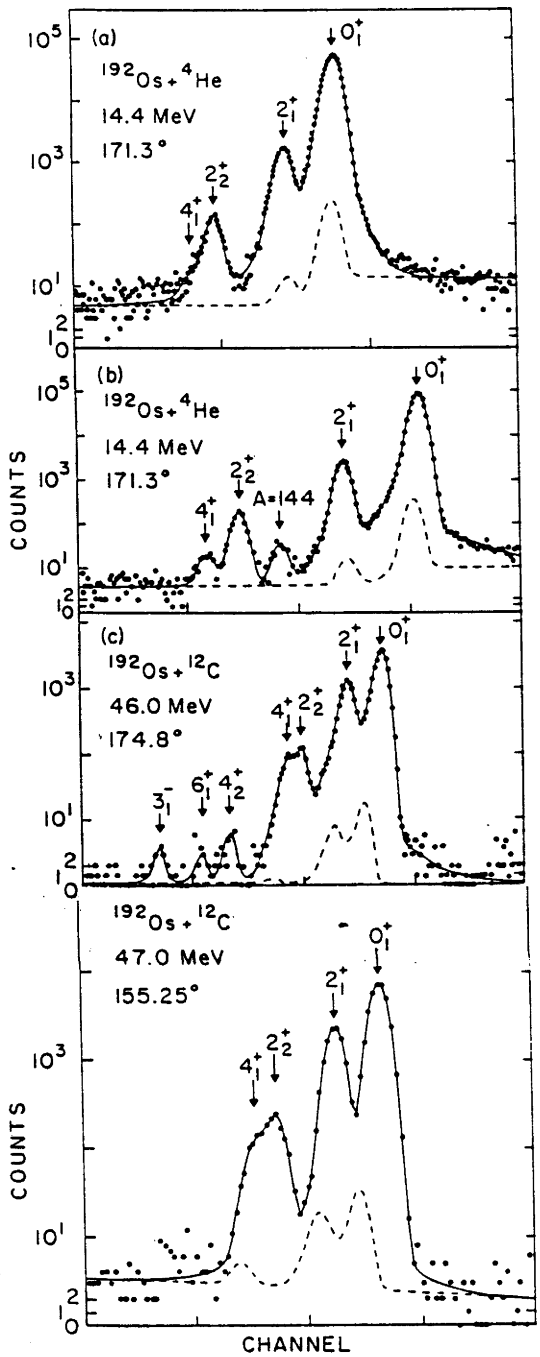

Figure 3.1: Representative spectra for configurations 1 to 4 (cf. table 3.4) respectively. The broken curves show the fitted background, including isotopic impurities. Peaks corresponding to states in ^{192}Os are indicated by J^{π}_{n} values. The peak in (b) labelled "A=144" is due to elastic scattering from a contaminant in the target backing.

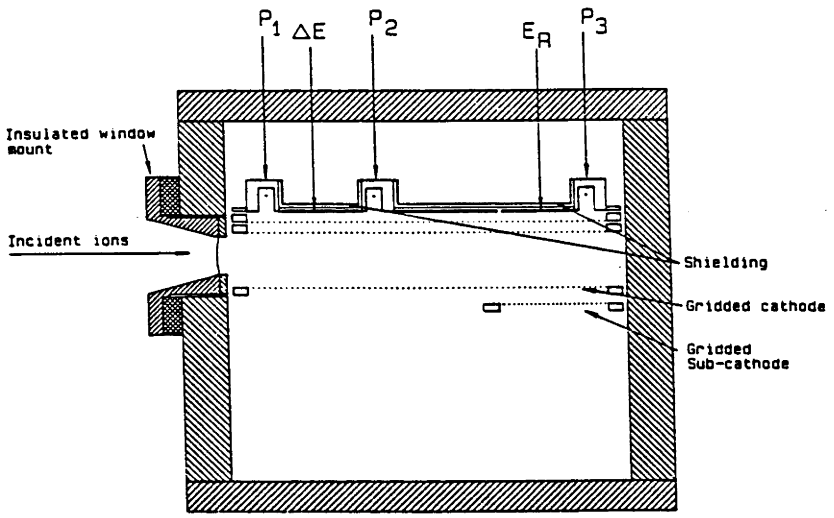

Figure 3.2: Focal-plane detector used in Enge split-pole magnetic spectrometer (taken from Op88). The detector has been modified from the standard model (Op78, see fig. 5.3) to allow for its orientation, which is normal to the scattered beam.

in the latter. Fig. 3.2 shows a cross-sectional view of the detector which is a modified version of that described by Ophel and Johnston (Op78). The major change made is that most electrodes have been constructed from printed circuit board to facilitate changes in electrode dimensions. The detector was filled with isobutane to a pressure of between 180 and 200 Torr. At this pressure, relatively thin (5 μg cm^{-2}) mylar windows can be used at the entrance aperture. The detector design allows acquisition of a number of signals; in this experiment, only the P_1 signal was collected. Appropriate allowances must be made in the fitting procedure for a variation in peak width, which becomes greater as the orientation of the detector moves away from an angle of 45° to the scattered beam.

Diagrams of the experimental arrangements used are shown in fig. 3.3. The target ladder in the target chamber of the Enge spectrometer was cooled by means of a cold shroud to prevent carbon build-up. Targets were inserted and removed through a vacuum lock. The ladder of the other chamber was constructed so as to accomodate up to five targets at any one time; this removed the need to let the chamber up to atmospheric pressure when changing targets. Two annular pieces of tantalum were used to define the acceptance angle of the silicon surface-barrier detector; the acceptance angles of the spectrometer were determined by a set of horizontal and vertical slits.

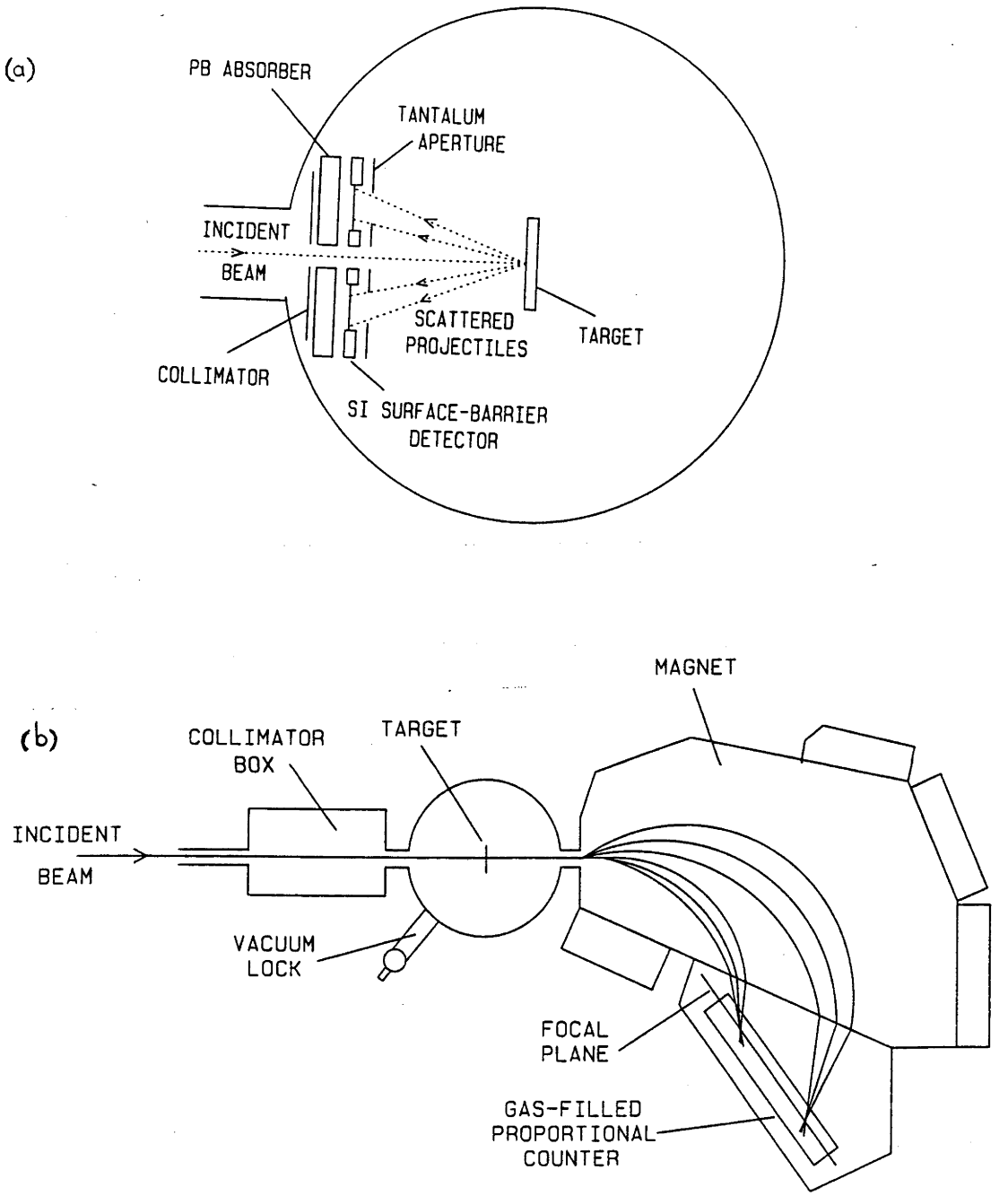

Figure 3.3: Diagrams of experimental arrangements involving (a) an annular silicon surface-barrier detector and (b) the Enge spectrometer.

The intrinsic resolution of a magnetic spectrometer is superior to that of a surface-barrier detector; however, the observed resolution is also dependent on target thickness and uniformity, straggling (statistical fluctuation in the energy of scattered projectiles) and kinematic factors. One advantage of using an Enge spectrometer is the kinematic compensation (Sp67) available which makes the use of larger solid angles possible. This is less important at backward scattering angles as the axial symmetry of an annular detector and the small amount of kinematic broadening at $\theta \sim 180°$ means that the maximum solid angle of an annular detector, which is about an order of magnitude greater than that of other surface-barrier detectors or a spectrometer, can be employed. Multiple pile-up from light contaminants (e.g. ^{12}C) in the target can result in significant background in spectra obtained with a surface-barrier detector; the use of an Enge spectrometer avoids this problem. A major disadvantage of the Enge is the splitting of scattered projectiles according to their charge states into several groups along the focal plane. This distribution of charge states must be considered in the extraction of excitation probabilities.

Analysis of the data was performed in the following way : first of all, the spectrum was fitted using a skew gaussian lineshape with exponential tails (Fe78t, Gy87t). The fit was used to estimate the shape of the background, including contributions from other isotopes of the target nucleus. These contributions are usually present to less than 5% of the isotope of interest when enriched targets are used, so it is generally accurate enough to calculate the contributions of these so-called "isotopic impurities" from the supplier's assay in conjunction with published matrix elements. In fig. 3.1 the dotted line in each spectrum indicates the total background contribution.

Next, contributions from other contaminant nuclei must be considered; this was done by determining the masses of nuclei whose elastic scattering peaks could not be resolved from those of interest and by bombarding the target with projectiles accelerated to an energy at which the elastic peaks of potential contaminants would no longer be masked by peaks due to states of the target nucleus, either because all the contaminant peaks could be resolved from the target peaks, or because the excitation probability for inelastic scattering from the target nucleus was negligible. Examination of data taken

at such energies provides an upper limit to, or a measure of the contribution of, these contaminants.

The fitted contributions from all the above sources were then subtracted from the number of counts in each peak of interest to give the area due to scattering from nuclei excited to the associated state. The measured excitation probabilities $P_{exp}(J_n^\pi)$, derived from the extracted peak areas as defined in equation (3.7), were iteratively fitted with calculated excitation probabilities $P_{calc}(J_n^\pi)$ which were obtained from the Winther-de Boer multiple Coulomb-excitation code (Wi66). Values for some of the matrix elements used in these calculations were varied to obtain a best fit to $P_{exp}(J_n^\pi)$. Corrections were included for electron screening, vacuum polarization, nuclear polarization, the use of the semi-classical approximation and the effects of interference from the GDR by using the formulae given in § 2.5 to calculate the total effect on the calculated excitation probability. A conservative estimate of the effect of virtual excitation from the GDR can be given by assuming that $k = 1.0 \pm 0.5$ [see equations (2.78) and (2.79)]. A correction for the finite energy loss of the projectile as it traverses the target was applied as described in § 2.5.6.

Values of $P_{calc}(J_n^\pi)$ are strongly dependent on the number of states included in the analysis as well as the values assumed for the matrix elements of those states. To decide whether a state should be considered, the effect of its inclusion in the Winther-de Boer program on the value of $P_{calc}(J_n^\pi)$ was determined. States which have negligible effect were omitted to reduce the CPU time required for the calculation. Experimentally determined values from the literature were used where possible; other matrix elements were set to zero. An alternative would have been to use model predictions for those matrix elements for which experimental values were not available. The relative phases of assumed matrix element values can have a large effect on the results obtained. As noted in § 2.5.4.1, $P_{calc}(2_1^+)$ in an even-even nucleus is especially influenced by the sign of the quantity $P_4(2_2^+)$, defined as the product of the four matrix elements $<2_1^+||\mathcal{M}(E2)||0_1^+>$, $<2_1^+||\mathcal{M}(E2)||2_1^+>$, $<2_2^+||\mathcal{M}(E2)||0_1^+>$ and $<2_2^+||\mathcal{M}(E2)||2_1^+>$; similarly, other low-lying states which are strongly coupled to the 0_1^+ or 2_1^+ states may lower (destructively interfere with) or raise (constructively interfere with) $P_{calc}(2_1^+)$, depending on the relative signs of the matrix elements concerned. In the nucleus ^{192}Os, the 4_1^+ and 2_2^+ states

Table 3.3: Percentage isotopic composition of target material, as provided by supplier (Oak Ridge National Laboratory).

Isotope	A[a])	B[a])
^{187}Os	<0.005	0.04
^{188}Os	0.101	0.10
^{189}Os	0.160	0.17
^{190}Os	0.344	0.66
^{192}Os	99.395	99.03

[a]) see table 3.4

are nearly energy-degenerate, so interference from both must be considered.

3.3.2 Data Obtained

In the present experiment ^{4}He and ^{12}C projectiles were used. Some difficulty was experienced in obtaining acceptable spectra; this was mainly due to the extremely low excitation energy of the 2_1^+ state in ^{192}Os (205.8 keV). This was far lower than that of any nucleus previously studied by the ANU group.

The ^{4}He and ^{12}C beams obtained from the ANU 14UD pelletron were used to bombard targets of isotopically enriched osmium, evaporated onto thin carbon foils. The isotopic compositions of the material used is shown in table 3.3. The four experimental configurations used are listed in table 3.4. An annular silicon surface-barrier detector was used in three of the configurations, and an Enge split-pole magnetic spectrometer in the fourth.

A typical spectrum is shown for each configuration in fig. 3.1. The effects of target thickness on spectrum quality are evident when figs. 3.1a and 3.1b are compared; reduction of the target thickness results in a clear improvement of resolution.

A number of spectra were taken with each experimental configuration at a series

Table 3.4: Details of experimental configurations.

Configuration number	Projectile	Detector	θ_{lab} [a])	Target thickness (μg cm^{-2})	Target material[b])
1	^{4}He	SB[c])	171.3°	72	A
2	^{4}He	SB[c])	171.3°	21	A
3	^{12}C	SB[c])	174.8°	1.9	B
4	^{12}C	MS[d])	155.25°	3.5	B

[a]) mean scattering angle in laboratory system
[b]) see table 3.3
[c]) annular silicon surface-barrier detector
[d]) Enge split-pole magnetic spectrometer

of bombarding energies. This was done to ensure that only data which were free from significant Coulomb-nuclear interference were included in the determination of matrix-element values for ^{192}Os. The bombarding energy at which the onset of significant nuclear interference occurs was accurately determined by plotting P_{exp}/P_{calc} as a function of s, the distance of closest approach of the nuclear surfaces, and rejecting all data taken at energies higher than that at which the ratio deviates from a constant value. This ratio is plotted in fig. 3.4 as a function of s, which is defined as

$$s = \frac{0.72 Z_p Z_t}{E_p}(1 + A_p/A_t)(1 + \mathrm{cosec}\frac{\theta_{CM}}{2}) - 1.25(A_p^{1/3} + A_t^{1/3}) \text{ fm} \qquad (3.8)$$

where E_p is in units of MeV and θ_{CM} is the scattering angle in the centre-of-mass frame. It should be noted that P_{exp}/P_{calc} will not necessarily be equal to unity at 'safe' energies if the matrix element values used to obtain P_{calc} were significantly different from the true values.

Data were collected at 171.3° with ^{4}He projectiles for a range of bombarding energies using two different targets. The excitation probabilities for the first excited state, $P_{exp}(2_1^+)$, are listed in table 3.5. The bombarding energies have been corrected for

Table 3.5: Measured excitation probabilities P_{exp} for the 2_1^+ state of ^{192}Os.

Configuration number	Projectile	θ_{lab} [a])	E_p [b]) (MeV)	P_{exp} ($\times 10^{-2}$)
1	^{4}He	171.3°	14.190	2.84(5)
			14.390	2.91(4)
			14.590	3.09(3)
			14.790	3.21(3)
			14.990	3.33(4)
			15.190	3.47(3)
			15.391	3.64(4)
			15.591	3.74(6)
			15.791	3.74(9)
2	^{4}He	171.3°	14.197	2.836(21)
			14.397	2.943(22)
			14.597	3.088(23)
			14.797	3.226(24)
			14.997	3.386(25)
			15.197	3.533(25)
			15.397	3.62(4)
			15.597	3.72(3)
			15.797	3.99(4)
			16.197	4.25(7)
			16.497	4.45(8)

Table 3.5 (cont.)

Configuration number	Projectile	θ_{lab}[a])	E_p[b]) (MeV)	P_{exp} ($\times 10^{-2}$)
3	^{12}C	174.8°	39.998	16.3(4)
			40.998	17.4(4)
			41.998	18.3(4)
			42.998	20.1(3)
			43.998	21.6(4)
			44.998	22.9(6)
			45.998	24.6(5)
			47.998	26.8(5)
			49.998	29.4(8)
			51.998	29.9(11)
			53.998	29.8(11)
			54.998	30.6(11)
4	^{12}C	155.25°	43.996	20.3(3)
			44.996	21.6(3)
			45.996	23.2(3)
			46.996	24.1(3)

[a]) mean scattering angle in the laboratory system
[b]) bombarding energy

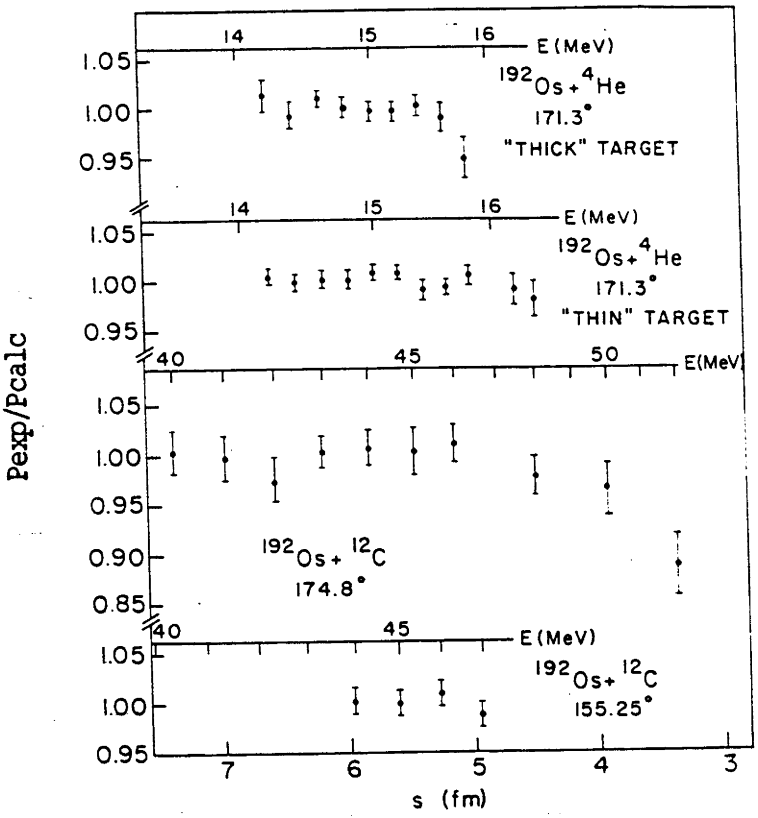

Figure 3.4: Safe-energy plots for each configuration.

the effects of target thickness; the magnitudes of this correction for the energies used in configurations 1 and 2 were 10 and 3 keV respectively. Energy loss in the target was calculated by assuming a constant stopping cross-section equal to that at the front of the target. This assumption had a negligible effect on the calculated excitation probabilities and its use removed the need for calculation of integrated excitation cross-sections. The uncertainties quoted in table 3.5 are due to statistical uncertainties and uncertainties arising from spectrum analysis. The enhanced resolution of spectra obtained with the thinner target (configuration 2) is reflected in the smaller uncertainties of the excitation probabilities extracted from those spectra. The quality of resolution of the spectrum of an even-even nucleus in particle singles spectroscopy is often indicated by the ratio of the height of the 2_1^+ peak to the lowest point reached in the valley between the elastic scattering and 2_1^+ peaks; this ratio, which is known as the peak-to-valley ratio of the 2_1^+ state, was of the order of 4:1 for spectra obtained with the thicker target but 30:1 for those obtained with the thinner target. The excellent agreement between the excitation probabilities obtained for the two targets indicates that the method of analysis used is

reproducible and hence reliable. On the basis of the safe-energy plots (fig. 3.4), 15.6 MeV was chosen to be the maximum safe energy, i.e. the highest bombarding energy for which Coulomb-nuclear interference could be seen to be insignificant.

Data were also collected with ^{12}C projectiles at 174.8° with an annular detector and at 155.25° with a position-sensitive gas-filled detector in an Enge spectrometer. Typical spectra are shown in figs. 3.1c and 3.1d. The safe-energy plots (fig. 3.4) show no sign of significant Coulomb-nuclear interference for the energies used in configuration 4 (cf. table 3.4); for configuration 3 the highest energy deemed to be safe was 46 MeV. Peak-to-valley ratios for the 2_1^+ state were 3:1 and 10:1 for spectra obtained with an annular counter and the Enge respectively; corrections for target thickness were 2 and 4 keV. The widths of peaks in the lineshape for spectra taken with configuration 4 were allowed to vary as a function of distance from the position at which the peak width was a minimum. Two charge states (5^+ and 6^+) were observed; to take this into account, the excitation probability of a state J_n^π was defined to be the ratio of the total number of counts in the two J_n^π peaks to the total number of counts in the two elastically scattered peaks.

Checks were made to ascertain whether the presence of any elements other than the osmium isotopes could affect the values obtained for $P_{exp}(2_1^+)$. Spectra taken with 8.0 and 9.5 MeV ^4He, 12 MeV ^{12}C and 24 MeV ^{16}O projectiles were examined for the presence of peaks due to elastic scattering from nuclei which would affect any of the values of $P_{exp}(2_1^+)$ used to obtain $B(E2;0_1^+ \rightarrow 2_1^+)$ and $Q(2_1^+)$. The upper limits for such contributions were measured to be 0.1% of $P_{exp}(2_1^+)$ for the ^4He data; for the ^{12}C data, the upper limits were found to be 0.35% and 0.5% of $P_{exp}(2_1^+)$ for configurations 3 and 4 respectively. It was concluded that contributions from contaminants were insignificant because these limits are far smaller than the corresponding uncertainties in $P_{exp}(2_1^+)$ (at least 0.8%, 0.7%, 1.8% and 1.3% of $P_{exp}(2_1^+)$ for configurations 1, 2, 3 and 4 respectively). A contaminant of about A=144 was present in the carbon backing of the thinner target used in configuration 2, but did not affect extraction of the peaks of interest.

Table 3.6: Magnitudes of reduced matrix elements $< J_f^+ \| \mathcal{M}(E\lambda) \| J_i^+ >$ used in the multiple Coulomb-excitation analysis.

J_i^+	J_f^+	λ	Value	Ref.
0_1^+	2_2^+	2	0.44(1) e b	Ca69, Re84
0_1^+	4_1^+	4	0.19(1) e b^2	Re84
2_1^+	2_2^+	2	1.33(4) e b	Ca69, Ho81
2_1^+	4_1^+	2	2.21(8) e b	Ca69, Mi71
2_2^+	4_2^+	2	1.25(12) e b	Ca69
4_1^+	4_2^+	2	1.8(5) e b	Ca69
4_1^+	6_1^+	2	3.4(3) e b	Ca69

3.3.3 Analysis of Excitation Probabilities

Six energy levels were included in the multiple Coulomb excitation analysis : 0.0 keV (0_1^+), 208.5 keV (2_1^+), 489.1 keV (2_2^+), 580.3 keV (4_1^+), 909.6 keV (4_2^+) and 1089.0 keV (6_1^+). Published matrix element values listed in table 3.6 were used. Other matrix element values available were not included as they had a negligible effect on the predicted excitation probability. The two cases of interference from higher states which are important for ^{192}Os,

$$P_4(2_2^+) = <2_1^+ \| \mathcal{M}(E2) \| 2_1^+ > <2_1^+ \| \mathcal{M}(E2) \| 0_1^+ > <2_2^+ \| \mathcal{M}(E2) \| 2_1^+ > <2_2^+ \| \mathcal{M}(E2) \| 0_1^+ > \tag{3.9}$$

and

$$P_3(4_1^+) = <4_1^+ \| \mathcal{M}(E4) \| 0_1^+ > <4_1^+ \| \mathcal{M}(E2) \| 2_1^+ > <2_1^+ \| \mathcal{M}(E2) \| 0_1^+ >, \tag{3.10}$$

have been examined by Baker *et al.* using inelastic scattering (Ba76b, Ba85) and both have been found to be negative for ^{192}Os.

Table 3.7: Corrections to and uncertainties in measured $B(E2;0_1^+ \rightarrow 2_1^+)$ and $Q(2_1^+)$ for ^{192}Os.

Source of correction	$\Delta B(E2;0_1^+ \rightarrow 2_1^+)$ (e^2b^2)	$\Delta Q(2_1^+)$ (e b)
Electron screening	−0.013	+0.02
Vacuum polarization	+0.029	−0.04
Nuclear polarization	−0.001	−0.04
Quantal corrections	+0.020	−0.04
GDR	0.000	+0.10
Total correction	+0.035	0.00
	$B(E2;0_1^+ \rightarrow 2_1^+)$ (e^2b^2)	$Q(2_1^+)$ (e b)
Final values	2.030(13)	−0.86(20)

An iterative least-squares fitting procedure (Fe78t) was used to extract values for $B(E2;0_1^+ \rightarrow 2_1^+)$ and $Q(2_1^+)$. Only data taken at safe bombarding energies were used. The final values obtained were $B(E2;0_1^+ \rightarrow 2_1^+) = 2.030(13)$ e^2b^2 and $Q(2_1^+) = -0.86(20)$ e b. Corrections for various effects were applied, as shown in table 3.7. The quoted uncertainties include uncertainties from statistics, spectrum analysis, beam energy, scattering angle, higher-state matrix elements and the GDR correction.

Preliminary unpublished values reported by Wu (Wu87) for $<4_2^+||\mathcal{M}(E2)||2_1^+>$, $<2_2^+||\mathcal{M}(E2)||2_2^+>$, $<4_1^+||\mathcal{M}(E2)||2_2^+>$, $<4_1^+||\mathcal{M}(E2)||4_1^+>$, $<4_2^+||\mathcal{M}(E2)||4_2^+>$, $<6_1^+||\mathcal{M}(E2)||4_2^+>$ and $<6_1^+||\mathcal{M}(E2)||6_1^+>$ were not included in obtaining the final values of $B(E2;0_1^+ \rightarrow 2_1^+)$ and $Q(2_1^+)$; their effect would have been to increase $Q(2_1^+)$ by 0.10 e b and decrease $B(E2;0_1^+ \rightarrow 2_1^+)$ by 0.004 e^2b^2.

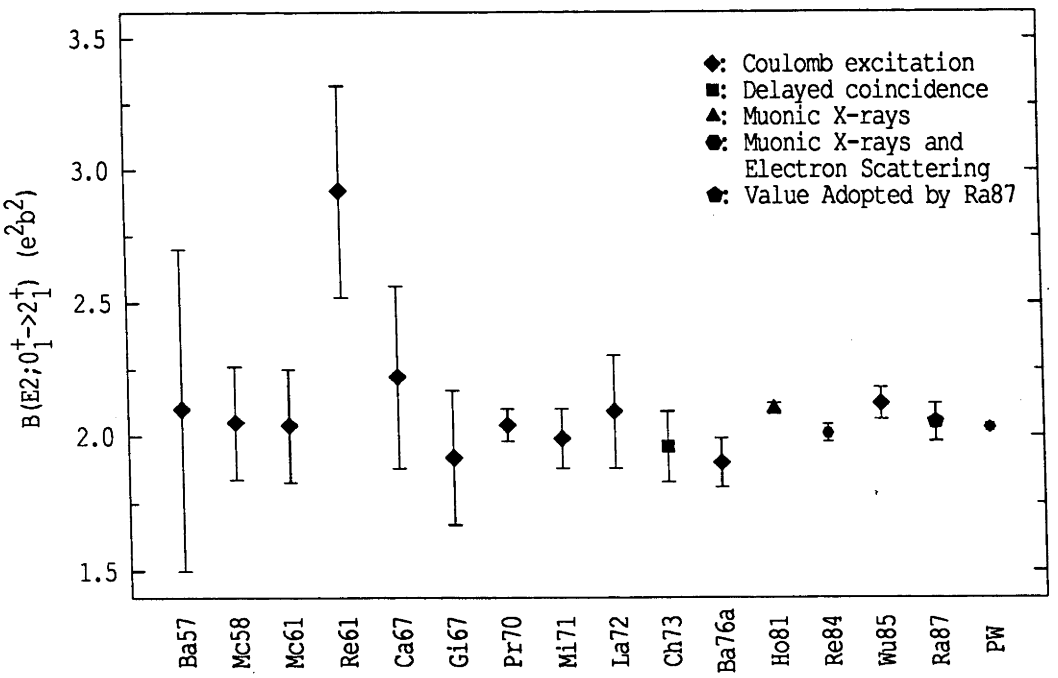

Figure 3.5: Experimental values of $B(E2;0_1^+ \rightarrow 2_1^+)$ for ^{192}Os taken from the compilation of Raman *et al.* (Ra87), together with the result of the present work

3.4 Discussion

3.4.1 Comparison of Results with Previous Experiments

In fig. 3.5, values of $B(E2;0_1^+ \rightarrow 2_1^+)$ listed in the recent compilation of Raman *et al.* (Ra87) are shown in chronological order, together with the adopted value of Raman *et al.* and the result of the present work (cf. table 3.8). The latter measurement of $B(E2;0_1^+ \rightarrow 2_1^+)$ is in good agreement with the value adopted by Raman *et al.*, as well as with the result of an experiment by Reuter *et al.* (Re84) in which they combined electron scattering data with muonic X-ray data obtained by Hoehn *et al.*, but disagrees with that obtained from the muonic X-ray data alone (Ho81), which is significantly larger than that of Reuter *et al.* due to differences in the transition charge density used in their analysis.

The effect of this uncertainty in charge density on $Q(2_1^+)$ is expected to be negligible (Sh87) as changing from a symmetric to a triaxial charge density had no effect on the value obtained for $Q(2_1^+)$ (Ho81). The result obtained in the present work for $Q(2_1^+)$

Table 3.8: Values of $B(E2;0_1^+ \rightarrow 2_1^+)$ for ^{192}Os from Raman *et al.* (Ra87).

Source	Method	$B(E2;0_1^+ \rightarrow 2_1^+)$ (e^2b^2)
Barloutaud *et al.* (Ba57)	Coulomb excitation	2.1(6)
McGowan and Stelson (Mc58)	Coulomb excitation	2.05(21)
McGowan and Stelson (Mc61)	Coulomb excitation	2.04(21)
Rester *et al.* (Re61)	Coulomb excitation	2.9(4)
Casten *et al.* (Ca67)	Coulomb excitation	2.2(3)
Gilad *et al.* (Gi67)	Coulomb excitation	1.92(25)
Pryor and Saladin (Pr70)	Coulomb excitation	2.04(6)
Milner *et al.* (Mi71)	Coulomb excitation	1.99(11)
Lane and Saladin (La72)	Coulomb excitation	2.09(21)
Chopra *et al.* (Ch73)	Delayed coincidence	1.96(13)
Baker *et al.* (Ba76a)	Coulomb excitation	1.90(9)
Wu (Wu85)	Coulomb excitation	2.12(6)
Hoehn *et al.* (Ho81)	Muonic X-ray	2.10(2)
Reuter *et al.* (Re84)	Muonic X-ray and electron scattering	2.01(3)
Raman *et al.* (Ra87)	Adopted value	2.05(7)
Present work	Coulomb excitation	2.030(13)

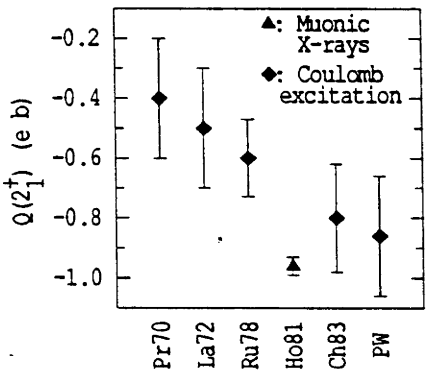

Figure 3.6: Values of $Q(2_1^+)$ for ^{192}Os obtained in the present and previous experiments.

is in excellent agreement with the muonic X-ray result of Hoehn *et al.* (Ho81), as seen from fig. 3.6. However, the apparent agreement with the result of Chen *et al.* (Ch83) may be misleading, as their assumption of the incorrect sign for the 2_2^+ interference term can significantly change the value obtained for $Q(2_1^+)$. For example, if the opposite sign of $P_4(2_2^+)$ were used in the present analysis, the result for $Q(2_1^+)$ would be changed by approximately 1 e b. [Pryor and Saladin (Pr70) also reported a shift of about 1 e b in their results for $Q(2_1^+)$ when they changed the sign assumed for $P_4(2_2^+)$.] Furthermore, Chen *et al.* base their magnitudes for higher-state matrix elements on model predictions rather than deriving them from measured transition probabilities as done in this work. The effect of this difference is quite significant : analysis of the data obtained using the matrix element magnitudes quoted by Chen *et al.* (but with the experimentally determined phases) results in a decrease of 0.4 e b in the deduced value of $Q(2_1^+)$. The early Pittsburgh experiments did not include matrix elements for states other than the 2_2^+ and 4_1^+, while the report of the Rochester experiment did not indicate what matrix element values were assumed. In addition, the reports of the early Coulomb excitation experiments do not mention whether any of the corrections for electron screening, vacuum polarization, etc., were included. Any of these factors may have contributed to the disagreement with the muonic X-ray data.

3.4.2 Comparison with Theory

In fig. 3.7 and table 3.9 the predictions of various models for $Q(2_1^+)$ of the stable even-mass Os isotopes are compared with the experimentally determined values from both

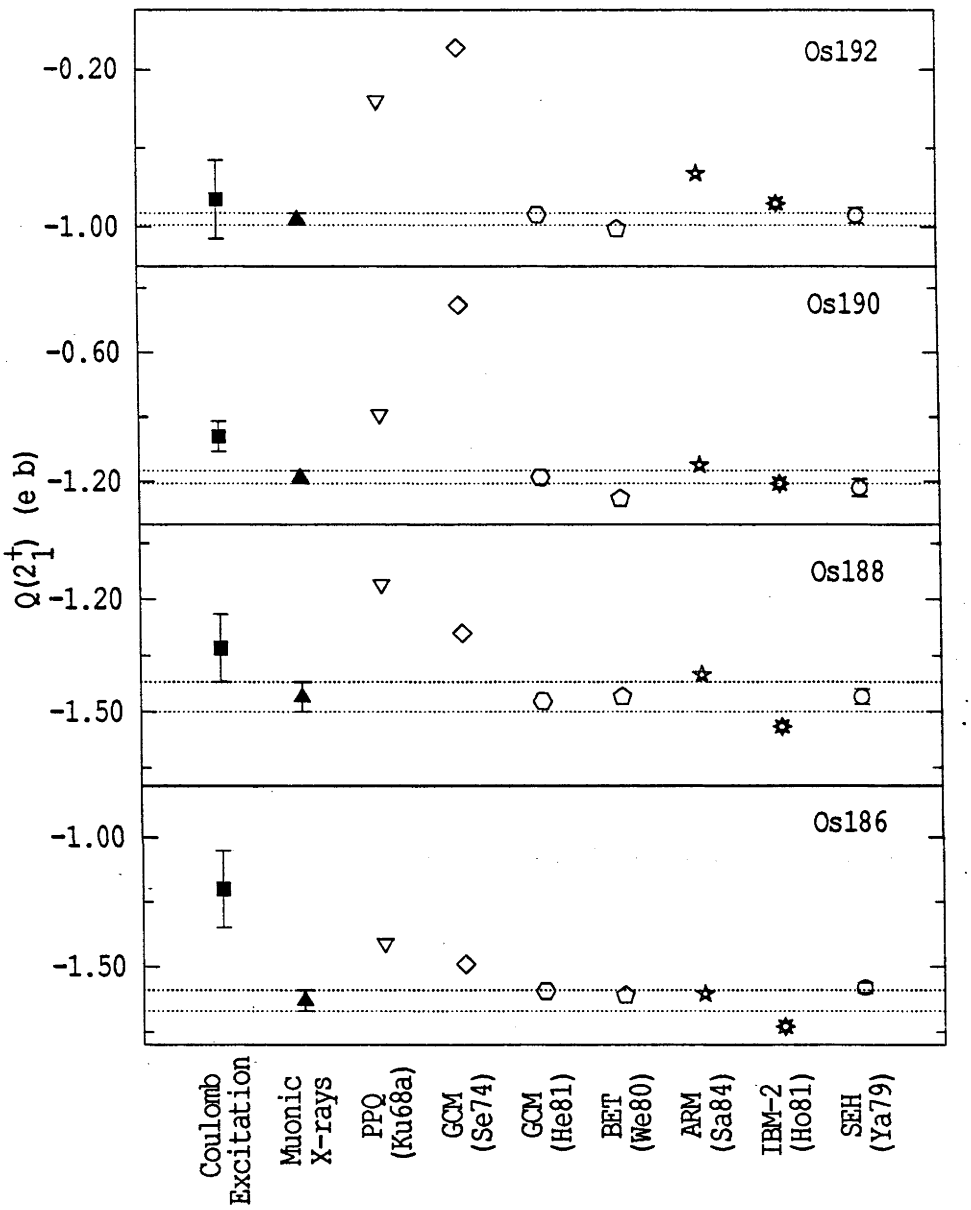

Figure 3.7: Values of $Q(2_1^+)$ in e b for the stable even-mass Os isotopes given by model predictions and experiment. The lines indicate the level of uncertainty assigned to the muonic X-ray data (Ho81) and are included to facilitate comparison.

Table 3.9: Values of $Q(2_1^+)$ in e b for the stable even-mass Os isotopes given by model predictions and experiment.

	^{186}Os	^{188}Os	^{190}Os	^{192}Os	^{194}Os
Experiment					
Coulomb excitation	−1.20(15)[a])	−1.33(9)[a])	−0.99(7)[a])	−0.86(20)[b])	
Muonic X-rays[c])	−1.63(4)	−1.46(4)	−1.18(3)	−0.96(3)	
Theory					
PPQ (Ku68a)	−1.41	−1.16	−0.89	−0.36	
PPQ (Ku82)	1.43	1.38	−1.34	−1.29	
GCM (Se74)	−1.49	−1.29	−0.38	−0.09	
GCM (He81)	−1.593	−1.472	−1.180	−0.937	
BET (We80)	−1.61	−1.46	−1.28	−1.01	−0.90
ARM (Sa84)	−1.604	−1.401	−1.124	−0.729	
IBM-1 (Ba81a)				−1.03	
IBM-2 (Ho81)	−1.73	−1.54	−1.21	−0.88	
SEH (Ya79)	−1.58(2)	−1.46(2)	−1.23(4)	−0.94(4)	

[a]) weighted mean of Pr70, La72, Ru78
[b]) present work
[c]) from Ho81

Coulomb excitation and muonic X-ray data. The models listed in table 3.9 consist of the Pairing-Plus-Quadrupole Model (PPQ), General Collective Model (GCM), Boson Expansion Theory (BET), Asymmetric Rotor Model (ARM), Interacting Boson Model (IBM), and Spin-Expansion Hamiltonian (SEH) model. The only prediction for ^{194}Os (that of the BET) is also included. As a detailed description of most of these models will be given in the next chapter, only those points which are central to the present discussion are included here. The Coulomb-excitation measurements presented for ^{186,188,190}Os are the weighted means of the results of Pr70, La72 and Ru78; the value for ^{192}Os is that obtained in the present work. The values for $Q(2_1^+)$ of ^{186,190}Os taken from Coulomb excitation do not agree with those from muonic X-ray data; those for ^{188}Os are only just consistent with each other. However, it has already been noted that these values from the early experiments of the Pittsburgh group and from the unpublished data of Russo *et al.* are probably less reliable than the muonic X-ray data for these nuclei.

Fig. 3.7 illustrates that the values of $Q(2_1^+)$ from the PPQ calculations of Kumar and Baranger (Ku68a) (see also § 4.2.2) for the Os isotopes are consistently smaller in magnitude than experiment; the magnitude of the discrepancy increases with mass number. In other words, they obtained a lesser degree of deformation and a more rapid transition towards a spherical shape [$Q(2_1^+) = 0$]. Although Kumar and Baranger predicted an oblate shape for ^{192}Os, their calculations (Ku68a) suggested that anharmonic effects would delay the expected change of sign in the quadrupole moment of the first 2^+ state, $Q(2_1^+)$, in ^{192}Os so that the sign of $Q(2_1^+)$ for ^{192}Os would be the same as that for ^{190}Os. The PPQ calculations of Kumar and Gunye (Ku82) have not been included in fig. 3.7, as it is clear that they have either omitted a minus sign in at least one of their values of $Q(2_1^+)$ or have obtained results which are in extreme disagreement with experiment. The latter appears more likely as their predicted $B(E2;0_1^+ \rightarrow 2_1^+)$ values are also quite different from experiment.

The General Collective Model (GCM) (§ 4.2.3) was designed to provide a means of solving any collective Hamiltonian. For the purposes of the present discussion, it is necessary only to know that the parameters, which are determined by fitting data from low-energy states, are used to calculate potential energy surfaces (PES) from which the

nuclear shape can be deduced. In the calculations of Sedlmayr *et al.* (Se74), parameters were fitted to observed excitation energies and B(E2)'s whereas Hess *et al.* (He81) included the experimental values of $Q(2_1^+)$ in their fit. Thus, the extraordinarily good agreement obtained by the latter is not surprising. However, their procedure does not invalidate the use of their PES as an accurate source of information on the shape of the Os isotopes, in particular, their conclusion that the Os isotopes change from a more rigid rotational shape for ^{186,188}Os to a γ-soft and nearly triaxial, but mainly prolate structure at ^{192}Os. Similarly, the poor agreement obtained by Sedlmayr *et al.* for their calculated $Q(2_1^+)$ values of the heavier Os isotopes suggests that their description of ^{192}Os as a slightly oblate nucleus is inappropriate.

The Boson Expansion Theory (BET) (§ 4.2.4) predicts a slightly slower shape transition than seen in experiment; these calculations of Weeks and Tamura (We80) used experimental single-particle energies for the region around ^{208}Pb to fit the excitation energies of the Os and Pt isotopes. The effective charge, which is used in the calculation of E2 moments, was fitted for each isotope to the experimental value of $B(E2;0_1^+ \rightarrow 2_1^+)$. As is usual for this model, good agreement was obtained for most predictions and for $Q(2_1^+)$ in particular. Weeks and Tamura concluded from their calculations that the Os isotopes were best described in terms of a transition from well-deformed prolate shapes for the lighter isotopes to prolate shapes with some γ-instability for the heavier isotopes. They noted also that they predict ^{194}Os to be prolate but expect ^{196}Os to have an oblate shape.

The Asymmetric Rotor Model (ARM) calculations of Sahu (Sa84) were carried out on the assumption that the nucleus is γ-rigid. The value of γ was fixed so that the experimental excitation energies of the 2_1^+ and 2_2^+ states were fitted. The quadrupole deformation parameter, β_2, was varied for each state in the ground band. These values of β_2 and γ were used to calculate electromagnetic moments. Sahu's predictions give good agreement with most of the data except for the prediction of a less deformed shape for ^{192}Os than is experimentally observed. This indicates that the lighter Os isotopes are γ-rigid with the degree of γ-softness increasing around ^{192}Os.

The two values of $Q(2_1^+)$ for ^{192}Os calculated using the Interacting Boson Model

(IBM) (§ 4.2.1) do not agree with each other. The major difference between the two is that the calculation by Baker *et al.* (Ba81a) assumes that neutrons and protons are indistinguishable (IBM-1) while the IBM-2 calculations quoted by Hoehn *et al.* (Ho81) include a distinction between neutrons and protons. The value of Baker *et al.* has been omitted from fig. 3.7 but can easily be compared with the experimental values as it is very similar to the BET result. The IBM-2 calculations predict a transition that is slightly faster than experimentally observed.

Yamazaki *et al.* (Ya79) used a Spin-Expansion Hamiltonian (SEH) to simultaneously fit excitation energies and E2 transition matrix elements for ^{186,188,190,192}Os. The parameters thus obtained produced values of $Q(2_1^+)$ which were in good agreement with experiment. The major difference between their Hamiltonian and that used by Kumar and Baranger (Ku68a) was the inclusion of the spin-dependence of band-mixing parameters. The excellent performance of the SEH calculations of Yamazaki *et al.* supports their conclusion that this spin-dependence should be taken into account to adequately describe the characteristics of the heavier Os nuclei, thus indicating a faster rotational motion in ^{190,192}Os as compared to the lighter Os isotopes.

3.4.3 Significance of Results

The results of the present experiment confirm both the negative sign and relatively large magnitude measured by Hoehn *et al.* for the spectroscopic electric quadrupole moment of the first 2^+ state in ^{192}Os. Thus, there is no evidence for any dependence of $Q(2_1^+)$ on the technique used. It has been pointed out already that inadequate values for the higher state matrix elements or neglect of various corrections in the analysis of previous reorientation effect experiments may have been at least partially responsible for the discrepancy in earlier results. For these reasons it is probably safe to ignore the disagreement of prior Coulomb excitation experiments with the muonic X-ray result.

The relationship between the sign of the spectroscopic quadrupole moment and the shape of the nuclear charge distribution has already been mentioned. The value observed in this experiment for $Q(2_1^+)$ [−0.86(20) e b] indicates a well-deformed prolate shape for

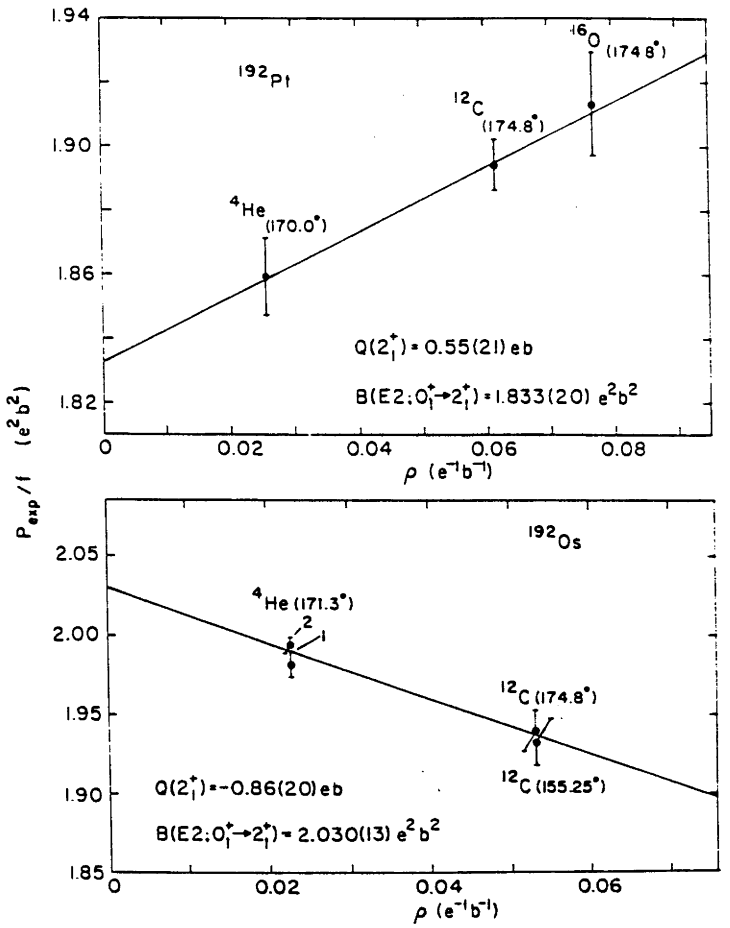

Figure 3.8: Plots of P_{exp}/f against the sensitivity parameter ρ for ^{192}Os (present work) and ^{192}Pt (Gy87). For simplicity of presentation each data point shows the average of results obtained at all safe energies for the experimental configuration concerned.

^{192}Os, not very different to[1] that of ^{188}Os and ^{190}Os. This can be contrasted with the moderately large and positive value [0.55(21) e b], corresponding to an oblate deformation, obtained for ^{192}Pt using the same equipment and analytical procedures (Gy87). A visual representation of the data, based on equation (3.5), is given in fig. 3.8 as a plot of the quantity P_{exp}/f vs. the sensitivity parameter ρ for both ^{192}Os and ^{192}Pt. Equation (3.5) implies that the fit to the data should be a straight line with y intercept equal to $B(E2;0_1^+ \rightarrow 2_1^+)$ and slope equal to the product of $B(E2;0_1^+ \rightarrow 2_1^+)$ and $Q(2_1^+)$. Since $B(E2;0_1^+ \rightarrow 2_1^+)$ is always positive, the sign of the slope indicates the sign of $Q(2_1^+)$. Fig. 3.8 clearly shows the change in the sign of $Q(2_1^+)$ between ^{192}Os and ^{192}Pt, which is indicative of a change in shape.

It has been suggested that the large decrease in the magnitude of $Q(2_1^+)$ formerly

[1] "That *different* can only be followed by *from* and not by *to* is a SUPERSTITION." (Fo65)

observed in reorientation effect experiments when going from ^{190}Os [0.99(7) e b] to ^{192}Os [0.53(10) e b; cf. table 3.1] indicates a change in the Os isotopes towards a more spherical structure (Ca69). The results of the present work together with the muonic X-ray data of Hoehn *et al.* imply quite the opposite : the similarity in magnitude of $Q(2_1^+)$ for ^{192}Os and ^{190}Os, as well as the negative sign obtained in both cases, can be taken as evidence that significant prolate deformation exists in ^{192}Os just as in the lighter Os isotopes. The only calculations which predict an oblate shape for ^{192}Os are those of Kumar and Baranger and of Sedlmayr *et al.*; it is worth noting that both results for $Q(2_1^+)$ give poor agreement with experiment for that nucleus. In general, experimental data are best fitted by those calculations which describe ^{192}Os as a prolate and moderately γ-soft nucleus which is not much different from the more γ-rigid lighter Os isotopes.

3.5 Conclusions

The values of $B(E2;0_1^+ \rightarrow 2_1^+)$ and $Q(2_1^+)$ for ^{192}Os have been measured to be 2.030(13) e^2b^2 and $-0.86(20)$ e b respectively. The latter result is in good agreement with that obtained from muonic X-ray data, and hence does not support the suggestion of a discrepancy in measurements of $Q(2_1^+)$ carried out using different techniques. Comparison of the value of $Q(2_1^+)$ measured for ^{192}Os with that obtained in this laboratory for ^{192}Pt (Gy87) illustrates the dramatic effect of the interchange of two protons for two neutrons and supports the prediction of a prolate-to-oblate transition in this region. However, the relatively large magnitude observed for $Q(2_1^+)$ indicates that the change of shape toward sphericity is not as rapid between ^{186}Os and ^{192}Os as previously suggested.

Chapter 4

Coulomb Excitation Of ^{194,196}Pt

4.1 Introduction

The Pt nuclei have been the subject of extensive research regarding the prediction of a prolate-to-oblate transition by Kumar and Baranger (Ku68, Ku68a). The transitional nature of these nuclei, due to their position between the well-deformed rare-earth nuclei and the doubly-closed shell nucleus ^{208}Pb, makes them important to our understanding of nuclear collective behaviour. The results of some of the investigations of the Pt nuclei have indicated that they may be rigid triaxial rotors (e.g. Le77) or γ-unstable (e.g. Ca78). Measurements have shown that the quadrupole moments of the first excited state in many of these nuclei have large magnitudes which are difficult to reconcile with certain other experimental data. In particular, experimental data on the dynamic E2 moments of ^{196}Pt support the proposal that this nucleus is an excellent example of the O(6) limit of the IBM (Ca78, Ci78, Ci79) which corresponds in most respects to the γ-unstable model of Wilets and Jean (Wi56), whereas the large quadrupole moment measured for the first excited state (Gy86) is inconsistent with this interpretation.

It has been suggested (Fe86) that a better alternative to the O(6) description of ^{196}Pt may be provided by the U(5) limit of the IBM, an idea which would have important consequences for the well-known and generally accepted interpretation of the Os and Pt nuclei in terms of a transition from SU(3) to O(6) (Ca78). It appears possible that measurements of the quadrupole moments of higher-excited states may clarify the situation

by showing whether $Q(2_1^+)$ for the Pt nuclei is anomalously large in comparison to, say, $Q(2_2^+)$ or $Q(4_1^+)$. If, on the other hand, all the static E2 moments are inconsistent with the picture suggested by the dynamic moments, then extensive changes to the present view of these nuclei might be necessary. The aim of the experiments described in this chapter was to initiate measurements of the quadrupole moments of the 2_2^+ and 4_1^+ states of ^{196}Pt as well as those of ^{194}Pt. Data for the former are complete; the ^{194}Pt data are not yet complete but are included in this chapter as they provide information on other matrix elements which is of greater precision than that previously available.

4.2 Theoretical Work on the Pt Nuclei

4.2.1 The Interacting Boson Model

The Interacting Boson Model (IBM) has been extensively discussed in many reviews (see, for example, Ar81 and Bo88a) so only the salient points will be mentioned here. The original model (IBM-1) treats collective motion by neglecting the contribution of closed shells and assuming that the valence shell nucleons are coupled together in pairs (bosons) with angular momentum J=0 (s-bosons) or J=2 (d-bosons). No distinction is made between protons and neutrons. If the valence shell is less than half full, the number of bosons, N, is taken to be the number of particle pairs; otherwise, the number of pairs of holes is used.

Only one- and two-body terms are included in the Hamiltonian, which can be written in terms of the pairing, angular momentum, quadrupole, octupole and hexadecapole operators P, L, Q, T_3 and T_4 :

$$H = \epsilon'' n_d + a_0 P^\dagger . P + a_1 L . L + a_2 Q . Q + a_3 T_3 . T_3 + a_4 T_4 . T_4 \qquad (4.1)$$

where n_d is the d-boson number operator and $\epsilon'', a_0, a_1, a_2, a_3$ and a_4 are parameters which can be varied to fit the data. The various operators can be written in terms of the boson creation and annihilation operators $s^\dagger, d^\dagger, \tilde{s}$ and $\tilde{d}$ as :

$$
\begin{aligned}
n_d &= d^\dagger . \tilde{d} \\
P &= \frac{1}{2}(\tilde{d}.\tilde{d}) - \frac{1}{2}(\tilde{s}.\tilde{s}) \\
L &= \sqrt{10}[d^\dagger \times \tilde{d}]^{(1)} \\
Q &= [d^\dagger \times \tilde{s} + s^\dagger \times \tilde{d}]^{(2)} - \frac{1}{2}\sqrt{7}[d^\dagger \times \tilde{d}]^{(2)} \\
T_3 &= [d^\dagger \times \tilde{d}]^{(3)} \\
T_4 &= [d^\dagger \times \tilde{d}]^{(4)} .
\end{aligned}
$$

The ranks of the tensor operators L, Q, T_3 and T_4 are given by the bracketed superscripts. Diagonalization of the Hamiltonian provides a solution to the energy level spectrum. Since the IBM utilizes a six-dimensional system of bosons, it is sensible to use the symmetric irreducible representations of U(6) as a basis for the diagonalization.

Analytic solutions to the Hamiltonian can be found by using its dynamical symmetries; this means writing the Hamiltonian in terms of invariant (or Casimir) operators of a chain of subgroups of U(6). The rotational group O(3) has to be a member of this chain for the angular momentum, L, to be a good quantum number. This limits the possible analytic solutions to three cases, obtained by using generators of the subgroups U(5) (Ar76), SU(3) (Ar78) and O(6) (Ar79). In the limit $N \rightarrow \infty$, these correspond most closely to the geometric cases of the anharmonic vibrator, the axially symmetric deformed rotor and the γ-unstable nucleus of Wilets and Jean (Wi56), respectively. Table 4.1 lists some of the major predictions of the three limits of the IBM-1.

Casten and Cizewski noticed that many of the features of the Os and Pt nuclei could be described in terms of a transition moving from the SU(3) to O(6) limits as A increases (Ca78). They emphasized the presence of particular characteristic features of the O(6) limit in the Pt nuclei, namely, the good agreement of observed E2 transition strengths with the $\Delta\sigma = 0, \Delta\tau = 1$ selection rules [σ and τ are quantum numbers associated with the O(6) limit] and a repeating $0^+ - 2^+ - 2^+$ level sequence with strong cascading E2 transitions within the group. As part of their description of the Os and Pt nuclei, Casten and Cizewski proposed ^{196}Pt to be a paradigm of the O(6) limit of the IBM-1.

Table 3.1: Some major predictions of the different limits of IBM-1. N denotes the number of bosons.

	U(5)	SU(3)	O(6)
$\frac{B(E2;J+2\rightarrow J)}{B(E2;2_1^+\rightarrow 0_1^+)}$	$\frac{(J+2)(2N-J)}{4N}$	$\frac{5(J+2)(J+1)(2N-J)(2N+J+3)}{(2J+3)(2J+5)N(2N+3)}$	$\frac{5(J+2)(2N-J)(2N+J+8)}{8N(J+5)(N+4)}$
$\frac{B(E2;2_2^+\rightarrow 0_1^+)}{B(E2;2_2^+\rightarrow 2_1^+)}$	0	7/10	0
$\frac{B(E2;4_1^+\rightarrow 2_1^+)}{B(E2;2_1^+\rightarrow 0_1^+)}$	2(N-1)/N	$\frac{10(N-1)(2N+5)}{7N(2N+3)}$	$\frac{10(N-1)(N+5)}{7N(N+4)}$
$\frac{B(E2;0_2^+\rightarrow 2_1^+)}{B(E2;2_1^+\rightarrow 0_1^+)}$	2(N-1)/N	0	0
$Q(2_1^+)$			0[a]
$Q(4_1^+)/Q(2_1^+)$	2	14/11	
$Q(2_2^+)/Q(2_1^+)$	-3/7	1	
$E_x(4_1^+)/E_x(2_1^+)$	2	3.3	2.5

[a]) all quadrupole moments are zero in the O(6) limit

In this limit, the contributions of quadrupole interactions and hexadecapole interactions are zero, as is the coefficient of the d-boson number operator, thus reducing the standard IBM Hamiltonian to the form :

$$H = a_0 P^\dagger . P + a_1 L . L + a_3 T_3 . T_3. \tag{4.2}$$

The O(6) assignment was made because of excellent agreement between observed and calculated energy levels and E2 transition strengths. However, Fewell *et al.* (Fe85) point out that the quadrupole moment of the first excited state has been measured to be quite large [0.66(12) e b in Gy86], whereas the O(6) limit predicts all quadrupole moments to be zero, a consequence of the form of the electric quadrupole operator in the IBM-1 :

$$T^{E2} = \alpha[s^\dagger \times \tilde{d} + d^\dagger \times \tilde{s}]^{(2)} + \beta[d^\dagger \times \tilde{d}]^{(2)}. \tag{4.3}$$

In the pure O(6) limit, the parameter β is zero. The first term describes transitions which change n_d by 1. However, O(6) wave functions are built on basis states with $\Delta n_d = 2$. Hence, the only way to obtain non-zero quadrupole moments is to modify the O(6) form of the E2 operator by allowing β to have non-zero values or by replacing the pure O(6) treatment with an admixture of O(6) and SU(3).

Fewell (Fe86) suggested that a more satisfactory alternative was to use the U(5) limit (Ar76). In this limit the Hamiltonian has the form :

$$H = \epsilon'' n_d + a_1 L . L + a_3 T_3 . T_3 + a_4 T_4 . T_4. \tag{4.4}$$

One obtains the parameters α and β in equation (4.3) by varying α to fit the observed value of the $B(E2;0_1^+ \rightarrow 2_1^+)$ and varying β to fit $Q(2_1^+)$. Fewell used this procedure to obtain values of α and β for four cases : the U(5) limit, the O(6) limit with $\beta \neq 0$, the O(6) + SU(3) admixture with $\beta = 0$, and a solution which is a mixture of O(6) and U(5), taken from Ch85. He then compared the consequent predictions of various E2 transition probabilities with experimental measurements and concluded from this comparison that "the U(5) limit gives just as good a description of ^{196}Pt as does the O(6) limit" and

that "the best fits to the known E2 matrix elements of ^{196}Pt are provided by the U(5) limit and the O(6) limit with β=0". Fewell suggested that measurements of higher state quadrupole moments would provide strong support for one or the other limit.

Fewell's conclusion was disputed by Casten and Cizewski (Ca87) on the grounds that the energy level scheme when considered up to the 2_6^+ state strongly favours the O(6) predictions over those of the U(5) limit. In addition, the O(6) predictions of B(E2) values are in better agreement with experiment than the U(5) predictions. Casten and Cizewski appeared to regard as unnecessary any modification to the strict O(6) limit of the IBM-1 and attributed the disagreement of theory with experiment in the case of $Q(2_1^+)$ to the assumption in IBM-1 that neutrons and protons are indistinguishable. They suggested that this discrepancy might also be avoided by using a non-zero value of β [equation (4.3)] as considered by Fewell. However, as Fewell pointed out, the latter method also results in non-zero values for $B(E2;2_2^+ \rightarrow 0_1^+)$, which is forbidden in the U(5) and strict O(6) limits and which has been found experimentally to have a small upper limit.

The effect of differentiating between neutron and proton bosons has been considered by various workers using IBM-2, the version of the IBM which incorporates the neutron-proton interaction (Ot78). In this model, the total number of bosons N is the sum of the number of neutron bosons, N_ν and the number of proton bosons N_π. The group structure SU(6)⊗SU(6) is used, and there are limiting solutions equivalent to the SU(3), U(5) and O(6) dynamical symmetries of IBM-1. As in the case of IBM-1, the assumption is made that excitation of the valence particles dominates the observed collective quadrupole structure. The IBM-2 Hamiltonian is usually written as :

$$H = \epsilon(n_{d_\pi} + n_{d_\nu}) + V_{\pi\pi} + V_{\nu\nu} + aM_{\pi\nu} + \mathcal{K}Q_\pi.Q_\nu \tag{4.5}$$

where $M_{\pi\nu}$ is the Majorana operator and

$$Q_\sigma = [d_\sigma^\dagger \times \tilde{s_\sigma} + s_\sigma^\dagger \times \tilde{d_\sigma}]^{(2)} + \chi_\sigma[d_\sigma^\dagger \times \tilde{d_\sigma}]^{(2)}, \tag{4.6}$$

with the symbol σ denoting either protons (π) or neutrons (ν). The neutron-neutron and proton-proton interaction terms $V_{\nu\nu}$ and $V_{\pi\pi}$ are often omitted as quadrupole deformation

is primarily affected by the neutron-proton interaction (Fe79). Thus, in most cases, this simplifies to :

$$H = \epsilon(n_{d_\pi} + n_{d_\nu}) + \mathcal{K} Q_\pi . Q_\nu \tag{4.7}$$

with only four parameters : $\epsilon, \mathcal{K}, \chi_\pi$ and χ_ν. The latter two parameters are dependent on N_π and N_ν respectively, so in a situation where the total number of bosons is constant, the number of parameters is further reduced to three. In the strict O(6) limit, both χ_ν and χ_π, which are the IBM-2 equivalent of the parameter β, are equal to zero. The general E2 transition operator in this model is written :

$$T^{E2} = e_\pi Q_\pi + e_\nu Q_\nu \tag{4.8}$$

where the boson effective charges, e_π and e_ν, depend only on the boson numbers, N_π and N_ν. Bijker *et al.* (Bi80) carried out an investigation of the Pt and Os nuclei using this model. The predicted E2 transition strengths are in good agreement with experiment; in particular, weak transition strengths are predicted to be non-zero unlike those given by the O(6) limit of IBM-1 where they are strictly forbidden. The quadrupole moments of the first excited states of ^{194}Pt and ^{196}Pt are greatly underpredicted by IBM-2, just as with the IBM-1, though the IBM-2 values are slightly larger than zero. Bijker *et al.* stated that increasing the sum of the parameters χ_π and χ_ν would increase the predicted value of $Q(2_1^+)$. However, they did not fully investigate the effect of this increase on predictions of other observables although they stressed the importance of χ_π and χ_ν in determining most properties. For instance, they noted that the gradual transition to an SU(3)-like spectrum seen in the Os nuclei is reproduced by an increase in $\mid \chi_\pi + \chi_\nu \mid$ in conjunction with an increase in the number of bosons. The sign of $P_4(2_2^+)$ is also extremely sensitive to the value of $(\chi_\pi + \chi_\nu)$.

There are several other IBM calculations involving ^{196}Pt; each of these has sought to remove the discrepancy between measured and predicted $Q(2_1^+)$ by introducing different modifications to the original O(6) limit. Bolotin *et al.* (Bo81) published a calculated value of 0.79 e b which agrees very well with the accepted experimental value of 0.66(12) e b (Gy86); however, their calculation overpredicts the strength of the E2

transition from the 2_2^+ state to the ground state. Van Isacker (Is87) calculated a value of 0.21 e b, a result similar to that obtained by Bijker *et al.*, by using a general E2 transition operator rather than an O(6) one. Novoselsky and Talmi (No86) suggested a procedure of fitting the parameters to the level energies and B(E2) values, then interchanging the signs of the strength parameters χ_π and χ_ν for the quadrupole moment calculation. They claimed that the latter step does not affect the other predictions but did not explain why, if this is so, the values of χ_π and χ_ν used to calculate $Q(2_1^+)$ are not one of the solutions obtained from their initial fitting procedure. In addition, they allowed significant departure from the strict O(6) limit, in particular, by allowing χ_π and χ_ν to take values intermediate to those of the O(6) and SU(3) limits, and consequently overpredicted the transitions which are forbidden in the original O(6) limit such as $B(E2;0_1^+ \rightarrow 2_2^+)$.

The apparent inability of all limits in both IBM-1 and IBM-2 to simultaneously provide a satisfactory fit to all major observables in ^{196}Pt is quite unexpected, given its extraordinary success with the low-lying states of so many even-even nuclei. It was hoped that further investigation of E2 matrix elements, especially of static quadrupole moments of states above the 2_1^+, would provide information that could throw some light on this problem.

4.2.2 Pairing-Plus-Quadrupole Calculations of Kumar and Baranger

In 1968 Kumar and Baranger published a series of papers describing some detailed microscopic calculations in the Os-Pt nuclei (see, for example, Ku68, Ku68a). They pointed out the importance of this region as a transitional region in which the onset or disappearance of deformation could be used as a test of nuclear models. For example, comparison of the experimentally observed properties of osmium and platinum with those predicted by the rotational and vibrational models (Bo52,Bo53) shows that although the enhanced E2 transition strengths found in osmium and platinum are a feature of the collective quadrupole motion described by Bohr and Mottelson, other characteristic experimental features, such as large electromagnetic moments, cannot be accounted for by the inclusion of small corrections such as the effect of band-mixing. Kumar and Baranger proposed a Pairing-Plus-Quadrupole (PPQ) Model which was basically a spherical shell model with

PPQ residual interactions. Non-linear adiabatic motion was assumed and neutron-proton pairing neglected. No assumptions were made concerning the shape of the nucleus or the harmonicity of the vibrations, and the validity of the model was restricted to cases where hexadecapole and higher order vibrations were negligible. The Hamiltonian used by Kumar and Baranger is based on that of the Bohr collective Hamiltonian and consists of three parts :

$$H = H_s + H_p + H_q \tag{4.9}$$

where H_s denotes the spherical single-particle energy while H_p and H_q describe the competing pairing and quadrupole forces. The quadrupole force tends to deform the nucleus while the pairing force tends to keep it spherical. The forms of the three parts of the Hamiltonian are :

$$H_s = \sum_{\alpha} \epsilon_\alpha c_\alpha^\dagger c_\alpha \tag{4.10}$$

where α denotes the state (n, l, j, m), the summation is over all four quantum numbers, $c_\alpha^\dagger$, c_α are creation and annihilation operators and the single-particle level energies in a spherical nucleus are given by ϵ_α;

$$H_p = -\frac{1}{4} g \sum_{\alpha\gamma} s_\alpha s_\gamma c_\alpha^\dagger c_{\bar{\alpha}}^\dagger c_\gamma c_{\bar{\gamma}} \tag{4.11}$$

where $\bar{\alpha}$ is the state $(n, l, j, \bar{m})$, $s_\alpha = (-)^{j-m}$; and

$$H_q = -\frac{1}{2}\chi \sum_{\alpha\beta\gamma\delta} \sum_{M} < \alpha \mid Q_M \mid \gamma >< \delta \mid Q_M \mid \beta > c_\alpha^\dagger c_\beta^\dagger c_\delta c_\gamma \tag{4.12}$$

where $Q_M = r^2 Y_{2M}(\theta, \phi)$ is the quadrupole moment operator, and g and χ are the strengths of the pairing and quadrupole forces respectively.

Kumar and Baranger use the Hartree-Bogoliubov approximation which is valid only if one assumes that the contribution of pairing forces to the Hartree potential, the contribution of quadrupole forces to the pairing potential and the contribution of quadrupole forces to the exchange term are all negligible. The model as employed in this way is really applicable only to quadrupole deformations in nuclei where the deviation from sphericity

is small. Hence Kumar and Baranger's Pairing-Plus-Quadrupole Model cannot be used to investigate octupole structure or the structure of well-deformed nuclei. In addition, the assumption of adiabaticity implies that the vibrational nuclei, in which higher order kinetic energy terms are expected to be important (Bo75), cannot be studied with this model.

The best-known prediction made by Kumar and Baranger is that of a change of shape in the nuclear charge distribution from prolate deformation to oblate as the mass number increases. They found that this transition was expected to occur between A=190 and 192 for Os and between A=188 and 190 for Pt on the basis of their potential energy calculations and predicted signs of quadrupole moments, $Q(J_n^\pi)$. Although their potential energy calculations indicated that both ^{192}Os and ^{192}Pt would be oblate, they predicted that there would be a change in sign for $Q(2_1^+)$ between ^{192}Os and ^{192}Pt, as explained in § 3.4.2.

4.2.3 General Collective Model

Another model which has been applied to the Pt nuclei is the General Collective Model (GCM). It was first proposed by Gneuss and Greiner (Gn71) and has been employed to describe a wide range of nuclei, including the Os-Pt region (He81). As the name implies, the GCM attempts to provide a solution which can be used for any collective Hamiltonian. This is done by finding a set of scalar wave functions that fulfil the specific collective Hamiltonian chosen. The harmonic quadrupole oscillator Hamiltonian is used frequently. GCM calculations for Pt and Os nuclei were carried out by Hess *et al.* (He81) by diagonalizing the Hamiltonian using a five-dimensional harmonic oscillator basis to calculate potential energy surfaces (PES) from which collective properties were deduced. Four assumptions were made to obtain a useful form of the quadrupole operator Q_2 : a uniform charge distribution, the incompressibility of nuclear matter, the unimportance of terms higher than second order and the indistinguishability of neutrons and protons. The usual definitions of B(E2) values and quadrupole moments were used :

$$B(E2; J_i \rightarrow J_f) = \frac{1}{2J_i+1} |< J_f||Q_2||J_i >|^2 \qquad (4.13)$$

$$Q(J) = (\frac{16\pi}{5})^{1/2} \begin{pmatrix} J & 2 & J \\ J & 0 & -J \end{pmatrix} < J||Q_2||J > . \qquad (4.14)$$

Parameter values were obtained for each nucleus by fitting experimental values for excitation energies of levels with J≤6, $Q(2_1^+)$ and certain B(E2) values. The PES calculations of Hess *et al.* indicated that ^{196}Pt is "nearly triaxial, ...[and] soft against γ-vibrations but stiff against β-vibrations".

4.2.4 Boson Expansion Theory

The final model to be considered is the boson expansion theory (BET) developed by Tamura and his collaborators. The idea behind the BET is to use boson operators to describe the nucleus in order to facilitate numerical calculations. As nucleons obey fermion statistics rather than boson statistics, this is done by writing the Hamiltonian in terms of quasiparticle fermion pair operators up to quadratic order and then carrying out a power series expansion of the fermion operators in terms of boson operators.

As a starting point, the Hamiltonian is written in the form :

$$H = H_{sp} + H_{2-ph} + H_{0-pair} + H_{2-pair} \qquad (4.15)$$

i.e., as the sum of a single-particle contribution, H_{sp}, a quadrupole-quadrupole particle-hole contribution, H_{2-ph}, a monopole pairing interaction, H_{0-pair} and a quadrupole pairing interaction, H_{2-pair}. Each of these contributions is written in terms of $a_{jm}^{\dagger}$ and a_{jm}, the creation and annihilation operators of a particle in a single-particle orbit with energy ϵ_j, spin j and projection m. As in the Kumar-and-Baranger Hamiltonian, the interaction strengths of the quadrupole and pairing terms are denoted by χ_2 and g. The single-particle Hamiltonian is written:

$$H_{sp} = \sum_j N_j[(\epsilon_j - \lambda_F)^2 + \Delta^2]^{1/2} \qquad (4.16)$$

where the pairing gap and Fermi energy parameters, Δ and λ_F, are determined from experimental binding energies and occupation numbers. N_j is equivalent to n_d in the

IBM. A Bogoliubov transformation is performed to replace the particle operators with quasi-particle operators and the Hamiltonian is written in a form which is quadratic in these quasi-particle operators. An orthogonal transformation is then performed so as to isolate two collective particle-hole (fermion pair) operators, which are then expanded in an infinite series of boson operator products. The expansion is carried out so that the fermion commutation relations are satisfied by the boson operators for each order.

Originally the theory was used to describe nuclei in the Sm, Ru and Pd regions, all of which are known to have prolate deformation. Weeks and Tamura (We80) were the first to apply this theory to a region where both oblate and prolate deformation were believed to exist, viz. the Os and Pt nuclei. They were particularly interested in investigating the observation of large $Q(2_1^+)$ values for these nuclei, which were believed to be almost 'ideally γ-unstable', i.e., to have a potential energy surface with little dependence on γ. This is indicated by the presence of certain characteristic features of strong γ-instability [a value of $E_x(2_2^+)/E_x(2_1^+)$ of about 2, the repeating $0^+ - 2^+ - 2^+$ level sequence and the suppressed E2 crossover transition within that sequence (Wi56)]. The deformation of such nuclei was expected to have prolate and oblate components of roughly equal importance ($\gamma \simeq 30°$). This would result in near-zero $Q(2_1^+)$ values, as predicted by the O(6) limit of the IBM, which gives $\gamma_{\rm eff}$, the mean value of γ, to be 30° and $Q(J^\pi)$=0. Weeks and Tamura were able to fit the apparently contradictory features of a vanishing $B(E2;0_1^+ \rightarrow 2_2^+)$ and a large $Q(2_1^+)$. They obtained excellent agreement with most energies, transition strengths and static moments in the Os-Pt isotopes but noted that realistic starting values for the single-particle energies had to be used. In their calculations, they began with experimental single-particle energies obtained from nuclei in the neighbourhood of ^{208}Pb and then included residual interactions. Electromagnetic transition strengths were calculated using Q_π and Q_ν, microscopically derived E2 operators for protons and neutrons; specifically, the E2 transition operator is :

$$Q_2 = Q_\pi + e_{\rm eff}(Q_\pi + Q_\nu) \tag{4.17}$$

where the parameter $e_{\rm eff}$ is included to take care of the effect of core polarization due

to the deformation of the nucleus. Weeks and Tamura assumed that $e_{\rm eff}$ is independent of the contribution of particle-hole pairs, and varied it to fit the observed value of $B(E2;0_1^+ \rightarrow 2_1^+)$. They found that it decreased as the mass number A increased.

Weeks and Tamura also predicted values for the quadrupole moments of the $2_2^+, 4_2^+, 6_2^+$, 3_1^+ and 5_1^+ states on the assumption that these states form the γ band, i.e., the band of states with $K^\pi = 2^+$ which can be found in the spectrum of either an asymmetric rotor or of an axially symmetric vibrator (Bo75). Their conclusion was that "... Experimental information on the quadrupole moments of higher excited states in both osmium and platinum is needed."

4.3 Prior Experimental Work on Higher State Quadrupole Moments

There have been three studies of higher state quadrupole moments in stable even-mass Pt isotopes. So far, only one of these, a particle-γ coincidence and particle singles experiment by Baktash *et al.* (Ba78), has been published.

Baktash *et al.* used α and ^{16}O beams to measure excitation probabilities for states up to and including the 4^+ state in both the ground state band and γ band in ^{194}Pt (cf. fig. 4.1). Their results included values for $Q(2_2^+)$ and $Q(4_1^+)$ which had large uncertainties (100% and 200% respectively).

Unpublished data was obtained by Wu (Wu83t) at Rochester using ^{40}Ca, ^{58}Ni, ^{136}Xe and ^{208}Pb ions to bombard a self-supporting ^{194}Pt target. States up to and possibly including the 10^+ state in the ground state band and the 6^+ state in the γ band were populated and de-excitation γ-rays from those states observed. A number of E2 transition matrix elements and diagonal matrix elements were derived from the data with the program GOSIA. As no published reference to GOSIA includes as many of the necessary details of its operation as Wu83t, a summary of his description is included here : GOSIA employs a steepest descent minimization of the least squares search of the matrix elements. To reduce the large amount of CPU time needed, an approximation in the calculation of excitation amplitudes is made. The coupled differential equations which

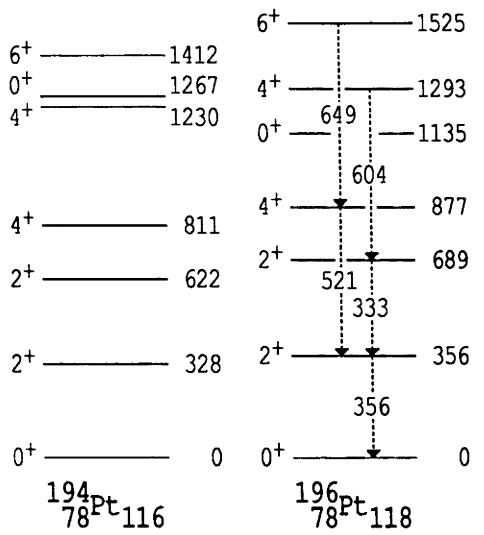

Figure 4.1: Level schemes of ^{194}Pt and ^{196}Pt up to the 6_1^+ state. Only the γ-ray transitions observed in the present work are shown. Excitation energies are given in keV.

describe the time evolutions of the excitation amplitudes [equation (2.6)] are re-written in the form :

$$\frac{d}{dw}a_n(w) = \sum_{\lambda\mu m} \zeta_{nm}^{(\lambda\mu)} f_{\lambda\mu}(w) a_m(w) < I_n \| \mathcal{M}(E\lambda) \| I_m > \tag{4.18}$$

where

$$\zeta_{nm}^{(\lambda\mu)} = \sqrt{2\lambda+1}(-1)^{I_m - M_m} \begin{pmatrix} I_m & \lambda & I_n \\ -M_m & \mu & M_n \end{pmatrix} \psi_{nm}, \tag{4.19}$$

$$f_{\lambda\mu}(w) = -iQ_{\lambda\mu}(w) \exp\left[i\xi_{nm}(\epsilon \sinh w + w)\right] a_m(w) \tag{4.20}$$

and $a_m(w)$ is the excitation amplitude of state m. The functions ψ_{nm} and $Q_{\lambda\mu}(w)$ depend on experimental parameters such as the bombarding energy, scattering angle and the multipolarity of the excitation. The parameter w was defined in equation (2.29). The approximation is made by considering only terms with μ=0,$\pm$1 and by assuming that the function $f_{\lambda\mu}(w)$ can be written as the sum of two constants, one of which is real and centred about $w = 0$; the other is imaginary and centred about $\pm w_0$. Thus,

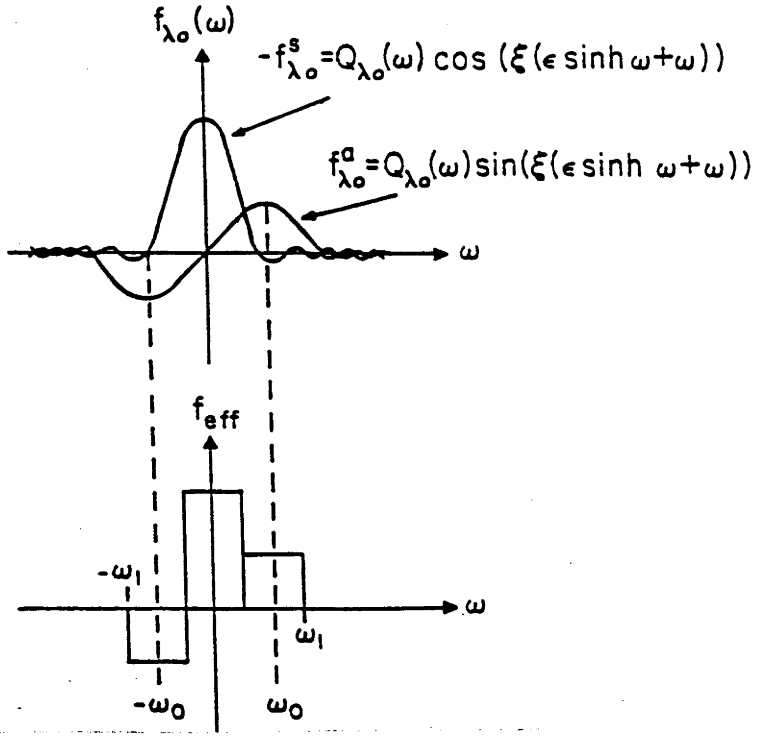

Figure 4.2: Schematic diagram of the "fast approximation" used by GOSIA (from Wu83t).

equation (4.18) can be represented by three independent equations :

$$\frac{d\bar{a}}{dw} = \hat{A}_1\bar{a}(w) \qquad \text{in the region} \qquad -w_1 \le w < (-2w_0 + w_1) \tag{4.21}$$

$$\text{with initial condition} \quad \bar{a}_0 = \bar{a}(-\infty)$$

$$\frac{d\bar{a}}{dw} = -i\hat{A}_2\bar{a}(w) \qquad \text{in the region} \qquad (-2w_0 + w_1) \le w < (2w_0 - w_1) \tag{4.22}$$

$$\text{with initial condition} \quad \bar{a}_0 = \bar{a}(-2w_0 + w_1)$$

$$\frac{d\bar{a}}{dw} = -\hat{A}_1\bar{a}(w) \qquad \text{in the region} \qquad (2w_0 - w_1) \le w < w_1 \tag{4.23}$$

$$\text{with initial condition} \quad \bar{a}_0 = \bar{a}(2w_0 - w_1).$$

The matrix operators $\hat{A}_1$ are independent of w; evaluation of these operators is performed numerically and the use of the approximation is claimed to give a 200-fold increase in speed. Wu's pictorial view of the approximation is reproduced in fig. 4.2. He justifies the use of this approximation by comparing amplitudes calculated for the excitation of ^{110}Pd by a 200 MeV ^{58}Ni beam by the exact method with those calculated by the method used in GOSIA. However, the magnitudes obtained by the approximate method differ from

those of the exact solution by up to 17% for the real component and by up to 80% for the imaginary component. In half of the states considered, the relative phases predicted for the real and imaginary parts are different for the two methods. The values predicted for the population of the states agree to ~10%.

Another experiment was performed at GSI by Mauthofer (Ma86t) and involved the measurement of static and dynamic E2 moments for ^{195,196}Pt by particle-γ and γ-γ coincidence measurements. He and his collaborators bombarded their ^{196}Pt target with ^{208}Pb ions and detected emitted γ-rays in coincidence with scattered projectiles and recoiling target nuclei. Mauthofer measured E2 matrix elements for states up to and including the 8^+ state in the ground state band and up to and including the 8^+ state in the γ band, but noted that the high bombarding energies and very heavy projectiles used in their experiment were not suitable for the determination of matrix elements for the low-lying states. Their analysis was carried out using the program ALADIN (Gr84) which obtains electromagnetic matrix elements by iterating Coulomb excitation calculations to minimize a quantity F^2 defined as :

$$F^2 = \sum_i \frac{\sum_j([Y_i^{expt} - Y_i(M_j)].S_i(M_j) - C_i(M_j).\Delta M_j)^2}{\sigma_i^2} \qquad (4.24)$$

where Y_i and σ_i denote the γ-yields from nuclear decay and the statistical errors respectively. The so-called sensitivity matrix $C_i(M_j)$ describes the correlation between the parameters M_j, while $S_i(M_j)$ are non-statistical weights which take into account the sensitivity of each parameter to the calculated yields.

In summary, accurate measurements of the reduced electric transition matrix elements of the higher states of ^{196}Pt and, to a lesser extent, ^{194}Pt are crucial to an understanding of these two nuclei. As outlined above, many have recognized the importance of static quadrupole moments of the excited states in ascertaining which nuclear model best describes observed properties in this region. New measurements of $Q(2_2^+)$ and $Q(4_1^+)$ were deemed necessary despite the prior work of Baktash *et al.*, Wu and Mauthofer. There were two main reasons for this decision : firstly, the use of relatively heavy projectiles and correspondingly high bombarding energies in both the GSI and Rochester work precludes

the precise measurements of matrix elements of the lower-lying excited states because the excitation probabilities of the lowest excited states are not very sensitive to changes in the experimental configurations due to the large component of multiple excitation which is present when heavy projectiles are used; secondly, the large uncertainties quoted by Baktash *et al.* make any comparison with model predictions meaningless, while the unpublished work of Wu and Mauthofer needs to be confirmed, particularly as the fast approximation used in GOSIA could be expected to introduce an uncertainty in calculated excitation probabilities of at least 10% (the value quoted by Wu for agreement of calculations of population of excited states although the measured matrix element values given for ^{194}Pt in Wu83t have quoted uncertainties of as little as 2%) whereas excitation probabilities for the lowest excited states are now commonly measured with a precision of 1%. The 14UD pelletron accelerator at ANU is particularly suitable for the production of beams of lighter ions than those employed in the other two experiments, which is advantageous for the measurement of the matrix elements of states such as the 2_1^+, 2_2^+ and 4_1^+ states.

4.4 Experimental Procedures and Analysis

To make optimal use of the facilities available, excitation probabilities were measured with as wide a range of projectiles as possible. The particle singles spectroscopy technique is especially suited to very light ions such as alpha particles and, in most cases, projectiles of about mass 10 to 20. However, the increase in straggling with the atomic number of the projectile, Z_p, and the atomic density of the target material (Be53) obviates the use of this technique for projectiles with $Z_p \geq 20$. The particle-γ coincidence technique was selected for the detection of ^{58}Ni projectiles whilst the particle singles technique was retained for lighter ions such as ^{4}He and ^{12}C. A more detailed discussion of the relative merits of these two techniques is included later in this chapter.

4.4.1 Particle-Gamma Coincidence Measurements

In this technique de-excitation γ-rays are detected in coincidence with scattered particles. The coincidence requirement provides a means of identification of the nucleus from which the γ-rays originate. More than one γ-ray detector can be used simultaneously, if γ-ray data are required at different angles; the maximum number of detectors is usually limited by space or equipment constraints.

As explained in § 3.3.1, absolute measurements of excitation probabilities can be derived directly from the areas of peaks seen in particle singles spectra. With the particle-γ coincidence technique, such direct measurements of absolute excitation probabilities are not possible. This is primarily due to two factors : the absence of some observable which indicates the amount of elastic scattering, and the variation of γ-ray intensity with angle. The former can readily be dealt with by normalizing the observed γ-ray intensities to the intensity of one particular γ-ray for which the transition probability is known or by using a calibrated γ-ray source to determine the efficiency of the γ-ray detector. The anisotropy of the γ-ray correlation can be written in terms of a sum of even-order Legendre polynomials P_k [cf. equation (2.53)] :

$$W(\theta) = A_0[1 + Q_2 A_2 P_2(\cos\theta) + Q_4 A_4 P_4(\cos\theta)] \tag{4.25}$$

where the parameter A_0 indicates the γ-ray intensity integrated over all angles and is the quantity from which excitation probabilities are derived. The parameters A_2 and A_4 depend on the nuclear matrix elements of the excited nucleus, the multipolarity of the transition and J_i and J_f, which are the spins of the states involved; Q_2 and Q_4 are calculable attenuation coefficients which describe the effect of the finite solid angle of the γ-ray detectors (Kr72). However, the observed angular correlation is also affected by the angular correlations of γ-rays which 'feed' the state J_i. For example, in the case of ^{196}Pt (see fig. 4.1), the observed angular correlation of the 356 keV γ-ray ($2_1^+ \rightarrow 0_1^+$) will depend to some extent on the angular correlations of the 521 keV ($4_1^+ \rightarrow 2_1^+$) and 333 keV ($2_2^+ \rightarrow 2_1^+$) γ-rays. The effect of feeding from higher states is dependent on the population of those states relative to that of the state being fed. It is possible to

estimate the values of A_2 and A_4 [cf. equation (2.50)] from the observed populations of the various states and hence to predict the values of A_2 and A_4 that should be deduced from the observed angular correlation. In principle, it should even be possible to predict the intensity of a γ-ray at any angle from a measurement of its intensity at one angle by calculating the angular correlation of the γ-ray. However, this is precluded by certain higher-order processes such as the deorientation effect, which is the distortion of the angular correlation by the variation of the hyperfine field of the nucleus. In addition, the deviation of the projectile beam with respect to the optically-aligned beam axis can result in an apparent rotation of the angular correlation by an angle ϕ, i.e. :

$$W_{obs}(\theta) = A_0(1 + Q_2A_2P_2[\cos(\theta - \phi)] + Q_4A_4P_4[\cos(\theta - \phi)]). \qquad (4.26)$$

The difficulties inherent in the estimation of a random effect, such as the movement of the beam, are insurmountable; for this reason it is better to take γ-ray data in coincidence with backscattered particles at a number of angles. It should be noted that, for the purposes of the present work, the actual values of A_2 and A_4 are not important in themselves as the primary aim of the experiment was to obtain measurements of A_0 which were of sufficient precision (better than 10% for the $2_2^+ \rightarrow 2_1^+$ and $4_1^+ \rightarrow 2_1^+$ transitions) to allow an accurate and unambiguous determination of the quadrupole moments of the 2_2^+ and 4_1^+ states; however, measurement of the angular correlation provided a means of checking for incorrect normalization of the data (cf. § 4.4.4) by comparison of experimental values of A_2 and A_4 with calculated values, as well as removing the need to estimate the perturbation of the angular correlation due to effects such as deorientation.

Some new equipment was designed for the particle-γ coincidence measurements in this experiment. There were a number of requirements which had to be considered : firstly, the coincidence requirement on detected γ-rays results in a fairly low counting rate compared with singles technique. This can be partially compensated for by using relatively thick ($\sim 1-3$ mg cm^{-2}) targets, but it is also important to be able to position the γ-ray detectors very close to the target. Secondly, to minimize the running time necessary, as many γ-ray detectors as possible should be used simultaneously. Thirdly, to

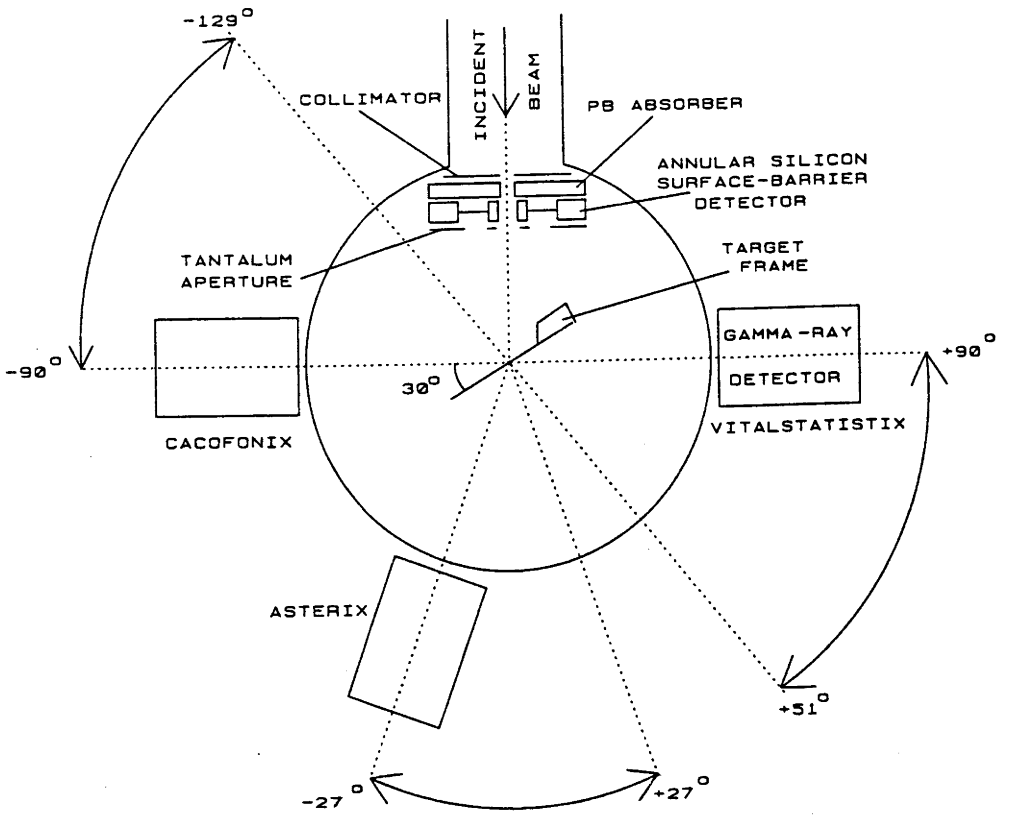

Figure 4.3: Experimental arrangement used for particle-gamma coincidence measurements.

measure a γ-ray angular correlation accurately, one should measure the γ-ray intensities in at least three quadrants, and also at certain angles such as 0° and ±90°, where minima occur in the angular correlation. Fourthly, it is desirable that the position of the particle detector can be varied so as to change the solid angle and scattering angle. The experimental arrangement used is shown in fig. 4.3. The target chamber is four inches in diameter, which is small enough so that the γ-ray detectors can be placed reasonably close to the target. To fulfil the third requirement, the target mount was inclined at 60° with respect to the beam axis so that the γ-ray detector angles ±90° could both be used. In addition, one side of the target frame has been removed so as to maximize the range of angles at which a γ-ray detector can view the target. This makes it much easier to select detector angles in three quadrants. The target and particle detector mounts are appropriately insulated so that incident beam current can be measured for both the collimator, which is situated upstream of the annular silicon surface-barrier detector with

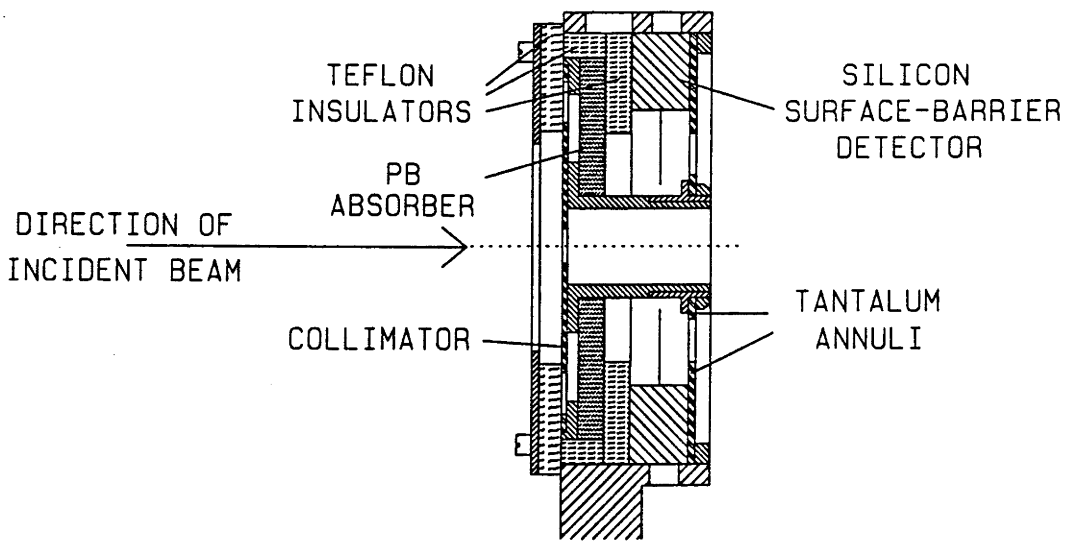

Figure 4.4: Cross-sectional view of the particle detector mount

which backscattered particles are detected, and the target. Annular apertures of varying diameter are used to define the solid angle of the particle detector. These features are shown in plate 4.1 and fig. 4.4.

In this experiment, it was not possible to use more than three γ-ray detectors around the target simultaneously; this restriction was due partly to the size of the detectors and partly to the ADC-to-computer interface which was not able to accomodate inputs from more detectors. One detector was used to measure γ-ray intensities at the angles $-129°, -117°$ and $-90°$; another was placed at $-27°, 0°$ and $27°$ while the third was used at $51°, 63°$ and $90°$; these angles were measured with respect to the beam axis. The angles were chosen to give equal steps in $\cos^2\theta$ between 0° and 90° (omitting 39° due to lack of space and time). Note that angles were selected in three quadrants, and each angle is supplementary or complementary to at least one other. This is valuable in checking the shape of the γ-ray angular correlation and when considering the relative efficiencies of the γ-ray detectors. The particle detector was positioned at a distance of 26.4 mm from the target, subtending a range of scattering angles from 165.9° to 170.1°.

Plate 4.1: View of the mounts for the target and annular silicon surface-barrier detector on the base of the target chamber as positioned during the particle-γ coincidence measurements in the present work. One side of the target frame has been removed to increase the number of angles at which a γ-ray detector can be placed to view the target. The target mount is positioned at an angle of 60° to the beam direction; the angle of inclination is measured from the scale that is engraved on the base. Similarly, the distance of the particle detector from the centre of the target chamber can be read from a scale that has been engraved between two plates which constrain the particle detector mount to an alignment along the beam axis. The scattering angle for particles is defined by the tantalum annuli just downstream of the surface-barrier detector (cf. fig. 4.4). The collimator (at the upstream end of the particle detector mount; cf. fig. 4.4), the target and the particle detector are electrically isolated using macor and teflon pieces, which appear white in the photographs. Target and collimator currents are monitored externally by means of two electrical feedthroughs in the base of the target chamber. Pulses from the particle detector are collected using the third feedthrough.

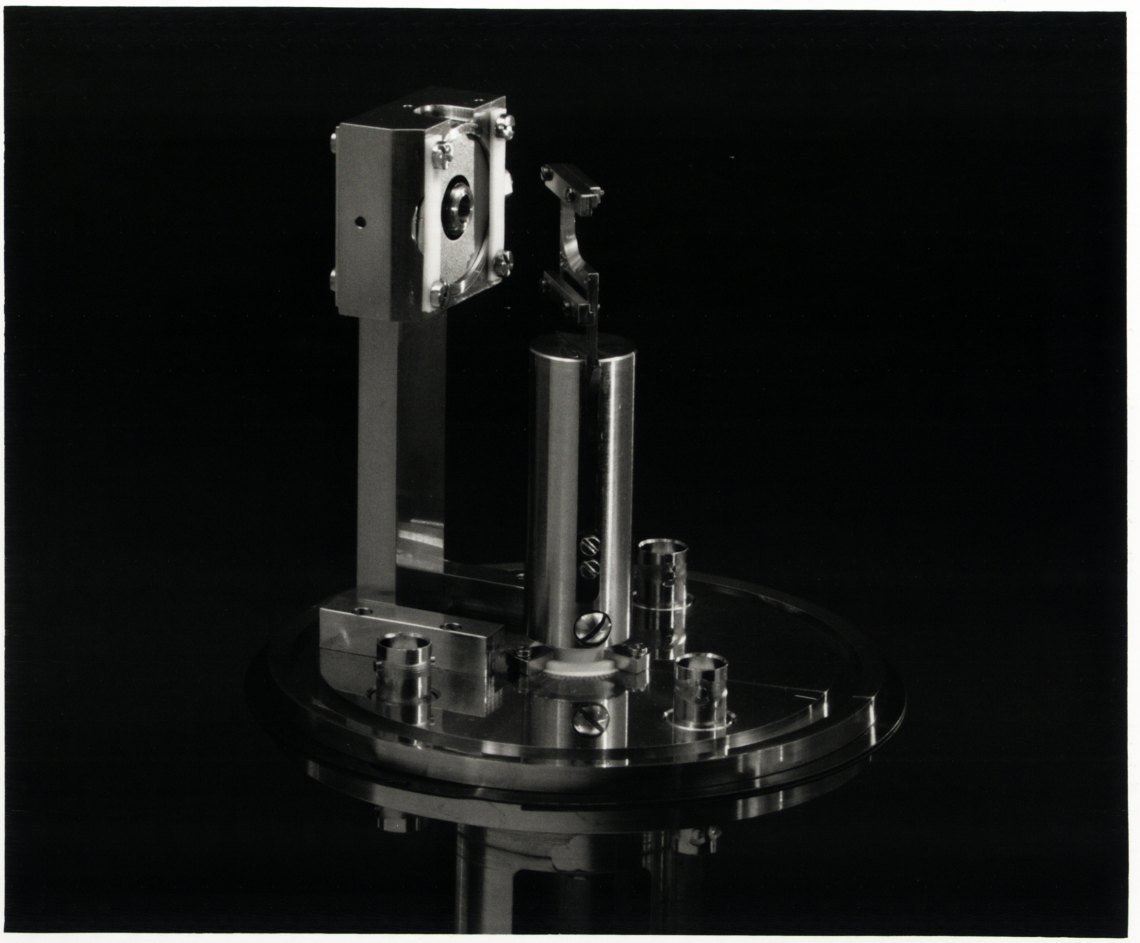

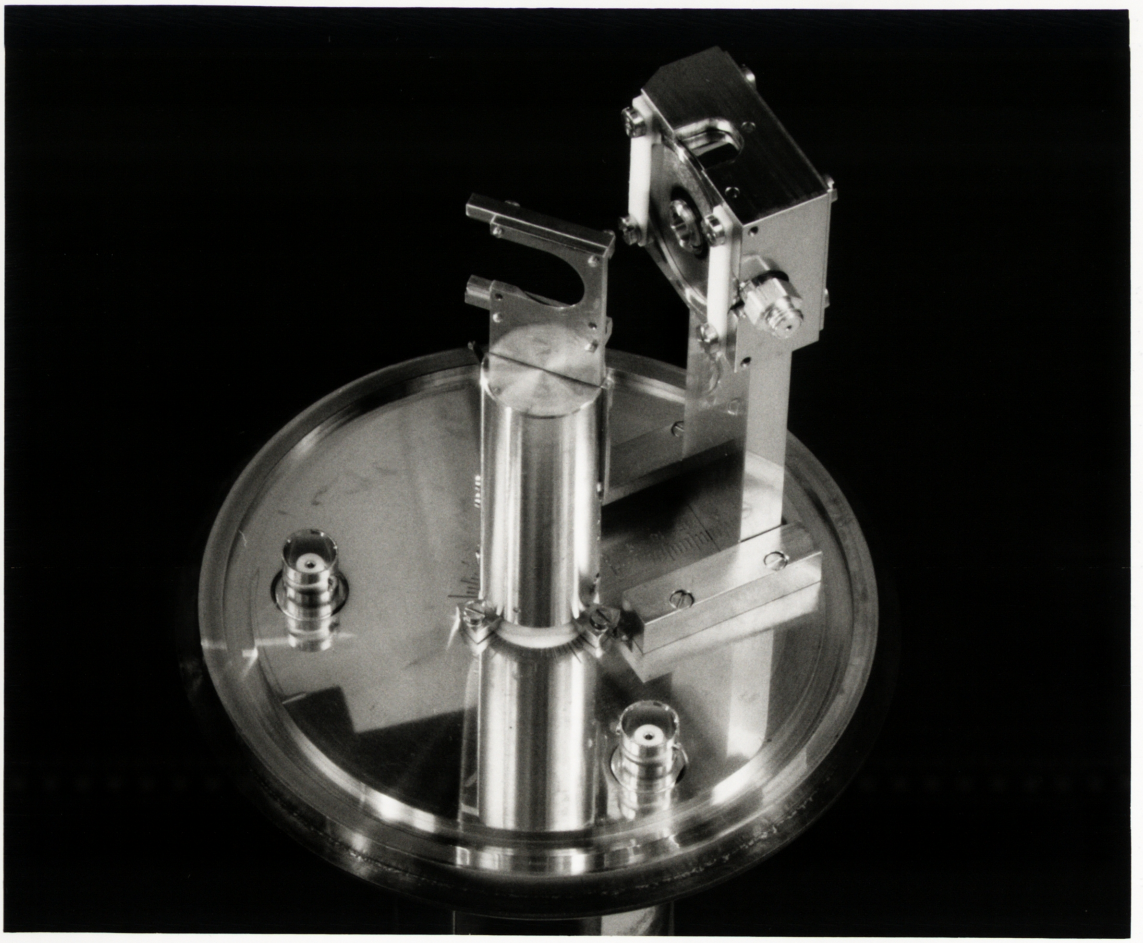

4.4.2 Particle-Gamma Coincidence Electronics

Signals were collected from the particle detector and each of the γ-ray detectors and passed through a standard fast-slow coincidence circuit in such a way that pulses from the γ-ray detectors were only passed to the computer if they arrived within $\sim$ 500 ns of a pulse from the particle detector. As shown in fig. 4.5, pulses from all the γ-ray detectors were first sent to timing filter amplifiers (TFA). Constant fraction discriminators (CFD) were then used to both cut out low-level noise and provide fast timing signals. The output of each CFD was monitored during the experiment to ensure that the count rates were not high enough to result in significant dead time in the detectors and amplifiers. During the experiment, count rates were of the order of 10^2 Hz for the particle detector and 10^3 Hz for the γ-ray detectors. The output of the CFD for each γ-ray detector was used as a 'Stop' signal for a Timing-to-Analog-Converter (TAC) which was started by the output of the particle detector CFD, thus providing a count of the total number of coincidence events.

The output of the particle detector was also sent to the computer after amplification, where it was collected in singles mode and later stored on tape. In addition, the signal from the particle detector was gated by the coincidence events to provide an alternative count of the total number of coincidence events which were stored in event-by-event mode.

Similarly, the energy signal from each γ-ray detector was amplified and gated by the output of a coincidence box which produced a signal if signals from the particle detector and γ-ray detector both arrived in coincidence with a signal from the appropriate TAC.

4.4.3 Comparison of Particle-Gamma Coincidence Technique with Particle Singles Spectroscopy

There are many advantages to the particle singles spectroscopy technique described in § 3.3.1; two obvious ones are that the method is relatively straightforward and provides a means of obtaining absolute excitation probabilities. However, it is clear that the quality of any results obtained from this technique will be strongly dependent on the resolution

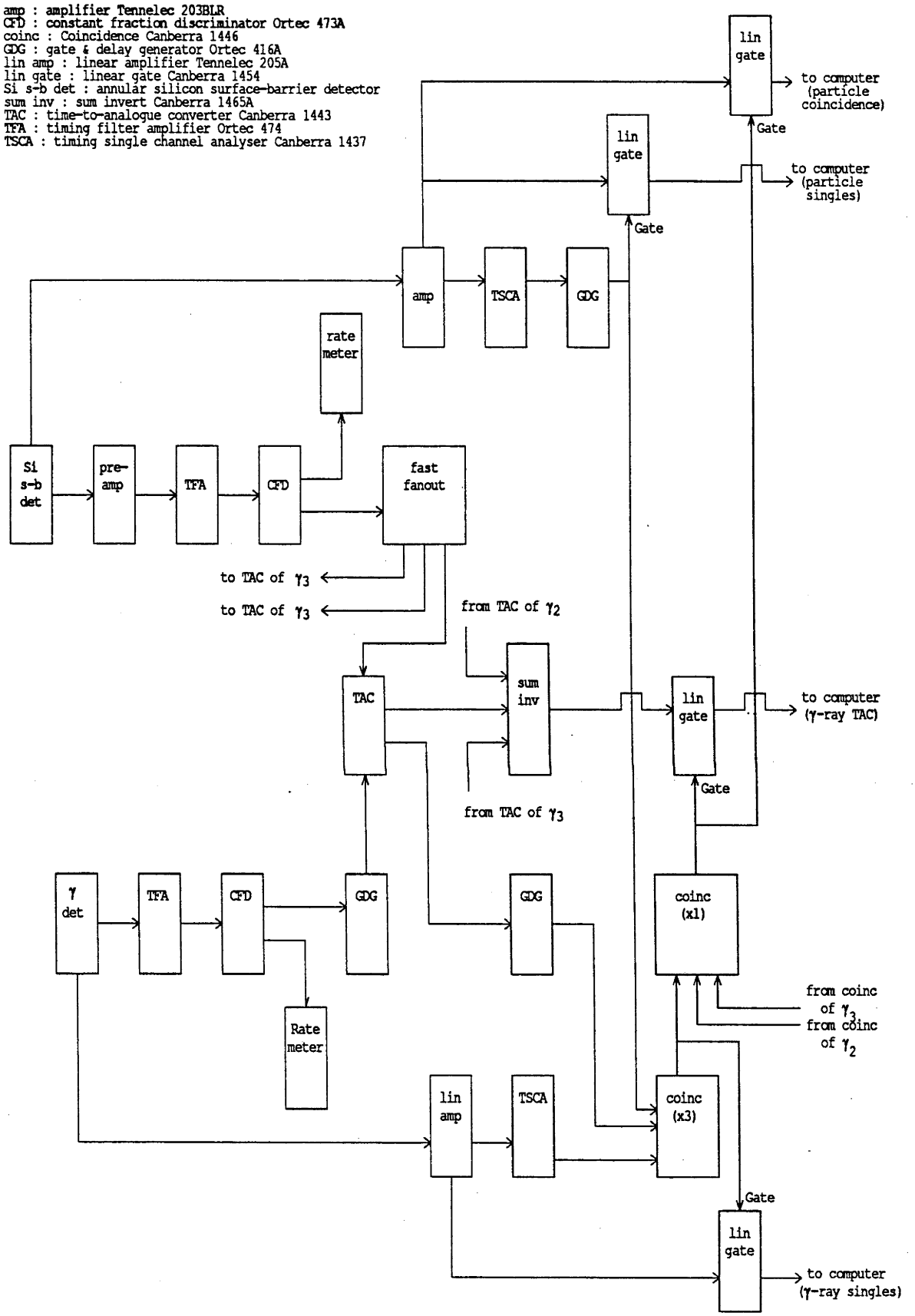

Figure 4.5: Diagram of the particle-gamma coincidence electronics. Circuitry is shown for one γ-ray detector only.

of peaks in the spectra. An important factor which determines the resolution for a given target is the mass of the projectile. As explained earlier, the use of heavier projectiles results in increased straggling which in turn causes worse resolution. Compare, for example, the resolution of the 0_1^+ and 2_1^+ peaks in figs. 4.6a and b. As bombardment with low mass (and hence energy) projectiles primarily results in single-step excitation, investigation of states such as the 4_2^+ and 6_1^+ states must be done with high mass projectiles and by a means other than particle singles spectroscopy. This is also evident from fig. 4.6 where the excitation of the 2_2^+ and 4_1^+ states relative to the 0_1^+ can be seen to be smaller for ^{4}He projectiles. In addition, the presence of contaminant material in the target can pose a significant problem. Provided that the states of interest have a reasonably large excitation probability ($\sim 10^{-3}$, for example), a sensible upper limit on the contribution of contaminant peaks can be measured by the procedure of examining spectra collected under different experimental conditions as described in § 3.3.1; however, when examining states with an extremely low excitation probability, this is no longer practical due to the long running time necessary. This procedure is also difficult to implement when a large number of states are being examined as this involves checking for a wide range of contaminant masses. In such a situation, it becomes nearly impossible to find a single bombarding energy at which peaks from all important contaminants would have energies sufficiently different to those of strongly excited states in the target nucleus and hence be clearly visible in the spectrum.

By contrast, the particle-gamma coincidence technique is highly suitable for such measurements. The coincidence requirement ensures that all the above problems are obviated. Another advantage is the superior resolution of γ-ray spectra recorded with Ge detectors as compared to spectra obtained with particle detectors. The major disadvantage of the particle-γ coincidence technique is that absolute measurements of excitation probabilities cannot be extracted readily from the data. A second disadvantage of particle-gamma coincidence measurements as compared with particle singles is a much lower count rate. Some compensation can be made for this by using targets which may be up to 1000 times thicker than the thin targets necessary for particle singles; however, this introduces additional uncertainties into the calculation of excitation probabilities since

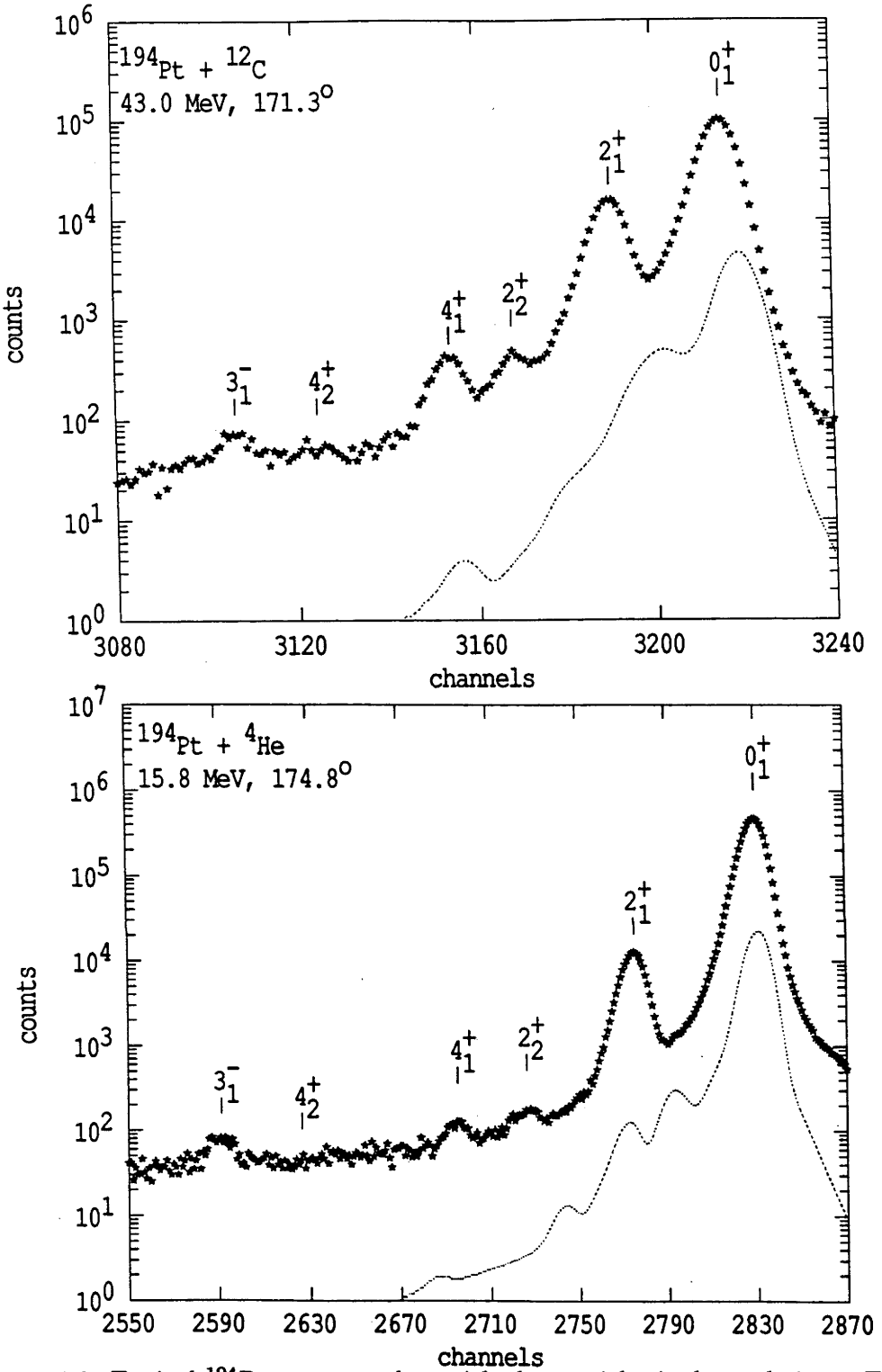

Figure 4.6: Typical ^{194}Pt spectra taken with the particle singles technique. The broken curves denote calculated contributions due to isotopes of the target nucleus other than the one of interest. Peaks corresponding to excited states in the target nucleus are indicated by J^{π}_{n} values.

integration over energy loss in the target must be included. In particular, few stopping cross-sections have been measured for heavy projectiles and the quoted uncertainty on values which have been extrapolated from light-projectile data is of the order of 10% (Zi80).

4.4.4 Analysis of Data

Analytical procedures for data obtained from particle singles spectroscopy have been given in § 3.3.1. In this section, only the analysis of data obtained from particle-gamma coincidence measurements will be described.

Data were collected in event-by-event mode. As can be seen from fig. 4.5, a spectrum from each γ-ray detector, a coincidence spectrum from the particle detector, a TAC signal from each γ-ray detector, and a particle singles spectrum were collected. Hence the spectra at the end of an experiment consisted of at least nine γ-ray spectra, taken in sets of three (i.e. $-129°, -27°$ and $51°; -117°, 0°$ and $63°; -90°, 27°$ and $90°$), three particle coincidence spectra, nine TAC spectra and three particle singles spectra. For the purposes of normalization, four sets of spectra were collected with the γ-ray detector angles for the fourth set being $-129°, 0°$ and $90°$. The reason for the additional set is explained later in this section.

The first step was to sort each γ-ray energy spectrum (fig. 4.7a) with gates on the particle spectrum and the TAC peak as shown in figs. 4.7b and c. A second sort was done with gates on one side of the TAC peak to give a random coincidence spectrum. This random coincidence spectrum was then subtracted from the first spectrum, thus giving only those γ-rays in true coincidence with backscattered particles (fig. 4.7d).

The next stage in the analysis was the extraction of γ-ray intensities. From fig. 4.7d, it can be seen that the coincidence spectrum was very clean so the area of each peak, I_{obs}, could be measured by drawing a linear background below it from the two regions on either side of the peak. In the present experiment, dead time was found to be less than 4% for the γ-ray detector electronics and less than 1% for the particle coincidence electronics. Dead time was taken into account and I_{obs} increased by the appropriate factor. At the end of the run the target was replaced with an ^{152}Eu source and care was

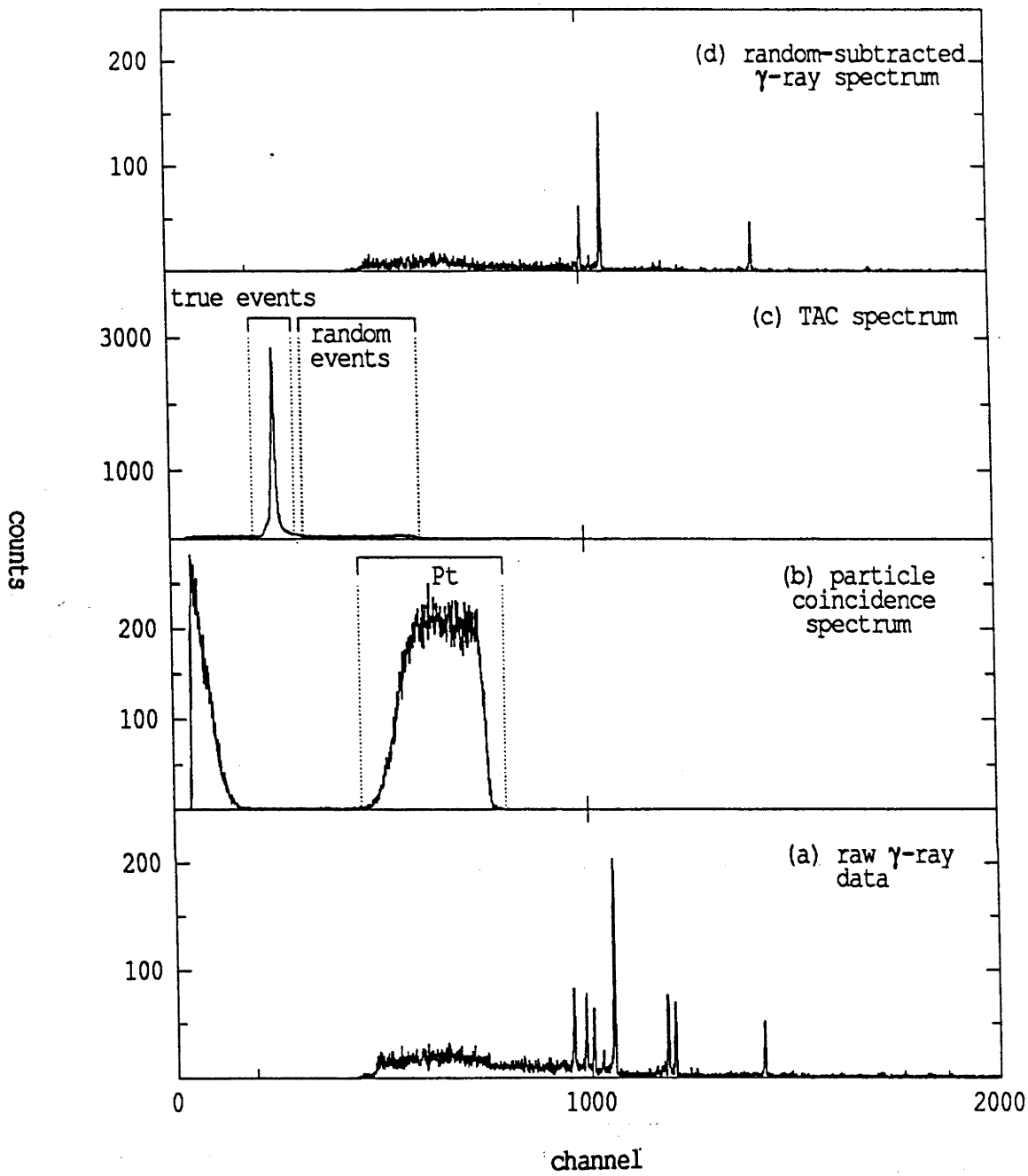

Figure 4.7: Representative spectra showing, respectively : (a)γ-ray singles spectrum, (b)particle spectrum with gates set on either side of the Pt peak, (c)TAC spectrum with true and random coincidence events marked, and (d)γ-ray spectrum after sorting with gates as shown in (b) and (c).

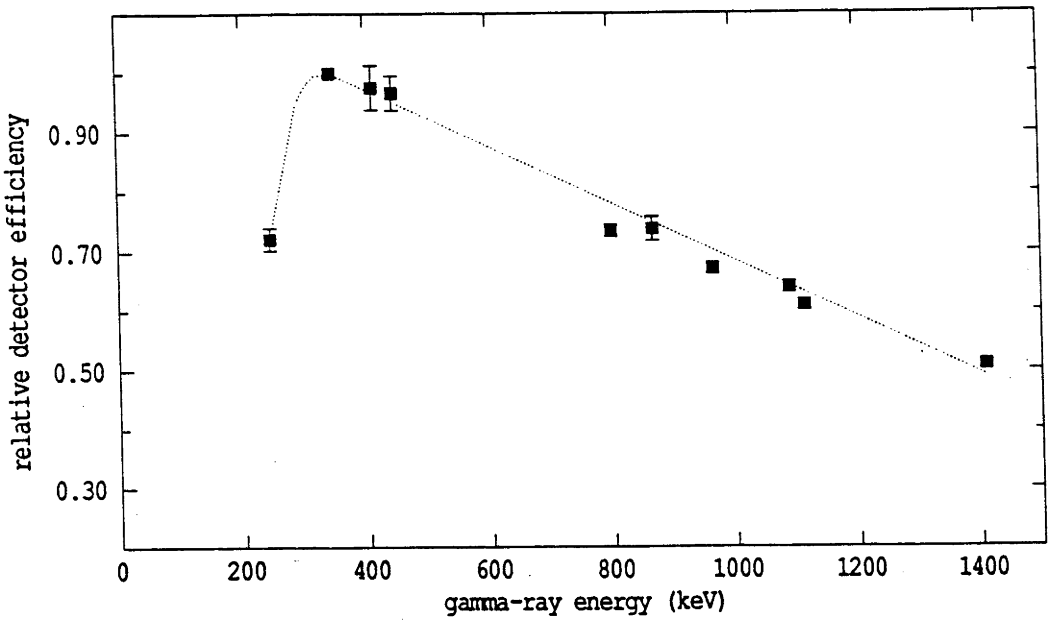

Figure 4.8: γ-ray detector efficiency (Cacofonix) as a function of γ-ray energy.

taken to ensure that the source was located at the same position as that where the beam hit the target. The γ-ray singles spectra obtained from the three detectors were used to measure the relative efficiency of the different detectors as a function of energy (cf. fig. 4.8). The γ-ray intensities I_{obs} were normalized with respect to Cacofonix, the detector at back angles $(-129°, -117°, -90°)$ i.e. :

$$I_{norm} = I_{obs} \times (1 - DT_\gamma)^{-1} \times (1 - DT_p)^{-1} \times \frac{I(E_\gamma)_{\mathrm{Cac}}}{I(E_\gamma)_{\mathrm{det}}} \tag{4.27}$$

where I_{norm} is the γ-ray intensity after correction for DT_γ, the dead time of the γ-ray detector electronics, DT_p, the dead time of the particle coincidence electronics, and $I(E_\gamma)_{\mathrm{det}}$ is the intensity of the γ-ray of energy E_γ observed in the γ-ray detector 'det'. [The three detectors used, as shown in fig. 4.3, were Cac(ofonix) at back angles, Ast(erix) at 0° and ±27°, and Vi(talstatisti)x at 51°, 63° and 90°.]

The γ-ray intensities were also normalized with respect to incident charge. This was done in two ways. Firstly, the number of projectiles scattered from platinum nuclei at the particle detector angle was assumed to be proportional to the incident charge and the number of counts in the appropriate peak in the particle singles spectrum was taken to be a measure of this. The γ-ray intensities are then normalised relative to the set of

three γ-ray spectra taken at $-129°, 0°$ and $90°$, i.e. :

$$I_p = I_{norm} \times \frac{\Sigma Pt_N}{\Sigma Pt_x} \tag{4.28}$$

where I_p is the γ-ray intensity normalised using the particle singles spectra, ΣPt_x denotes the number of projectiles scattered from platinum in the particle singles spectrum for set x and N is the set of spectra to which all intensities are being normalized. Although in principle this is an accurate method of normalization, in practice there can be at least one major problem. The particle singles data were being collected through a different interface to the event-by-event data so if either interface stopped, the normalization would be wrong. This problem did in fact occur and appropriate action was taken by using the numbers of records collected for the different angle sets to estimate the true value of ΣPt. It was noted that the fitted values of A_2 and A_4 showed significant disagreement with the calculated values when a single incorrect value of ΣPt was used, although A_0 was unaffected.

The second way of taking incident charge into account is to assume that, within statistical errors, the observed intensity of a γ-ray at a particular angle should only depend on the efficiency of the γ-ray detector and the incident charge. If the same detector is used, the γ-ray intensity will be directly proportional to the incident charge. Multiplying I_{norm} by the ratio of the intensity of the 356 keV γ-ray found in the two spectra of interest was found to give the same value as the first method. In other words, values determined for

$$I_\gamma = I_{norm} \times \frac{I(356\text{ keV})_{(N)}}{I(356\text{ keV})_{(x)}} \tag{4.29}$$

were found to verify the values obtained for I_p.

Next, the intensities I_p (or I_γ) were fitted to equation (4.26), the standard expression for the angular correlation. As explained earlier, the variable ϕ was included to take care of any deviation of the beam from the optically-determined axis. The values of A_2 and A_4 can be calculated [cf. equation (2.53)] using the expression :

$$A_k = a^{E\lambda}_{k_{fed}} F_k \tag{4.30}$$

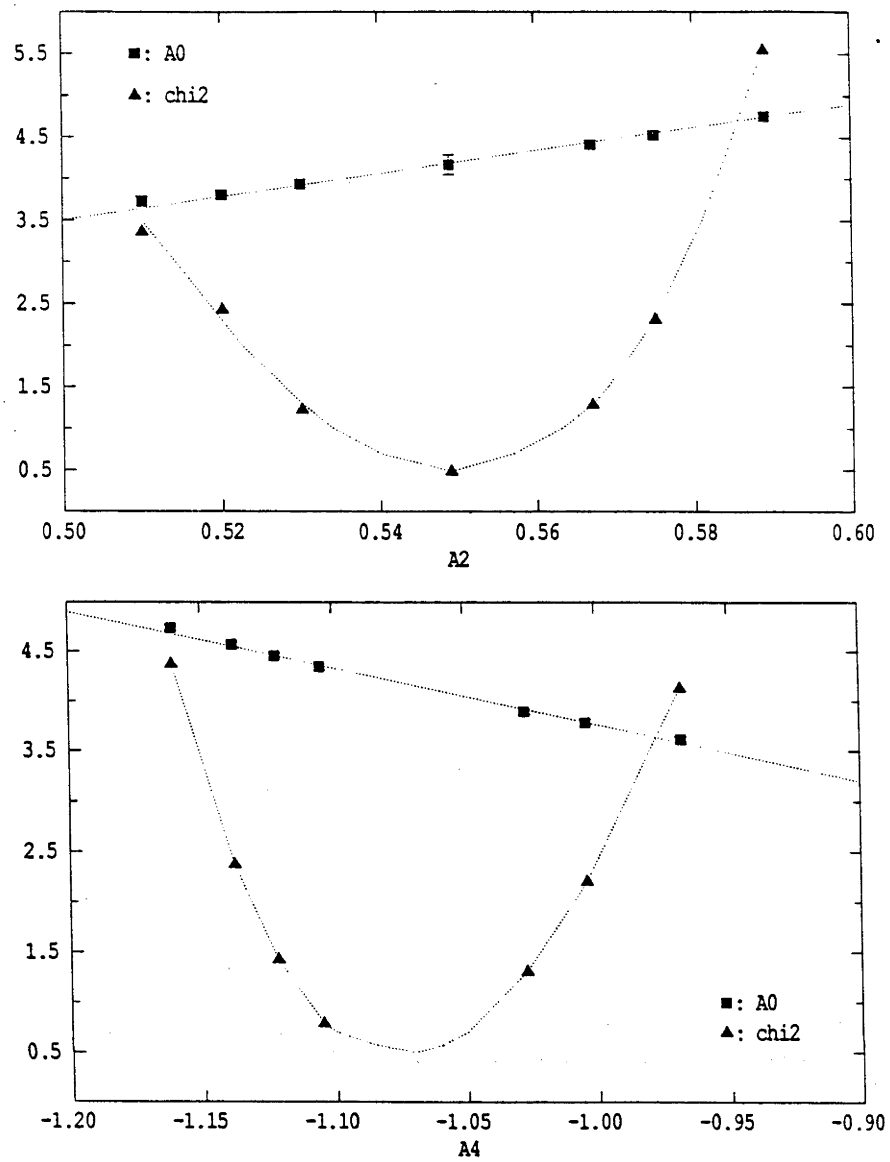

Figure 4.9: A_0 and chi^2 for the 356 keV γ-ray, 226 MeV ^{58}Ni projectiles, as a function of A_2 and A_4. Lines are drawn to guide the eye.

where the particle parameters $a_{k_{fed}}^{E\lambda}$, which are obtained from the Winther-de Boer code, have to be corrected for feeding from higher states as well as E2/M1 mixing, and the coefficients F_k, which can be calculated or found in various tables (Ya67), are determined by the multipolarity of the transition and by the spins of the two states involved. It is useful to compare the calculated values of A_2 and A_4 to those obtained experimentally as a single incorrect value of I_p or I_γ will change A_2 and A_4 significantly whilst A_0 is usually unaffected. Fig. 4.9 shows the relative insensitivity of A_0 to A_2 and A_4, whereas the chi^2 distribution is seen to change much more rapidly.

The next stage was the extraction of equivalent excitation probabilities from the A_0

values. This has to take account of the variation of absolute efficiency of the γ-ray detector as a function of γ-ray energy, and the incident charge. The observed γ-ray intensity per incident projectile can be written as :

$$I(\theta_\gamma, E_\gamma) = \rho \int_{E_i}^{E_f} \frac{dE_p}{S(E_p)} \int_{\theta_l}^{\theta_u} d\theta_p \epsilon(\theta_p, E_p; \theta_\gamma, E_\gamma) \frac{\sum_n f_n d\sigma_n(\theta_p, E_p)}{d\Omega} 2\pi \sin\theta_p \qquad (4.31)$$

where ρ is the number of target nuclei per unit mass, $S(E_p)$ is the stopping cross-section of the target material in MeV cm^2 g^{-1}, ϵ is the full-energy peak γ-ray detection efficiency, f_n is the fraction of decays of the state n that results in a gamma-ray transition of energy E_γ, $d\sigma_n$ is the differential cross-section of state n and

$$\epsilon(\theta_p, E_p; \theta_\gamma, E_\gamma) = \epsilon_0(E_\gamma) W(\theta_p, E_p; \theta_\gamma, E_\gamma). \qquad (4.32)$$

The angles θ_γ and θ_p are, respectively, the angle of the detected gamma-ray and the angle of the scattered projectile relative to the beam direction; E_p is the energy of the detected projectile just before collision, E_i is the incident beam energy, E_f is the energy of the beam after traversing the target, and θ_l and θ_u are the minimum and maximum angles at which a scattered projectile would be detected. The full-energy peak efficiency for an isotropic source of γ-rays of energy E_γ and the angular correlation of the γ-rays are denoted by $\epsilon_0(E_\gamma)$ and $W(\theta_p, E_p; \theta_\gamma, E_\gamma)$ respectively. The intrinsic efficiency of the particle detector is assumed to be 100% - this is true in practical terms, and makes no difference to the following derivation.

For the case of a γ-ray transition $J_i \rightarrow J_f$ where there is only one state i that deexcites to produce E_γ,

$$\begin{aligned} I(\theta_\gamma, E_\gamma) &= \rho \int_{E_i}^{E_f} \frac{dE_p}{S(E_p)} \int_{\theta_l}^{\theta_u} d\theta_p \epsilon(\theta_p, E_p; \theta_\gamma, E_\gamma) \frac{d\sigma(J_i)}{d\Omega} 2\pi \sin\theta_p \\ &= 2\pi\rho\epsilon_0(E_\gamma) W(\theta_p, E_p; \theta_\gamma, E_\gamma) \int_{E_i}^{E_f} \frac{dE_p}{S(E_p)} \int_{\theta_l}^{\theta_u} d\theta_p \frac{d\sigma(J_i)}{d\Omega} 2\pi \sin\theta_p. \end{aligned} \qquad (4.33)$$

Experimentally the observed angular correlation is described by equation (4.26) for a

given number of backscattered projectiles n_{obs} which is related to the total number of incident projectiles n_{inc} by :

$$n_{inc} = n_{obs} \int_{E_i}^{E_f} \frac{dE_p}{S(E_p)} \int_{\theta_l}^{\theta_u} d\theta_p \, \frac{d\sigma(R)}{d\Omega} \sin\theta_p \tag{4.34}$$

where $d\sigma(R)/d\Omega$ denotes the Rutherford cross-section. Hence the observed value of A_0 can be related to the γ-ray yield by :

$$\frac{A_0(J_i \rightarrow J_f)}{n_{inc}} = 2\pi\rho\epsilon_0(E_\gamma) \int_{E_i}^{E_f} \frac{dE_p}{S(E_p)} \int_{\theta_l}^{\theta_u} d\theta_p \, \frac{d\sigma(J_i)}{d\Omega} \sin\theta_p \tag{4.35}$$

which gives the following relation between the observed value of A_0 and the excitation probability $P(J_i)$:

$$\frac{A_0(J_i \rightarrow J_f)}{n_{obs} P(J_i)} = 2\pi\rho\epsilon_0(E_\gamma) \tag{4.36}$$

where $P(J_i)$ is defined as

$$[\int_{E_i}^{E_f} \frac{dE_p}{S(E_p)} \int_{\theta_l}^{\theta_u} d\theta_p \, \frac{d\sigma(J_i)}{d\Omega} \sin\theta_p] / [\int_{E_i}^{E_f} \frac{dE_p}{S(E_p)} \int_{\theta_l}^{\theta_u} d\theta_p \, \frac{d\sigma(R)}{d\Omega} \sin\theta_p]. \tag{4.37}$$

Therefore, equation (4.35) can be generalised to be

$$\frac{A_0(J_i \rightarrow J_f)}{n_{obs} \int_{E_i}^{E_f} \frac{dE_p}{S(E_p)} \int_{\theta_l}^{\theta_u} d\theta_p \, \frac{d\sigma(R)}{d\Omega} \sin\theta_p} = 2\pi\rho\epsilon_0(E_\gamma) \int_{E_i}^{E_f} \frac{dE_p}{S(E_p)} \int_{\theta_l}^{\theta_u} d\theta_p \, \sum_n f_n \frac{d\sigma(J_n)}{d\Omega} \sin\theta_p \tag{4.38}$$

where J_n are states (including J_i) that feed directly into J_i. Hence

$$\frac{A_0(J_i \rightarrow J_f)}{n_{obs} 2\pi\rho\epsilon_0(E_\gamma)} = \sum_n f_n P(J_n) \tag{4.39}$$

$$= P(J_i) + \sum_{n \neq i} P(J_n) \tag{4.40}$$

since $f_n = 1$ for all n in the case of ^{196}Pt. From equation (4.40), excitation probabilities can be deduced for each state J_n from which emitted γ-rays are observed.

The extraction of excitation probabilities from γ-ray angular correlations requires some form of normalization, as the detector efficiency ϵ_0 will be different for every system. One method is to normalise all observed γ-ray intensities to the intensity of a γ-ray for

which the yield can be calculated with some degree of accuracy. In this experiment, the particle singles data obtained were used to extract matrix elements for the lowest-lying states; from these matrix elements, reasonably accurate and precise values of $P(2_1^+)$ were calculated. In general, the new data obtained were as precise as, or more precise than, that previously available. γ-ray yields for all transitions other than the $2_1^+ \rightarrow 0_1^+$ (356 keV) transition were measured relative to that transition. The variation of ϵ_0 with γ-ray energy can be determined from the γ-ray spectrum of the ^{152}Eu source mentioned earlier; this function is plotted in fig. 4.8 for Cacofonix [the detector to which the γ-ray intensities were normalized; cf. equation (4.27)]. Values for ϵ_0 of Cacofonix at different E_γ, assuming $\epsilon_0(344 \text{ keV})=1$, are tabulated (table 4.2).

Values of A_0 also need to be corrected for internal conversion. This can be done by multiplying A_0 by the factor $(1+\alpha_x)/(1+\alpha_N)$, where α_x and α_N are, respectively, the internal conversion coefficients of the γ-ray transition of interest and the transition to which other γ-ray yields are to be normalized.

4.5 Experimental Results

4.5.1 ^{194}Pt

4.5.1.1 Particle singles data

Data were collected for the $2_1^+, 2_2^+$ and 4_1^+ states of ^{194}Pt using ^{4}He and ^{12}C projectiles scattered at various back angles ranging from 169.9° to 174.8°, and at a range of bombarding energies (see table 4.3). Typical spectra for each of the projectiles are shown in fig. 4.6. Peak-to-valley ratios for the 2_1^+ state were of the order of 100:1 for ^{4}He spectra and 3:1 for ^{12}C spectra.

Spectra obtained were fitted using a skew gaussian lineshape as described in § 3.3.1, and the areas of peaks of interest were extracted to give excitation probabilities for each state. Only data taken at bombarding energies where Coulomb-nuclear interference is insignificant were used in the extraction of matrix elements. The safe energy plots are shown in fig. 4.10. In principle, a plot should be made for each projectile used and for every state under examination, as the distance at which nuclear interference becomes

Table 4.2: γ-ray detector efficiency as a function of γ-ray energy obtained from ^{152}Eu spectrum; I_{rel} denotes the intensity of E_γ relative to that observed in Cacofonix.

E_γ (keV)	I[a]) (Le78)	I_{rel} (Ast)	I_{rel} (Vix)	ϵ_0[b])
244	358	0.92(3)	1.04(4)	0.72(2)
296	21.1	1.2(3)	1.2(3)	1.37(24)
344	1275	0.920(9)	1.074(11)	1
411	107	0.89(5)	1.03(6)	0.98(4)
444	148	0.94(4)	1.04(4)	0.97(3)
799	619	0.912(15)	1.071(19)	0.735(10)
867	199	0.98(4)	1.14(5)	0.738(20)
964	692	0.904(15)	1.120(19)	0.671(9)
1088[c])	547	0.953(19)	1.107(23)	0.640(10)
1112	649	0.909(16)	1.101(20)	0.610(9)
1408	1000	0.923(13)	1.555(23)	0.509(6)
1458	23.3	0.92(3)		

[a]) relative intensities from Le78
[b]) efficiency of Cacofonix as a function of E_γ, normalized to the 344 keV γ-ray
[c]) combined values for the 1086 and 1090 keV γ-rays

Table 4.3: Experimental configurations and measured excitation probabilities for ^{194}Pt.

Projectile	E_p[a] (MeV)	θ_{lab}[b]	s[c] (fm)	$P_{exp}(2_1^+)$ ($\times 10^{-2}$)	$P_{exp}(2_2^+)$ ($\times 10^{-4}$)	$P_{exp}(4_1^+)$ ($\times 10^{-4}$)
^{4}He	14.0	174.8°	7.18	1.76(7)	0.90(11)	0.38(8)
	14.8		6.29	2.13(9)	1.13(13)	0.54(10)
	15.0		6.09	2.233(15)	1.3(3)	0.73(22)
	15.4		5.69	2.414(20)	1.7(3)	0.7(3)
	15.6		5.50	2.525(11)	1.96(17)	1.08(12)
	15.8		5.31	2.650(13)	1.7(3)	1.46(23)
	16.0		5.13	2.716(11)	1.62(18)	1.17(12)
	14.4	171.3	6.74	1.93(8)	0.99(6)	0.44(4)
	14.6		6.52	2.02(8)	1.12(15)	0.46(13)
^{12}C	42.0	171.3°	6.98	12.57(9)	22.3(16)	25.5(10)
	43.0		6.58	13.62(8)	25.9(15)	31.4(10)
	44.0		6.19	15.03(15)	37.0(25)	40.8(22)
	44.0	175.0°	6.19	14.82(7)	33.9(13)	42.0(10)
	44.0	169.9°	6.21	14.45(11)	32.2(22)	43.1(17)
	45.0		5.85	15.68(8)	39.9(14)	50.3(9)
	46.0		5.50	16.68(10)	43.9(18)	59.0(11)

[a]) bombarding energy
[b]) mean scattering angle in the laboratory system
[c]) distance of closest approach of the nuclear surfaces

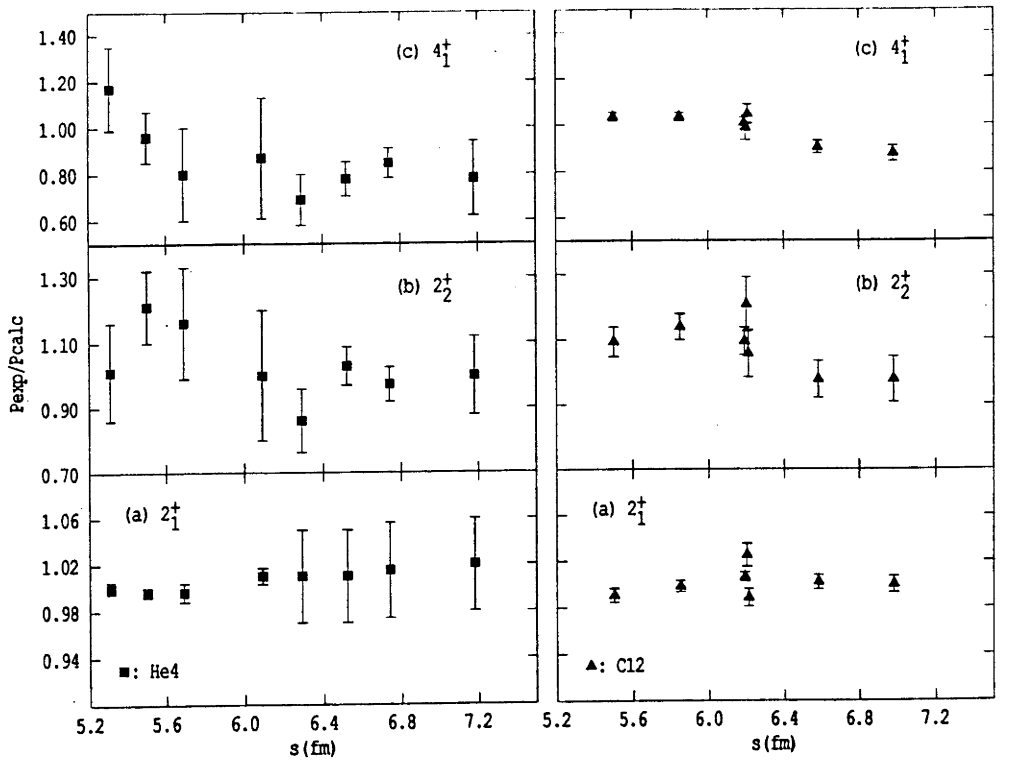

Figure 4.10: Safe energy plots for ^{194}Pt.

important may be different for different projectiles and can even vary from state to state. However, perusal of fig. 4.10 shows that this does not have to be strictly adhered to in practice as the uncertainties in P_{exp} for higher states are usually relatively large, effectively swamping any small deviation from P_{calc}. For this reason, the value of s obtained for the first excited state may be the best choice for higher states, provided the data show no evidence to the contrary. It can be seen from fig. 4.10 that data taken for a distance of closest approach of 5.3 fm or more were not significantly affected by Coulomb-nuclear interference.

Contributions to the peaks of interest from other platinum isotopes were calculated using the isotopic assay provided by the supplier (table 4.4) and matrix element values from the literature (table 4.5). These are indicated in fig. 4.6 by the dashed line. The presence of certain other nuclei in the target could have affected the measurement of excitation probabilities; for the ^{4}He spectra, these were nuclei in the mass range A$\sim$152-154 (under the 2_1^+ peak), 126-129 (under the 2_2^+ peak) and 114-117 (under the 4_1^+ peak). For the ^{12}C spectra, potential contaminant nuclei were A$\sim$187-188, 182-184 and 179-180 respectively. The presence of such contaminants was checked for by bombardment with

Table 4.4: Isotopic composition of target material, as provided by supplier (Oak Ridge National Laboratory) and target thicknesses as measured by Rutherford scattering.

	Target	
Isotope	^{194}Pt	^{196}Pt
192	0.04 ± 0.01	–
194	95.06 ± 0.15	0.78 ± 0.02
195	3.78 ± 0.10	2.39 ± 0.05
196	0.97 ± 0.05	96.54 ± 0.10
198	0.15 ± 0.02	0.29 ± 0.02

	Thickness (μg cm^{-2})	
Projectile	^{194}Pt	^{196}Pt
^{4}He	20–25	69,89
^{7}Li	–	51
^{12}C	2–3	1,6

Table 4.5: Magnitudes of matrix elements for the Pt isotopes in e $b^{\lambda/2}$; v denotes matrix elements which were fitted in the analysis. Fixed values taken from Ba78, Ha78, Au83, Sh83, Gy86, Ma86t, Wu87.

	^{195}Pt
$<3/2_1^- \|\mathcal{M}(E2)\|1/2_1^->$	0.42
$<5/2_1^- \|\mathcal{M}(E2)\|1/2_1^->$	0.62
$<3/2_2^- \|\mathcal{M}(E2)\|1/2_1^->$	0.27
$<3/2_3^- \|\mathcal{M}(E2)\|1/2_1^->$	0.88
$<5/2_2^- \|\mathcal{M}(E2)\|1/2_1^->$	1.01
$<5/2_2^- \|\mathcal{M}(E2)\|3/2_1^->$	0.60
$<5/2_3^- \|\mathcal{M}(E2)\|1/2_1^->$	0.205
$<5/2_3^- \|\mathcal{M}(E2)\|3/2_1^->$	1.095
$<5/2_3^- \|\mathcal{M}(E2)\|5/2_1^->$	0.29
$<3/2_4^- \|\mathcal{M}(E2)\|1/2_1^->$	0.24
$<3/2_4^- \|\mathcal{M}(E2)\|3/2_1^->$	0.14
$<5/2_4^- \|\mathcal{M}(E2)\|1/2_1^->$	0.015
$<3/2_5^- \|\mathcal{M}(E2)\|1/2_1^->$	0.26
$<3/2_5^- \|\mathcal{M}(E2)\|3/2_1^->$	0.36
$<3/2_5^- \|\mathcal{M}(E2)\|5/2_1^->$	0.19

Table 4.5 (cont.)

	^{192}Pt	^{194}Pt	^{196}Pt	^{198}Pt
$<2_1^+\|\|\mathcal{M}(E2)\|\|0_1^+>$	1.354	v	v	1.044
$<2_1^+\|\|\mathcal{M}(E2)\|\|2_1^+>$	0.73	v	v	0.554
$<2_2^+\|\|\mathcal{M}(E2)\|\|0_1^+>$	0.12	v	v	0.039
$<2_2^+\|\|\mathcal{M}(E2)\|\|2_1^+>$	1.49	v	v	1.020
$<2_2^+\|\|\mathcal{M}(E2)\|\|2_2^+>$		-0.66	v	
$<0_1^+\|\|\mathcal{M}(E4)\|\|4_1^+>$	0.2	v	v	-0.09
$<4_1^+\|\|\mathcal{M}(E2)\|\|2_1^+>$	2.29	v	v	1.56
$<4_1^+\|\|\mathcal{M}(E2)\|\|2_2^+>$		0	0	
$<0_2^+\|\|\mathcal{M}(E2)\|\|2_1^+>$		0.07	v	0.44
$<0_2^+\|\|\mathcal{M}(E2)\|\|2_2^+>$		0.231	v	
$<0_1^+\|\|\mathcal{M}(E4)\|\|4_2^+>$		0.13	0	
$<4_2^+\|\|\mathcal{M}(E2)\|\|2_1^+>$		0.30	v	
$<4_2^+\|\|\mathcal{M}(E2)\|\|2_2^+>$		2.5	v	
$<4_2^+\|\|\mathcal{M}(E2)\|\|4_1^+>$		2.8	v	
$<2_3^+\|\|\mathcal{M}(E2)\|\|2_1^+>$				0.14
$<2_3^+\|\|\mathcal{M}(E2)\|\|2_2^+>$				0.85
$<6_1^+\|\|\mathcal{M}(E2)\|\|4_1^+>$	2.5	2.9	v	2.34
$<6_1^+\|\|\mathcal{M}(E2)\|\|4_2^+>$		0.16		
$<6_1^+\|\|\mathcal{M}(E2)\|\|6_1^+>$		0.28	v	
$<6_2^+\|\|\mathcal{M}(E2)\|\|4_2^+>$			2.13	
$<6_2^+\|\|\mathcal{M}(E2)\|\|6_2^+>$			-1.6	
$<8_1^+\|\|\mathcal{M}(E2)\|\|6_1^+>$			3.13	
$<8_1^+\|\|\mathcal{M}(E2)\|\|8_1^+>$			0.226	

Table 4.6: Measured upper limits to the contribution of potential contaminants of mass A for ^{194}Pt.

Projectile	J_n^+	A[a])	% of $P_{exp}(J_n^+)$
^{4}He	2_1^+	152–154	0.1
	2_2^+	126–129	10
	4_1^+	114–117	10
^{12}C	2_1^+	187–188	0.1
	2_2^+	182–184	5
	4_1^+	179–180	5

[a]) mass of nuclei which could affect the measured excitation probability $P_{exp}(J_n^+)$

12.0 MeV beams of ^{12}C projectiles. The upper limits to the contributions of these nuclei listed in table 4.6 show that any such contaminants would have had a negligible effect on the values measured for the excitation probabilities.

4.5.1.2 Analysis of excitation probabilities

The measured excitation probabilities for the 2_1^+ state listed in table 4.3 were put into a least-squares fitting program together with those calculated using the Winther-de Boer Coulomb-excitation program. An iterative procedure was employed to obtain 'best fit' values for B(E2;$0_1^+ \rightarrow 2_1^+$) and Q(2_1^+) which were used in the Winther-de Boer program to optimise the values of the matrix elements $<2_2^+||\mathcal{M}(E2)||0_1^+>$, $<2_2^+||\mathcal{M}(E2)||2_1^+>$, $<2_2^+||\mathcal{M}(E2)||2_2^+>$, $<4_1^+||\mathcal{M}(E4)||0_1^+>$, $<4_1^+||\mathcal{M}(E2)||2_1^+>$, $<4_1^+||\mathcal{M}(E2)||2_2^+>$ and $<4_1^+||\mathcal{M}(E2)||4_1^+>$. This was done by varying each of these matrix elements in turn to find the value which gave the best fit to $P_{exp}(2_2^+)$ and $P_{exp}(4_1^+)$. Having obtained a first approximation to the result in this way, final values were obtained by using the fitting program Minuit (Ja75) into which the Winther-de Boer code had been incorpo-

rated as a subroutine. The fitting procedures are described in Appendix B. The final results obtained are listed in table 4.7, together with those of previous experiments for the sake of comparison. Due to time constraints, particle-γ coincidence measurements of excitation probabilities of ^{194}Pt under bombardment with ^{58}Ni projectiles were not completed; consequently, a value for $Q(2_2^+)$, which has little effect on the predicted excitation probabilities for lighter projectiles, could not be obtained.

4.5.1.3 Corrections and uncertainties

The most important uncertainty to be considered is that of the magnitudes and signs of matrix elements which cannot be ascertained from the data as these can have a large effect on the results obtained. When determining the 2_1^+ matrix elements, the 2_2^+ and 4_1^+ matrix elements have the most effect, hence experiments which determine the signs of products of matrix elements are very important. In the present work, the signs of the 2_2^+ and 4_1^+ matrix elements relative to those of the 2_1^+ state are determined experimentally, so the influence of the values assumed for the 4_2^+ and 6_1^+ matrix elements must be assessed. Assumed values are listed in table 4.5. The unpublished values of Wu (Wu87)[1] have been used only in cases where no published values are available.

Corrections must also be made for the effects of vacuum polarization, nuclear polarization, electron screening, use of the semi-classical approximation and target thickness. The size of these corrections for $B(E2;0_1^+ \rightarrow 2_1^+)$ and $Q(2_1^+)$ are listed in table 4.8. In addition, uncertainty in beam energy and scattering angle, virtual excitation of the GDR and the uncertainty in values of assumed matrix elements all contribute to the uncertainty of the measured matrix element values. Estimates of these contributions are also shown in table 4.8. The effect of these uncertainties on the other matrix elements determined in the present work is small in comparison to the statistical uncertainties.

[1]The matrix element values quoted from Wu's experiment have been taken from Wu87 rather than from Wu83t; this was done at his request.

Table 4.7: Measured values for matrix elements $< J_f^+ \| \mathcal{M}(E\lambda) \| J_i^+ >$ (e $b^{\lambda/2}$) of ^{194}Pt; PW denotes present work.

J_i^+	0_1^+	2_1^+	0_1^+	2_1^+	0_1^+	2_1^+	4_1^+
J_f^+	2_1^+	2_1^+	2_2^+	2_2^+	4_1^+	4_1^+	4_1^+
λ	2	2	2	2	4	2	2
PW	1.273(4)	0.78(13)	0.095(4)	1.65(4)	−0.07(5)	2.28(4)	0.75(25)
Mc61	1.39(7)		0.093(20)	1.07(11)			
Gl69	1.28(12)	0.82(21)					
Br70			0.105(8)				
Mi71	1.37(3)					2.07(16)	
Be72	1.4(7)		0.087(5)	1.73(10)			
Ba76	1.293				−0.096		
Jo77	1.25(4)					2.26(6)	
Ro77	1.296(11)		0.097(7)				
St77			0.084(5)	1.70(10)		2.06(6)	
Ba78	1.273(6)		0.090(2)	1.455(25)		2.01(5)	
Ba79	1.269	0.612	0.0844	1.391	−0.1486	1.986	
Ch83		0.17(23)					
Wu87	$1.208(^{49}_{17})$	$0.54(^{8}_{6})$	0.0888(12)	$1.517(^{11}_{18})$		$1.935(^{21}_{13})$	$1.00(^{12}_{14})$
Gy86	1.289(4)	0.63(19)					
Bo88	1.279(19)				−0.175(16)		
Fe88					−0.23(9)	2.14(10)	

Table 4.8: Corrections to and uncertainties in measured $B(E2;0_1^+ \rightarrow 2_1^+)$ and $Q(2_1^+)$ for ^{194}Pt.

Source of correction	$\Delta B(E2;0_1^+ \rightarrow 2_1^+)$ (e^2b^2)	$\Delta Q(2_1^+)$ (e b)
Vacuum polarization	+0.0196	−0.079
Nuclear polarization	−0.0066	−0.063
Electron screening	−0.0122	+0.033
Quantal corrections	−0.0009	−0.038
Target thickness	−0.0085	+ 0.081
Total correction	−0.0086	−0.066
Sources of uncertainty		
GDR	0.0023	0.0033
Beam energy	0.001	0.001
Scattering angle	0.000	0.000
Higher state matrix elements	0.0015	0.042
Statistics and lineshape analysis	0.0084	0.10
Total uncertainty	0.0089	0.11
	$B(E2;0_1^+ \rightarrow 2_1^+)$ (e^2b^2)	$Q(2_1^+)$ (e b)
Final values	1.621(9)	0.59(11)

4.5.2 ^{196}Pt

4.5.2.1 Particle singles data

Data were obtained with the particle singles spectroscopy technique using ^{4}He projectiles at a range of bombarding energies between 14.2 and 15.8 MeV at 171.3° and 174.8°, ^{7}Li projectiles at 22.0 MeV and 22.5 MeV at 164.0°, 168.7° and 169.9°, and ^{12}C projectiles at a number of bombarding energies between 42 and 46 MeV at the angles 171.3°, 174.8° and 175.0° (see table 4.9). Typical spectra for each projectile are shown in fig. 4.11. The thicknesses of the targets used for these data are indicated in table 4.4. Peak-to-valley ratios ranged from 6:1 (^{12}C spectra) to 50:1 (^{4}He spectra). The spectra were fitted with a skew gaussian lineshape (§ 3.3.1). Contributions from other platinum isotopes are indicated by the dotted lines and were calculated using the published matrix elements listed in table 4.5 in conjunction with the supplier's assays (table 4.4). Excitation probabilities for the $2_1^+, 2_2^+, 4_1^+, 0_2^+$ and 4_2^+ states were extracted from these spectra; these are listed in table 4.9. Nuclei with A = 151-154 and 187-188 would have influenced the values measured for $P_{exp}(2_1^+)$; examination of spectra taken with 8.0 MeV and 10.5 MeV ^{4}He showed that such nuclei were not present to more than 0.1% of $P_{exp}(2_1^+)$. Similarly, upper limits on contributions of nuclei with A = 121-127, 110-115, 182-184 and 179-181, which could have affected the values extracted for $P_{exp}(2_2^+)$ and $P_{exp}(4_1^+)$ were found to be 5% of $P_{exp}(2_2^+)$ and 7% of $P_{exp}(4^+)$ respectively. Comparison of these upper limits with the uncertainties for P_{exp} quoted in table 4.9 show that the effect of any such nuclei would have been insignificant.

Safe energy plots for the various states under bombardment with the different projectiles are shown in fig. 4.12. There is no indication of significant Coulomb-nuclear interference at the bombarding energies used.

4.5.2.2 Particle-gamma coincidence data

Data were obtained using the particle-gamma coincidence technique with ^{58}Ni projectiles at 214, 220 and 226 MeV. The particle detector was placed at a mean scattering angle of 168.0° and the bombarding energies used correspond to a minimum separation of

Table 4.9: Experimental configurations and measured excitation probabilities for ^{196}Pt using particle singles technique.

Projectile	E_p [a] (MeV)	θ_{lab} [b]	s [c] (fm)	$P_{exp}(2_1^+)$ ($\times 10^{-2}$)	$P_{exp}(2_2^+)$ ($\times 10^{-4}$)	$P_{exp}(4_1^+)$ ($\times 10^{-4}$)
^{4}He	14.2	168.7°	6.95	1.479(4)	0.12(5)	0.59(6)
	15.8		5.31	2.146(7)	0.34(5)	0.76(7)
	15.0	174.8°	6.06	1.805(5)	0.22(4)	0.43(2)
	15.2		5.86	1.890(6)	0.27(9)	0.50(3)
	15.4		5.66	1.982(5)	0.29(3)	0.53(3)
	15.8		5.28	2.164(5)	0.39(3)	0.62(3)
^{7}Li	22.5	164.0°	5.94	4.25(3)	1.61(19)	2.3(3)
	22.0	168.7°	5.91	3.974(9)	1.61(14)	2.3(3)
	22.5		5.91	4.29(7)	1.68(7)	2.27(20)
	22.5	169.9°	5.90	4.300(23)	1.30(16)	2.9(3)
^{12}C	42.0	171.3°	6.98	10.16(11)	8.2(12)	15.6(13)
	43.0		6.55	11.39(6)	12.3(10)	20.0(11)
	44.0		6.17	12.05(15)	15.0(24)	23.9(19)
	44.0	170.0°	6.17	12.24(3)	14.8(4)	23.2(3)
	45.0		5.81	13.17(7)	16.9(5)	31.1(18)
	46.0		5.47	14.17(5)	20.3(6)	35.1(20)
	44.0	175.0°	6.15	12.20(9)	14.6(13)	23.3(11)

Table 4.9 (cont.)

Projectile	E_p[a]) (MeV)	θ_{lab}[b])	s[c]) (fm)	$P_{exp}(0_2^+)$ ($\times 10^{-5}$)	$P_{exp}(4_2^+)$ ($\times 10^{-5}$)
^{4}He	14.2	168.7°	6.95	3.1(6)	3.4(5)
	15.8		5.31	2.3(9)	
	15.0	174.8°	6.06	4.6(6)	2.3(4)
	15.2		5.86	3.33(6)	2.7(6)
	15.4		5.66	2.7(6)	2.7(6)
	15.8		5.28	2.1(5)	2.4(4)
^{12}C	42.0	171.3°	6.98	15(3)	17.0(23)
	43.0		6.55		10(4)
	44.0	170.0°	6.17	3.3(20)	9.4(10)
	45.0		5.81	4.3(10)	14.7(10)
	46.0		5.47	6.1(15)	14.6(16)
	44.0	175.0°	6.15		10.7(14)

[a]) bombarding energy
[b]) mean scattering angle in the laboratory system
[c]) distance of closest approach of the nuclear surfaces

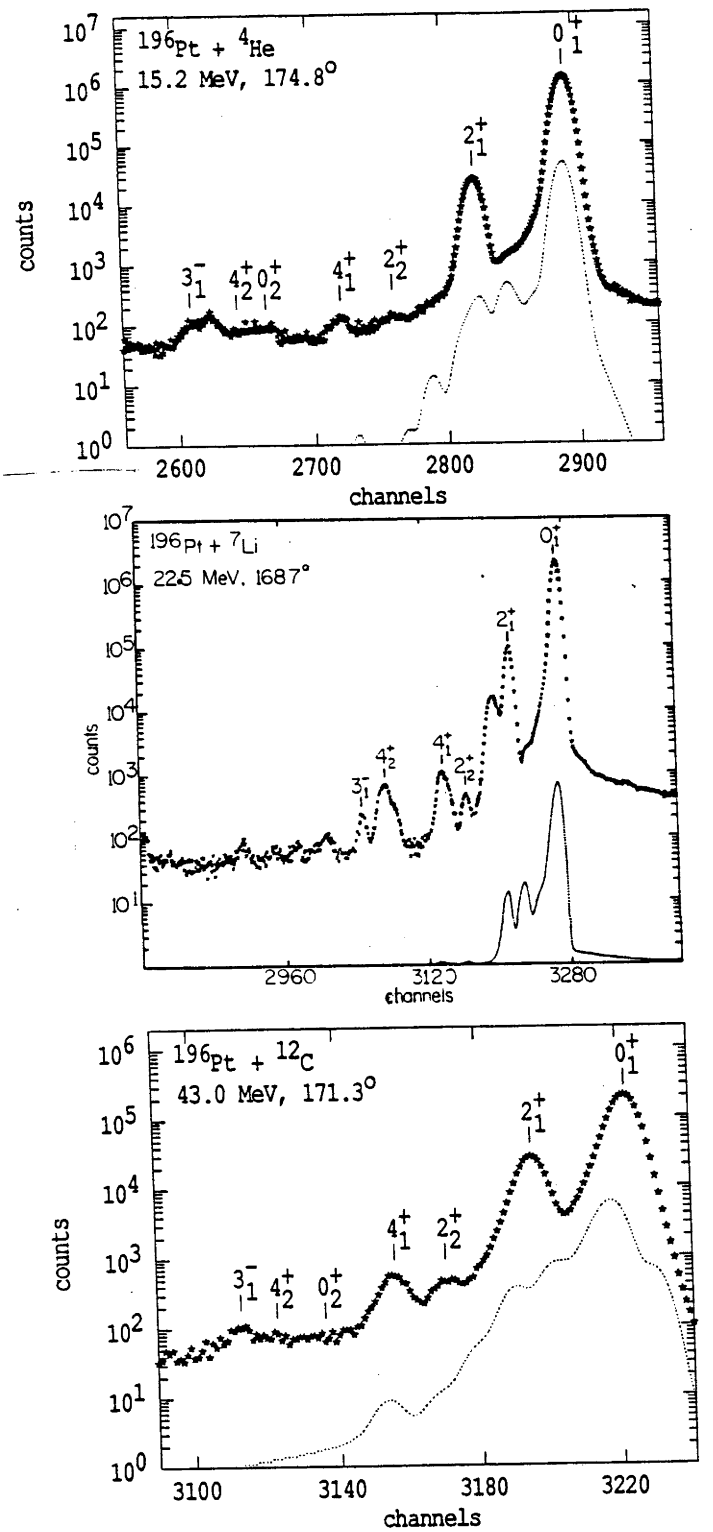

Figure 4.11: Typical particle singles spectra for ^{196}Pt. The broken curve and labelling of peaks are the same as for fig. 4.6.

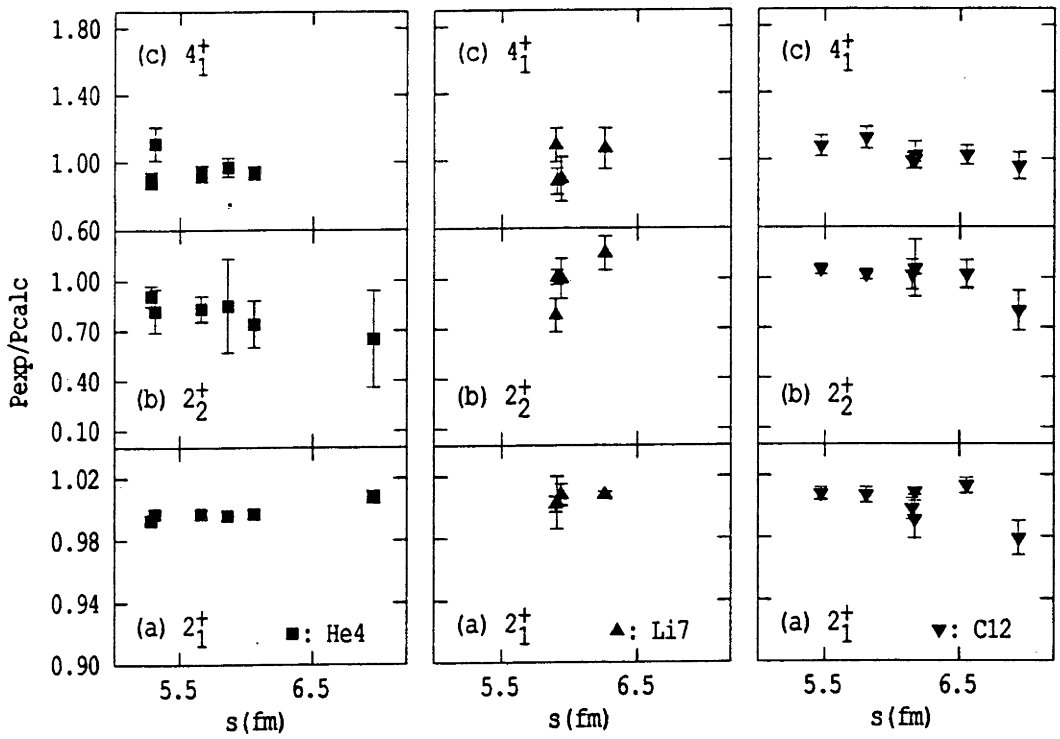

Figure 4.12: Safe energy plots for ^{196}Pt

target-projectile surfaces of 7.0, 6.5 and 6.0 fm. The angular correlations for each of the strongest γ-rays (333, 356 and 521 keV) are shown in fig. 4.13. Table 4.10 lists the fitted values of A_0, A_2, A_4 and ϕ as well as the calculated values of A_2 and A_4; good agreement between experiment and calculation is obtained for all the strongest γ-rays.

Five γ-rays from the 2_1^+, 2_2^+, 4_1^+, 4_2^+ and 6_1^+ states of ^{196}Pt were observed (cf. fig. 4.1). For these transitions, equation (4.40) takes the form :

$$\frac{A_0(356\text{ keV})}{n_{obs}2\pi\rho\epsilon_0(356\text{ keV})} = P(2_1^+) + P(2_2^+) + P(4_1^+) \quad (4.41)$$

$$\frac{A_0(333\text{ keV})}{n_{obs}2\pi\rho\epsilon_0(333\text{ keV})} = P(2_2^+) + P(4_2^+) \quad (4.42)$$

$$\frac{A_0(521\text{ keV})}{n_{obs}2\pi\rho\epsilon_0(521\text{ keV})} = P(4_1^+) + P(6_1^+) \quad (4.43)$$

$$\frac{A_0(604\text{ keV})}{n_{obs}2\pi\rho\epsilon_0(604\text{ keV})} = P(4_2^+) \quad (4.44)$$

$$\frac{A_0(649\text{ keV})}{n_{obs}2\pi\rho\epsilon_0(649\text{ keV})} = P(6_1^+). \quad (4.45)$$

Values of $A_0/n_{Pt}\epsilon_0$ for the $2_1^+ \to 0_1^+, 2_2^+ \to 2_1^+, 4_1^+ \to 2_1^+, 4_2^+ \to 2_2^+$ and $6_1^+ \to 4_1^+$ transitions at each bombarding energy are listed in table 4.11. Excitation probabilities for the

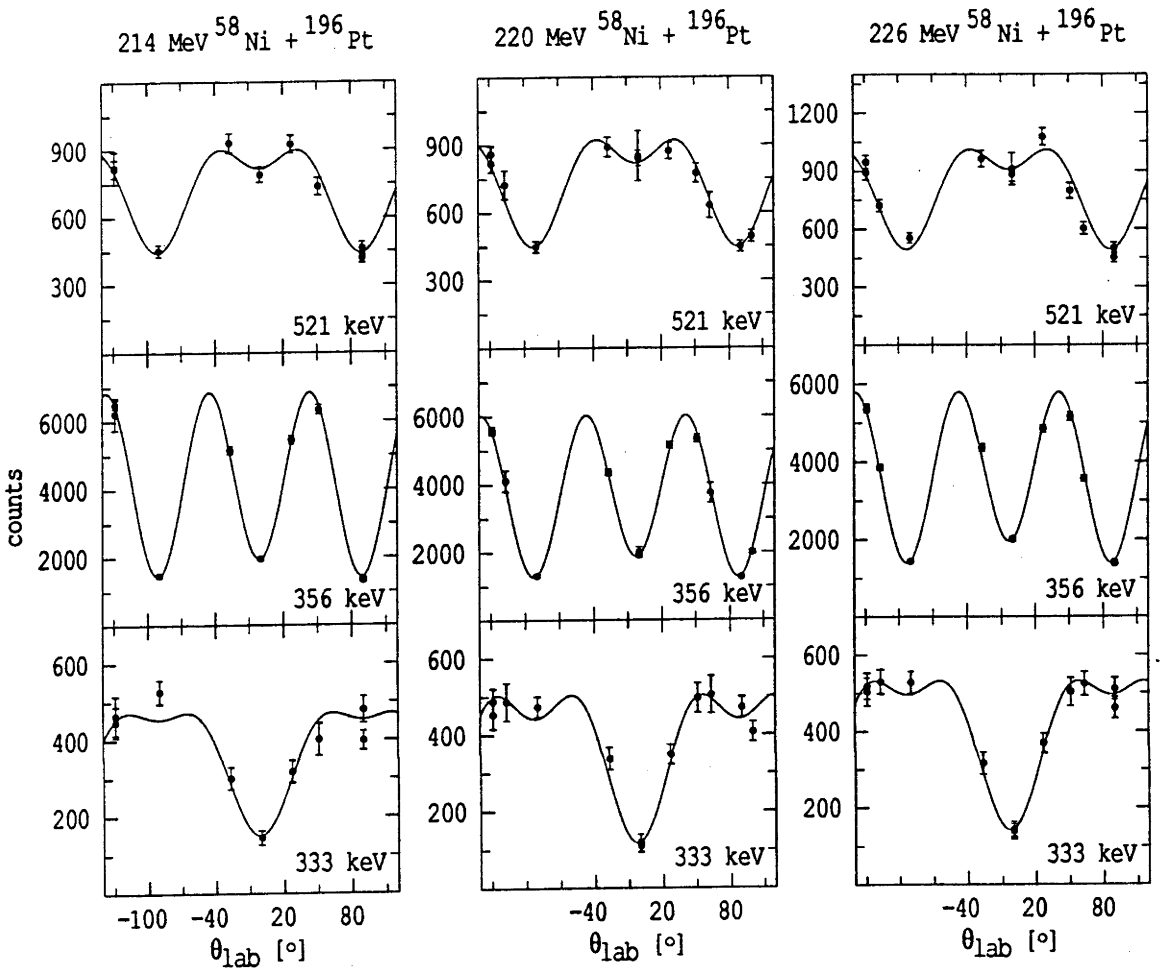

Figure 4.13: Angular correlations for the γ-rays of energy 356, 333, 521 keV. The fit to the data is shown.

Table 4.10: Fitted(f) values of A_0, A_2, A_4 and ϕ, and calculated(c) values of A_2 and A_4 for each observed γ-ray transition in ^{196}Pt.

E_p[a] (MeV)	E_γ[b] (keV)	A_0^f	A_2^f	A_4^f	$\phi(°)$	A_2^c	A_4^c
214	333	404(15)	−0.40(5)	−0.36(8)	1.5(12)	−0.39(7)	−0.43(7)
	356	4207(122)	0.574(13)	−1.43(3)		0.60(3)	−1.33(5)
	521	674(21)	0.53(4)	−0.41(7)		0.50(8)	−0.35(6)
	604	42(5)	0.59(16)	−0.24(20)		0.506	−0.358
	649	34(4)	0.62(17)	−0.23(22)		0.450	−0.235
220	333	430(12)	−0.41(6)	−0.49(8)	2.8(9)	−0.39(5)	−0.42(5)
	356	3836(75)	0.580(17)	−1.40(4)		0.576(17)	−1.28(3)
	521	713(15)	0.54(4)	−0.44(6)		0.50(8)	−0.35(5)
	604	50(4)	0.40(19)	−0.31(24)		0.506	−0.358
	649	38(4)	0.50(27)	0.25(34)		0.450	−0.235
226	333	464(11)	−0.40(4)	−0.44(6)	2.5(7)	−0.39(5)	−0.42(5)
	356	3761(53)	0.559(13)	−1.32(3)		0.563(13)	−1.241(26)
	521	765(13)	0.54(3)	−0.44(5)		0.50(5)	−0.35(3)
	604	56(3)	0.36(10)	−0.36(13)		0.506	−0.358
	649	56(4)	0.44(12)	−0.07(16)		0.450	−0.235

[a]) bombarding energy
[b]) γ-ray energy

Table 4.11: Normalized values of A_0 and equivalent excitation probabilities. P_{calc} values are calculated using the final matrix element values given in table 4.5; P_{norm} are the measured excitation probabilities normalized to $P_{calc}(2_1^+)$.

		E_γ[a] (keV)	333	356	521	604	649
		J_i^+[b]	2_2^+	2_1^+	4_1^+	4_2^+	6_1^+
E_p[c] (MeV)	n_{Pt}[d]	ϵ_0	1.010(5)	0.998(5)	0.920(16)	0.860(9)	0.830(5)
214	2271581	$A_0/n_{Pt}\epsilon_0$	24.9(1.1)	258(11)	42.7(1.9)	2.8(3)	2.4(3)
		$P_{calc}(J_i^+)$	0.065	0.574	0.129	0.0071	0.0064
		$P_{norm}(J_i^+)$	0.068(5)	0.574(30)	0.124(9)	0.0085(10)	0.0074(9)
220	2022596	$A_0/n_{Pt}\epsilon_0$	29.3(1.1)	262(9)	50.8(2.2)	3.8(3)	3.0(3)
		$P_{calc}(J_i^+)$	0.075	0.579	0.155	0.0097	0.0091
		$P_{norm}(J_i^+)$	0.082(6)	0.489(26)	0.153(11)	0.0121(11)	0.0095(12)
226	1867382	$A_0/n_{Pt}\epsilon_0$	34.5(1.1)	278(9)	59.0(2.2)	3.32(24)	4.8(3)
		$P_{calc}(J_i^+)$	0.086	0.576	0.183	0.0131	0.0125
		$P_{norm}(J_i^+)$	0.094(6)	0.576(26)	0.169(11)	0.0143(13)	0.0150(13)

[a]) γ-ray energy
[b]) initial state for γ-ray transition
[c]) bombarding energy
[d]) number of scattered Pt nuclei detected in surface-barrier detector

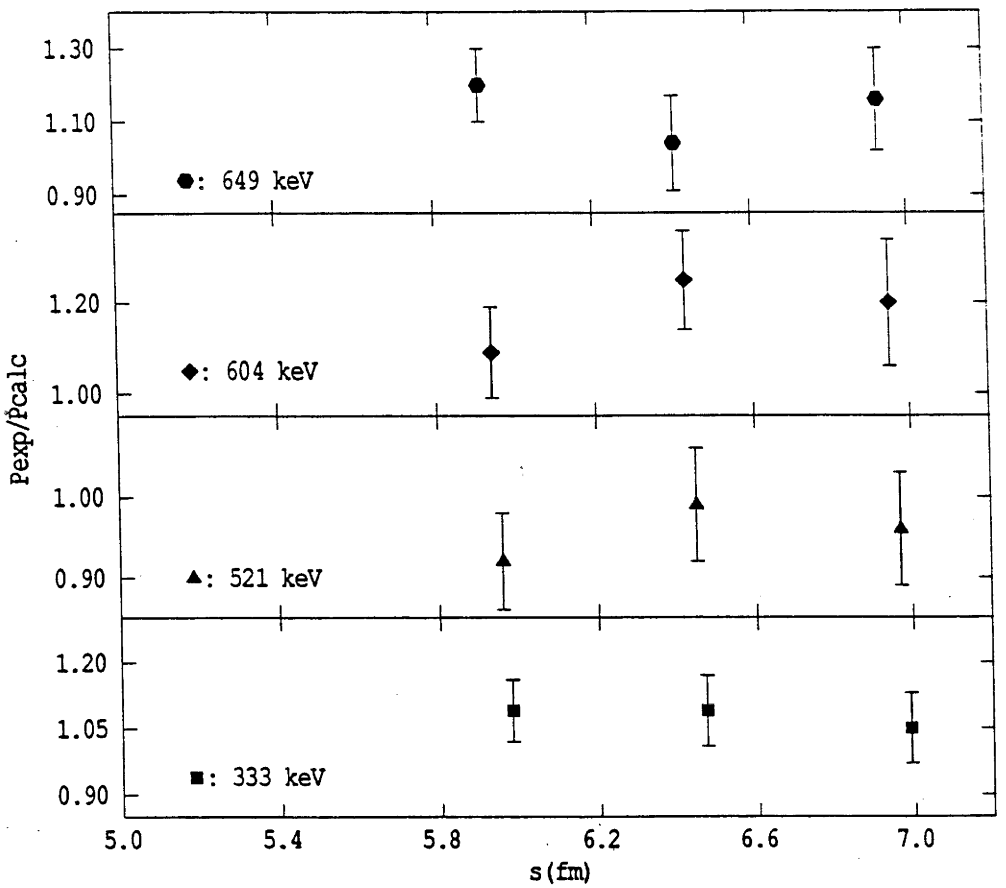

Figure 4.14: Safe-energy plots for the de-excitation γ-rays observed from ^{196}Pt.

$2_1^+, 2_2^+, 4_1^+, 4_2^+$ and 6_1^+ states were derived using the above equations and then normalized (denoted by P_{norm} in table 4.11) to the values of $P(2_1^+)$ calculated using the Winther-de Boer code, assuming the values of $<2_1^+||\mathcal{M}(E2)||0_1^+>$ and $<2_1^+||\mathcal{M}(E2)||2_1^+>$ obtained from the particle singles data. Corrections for internal conversion were applied.

It has already been noted that the coincidence requirement ensures that only γ-rays from transitions within the platinum nucleus are detected. (Although γ-rays may also be detected from nuclei of similar mass which cannot be resolved from Pt in the particle singles spectrum, there is no indication of the presence of such nuclei in the γ-ray spectrum.) As the main γ-rays from the other Pt isotopes [316.5 keV ($2_1^+ \rightarrow 0_1^+$ for ^{192}Pt), 328.5 keV ($2_1^+ \rightarrow 0_1^+$ for ^{194}Pt) and 407.4 keV ($2_1^+ \rightarrow 0_1^+$ for ^{198}Pt)] are easily resolved from those observed from ^{196}Pt in this experiment (333 keV, 356 keV, 521 keV, 604 keV and 649 keV), no corrections need to be made for contaminants. Safe-energy plots are shown in fig. 4.14 for each de-excitation γ-ray observed except for the 356 keV

γ-ray which was used for normalization purposes. Bombarding energies were chosen to result in distances of closest approach of $\sim$6 fm or greater to prevent the occurrence of significant Coulomb-nuclear interference. As expected, the safe-energy plots indicate that only pure Coulomb excitation has to be considered.

4.5.2.3 Analysis of excitation probabilities

Measured excitation probabilities were analysed using the Winther-de Boer Coulomb excitation program in the following way : first of all, values for Q(2_1^+) and B(E2;$0_1^+ \rightarrow 2_1^+$) were obtained from the particle singles data alone, using the procedures described for ^{194}Pt. These values were assumed to obtain $P_{calc}(2_1^+)$ for ^{58}Ni projectiles at the bombarding energies employed. In the case of the particle-γ coincidence data, the target thickness was determined by varying an estimate of the thickness until calculations based on semi-empirical formulae for the stopping cross-section of Pt (Zi80) gave the same value of the minimum scattered energy detected by the particle detector as that obtained from the particle singles spectrum collected during the experiment. Differential cross-sections and stopping cross-sections, calculated at equally spaced steps through the target, were then used to obtain a value of the total cross-section integrated over the range of energy loss in the target. Similar corrections were carried out to allow for variation of the differential cross-section across the range of angles subtended by the particle detector. The higher state excitation probabilities for the Ni data, normalized as described above, were combined with the particle singles data to obtain values for $<2_2^+||\mathcal{M}(E2)||2_1^+>$, $<2_2^+||\mathcal{M}(E2)||2_2^+>$, $<4_1^+||\mathcal{M}(E4)||0_1^+>$, $<4_1^+||\mathcal{M}(E2)||2_1^+>$, $<4_1^+||\mathcal{M}(E2)||4_1^+>$, $<0_2^+||\mathcal{M}(E2)||2_1^+>$, $<0_2^+||\mathcal{M}(E2)||2_2^+>$, $<4_2^+||\mathcal{M}(E2)||2_1^+>$, $<4_2^+||\mathcal{M}(E2)||2_2^+>$, $<4_2^+||\mathcal{M}(E2)||4_1^+>$, $<6_1^+||\mathcal{M}(E2)||4_1^+>$ and $<6_1^+||\mathcal{M}(E2)||6_1^+>$, and the corresponding B($E\lambda$) values. The particle singles data for the 2_1^+ state were then re-analysed, using the deduced higher state matrix elements to confirm the initial results for Q(2_1^+) and B(E2;$0_1^+ \rightarrow 2_1^+$), as there is a strong dependence of $P_{calc}(2_1^+)$ on some of the higher state matrix elements; iterative fitting was continued in this manner until a best fit was reached for all the matrix elements simultaneously. The final results obtained are listed in table 4.12. As the method of analysis employed here is sensitive to

Table 4.12: Measured B(Eλ) values (in e^2b^λ), quadrupole moments (in e b) and equivalent matrix elements (in e $b^{\lambda/2}$) for ^{196}Pt.

J_i^+	J_f^+	λ	B(Eλ;$J_i^+ \rightarrow J_f^+$)	$< J_f^+ \| \mathcal{M}(E\lambda) \| J_i^+ >$
0_1^+	2_1^+	2	1.368(3)	1.1697(13)
2_1^+	2_2^+	2	0.370(5)	1.36(1)
0_1^+	4_1^+	4	0.012(8)	−0.11(3)
2_1^+	4_1^+	2	0.73(1)	1.91(2)
2_1^+	0_2^+	2	0.0056(10)	0.167(15)
2_2^+	0_2^+	2	0.02(20)	−0.35(70)
2_1^+	4_2^+	2	0.002(4)	0.11(7)
2_2^+	4_2^+	2	0.33(3)	1.28(6)
4_1^+	4_2^+	2	0.084(14)	0.87(7)
4_1^+	6_1^+	2	0.65(4)	2.42(7)

J_n^+	$Q(J_n^+)$	$< J_n^+ \| \mathcal{M}(E\lambda) \| J_n^+ >$
2_1^+	0.62(8)	0.82(10)
2_2^+	−0.39(16)	−0.52(20)
4_1^+	1.03(12)	1.36(16)
6_1^+	−0.18(26)	−0.26(40)

the relative phases of the matrix elements investigated, the signs of the matrix elements were determined unambiguously. Signs and magnitudes for matrix elements involving the 6_2^+ and 8_1^+ states (table 4.5) have been taken from unpublished data (Ma86t) as no published values are available.

4.5.2.4 Corrections and uncertainties

Corrections have to be made for the effects of vacuum polarization, nuclear polarization, electron screening and, in the case of the particle singles data, finite energy loss in the target. In general, these corrections are only significant for the first excited state. Excitation probabilities were corrected for the effects of nuclear polarization, vacuum polarization and electron screening by using equations (2.71) to (2.73) to calculate the effect on the bombarding energy. The effect of these corrections on $B(E2;0_1^+ \rightarrow 2_1^+)$ and $Q(2_1^+)$ is given in table 4.13. Energy loss in the relatively thin targets used for the particle singles data was estimated to be no more than 60 keV, so the effect on differential cross-section was small (cf. § 2.5.6). It is interesting to note that the contribution from uncertainties in higher state matrix elements is almost equal to that from statistics and lineshape analysis. This implies that more precise measurements of $B(E2;0_1^+ \rightarrow 2_1^+)$ and $Q(2_1^+)$ can only be attained when the higher state matrix elements are known to greater precision and accuracy.

The effect of using the semi-classical approximation can be important for some of the higher states. Table 4.14 lists the change in calculated excitation probability for the 2_1^+, 2_2^+ and 4_1^+ states due to this correction which was calculated using the expressions derived in Al72 (§ 2.5.1). As expected, the fractional effect for any state, J_n^π, increases as the projectile mass decreases. Of the three states for which quantum mechanical corrections were calculated, excitation probabilities for the 2_2^+ state are the least affected. The large statistical uncertainties in $P_{exp}(4_2^+)$ and $P_{exp}(6_1^+)$ mean that quantal corrections for these states can be ignored.

As mentioned in § 2.5.4.2, depopulation of the ground state due to virtual excitation of the GDR may be significant for data obtained with ^{58}Ni projectiles. However, the uncertainties inherent in estimating this effect imply that a definite correction cannot be

Table 4.13: Corrections to and uncertainties in measured $B(E2;0_1^+ \rightarrow 2_1^+)$ and $Q(2_1^+)$ for ^{196}Pt.

Source of correction	$\Delta B(E2;0_1^+ \rightarrow 2_1^+)$ (e^2b^2)	$\Delta Q(2_1^+)$ (e b)
Vacuum polarization	+0.0149	-0.047
Nuclear polarization	-0.0050	-0.093
Electron screening	-0.0098	-0.001
Quantal corrections	-0.0025	-0.048
Target thickness	+0.0045	-0.045
Total correction	+0.0021	-0.234
Sources of uncertainty		
GDR	0.0003	0.045
Beam energy	0.0006	0.0105
Scattering angle	0.0000	0.0000
Higher state matrix elements	0.0006	0.030
Statistics and lineshape analysis	0.0032	0.054
Total uncertainty	0.0033	0.077
	$B(E2;0_1^+ \rightarrow 2_1^+)$ (e^2b^2)	$Q(2_1^+)$ (e b)
Final values	1.368(4)	0.62(8)

Table 4.14: Effect of the use of the semi-classical approximation on calculated excitation probabilities for the three lowest excited states in ^{196}Pt.

Projectile	E_p[a] (MeV)	θ_{lab}[b]	$\Delta P(2_1^+)$ ($\times 10^{-2}$)	$\Delta P(2_2^+)$ ($\times 10^{-4}$)	$\Delta P(4_1^+)$ ($\times 10^{-4}$)
^{4}He	14.2	168.7°	−0.003	+0.0008	+0.0115
	15.8		−0.006	+0.0024	+0.0288
	15.0	174.8°	−0.004	+0.0013	+0.0191
	15.2		−0.004	+0.0014	+0.0215
	15.4		−0.005	+0.0016	+0.0240
	15.8		−0.005	+0.0021	+0.0298
^{7}Li	22.5	164.0°	−0.013	+0.003	+0.061
	22.0	168.7°	−0.011	+0.002	+0.051
	22.5		−0.013	+0.003	+0.062
	22.5	169.9°	−0.014	+0.003	+0.062
^{12}C	42.0	171.3°	−0.03	+0.00	+0.20
	43.0		−0.04	+0.01	+0.23
	44.0		−0.04	+0.00	+0.29
	44.0	175.0°	−0.05	+0.00	+0.29
	44.0	170.0°	−0.04	+0.00	+0.28
	45.0		−0.05	+0.01	+0.34
	46.0		−0.05	+0.01	+0.40

[a]) bombarding energy
[b]) mean scattering angle in the laboratory system

assigned. The effect of depopulation on measured excitation probabilities was estimated using the method explained in § 2.5.4.2 to be of the order of 1.5% for the 2_1^+ state, 5% for the 2_2^+ and 4_1^+ states, and 10% for the 4_2^+ and 6_1^+ states.

4.6 Comparison with Previous Experiments

4.6.1 ^{196}Pt

Table 4.15 lists the values of the matrix elements determined in the present work together with those obtained in other measurements, including the recent unpublished work of Mauthofer (Ma86t). As the determination of higher state matrix elements in the present work is based on the particle singles measurements for the first excited state, it is crucial that accurate and precise values for $<2_1^+||\mathcal{M}(E2)||0_1^+>$ and $<2_1^+||\mathcal{M}(E2)||2_1^+>$ are obtained; for this reason the values for $B(E2;0_1^+ \rightarrow 2_1^+)$ and $Q(2_1^+)$ are first compared with those obtained by other experimenters. As can be seen from table 4.15 and fig. 4.15, the value obtained for $Q(2_1^+)$ [0.62(8) e b] is in good agreement with the two previously published values of 0.66(12) e b (Gy86) and 0.51(18) e b (Gl69). The situation regarding $B(E2;0_1^+ \rightarrow 2_1^+)$ is less straightforward; the value obtained in the present work is in good agreement with the measurements of Mc61, Gr66, Br70, Ba76, Bo81 and Mu84 (fig. 4.16), though in most cases the agreement is partly due to the large uncertainties of the early measurements. On the other hand, the present value disagrees with that of Gy86, Gl69, Mi71, Be72 and Bo88. In the case of Gy86, this difference appears to be due to a difference in spectrum quality. From fig. 4.17, which compares fits to spectra obtained in the present work with those obtained in the work of Gyapong *et al.* (Gy86,Gy87t), it can be seen that the improved statistics in the former, particularly in the cases of ^{4}He on ^{196}Pt and ^{12}C on ^{194}Pt, enable a more reliable estimate of the background on the low-energy side of the 2_1^+ peak to be made. Gyapong *et al.* appear to have set the background to be too low. It seems likely that they also underestimated the contribution of the uncertainty in setting the background to the total uncertainty.

Table 4.15: Experimental matrix elements for ^{196}Pt; PW denotes present work. (a)Values of $B(E2;0_1^+ \rightarrow 2_1^+)$ and $<2_1^+\|\mathcal{M}(E2)\|0_1^+>$ in chronological order.

	$B(E2;0_1^+ \rightarrow 2_1^+)$ (e^2b^2)	$<2_1^+\|\mathcal{M}(E2)\|0_1^+>$ (e b)
Mc61	1.27(13)	1.13(5)
Gr66	1.57(19)	1.25(8)
Gl69	1.49(5)	1.22(2)
Br70	1.35(4)[a])	1.161(18)
Mi71	1.55(8)	1.24(4)
Be72	1.55(10)	1.24(4)
Ba76	1.356	1.164
Bo81	1.44(7)	1.20(3)
Mu84	1.38(4)	1.17(2)
Gy86	1.382(6)	1.1756(25)
Bo88	1.42(4)	1.192(15)
PW	1.368(4)	1.1697(13)

[a]) re-normalized relative to $B(E2;0_1^+ \rightarrow 2_1^+)$ measured for ^{194}Pt in present work

(b) diagonal E2 matrix elements in e b.

J^+_n	PW	Gl69	Gy86	Ma86t
2^+_1	0.82(10)	0.67(24)	0.87(16)	
2^+_2	−0.52(20)			$-0.302(^{26}_{46})$
4^+_1	1.36(16)			$0.40(^{30}_{32})$
6^+_1	−0.26(40)			$0.18(^{75}_{79})$

(c) E2 transition matrix elements (in e b) for the 2^+_2, 4^+_1, 0^+_2, 4^+_2 and 6^+_1 states.

J^+_i	J^+_f	PW	Mi71	Be72	Bo81	Ma86t	Fe88
2^+_1	2^+_2	1.36(1)		1.31(6)	1.32(6)	1.14(12)	
2^+_1	4^+_1	1.91(2)	1.83(14)		1.90(8)	$2.00(^{7}_{5})$	2.07(7)
2^+_1	0^+_2	0.167(15)			0.15(3)	$0.182(^{13}_{27})$	
2^+_2	0^+_2	−0.35(70)			−0.38(9)		
2^+_1	4^+_2	0.11(7)			0.16(3)	$0.144(^{18}_{36})$	
2^+_2	4^+_2	1.28(6)			1.26(12)	$1.40(^{8}_{23})$	
4^+_1	4^+_2	0.87(7)			1.32(30)	$1.40(^{23}_{9})$	
4^+_1	6^+_1	2.42(7)			2.34(30)	$2.53(^{6}_{13})$	

(d) Measured values of $<0^+_1||\mathcal{M}(E4)||4^+_1>$ (in e b^2).

PW	Ba76	De81	Bo85	Bo88	Fe88
−0.11(3)	−0.084	−0.202	−0.155(16)	−0.131(7)	−0.11(11)

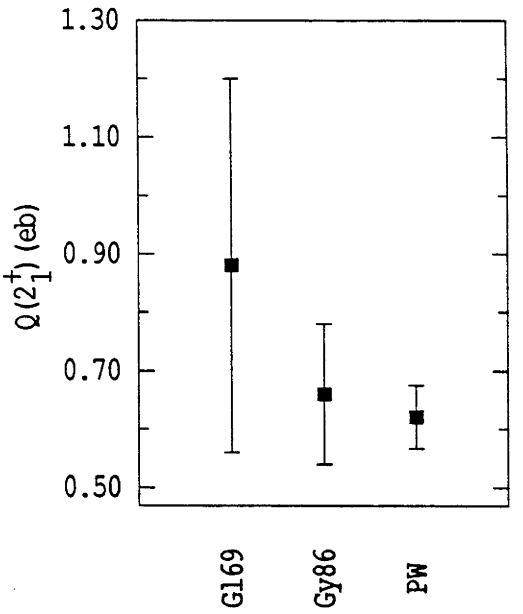

Figure 4.15: Experimental $Q(2_1^+)$ values for ^{196}Pt in chronological order; PW denotes the present work.

An improved value for the upper limit of $<2_2^+||\mathcal{M}(E2)||0_1^+>$, as compared with that set by Berkes *et al.* (Be72) [0.0017 e b], could not be obtained in the present work. The unpublished limit set by Mauthofer on the magnitude of this matrix element is higher (0.0032 e b) than that of Berkes *et al.*. Fig. 4.18 shows that the value of $<2_2^+||\mathcal{M}(E2)||2_1^+>$ obtained in the present work is in excellent agreement with the values published by Bolotin *et al.* (Bo81) and Berkes *et al.*; the unpublished value of Mauthofer is significantly lower than that obtained by both the lifetime measurements of Bolotin *et al.* and Berkes *et al.* and also than the value of the present work which is obtained primarily from analysis of particle singles data. The value obtained for $Q(2_2^+)$ in the present work of -0.39(15) e b is in agreement with the unpublished value of Mauthofer of $-0.23(\frac{2}{3})$ e b.

There are four published measurements of the E4 matrix element connecting the ground state and 4^+ state, as shown in fig. 4.19. Of these, one was made at ANU using Coulomb excitation (Fe88); two were carried out using inelastic electron scattering [Borghols *et al.* (Bo85) and Boeglin *et al.* (Bo88)]; the fourth was made by Baker *et al.* (Ba76) using Coulomb-nuclear interference. The value obtained in the present work, -0.11(3) e b^2, is more precise than and in excellent agreement with the other Coulomb excitation measurement (Fe88); it also agrees with the other values listed. It is interesting to note the effect of the semi-classical approximation on this value : if

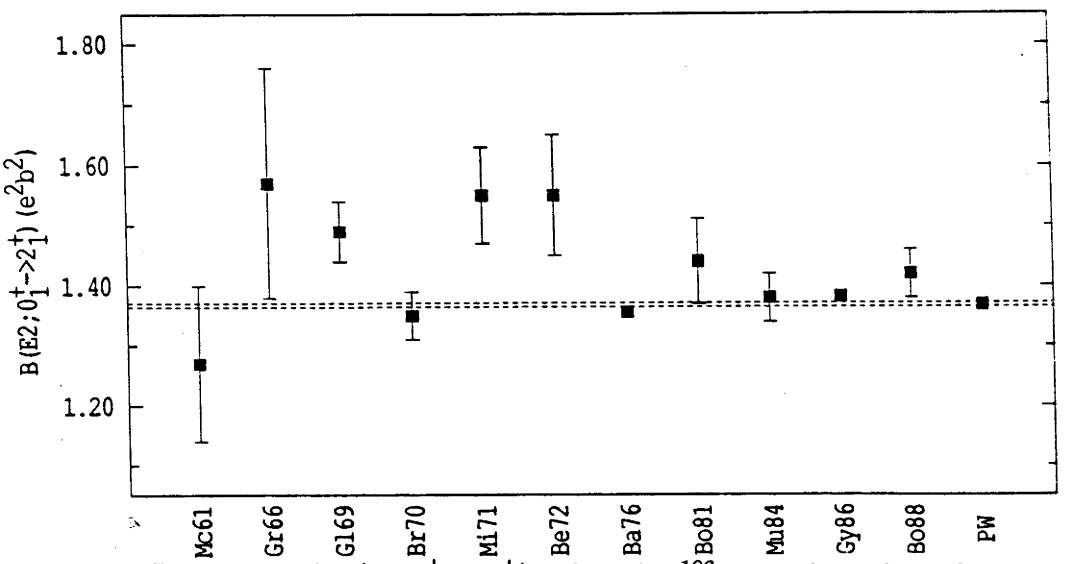

Figure 4.16: Experimental $B(E2;0_1^+ \rightarrow 2_1^+)$ values for ^{196}Pt in chronological order; PW denotes the present work. The levels of uncertainty obtained in the present work are indicated by dotted lines.

appropriate corrections are not applied, a value of -0.04(5) e b^2 is obtained.

The matrix element $<4_1^+||\mathcal{M}(E2)||2_1^+>$ was measured to be 1.91(2) e b, assuming $<4_1^+||\mathcal{M}(E2)||2_2^+> = 0$. This is in excellent agreement with the values of Mi71 [1.83(14) e b] and Bo81 [1.90(8) e b] though not with that of Fe88 [2.07(7) e b]. Fewell *et al.* suggest that their apparent overestimate for this matrix element may be due to their assumption that $Q(2_2^+) = 0$; this appears to be unlikely as $\tilde{Q}(2_2^+)$ has little effect on the excitation probability of the 4_1^+ state for ^{4}He, ^{12}C and ^{16}O projectiles, which were employed to obtain the data presented in Fe88. Some of the excitation probabilities used in Fe88 were taken from Gy87t; it is possible that these values were systematically overestimated, as explained earlier.

No measurements of the diagonal matrix element for either the 4_1^+ or 6_1^+ states have been published. As can be seen from table 4.15, the present value of 1.36(16) e b for the former is in significant disagreement with that of Mauthofer [$0.40(^{30}_{32})$ e b]. The measurements of $<6_1^+||\mathcal{M}(E2)||6_1^+>$, on the other hand, are consistent with each other.

In addition, values for $<0_2^+||\mathcal{M}(E2)||2_1^+>$, $<0_2^+||\mathcal{M}(E2)||2_2^+>$, $<4_2^+||\mathcal{M}(E2)||2_1^+>$, $<4_2^+||\mathcal{M}(E2)||2_2^+>$, $<4_2^+||\mathcal{M}(E2)||4_1^+>$ and $<6_1^+||\mathcal{M}(E2)||4_1^+>$ were obtained from excitation probabilities for the $0_2^+, 4_2^+$ and 6_1^+ states. Apart from $<4_2^+||\mathcal{M}(E2)||4_1^+>$, these are all in excellent agreement with both the lifetime measurements of Bolotin *et al.* (Bo81) and with the unpublished values of Mauthofer (see fig. 4.18).

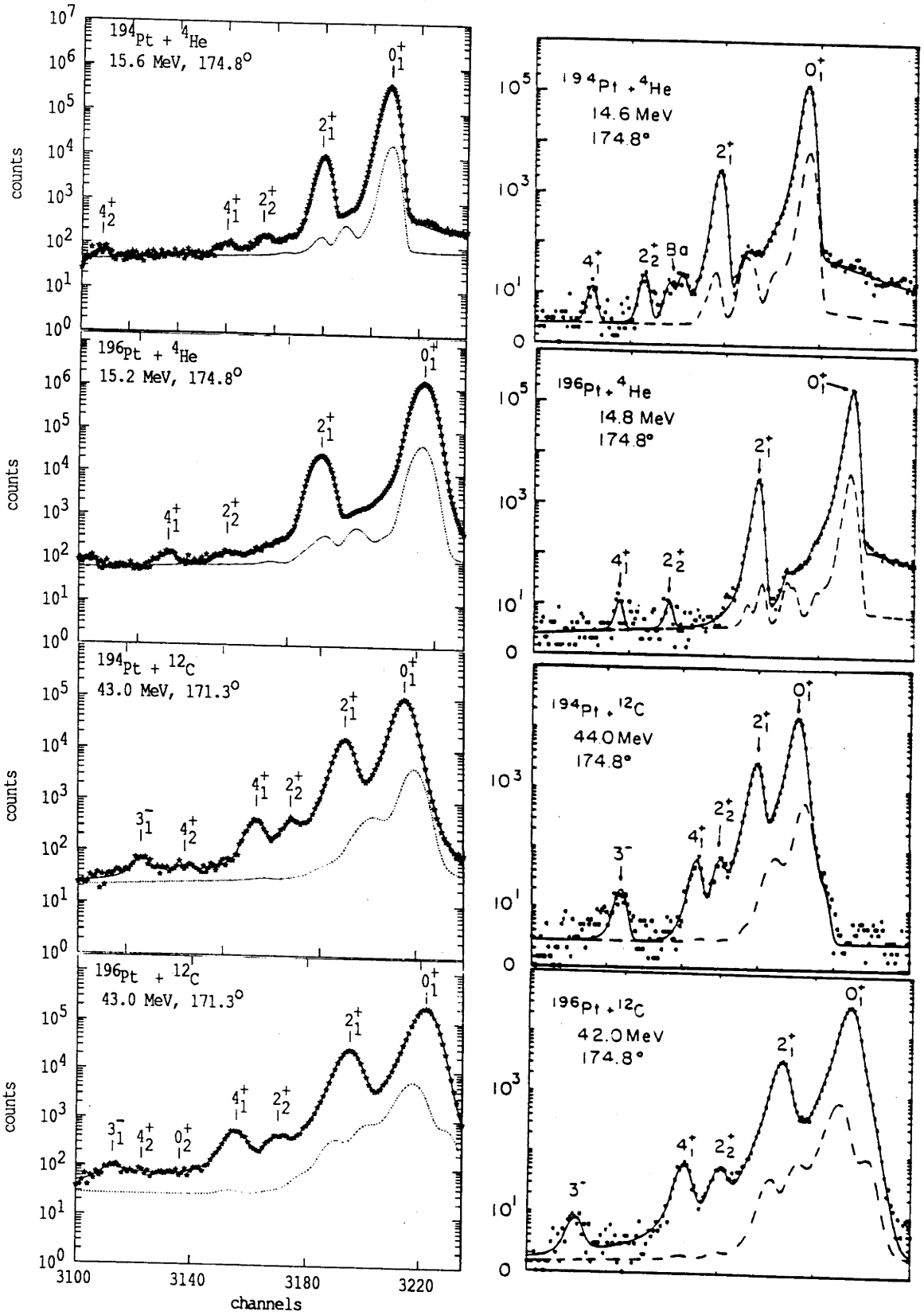

Figure 4.17: Typical spectra obtained in the present work (left column) and from Gy87t (right column) for ^{4}He and ^{12}C projectiles. To facilitate comparison, the broken curve indicates the total background contribution including contributions from Pt isotopes other than the one of interest. The solid curve is the fit to the data.

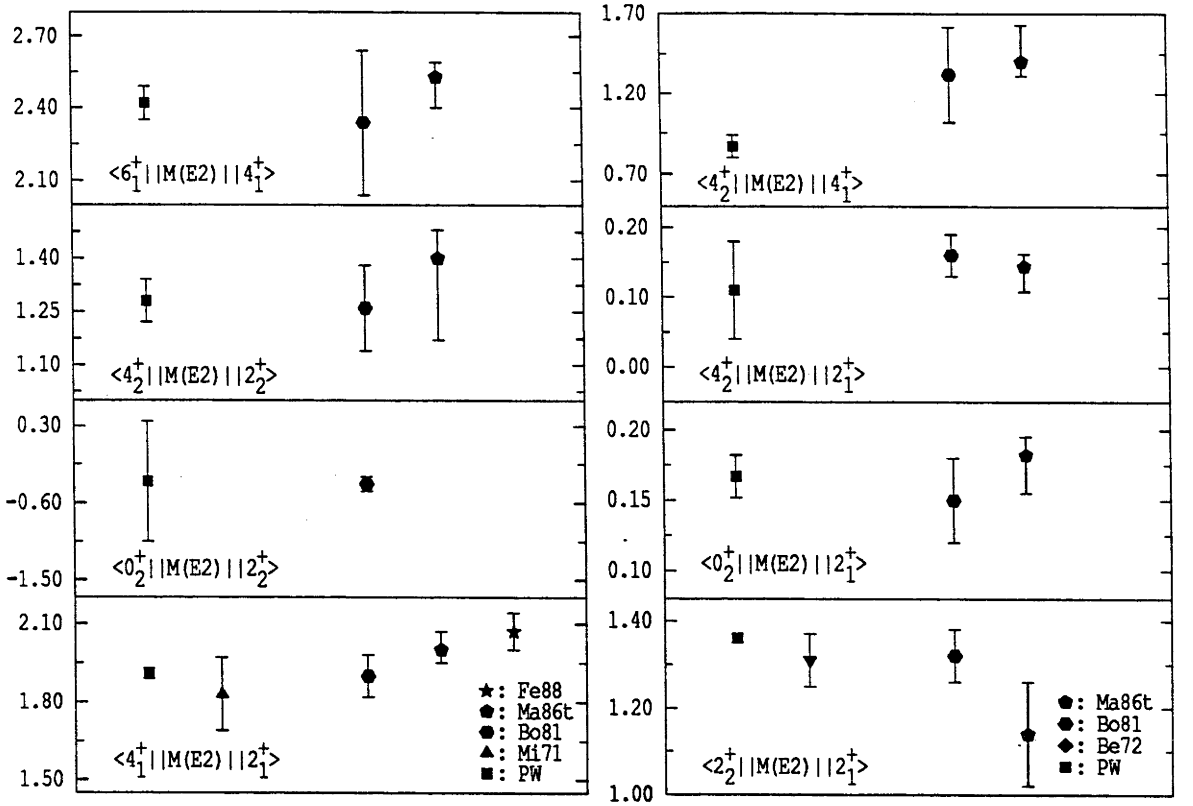

Figure 4.18: Experimental values in e b for higher state E2 transition matrix elements of ^{196}Pt; PW denotes the present work.

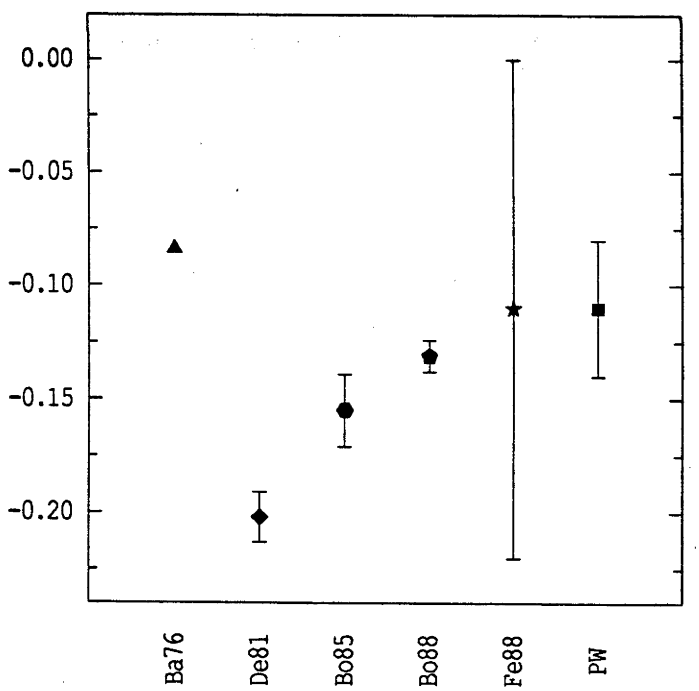

Figure 4.19: Experimental values in e b^2 for $< 0_1^+ |||\mathcal{M}(E4)|| 4_1^+ >$ of ^{196}Pt; PW denotes the present work.

Table 4.16: Experimental values of $B(E2;0_1^+ \rightarrow 2_1^+)$ and $Q(2_1^+)$ for ^{194}Pt in chronological order; PW denotes the present work.

	$B(E2;0_1^+ \rightarrow 2_1^+)$ (e^2b^2)	$Q(2_1^+)$ (e b)
Mc61	1.94(20)	
Gl69	1.64(4)	0.64(16)
Mi71	1.87(9)	
Be72	1.99(19)	
Ba76	1.671	
Jo77	1.55(10)	
Ro77	1.68(3)	
Ba78	1.621(15)	
Ch83		0.13(17)
Wu87	$1.46(^{12}_{4})$	$0.71(^{11}_{8})$
Gy86	1.661(11)	0.48(14)
Bo88	1.64(5)	
PW	1.621(9)	0.59(10)

4.6.2 ^{194}Pt

There are a large number of published measurements of $B(E2;0_1^+ \rightarrow 2_1^+)$ for ^{194}Pt. These values are listed in table 4.16 and also displayed in chronological order in fig. 4.20, together with the value obtained in the present work which is in excellent agreement with the results of Glenn *et al.* (Gl69), Baker *et al.* (Ba76), Johnson *et al.* (Jo77) and Baktash *et al.* (Ba78); the value obtained by Ronningen *et al.* (Ro77) is not inconsistent with that obtained in the present work. The discrepancy between the result of this experiment and that of Gyapong *et al.* (Gy86) may again be attributed to an

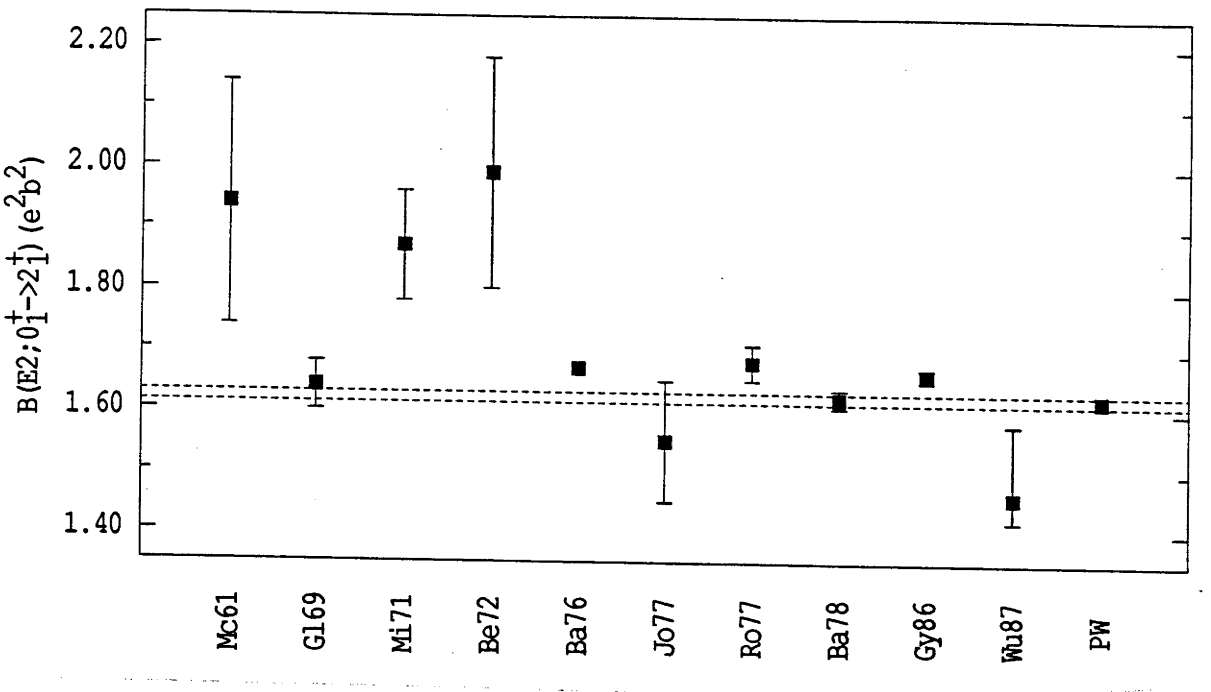

Figure 4.20: Experimental B(E2;$0_1^+ \rightarrow 2_1^+$) values for ^{194}Pt in chronological order; PW denotes the present work. The levels of uncertainty obtained in the present work are indicated by dotted lines.

underestimated background level in the latter. The measurement by Wu (Wu87) gives a value of 1.46($^{12}_{4}$) e^{2}b^2, differing significantly from the present value of 1.621(9) e^{2}b^2. This difference probably arises from a combination of two factors : their use of relatively heavy projectiles which are less sensitive to the matrix elements of the low-lying states and the "fast approximation" employed in their fitting program, GOSIA, which could be accurate to no more than 10%.

Previous measurements of Q(2_1^+) are compared with that of the present work in table 4.16 and fig. 4.21. The value obtained [0.59(10) e b] is in excellent agreement with all others except for that published by Chen *et al.* (Ch83), which appears to be anomalously low.

Data obtained with projectiles as light as ^{4}He and ^{12}C are much less sensitive to the quadrupole moments of the higher excited states than the dynamic E2 moments involving those states. As a consequence, only the values of $<2_2^+||\mathcal{M}(E2)||0_1^+>$, $<2_2^+||\mathcal{M}(E2)||2_1^+>$, $<4_1^+||\mathcal{M}(E4)||0_1^+>$, $<4_1^+||\mathcal{M}(E2)||2_1^+>$ and $<4_1^+||\mathcal{M}(E2)||4_1^+>$ were determined; these

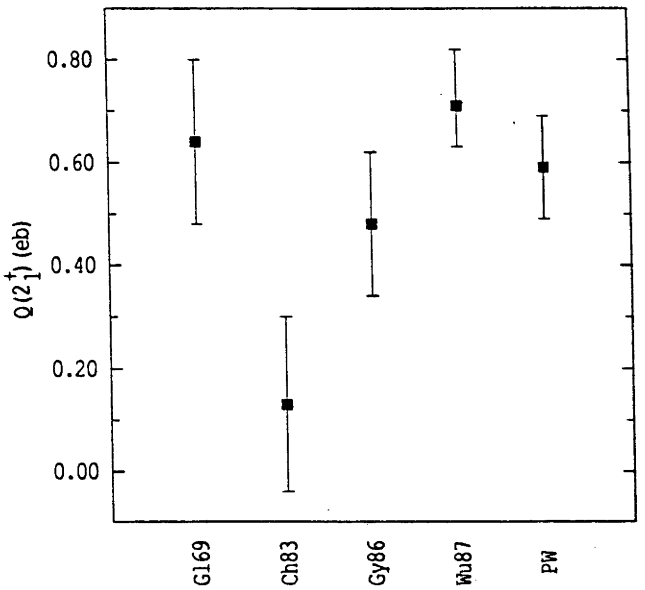

Figure 4.21: Experimental $Q(2_1^+)$ values for ^{194}Pt in chronological order; PW denotes the present work.

(Br70), Milner *et al.* (Mi71), Berkes *et al.* (Be72), Baker *et al.* (Ba76), Johnson *et al.* (Jo77), Ronningen *et al.* (Ro77) Stelzer *et al.* (St77), Baktash *et al.* (Ba78), Baker *et al.* (Ba79), Wu (Wu87), Boeglin *et al.* (Bo88) and Fewell *et al.* (Fe88) in table 4.7 and fig. 4.22. It can be seen that the result obtained for $<2_2^+||\mathcal{M}(E2)||0_1^+>$ is in excellent agreement with all other measurements; there is a greater scatter in the published values of $<2_2^+||\mathcal{M}(E2)||2_1^+>$ so that the result obtained here only agrees with two of the available values.

Values for $<4_1^+||\mathcal{M}(E4)||0_1^+>$ and $<4_1^+||\mathcal{M}(E2)||2_1^+>$ were obtained on the assumption that $<4_1^+||\mathcal{M}(E2)||2_2^+> = 0$; the result of -0.07(5) e b^2 for the former appears to be in disagreement with all other values apart from the earlier one of Baker *et al.* (Ba76) whilst the value of 2.28(4) e b for $<4_1^+||\mathcal{M}(E2)||2_1^+>$ is significantly higher than half of the other measurements of that matrix element (St77, Ba78, Ba79, Wu87). However, it is worth noting that the only model-independent measurement of the E4 matrix element are those of the present work and Fe88. The latter utilized the excitation probabilities obtained by Gyapong *et al.* (Gy86) which appear to have been consistently overestimated due to a setting of the background that was too low. The large difference in values of $<2_1^+||\mathcal{M}(E2)||0_1^+>$ obtained in the present work and in that of Wu may be the reason for the discrepancy in the two measurements for the 2_2^+ and 4_1^+ matrix elements. A value of

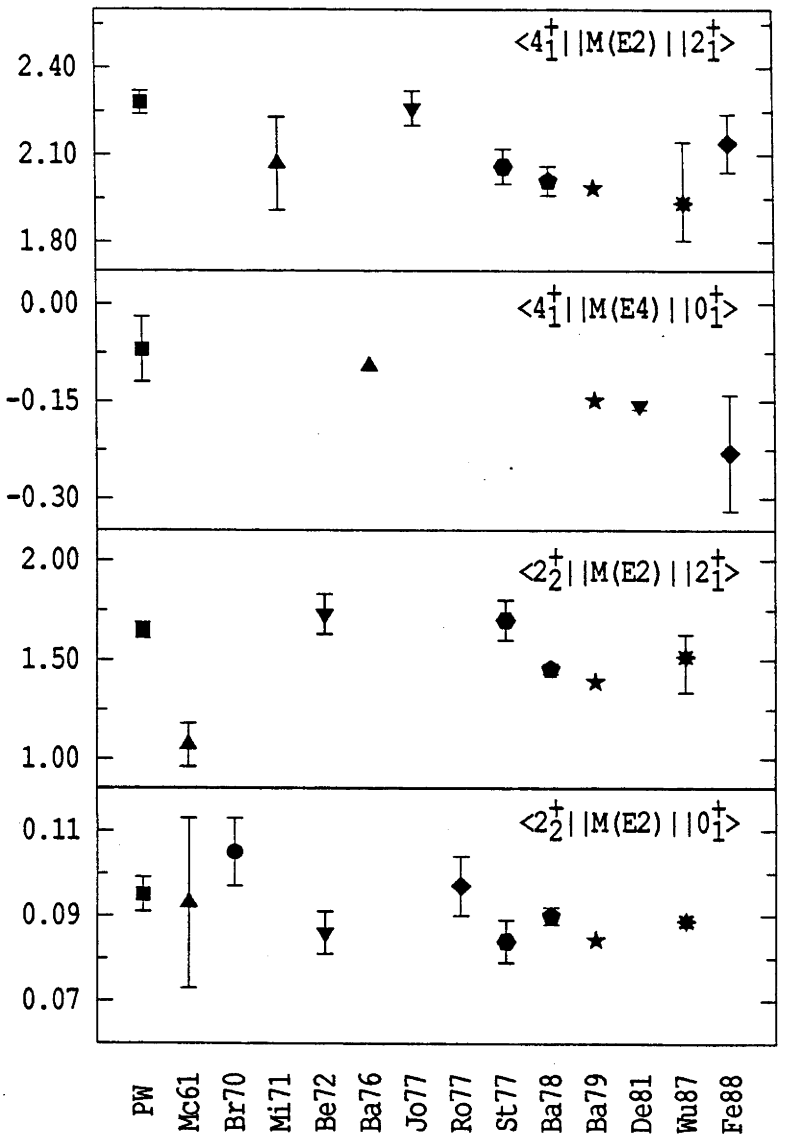

Figure 4.22: Experimental values in e $b^{\lambda/2}$ for higher state matrix elements of ^{194}Pt; PW denotes the present work.

the discrepancy in the two measurements for the 2_2^+ and 4_1^+ matrix elements. A value of 0.75(25) e b was obtained for $<4_1^+||\mathcal{M}(E2)||4_1^+>$, which is in reasonably good agreement with that of Wu [$1.00(^{12}_{14})$ e b].

4.7 Comparison with Theoretical Predictions

4.7.1 ^{196}Pt

An initial motivation for the experiment described in this chapter was to compare the quadrupole moments of the 2_2^+ and 4_1^+ states with $Q(2_1^+)$ for ^{196}Pt, and to see if the former would prove to be consistent with the small magnitudes predicted by the O(6) limit of the IBM. Clearly, this is not the case, as both the quadrupole moments of the 2_2^+ and 4_1^+ states have been measured to be of comparable magnitude to $Q(2_1^+)$. The ratios of these higher state quadrupole moments to $Q(2_1^+)$, assuming those values determined in the present work, are best fitted by Kumar and Baranger's PPQ calculations and less well by the U(5) limit and the BET, as shown in table 4.17.

However, as Casten and Cizewski (Ca87) pointed out, the properties of states at high excitation energies cannot be neglected if a convincing description of the nucleus is to be achieved. In particular, the experimental data on the decay modes of higher-lying 0^+ and 2^+ states are better fitted by the pure O(6) symmetry than by U(5) (Ca87). Nevertheless, satisfactory agreement of model predictions with data on the lowest-lying states is desirable. Table 4.18 lists experimental values for E2 matrix elements in ^{196}Pt up to and including the 6_1^+ and 6_2^+ states together with available predictions of the IBM. These are the IBM-1 calculations of Casten and Cizewski using the strict O(6) limit without any attempt to fit $Q(2_1^+)$ (Ca78,Ca87), the IBM-1 calculations of Mikhailov *et al.* which allow the parameter β [equation (4.3)] to have non-zero values so as to fit the experimentally observed value of $Q(2_1^+)$ (Mi86), the IBM-1 calculations of Fewell (Fe86) which consider the U(5) limit as well as an admixture of O(6) and SU(3), and the IBM-2 calculations of Bijker *et al.* who use the equivalent of the O(6) symmetry (Bi80). Perusal of table 4.18 and fig. 4.23 reveals that

(a) only the U(5) symmetry is able to fit both $<2_1^+||\mathcal{M}(E2)||2_1^+>$ and $<2_2^+||\mathcal{M}(E2)||0_1^+>$,

Table 4.17: Predictions of various models and experimental values for $B(E2;0_1^+ \rightarrow 2_2^+)$ (e^2b^2) and static quadrupole moments (e b) for the 2_1^+, 2_2^+ and 4_1^+ states of ^{196}Pt. PW denotes the present work.

	$B(E2;0_1^+ \rightarrow 2_2^+)$	$Q(2_1^+)$	$Q(2_2^+)$	$Q(4_1^+)$	$\frac{Q(2_2^+)}{Q(2_1^+)}$	$\frac{Q(4_1^+)}{Q(2_1^+)}$
Expt (PW)		0.62(8)	-0.39(16)	1.03(12)	-0.63(26)	1.66(24)
Expt (Be72)	$< 3 \times 10^{-6}$					
Expt (Ma86t)			-0.23($\frac{2}{3}$)	0.30($\frac{23}{24}$)		
IBM-1 O(6) (Ca78)	0	0	0	0		
IBM-1 O(6) (Mi86)	0.05	0.75				
IBM-1 U(5) (Fe85,Fe86)	0	0.79[a])	-0.34	1.58	-0.43	2
IBM-2 O(6) (Bi80)	9×10^{-7}	0.27				
PPQ (Ku68a)	0.022	0.70	-0.60	0.97	-0.85	1.38
GCM (He81)	0.002	0.48	-0.53		-1.10	
BET (We80,Ta87)	0.0022	0.58	-0.58	0.74	-1.0	1.28

[a]) assumed for calculations of $Q(2_2^+)$ and $Q(4_1^+)$

Table 4.18: Comparison of experimental values in e b for $< J_f \| \mathcal{M}(E2) \| J_i >$ of ^{196}Pt with various IBM calculations. Experimental values are taken from the present work except for those indicated (^{B} from Be72 and ^{M} from Ma86t).

J_i	J_f	Expt	Ca78/Ca87 O(6)	Mi86 O(6)	Fe86 U(5)	Fe86 O(6)+SU(3)	Bi80 O(6)
0_1^+	2_1^+	1.1697(13)	1.1747[a])	1.225[a])	1.176[a])	1.176[a])	1.202[a])
2_1^+	2_1^+	0.82(10)	0	0.99[a])	0.83[a])	0.83[a])	0.356
0_1^+	2_2^+	$< 0.0017^B$	0.0032/0	0.22	0	0.58	0.002
2_1^+	2_2^+	1.36(1)	1.23/1.34	1.125	1.52	1.35	1.414
2_2^+	2_2^+	−0.52(20)	0		−0.45		
2_1^+	4_1^+	1.91(2)	1.80	1.90	2.04	1.80	1.89
4_1^+	4_1^+	1.36(16)	0		2.10		
2_1^+	0_2^+	0.167(15)	0	0.075	0	0.030	0.16
2_2^+	0_2^+	−0.35(70)	−0.60	−0.56	−0.74	−0.607	−0.68
2_1^+	4_2^+	0.11(7)	0	0.15	0	0.65	0.21
2_2^+	4_2^+	1.28(6)	1.31	1.38	1.62	1.32	1.36
4_1^+	4_2^+	0.87(7)	1.27	1.53	1.54	1.26	1.36
4_2^+	4_2^+	$-0.34(^{60}_{21})^M$	0				
4_1^+	6_1^+	2.42(7)	2.16	2.30	2.68	2.19	2.31
6_1^+	6_1^+	−0.26(40)	0		2.84		
6_2^+	6_2^+	$-1.6(^{12}_{17})^M$	0		1.71		

[a])assumed for calculation of other matrix elements

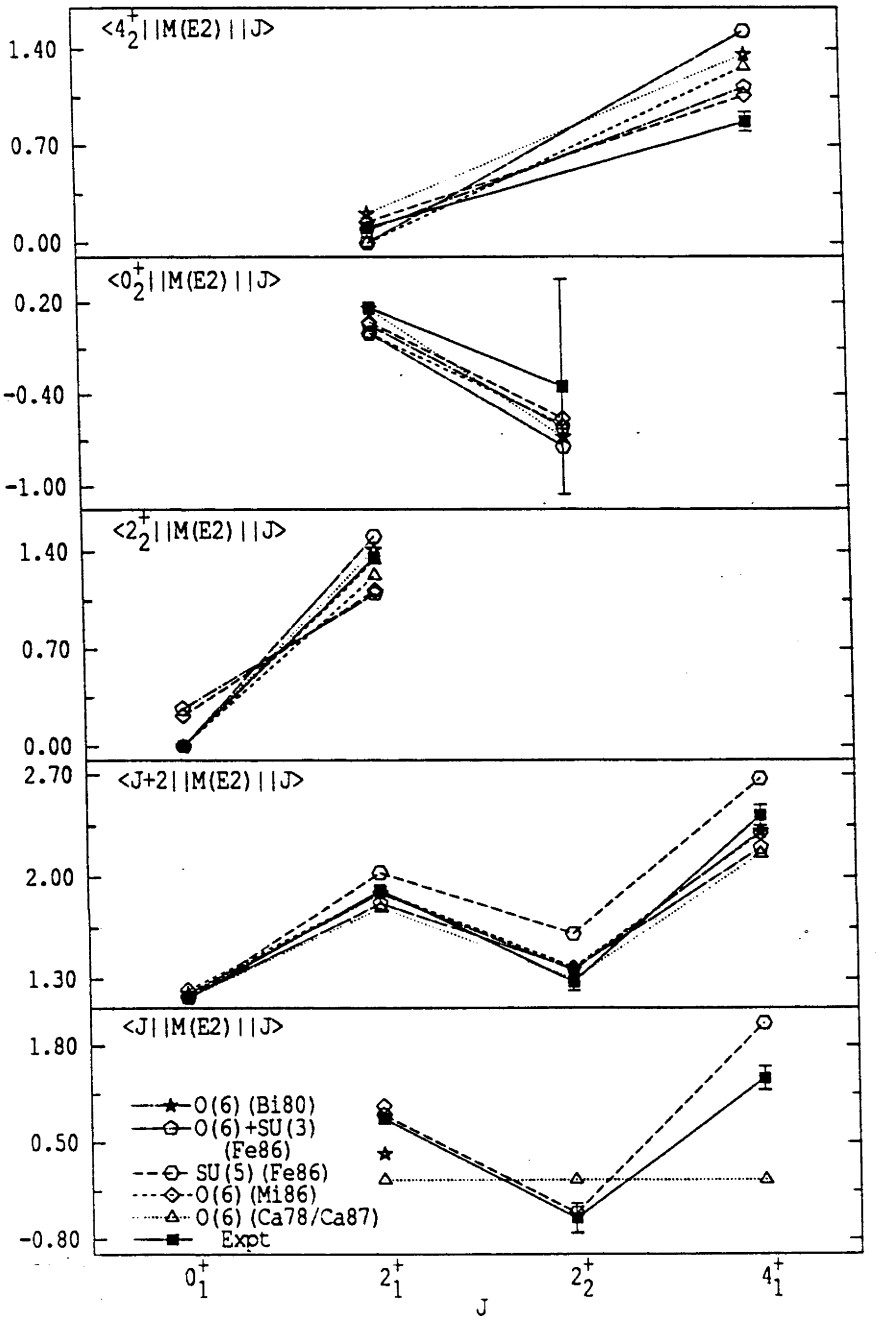

Figure 4.23: Comparison of IBM predictions with experiment for ^{196}Pt. The vertical axis is in units of e b.

(b) none of the O(6) calculations show particular success in fitting the data obtained in the present work,

(c) the O(6)/SU(3) admixture produces results which are similar to those of Mikhailov *et al.* (Mi86), thus illustrating the equivalence of the two methods,

(d) the predictions of Mikhailov *et al.* and the O(6)/SU(3) admixture are in as good agreement with experiment as those of Casten and Cizewski's,

(e) apart from $<2_1^+||\mathcal{M}(E2)||2_1^+>$ and $<2_2^+||\mathcal{M}(E2)||0_1^+>$, the experimental values are in excellent agreement with the calculations of Bijker *et al.*; however, these calculations do not include values for higher state quadrupole moments, which might reasonably be expected to agree poorly, and

(f) the U(5) symmetry does well on most of the quadrupole moments and the so-called "crossover" transition probability, $B(E2;0_1^+ \rightarrow 2_2^+)$, but only moderate agreement is attained for the other matrix elements and the prediction for $Q(6_1^+)$ far exceeds the experimental value. There may also be some significance in the fact that, when it disagrees with experiment, the U(5) limit tends to overpredict the matrix element magnitudes.

From the above evidence, it can be concluded that none of the different IBM calculations available can reproduce the observed values of the E2 matrix elements of the lowest-lying positive-parity states in ^{196}Pt. This is probably due to inherent limitations of the model in its simplest form. Presumably, using one of the modified versions of the IBM could result in a good fit to the data if sufficient parameters were included; however, this approach would be of limited value in terms of understanding the physical nature of the nucleus.

Some of the predictions of the GCM (He81), BET (We80) and PPQ (Ku68a) are compared with experiment in fig. 4.24 and table 4.19. The former presentation of results immediately suggests that the GCM tends to overestimate the magnitude of most matrix elements, a conclusion which is borne out by an examination of table 4.19. The PPQ calculations of Kumar and Baranger do rather well, considering that they were carried out

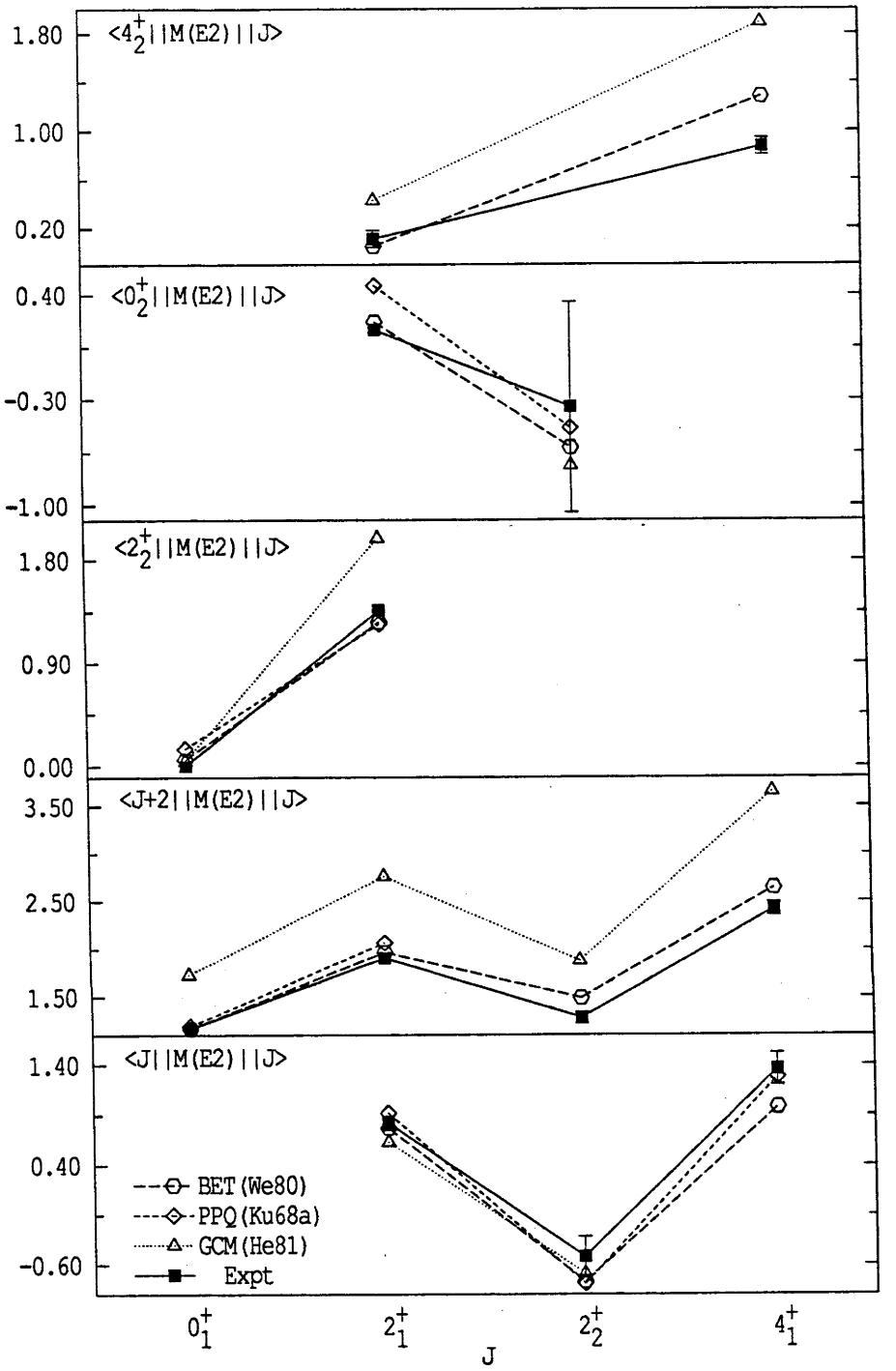

Figure 4.24: Comparison of experiment with the predictions of the GCM, BET and PPQ for ^{196}Pt. The vertical axis is in units of e b.

Table 4.19: Comparison of experimental values in e b for $< J_f||\mathcal{M}(E2)||J_i >$ of ^{196}Pt with predictions of the GCM, BET and PPQ. Experimental values are taken from the present work except for those indicated (^{B} from Be72 and ^{M} from Ma86t).

J_i	J_f	Expt	He81 GCM	Ku68a PPQ	We80, Ta87 BET
0_1^+	2_1^+	1.1697(13)	1.734	1.195	1.168
2_1^+	2_1^+	0.82(10)	0.63	0.92	0.77
0_1^+	2_2^+	$< 0.0017^B$	0.045	0.15	0.055
2_1^+	2_2^+	1.36(1)	1.99	1.24	1.26
2_2^+	2_2^+	−0.52(20)	−0.69	−0.79	−0.77
2_1^+	4_1^+	1.91(2)	2.76	2.07	1.97
4_1^+	4_1^+	1.36(16)		1.28	0.98
2_1^+	0_2^+	0.167(15)		0.46	0.22
2_2^+	0_2^+	−0.35(70)	−0.74	−0.49	−0.62
2_1^+	4_2^+	0.11(7)	0.43		0.05
2_2^+	4_2^+	1.28(6)	1.88		1.49
4_1^+	4_2^+	0.87(7)	1.89		1.28
4_2^+	4_2^+	$-0.34(^{60}_{21})^M$			0.38
4_1^+	6_1^+	2.42(7)	3.65		2.64
6_1^+	6_1^+	−0.26(40)			
6_2^+	6_2^+	$-1.6(^{12}_{17})^M$			0.83

at a time when only four or five of these matrix elements had been measured. The Boson Expansion Theory also gives satisfactory agreement in all cases considered except for the crossover transition for the 2_2^+ state, which is overpredicted by all three models. Most of the predicted quadrupole moments agree with experimental values where available.

4.7.2 ^{194}Pt

Three of the IBM calculations to be considered - those of Arima and Iachello (Ar79), Mikhailov *et al.* (Mi86) and Gyapong (Gy87t) - assume an O(6) Hamiltonian within the IBM-1. The IBM-2 calculations of Bijker *et al.* (Bi80) make use of the O(6) limit while the fifth set of calculations (Gy87t) were carried out in the context of the U(5) dynamical symmetry of the IBM-1. Gyapong selected his parameters for both sets of calculations to fit his measured values of B(E2;$0_1^+ \rightarrow 2_1^+$) and Q(2_1^+).

Table 4.20 and fig. 4.25 show that in general, all the O(6) predictions show the same level of agreement with experiment. The results of the IBM-2 calculations of Bijker *et al.* are almost the same as those of the IBM-1 calculations of Arima and Iachello; both underpredict the values of $<2_1^+||\mathcal{M}(E2)||2_1^+>$ and $<2_2^+||\mathcal{M}(E2)||0_1^+>$ and substantially overpredict $<6_1^+||\mathcal{M}(E2)||4_1^+>$. Both Mikhailov *et al.* and Gyapong have managed to fit the observed value of Q(2_1^+) with an O(6) Hamiltonian at the expense of agreement with either $<2_2^+||\mathcal{M}(E2)||0_1^+>$ or $<2_2^+||\mathcal{M}(E2)||2_1^+>$. The U(5) predictions agree with experiment for matrix elements involving states up to the 4_1^+; it should be noted that Gyapong (Gy87t) finds an increasing deviation from experiment as one moves to higher states.

The predictions of the GCM, PPQ and BET for ^{194}Pt are shown in table 4.21. It can be seen from fig. 4.26 that all three models give very similar results. The overall level of agreement with experiment is better than for the IBM.

4.7.3 Discussion

In general, the results presented show that the large quadrupole moments observed in experiment for the 2_1^+, 2_2^+ and 4_1^+ states of ^{196}Pt cannot be satisfactorily reproduced by the O(6) limit with either IBM-1 or IBM-2 calculations unless agreement with at least

Table 4.20: Comparison of experimental values in e b for $< J_f \| \mathcal{M}(E2) \| J_i >$ of ^{194}Pt with various IBM predictions. Experimental values are taken from the present work except for those indicated (^{W} from Wu87, ^{B} from Ba78 and ^{S} from St77).

J_i	J_f	Expt	Ar79 IBM-1 O(6)	Bi80 IBM-2 O(6)	Mi86 IBM-1 O(6)	Gy87t IBM-1 O(6)	Gy87t IBM-1 U(5)
0_1^+	2_1^+	1.273(4)	1.360	1.336	1.245	1.289	1.289
2_1^+	2_1^+	0.78(13)	0	0.17	0.88	0.63	0.63
0_1^+	2_2^+	0.095(4)	0	0.012	0.18	0.44	0
2_1^+	2_2^+	1.65(4)	1.57	1.61	1.24	1.49	1.69
2_2^+	2_2^+	-0.7(6)^B, -0.40($^{12}_5$)^W	0				-0.27
2_1^+	4_1^+	2.28(4)	2.10	2.11	1.93	2.00	2.26
4_1^+	4_1^+	0.75(25)	0				1.26
2_1^+	0_2^+	$\pm$0.070($^9_{21}$)^W					
2_2^+	0_2^+	0.231($^{30}_{21}$)^W					
2_1^+	4_2^+	0.30(7)^B		0.19	0.073	0.51	0
2_2^+	4_2^+	1.7(3)^{B,S}	1.56	1.57	1.43	1.48	1.83
4_1^+	4_2^+	2.8(7)^B		1.58	1.20	1.42	1.75
4_2^+	4_2^+	-0.07(14)^W	0				
4_1^+	6_1^+	2.03(25)^S	2.60	2.66	2.37	1.97	2.59

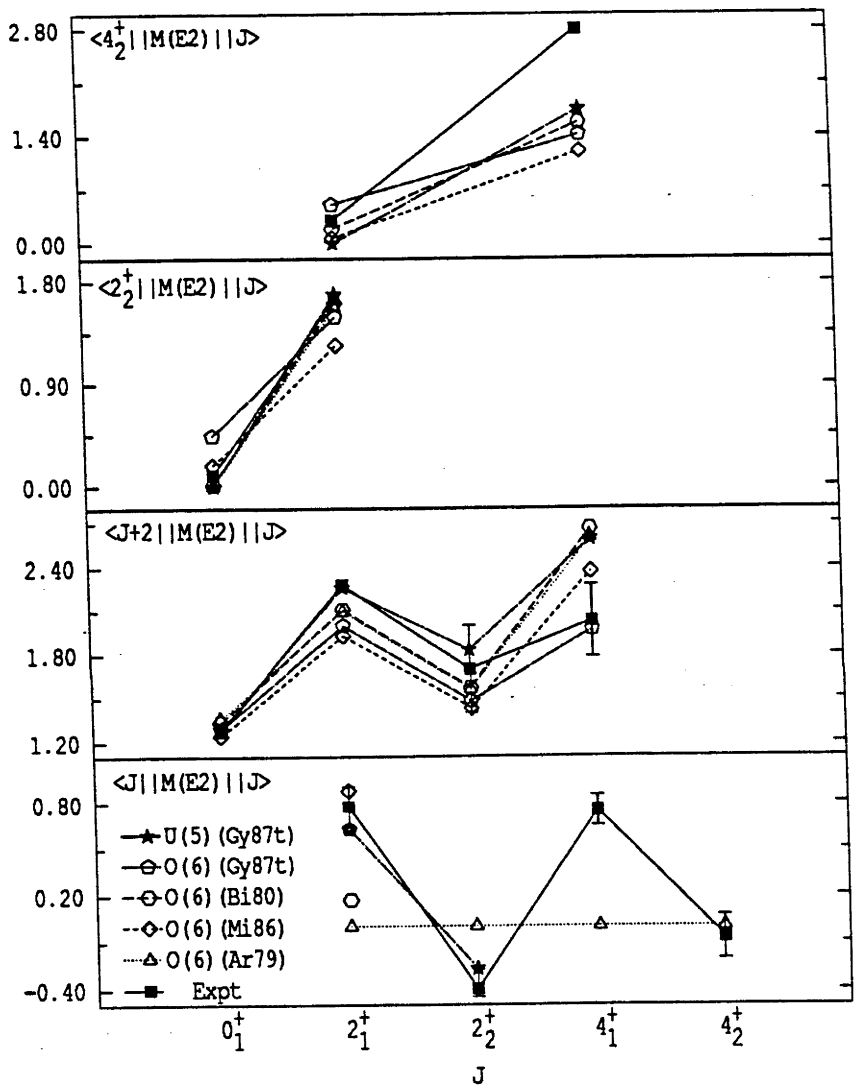

Figure 4.25: Comparison of experiment with IBM predictions for ^{194}Pt. The vertical axis is in units of e b.

Table 4.21: Comparison of experimental values in e b for $< J_f \| \mathcal{M}(E2) \| J_i >$ of ^{194}Pt with the GCM, BET and PPQ predictions. Experimental values are taken from the present work except for those indicated (^{W} from Wu87, ^{B} from Ba78 and ^{S} from St77).

J_i	J_f	Expt	He81 GCM	Ku68a PPQ	We80, Ta87 BET
0_1^+	2_1^+	1.273(4)	1.367	1.305	1.289
2_1^+	2_1^+	0.78(13)	0.60	0.65	0.71
0_1^+	2_2^+	0.095(4)	0.032	0.071	0.006
2_1^+	2_2^+	1.65(4)	1.53	1.50	1.43
2_2^+	2_2^+	$-0.40(^{12}_{5})^W$	-0.55	-0.56	-0.71
2_1^+	4_1^+	2.28(4)	2.17	2.19	2.14
4_1^+	4_1^+	0.75(25)		0.88	0.54
2_1^+	0_2^+	$\pm 0.070(^{9}_{21})^W$		0.38	0.12
2_2^+	0_2^+	$0.231(^{30}_{21})^W$	0.48	0.55	0.67
2_1^+	4_2^+	$0.30(7)^B$	0.32		0.14
2_2^+	4_2^+	$1.7(3)^{B,S}$	1.42		1.62
4_1^+	4_2^+	$2.80(7)^B$	1.39		1.44
4_2^+	4_2^+	$-0.07(14)^W$			0.36
4_1^+	6_1^+	$2.03(25)^S$	2.88		2.84

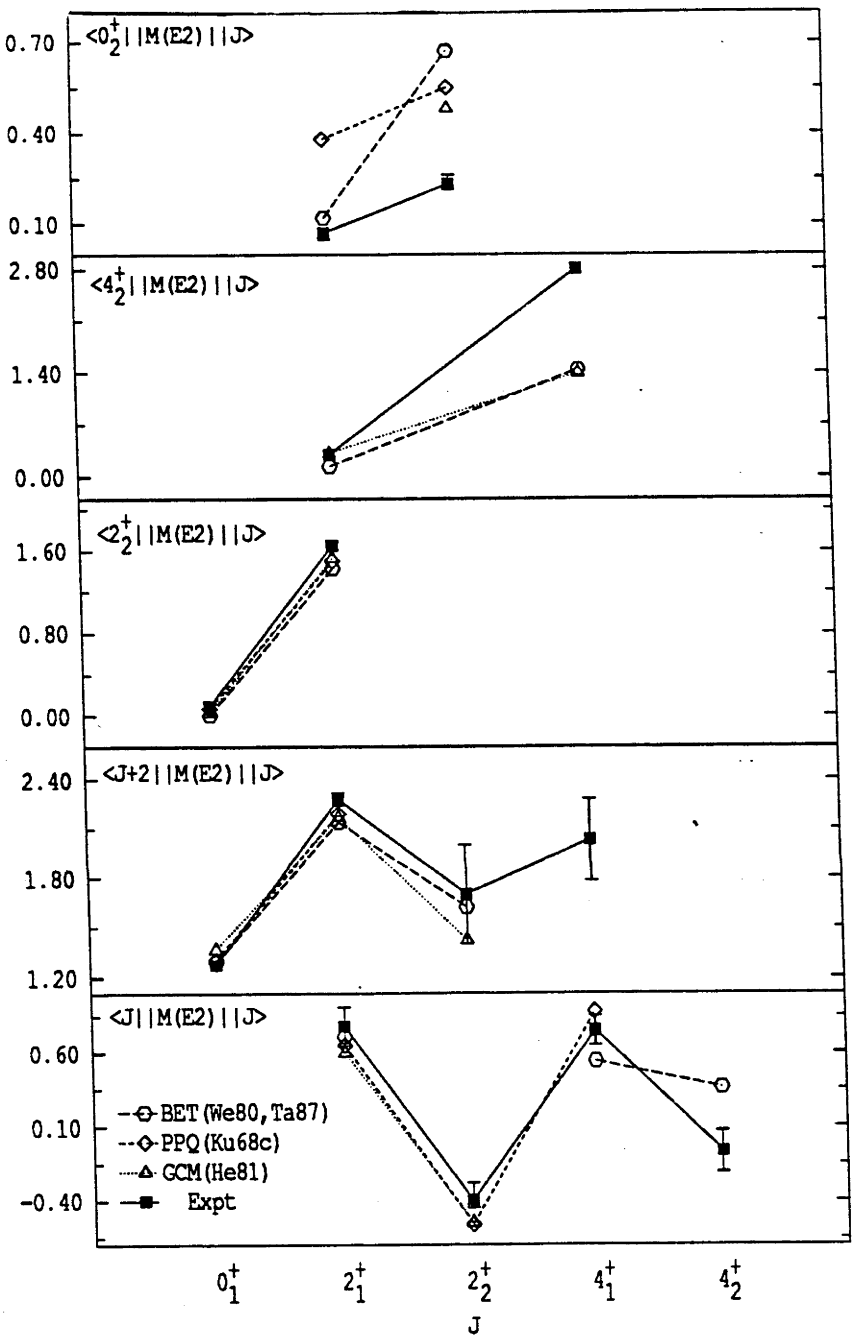

Figure 4.26: Comparison of experiment with GCM, BET and PPQ predictions for ^{194}Pt. The vertical axis is in units of e b.

one other matrix element is lost. This suggests that the large magnitudes may not be due solely to the distinction between neutrons and protons, as has been proposed by some workers (Ca87); this should be further investigated. It should be noted that the inability of the O(6) limit to predict large quadrupole moment magnitudes while maintaining a small value for the crossover transition $B(E2;0_1^+ \rightarrow 2_2^+)$ is an inherent property of the limit but not a characteristic of all γ-unstable nuclei.

None of the other possible modifications to the O(6) limit are able to produce predicted quadrupole moments of the correct magnitude apart from the inclusion of the symmetry-breaking quadrupole-quadrupole force (Mi86), which does reduce the discrepancy between experiment and theory for the quadrupole moment of the first excited state but only at the expense of agreement between experiment and theory for $B(E2;0_1^+ \rightarrow 2_2^+)$ in the case of ^{196}Pt. The U(5) limit is also unable to reproduce all the observed E2 transition strengths and quadrupole moments of this nucleus; in particular, the best U(5) predictions do not reproduce the observed decay modes of high-lying 2^+ and 0^+ states. It appears that it is not possible to describe the structure of ^{196}Pt satisfactorily using relatively simple IBM hamiltonians. This may reflect some fundamental problem with that model, as suggested by Tamura and his collaborators (We80, Ta86).

The microscopic models, on the whole, provide a better description of the data presented than the IBM. The superior performance of these models was also noted by Baktash *et al.* (Ba80). The performance of the BET, in particular, is consistently high. The PPQ calculations of Kumar and Baranger also perform well in comparison to the GCM and the IBM.

The degree to which predictions of the quadrupole moments $Q(2_1^+)$, $Q(2_2^+)$ and $Q(4_1^+)$, and the crossover transition probability $B(E2;0_1^+ \rightarrow 2_2^+)$ agree with experiment provides a stringent test of model descriptions of these nuclei. In certain γ-unstable nuclei, the prolate and oblate components are in balance (i.e. $\gamma = 30°$); one expects to observe a small $B(E2;0_1^+ \rightarrow 2_2^+)$ in such nuclei, accompanied by small quadrupole moments. The large quadrupole moment magnitudes measured for ^{192}Os and ^{194,196}Pt indicate that although these nuclei are γ-unstable, they have an overall tendency to a significant degree of quadrupole deformation. Table 4.17 summarizes the predictions of the various models

outlined in § 4.2 for the crossover transition of the 2_2^+ state and the quadrupole moments of the 2_1^+, 2_2^+ and 4_1^+ states, together with the experimentally determined values of those quantities. None of the models considered is able to fit both the crossover transition probability and any of the quadrupole moments for ^{196}Pt apart from the U(5) limit of IBM-1 (Fe86). This is due to the additional degree of freedom contained in the IBM, as noted by Fewell (Fe87), which is not found in the Bohr-Mottelson Hamiltonian. This degree of freedom, which is controlled by the parameter β [cf. equation (4.3)] in the IBM, allows the ratio $Q(2_1^+)/B(E2;0_1^+ \rightarrow 2_1^+)$ to vary. Fewell pointed out that the existence of this degree of freedom implies a "disjunction of the static quadrupole moment from the potential energy surface" in that model.

As far as ^{196}Pt is concerned, the U(5) and BET calculations probably give the best description of the experimental E2 matrix elements determined in the present work. Both are compared with the data in fig. 4.27. The excellent overall agreement obtained in both cases as compared with the O(6) calculations suggests that ^{196}Pt does not conform to the O(6) dynamical symmetry, which is equivalent to a γ-unstable nucleus in which neither oblate nor prolate minima dominate the PES. This is not surprising, as the large positive values of $Q(2_1^+)$ suggest an overall tendency to strong oblate deformation. At the same time, a high degree of γ-instability is indicated by a value of $E_x(2_2^+)/E_x(2_1^+)$ of about 2, the repeating $0^+ - 2^+ - 2^+$ level sequence and the suppressed E2 crossover transition within that sequence. This leads to the conclusion that the nuclear charge distribution of ^{196}Pt is γ-soft, and oblate when averaged over time. This is similar to the picture given by the BET calculations of Weeks and Tamura as well as the GCM calculations of Hess *et al.*, and is more consistent with the overall situation than the alternative view that the large quadrupole moments seen in the Pt nuclei are evidence for a more rigid triaxial deformation like that described by the Davydov-Fillipov model (Le77). The experimental data obtained for ^{194}Pt in the present work can be taken as evidence of a similar structure to that of ^{196}Pt but perhaps with less γ-instability, as suggested by the stronger crossover transition. The calculations of Hess *et al.* for the Pt nuclei show that, as the strength of the $2_1^+ \rightarrow 2_2^+$ transition decreases, the number of potential energy minima increases, i.e. the nucleus becomes increasingly γ-soft. However,

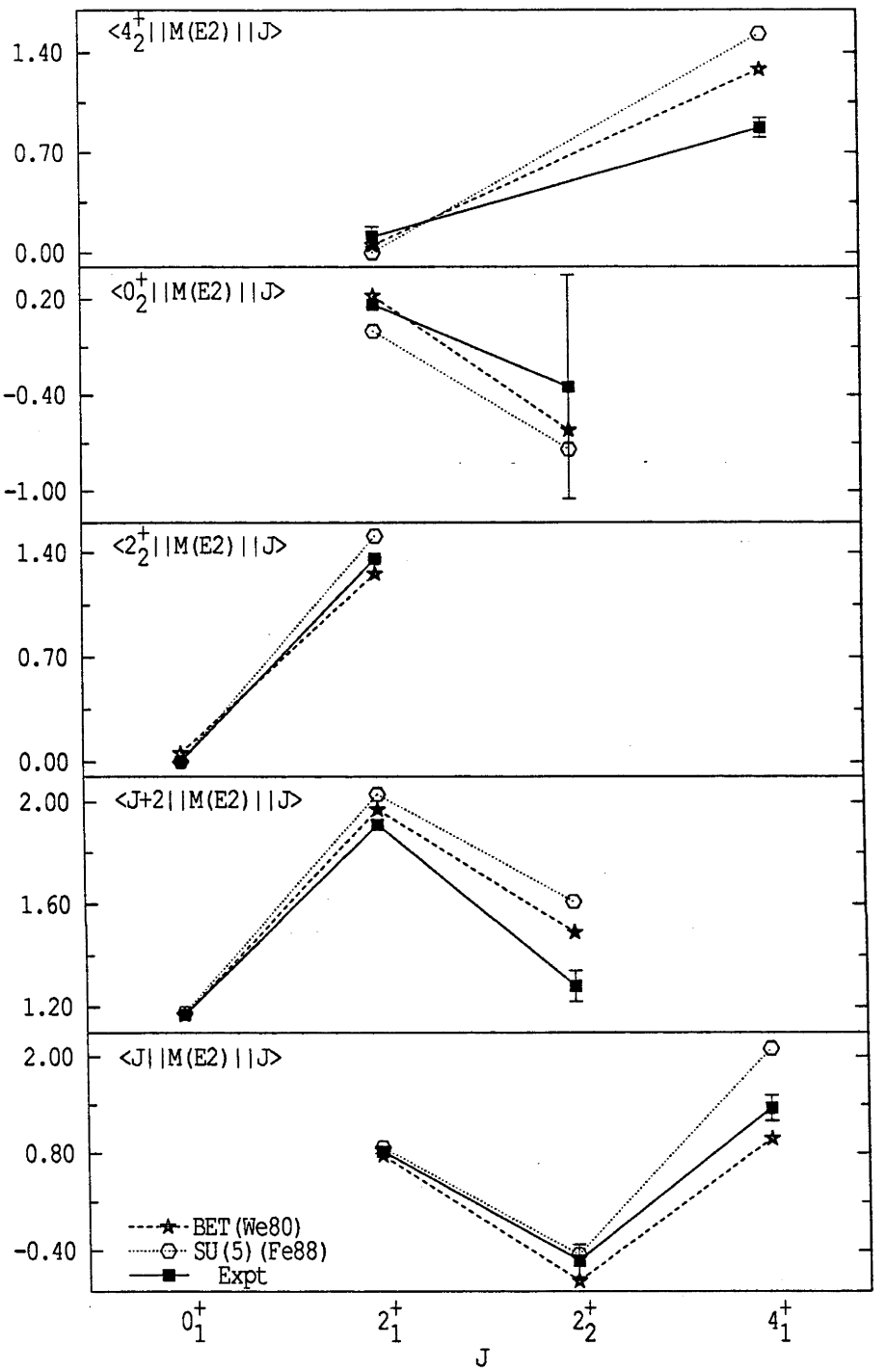

Figure 4.27: Comparison of experiment with BET and U(5) predictions for ^{196}Pt. The vertical axis is in units of e b.

Table 4.22: Predictions of the location (mass number) of the prolate-to-oblate transition in the Os and Pt nuclei.

Reference	Model	Os	Pt
Ku68a	PPQ	190-192[a])	188-190
Ra74	Strutinsky calculations	>192	184-186
Se74	GCM	>192	
We80	BET	>194	190-192
He81	GCM	>192	190[b])

[a]) predicts sign change for $Q(2_1^+)$ between ^{192}Os and ^{194}Os
[b]) predicts sign change for $Q(2_1^+)$ between ^{190}Pt and ^{192}Pt

the large quadrupole moment magnitudes are retained because the depth of the strongest minimum does not change greatly.

Predictions of the location of the prolate-to-oblate transition in the Os and Pt nuclei are listed in table 4.22. Most of these calculations have been carried out by fitting experimental values for various shape indicators such as $Q(2_1^+)$. It is interesting to note that whilst most models agree that the Os isotopes should become oblate at mass numbers greater than 192, there are widely-varying predictions of the exact location of the transition in the Pt isotopes. It is also noteworthy that the prolate-to-oblate transition is predicted to occur at a neutron number of about 118 (A=194) for Os but somewhere between 106 and 114 (A=184 and 192) for Pt.

The work presented in this chapter and the preceding one suggests that ^{192}Os is a well-deformed prolate nucleus while ^{194}Pt and ^{196}Pt are probably γ-soft with oblate deformation. Experimental studies of ^{185,187,189}Pt by Eder *et al.* (Ed88) in nuclear orientation experiments and by Roussière *et al.* (Ro88) using hyperfine structure measurements indicate that ^{185}Pt is prolate while ^{187,189}Pt are oblate or triaxial. The spectroscopy of odd-mass Au nuclei suggests that the Pt isotopes undergo a prolate-to-oblate transition between ^{186}Pt and ^{188}Pt (Wa85). Investigations of the energy level spectroscopy of ^{194}Os

by Casten *et al.* (Ca78a) and of ^{196}Os by Bond *et al.* (Bo83) point to a strongly deformed shape for ^{194}Os but a more spherical vibrator structure for ^{196}Os. When viewed in conjunction with the negative sign and large magnitude measured for the spectroscopic quadrupole moment of 2_1^+ for ^{192}Os (see chapter 3), very similar to that found for ^{188,190}Os, this interpretation of the spectroscopy of ^{194,196}Os supports a picture of rapid change from significant prolate deformation in ^{192}Os to greater prolate deformation in ^{194}Os with a possible reversion to sphericity in ^{196}Os. This is a contrast to the more gradual shape transition believed to occur in the Pt isotopes. The quadrupole moments measured for ^{194,196}Pt in the present work confirm that the prolate-to-oblate transition occurs at a very different neutron number for Os to that for Pt. In view of the prediction of a change in sign of $Q(2_1^+)$ between ^{190}Pt and ^{192}Pt by both BET (We80) and GCM (He81) calculations (cf. table 4.22), it would be very interesting to measure $Q(2_1^+)$ for ^{190}Pt; this has not been done in the past due to its low abundance even in isotopically enriched material ($\sim 4\%$).

4.8 Conclusion

Measurements of E2 matrix elements of ^{196}Pt and ^{194}Pt, in particular, of the large quadrupole moments of the 2_1^+, 2_2^+ and 4_1^+ states, provide strong evidence to show that these two nuclei are γ-soft with a definite oblate minimum in the potential energy surface. In general, the predictions of microscopic models agree better with experiment than the predictions of either IBM-1 or IBM-2.

Chapter 5

Coulomb Excitation Of 3_1^- States In Pt And Hg

5.1 Introduction

It has long been known that many even-even nuclei possess low-lying 3_1^- states with transition strengths to the ground state about an order of magnitude larger than the single-particle estimate. Such states are found, in particular, in the stable even-A platinum, mercury and lead nuclei. In general, the excitation energy of the first 3_1^- state, $E_x(3_1^-)$, varies smoothly as a function of the mass number A; however, a sudden increase of ~1 MeV is observed when going from ^{198}Pt to ^{198}Hg (fig. 5.1). In recent years this discontinuity has been the focus of much attention (see, for example, Ya88, Co88, Co88a, Co88b), providing further stimulus to the many attempts to describe these nuclei.

Such low-lying 3^- states with enhanced transition strengths from the ground state have been described (Li78) by both the collective vibrational model (Bo75) and by the Rotational Aligned (RAL) model (St72). In the case of the Pt-Hg-Pb region, experimentally-deduced single-particle energies (Ha77) show that 3^- states in the collective model can arise only from cross-shell excitations whereas in the RAL calculations, the octupole structure involves two quasi-particles in the same shell.

In the vibrational model, octupole states can be considered as the coherent sum of several one-particle-one-hole (1p1h) excitations between two single-particle orbitals with

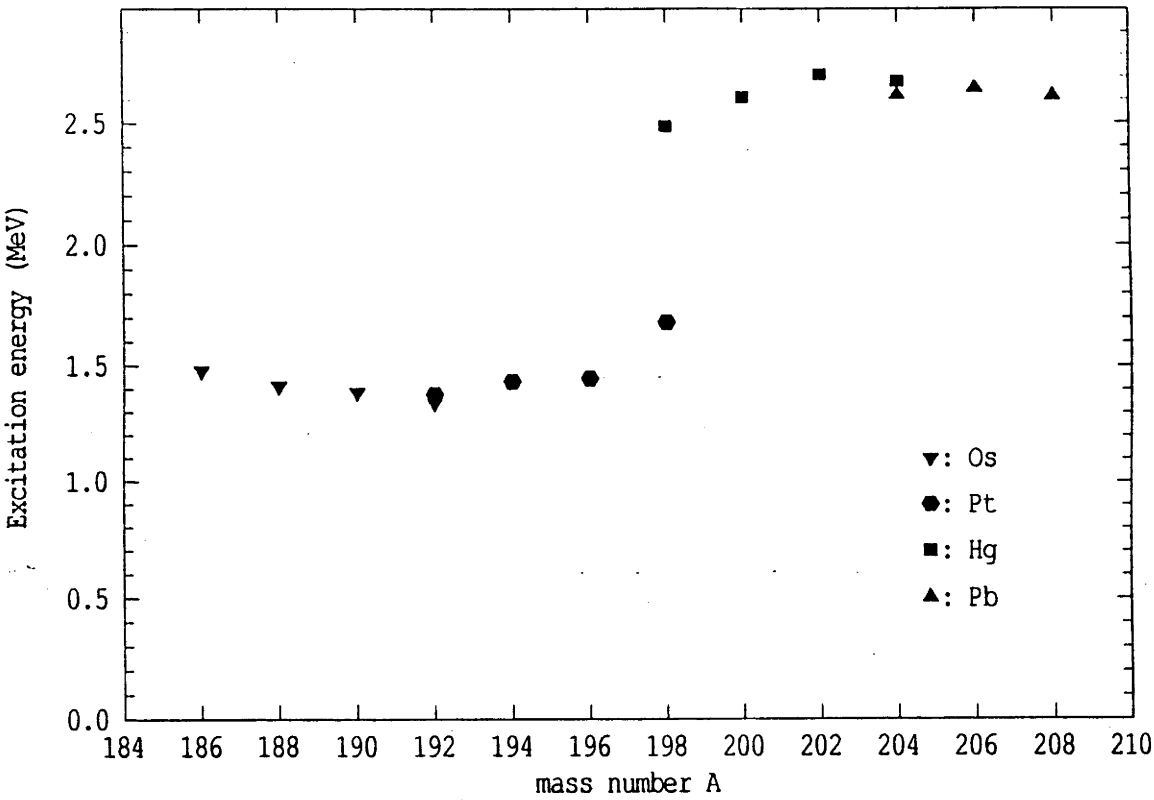

Figure 5.1: Excitation energies of the 3_1^- states of the stable even-mass Os, Pt, Hg and Pb isotopes vs. mass number A.

the difference in angular momentum Δl being $3\hbar$ (Bo75). Low energy octupole states are caused predominantly by 1p1h excitations between members of orbital pairs in which the lower orbital has l = (n-2)$\hbar$ and j = (2n-3)$\hbar/2$ while the higher has l = (n+1)$\hbar$, j = (2n+3)$\hbar/2$ and parity opposite to that of the lower orbital; n is the oscillator quantum number of the state with the same parity as the ground state. Excitations between such orbital pairs where $\Delta j = \Delta l$ are favoured because the change in intrinsic spin is zero (Bo75). An example of an orbital pair with $\Delta l = \Delta j = 3\hbar$ can be found in each proton or neutron valence shell in nuclei with neutron number N and atomic charge Z > 28. The probability of these Δl=3 excitations is expected to increase as more nucleons are added to the lower orbital until the subsequent filling of the higher energy orbital reduces the probability of excitation, leading to a predicted decrease of the energy eigenvalue of the coherent sum [equivalent to the frequency of the octupole vibration and hence to $E_x(3_1^-)$] to a minimum, followed by a subsequent increase as one approaches closed shells. This variation of $E_x(3_1^-)$ with N and Z has been found in several regions of the periodic table (Sp89).

Several versions of the RAL model have been proposed. However, the only application of the RAL model to the 3_1^- states of Pt and Hg is the semi-decoupled model of Neergård *et al.* (Ne75). In this model, two quasi-particles, one with high angular momentum and one with low angular momentum, are originally coupled to a rotating core. The Coriolis force decouples the quasi-particle (qp) with high angular momentum so that it aligns along the rotational axis of the core while the low angular-momentum qp remains coupled to the core. A more detailed discussion of the results of this model for the Pt and Hg nuclei is given below.

Determinations of $B(E3;0_1^+ \rightarrow 3_1^-)$ for ^{194,196}Pt from the data presented in the previous chapter were motivated by the recent interest in the 3_1^- states of the Pt and Hg isotopes. It seemed a natural step to go on to measure $B(E3;0_1^+ \rightarrow 3_1^-)$ for the stable even-mass Hg isotopes in order to investigate the apparent discontinuity in octupole behaviour between ^{198}Pt and ^{198}Hg.

5.2 Survey of Theoretical Studies of the Pt-Hg Region

It was explained in § 4.7.3 that the Pt isotopes are believed to undergo a prolate-to-oblate transition somewhere between A=184 and A=192. A great deal of effort has been expended on various theoretical descriptions of the behaviour of the even-mass Pt isotopes, encompassing both phenomenological [eg. the Interacting Boson Model (IBM)] and microscopic [eg. Boson Expansion Theory (BET), Pairing-Plus-Quadrupole (PPQ)] treatments. Most recent calculations have been able to describe the positive-parity states and dynamic E2 moments with reasonable success; however, a common problem has been an inability to fit simultaneously the large quadrupole moments observed in ^{196}Pt as well as the small crossover transition strength from the 2_2^+ state to ground. Of these calculations γ-soft descriptions have tended to have the greatest success.

Investigations have been carried out for the Hg isotopes in terms of the IBM, the symmetric rotor model and the particle-vibration coupling model. Covello and Sartoris (Co70) have found that the Hg nuclei do not fit the simple harmonic vibrator description. Tanaka and Sheline (Ta77) have observed that the symmetric rotor predictions give a

better fit to experiment than either of the asymmetric rotor model or the rotation-vibration model, both of which incorporate a certain degree of γ-deformation. The IBM calculations (Dr87, Se87) have shown that both the O(6) and U(5) symmetries give a good description of the Hg nuclei. A discontinuity in the mass-dependence of $E_x(2_1^+)$, $E_x(2_2^+)$ and $E_x(4_1^+)$ has been noticed in ^{200}Hg (Mo81), apparently signalling a sharp change in the relative proton and neutron distributions.

5.2.1 Theoretical Studies of 3^- States in Pt and Hg

Although the positive-parity states of the Pt and Hg nuclei have been examined many times in the framework of the IBM (see, for example, Ca78, Dr87, Se87, Fe85 and references therein), only one set of IBM calculations for the negative-parity states in Pt has been published (En86) while no such work has been carried out for the Hg isotopes. In his calculations Engel considered the negative-parity states in ^{190,192,194,196}Pt in terms of an O(6) core coupled to an f-boson. The resultant Hamiltonian was that of the standard O(6) limit of the IBM-1 with two additional terms ϵn_f and $\varepsilon Q^f.Q^{sd}$. The latter describes the interaction of f-bosons with s- and d-bosons and n_f is the number of f bosons. The parameters ϵ and ε, which determine the negative-parity level structure, were set to give agreement with the known excitation energy of the 3_1^- state of ^{194}Pt. This results in the interesting prediction of the existence of two other collective 3^- states in each nucleus at $\sim$ 2.1 and 2.3 MeV. The general expression for the E3 transition operator is (Sc78)

$$T_k^{E3} = \alpha_3(f^\dagger s + s^\dagger \tilde{f})_k^3 + \beta_3(f^\dagger d + d^\dagger \tilde{f})_k^3. \qquad (5.1)$$

which can be compared with the form of the E2 transition operator T^{E2} in the IBM [equation (4.3)].[1] Engel assumed that the second term is negligible, presumably in analogy to the O(6) form of T^{E2}. The parameter α_3 is subject to an arbitrary normalization (En88). Engel predicted that the two higher 3^- states will have E3 transition strengths which are comparable to, and in some cases larger than, the lowest 3^- state, as shown in fig. 5.2. Engel's predicted excitation energies agree with experiment only for negative-parity

[1] It should be noted that, apart from equation (5.1), the symbol β_3 will be used in this thesis to denote the octupole deformation parameter.

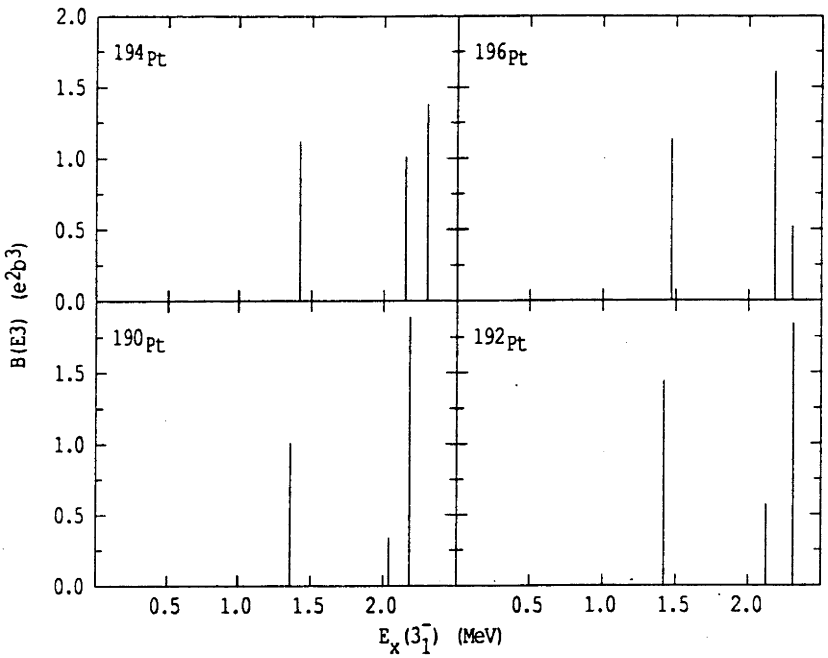

Figure 5.2: Excitation energies and relative E3 transition strengths to ground of the collective 3^- states in ^{190,192,194,196}Pt as predicted by the O(6) limit of the IBM-1 (En86).

states with $J \leq 4$.

The semi-decoupled model is the only RAL model to have been applied to 3^- states in the stable even-mass Pt and Hg nuclei. It was originally used by Neergård *et al.* (Ne75) to describe the Hg nuclei and later extended by Toki *et al.* (To77) to describe the Pt nuclei as well, while allowing for non-axial symmetry. This model has three basic features :

(a) the states are linear combinations of two quasi-particle states of a rotating deformed nucleus; one of the quasi-particle states has low angular momentum and the other has a relatively high angular momentum,

(b) the high-spin quasi-particle is partially decoupled from the core by the Coriolis force, resulting in a band which has minimum energy when its angular momentum is approximately equal to that of the high-spin quasi-particle, and

(c) the decoupled band has the spin sequence $\Delta J = 1$ but appears to have $\Delta J = 2$ because a short-range residual interaction raises the energy of the even-spin members significantly.

Both sets of semi-decoupled calculations produce values of $E_x(3_1^-)$ for the mercury isotopes which are lower than experimentally observed; the difference is $\sim$ 1 MeV for the

Table 5.1: Excitation energies in MeV of the first 3^- state, $E_x(3_1^-)$, of the stable even-mass Pt and Hg isotopes as determined from experiment (Sp89) and the semi-decoupled model calculations of Neergård *et al.* (Ne75) and Toki *et al.* (To77).

Isotope	Experiment	Ne75	To77
^{192}Pt	1.378		1.38
^{194}Pt	1.433		1.36
^{196}Pt	1.447		1.43
^{198}Pt	1.681		
^{198}Hg	2.486	1.94	1.60
^{200}Hg	2.609	2.28	1.77
^{202}Hg	2.709		
^{204}Hg	2.679		

calculations of Toki *et al.* and 300 to 500 keV for Neergård *et al.* (cf. table 5.1). Unfortunately, of the stable even-mass Hg isotopes, only ^{198}Hg and ^{200}Hg are considered in both sets of calculations. Toki's predictions of $E_x(3_1^-)$ for the platinum isotopes are in good agreement with experiment.

5.2.2 Interpretations of the $E_x(3_1^-)$ Discontinuity

Several explanations have been proposed for the observed discontinuity in $E_x(3_1^-)$ between ^{198}Pt and ^{198}Hg. These explanations fall into two categories : those which postulate a difference in the nature of 3_1^- states in the two elements and those which assert that 3_1^- states in both Pt and Hg are collective vibrational states like their counterparts in the Pb nuclei. The former position was taken by Yates and collaborators (Fi81, Ya83, Kh84, Ya88) who proposed that the 3_1^- states in the Pt nuclei are better described by the semi-decoupled model calculations of Toki *et al.* (To77) while the 3_2^- states are of the same collective octupole character as the 3_1^- states of the Hg and Pb nuclei. The

alternative view was taken by Cottle *et al.* (Co88a, Co88b) who suggested two different reasons for the discontinuity : first, that a sudden change in the single-particle excitation energies may occur; and, second, that the collective octupole strength is divided among several 3^- states, i.e. there is fragmentation of the octupole strength. They asserted that the relatively large E3 transition strengths for the 3_1^- states in Pt nuclei point to a collective octupole behaviour and noted the similarity of these strengths to that which they derived for ^{204}Hg from the sole measurement of octupole deformation in Hg prior to the present work (Ba81).

Evaluation of the above suggestions has been hampered by a lack of model-independent data which can be used, firstly, to confirm the proposed 3^- spin assignments of the strongly excited states seen at about 2.6 MeV in the Hg nuclei by Baxter *et al.* in an inelastic alpha scattering experiment, secondly, to investigate the presence (or absence) of other 3^- states in Pt or Hg, especially at the energies proposed by Cottle *et al.* for Pt and by Toki *et al.* for Hg, and, thirdly, to determine the extent of collectivity of the 3_1^- state in Pt relative to that in Hg and Pb by comparing the E3 transition strengths for the different nuclei in this region.

5.3 Summary of Prior Experimental Work on 3^- States in the Pt-Hg Region

It is clear from the preceding discussion that measurements of the E3 transition strengths for the 3_1^- states of the Pt and Hg isotopes are essential to elucidating the nature of those states. Before the present work was commenced, there had been no published model-independent measurements of $B(E3;0_1^+ \rightarrow 3_1^-)$ for any of the Hg isotopes or for ^{196,198}Pt, although some model-dependent measurements of $B(E3;0_1^+ \rightarrow 3_1^-)$ had been made for ^{196,198}Pt (Bo88, Co88a) and a value for the octupole deformation parameter, β_3, of 0.073 had been obtained for ^{204}Hg by Baxter *et al.* (Ba81) from angular distributions of inelastic alpha scattering above the Coulomb barrier. (As noted previously, the symbol β_3 will be used to denote the octupole deformation parameter rather than the parameter for the E3 transition operator in the IBM [cf. equation (5.1)].) The measured value of

β_3 corresponds to an E3 transition strength $|\mathcal{M}(E3)|^2$ of 14 Weisskopf units (W.u.) if one uses the conversion formula (Be69)

$$B(E3;0_1^+ \rightarrow 3_1^-)\ [\mathrm{e^2fm^6}] = (3\mathrm{ZR}_0^3\beta_3/4\pi)^2 \tag{5.2}$$

where a uniform mass distribution of radius $R_0=1.2A^{1/3}$fm is assumed for the nuclear potential. The quantity $|\mathcal{M}(E3)|^2$ is defined as (Al78)

$$|\mathcal{M}(E3)|^2 = \frac{B(E3;3^- \rightarrow 0_1^+)}{B_W(E3)} \tag{5.3}$$

where $B(E3;3^- \rightarrow 0_1^+)$ is the reduced transition probability for deexcitation and B_W is the single-particle strength given by

$$B_W(E3) = \frac{1}{16\pi}(1.2A^{1/3})^6\ \mathrm{e^2fm^6}\ . \tag{5.4}$$

This reduces to the form

$$|\mathcal{M}(E3)|^2 = 2.4\mathrm{B}(\mathrm{E3};0_1^+ \rightarrow 3_1^-)\ A^{-2} \tag{5.5}$$

where $B(E3;0_1^+ \rightarrow 3_1^-)$ is in $\mathrm{e^2fm^6}$ and $|\mathcal{M}(E3)|^2$ is in W.u. However, it has been argued by Spear (Sp89), from comparison of model-independent $B(E3;0_1^+ \rightarrow 3_1^-)$ measurements with those derived from β_3 values, that an empirical factor of 1.51 with an uncertainty of 50% in the final B(E3) value thus obtained should be applied when using values for β_3 derived from inelastic alpha scattering, corresponding to an E3 transition strength of 21(10) W.u. in the case of ^{204}Hg.

Values of $B(E3;0_1^+ \rightarrow 3_1^-)$ for ^{192,194}Pt have been measured using Coulomb excitation with ^{4}He projectiles by Ronningen *et al.* (Ro77). They obtained E3 transition strengths to the ground state of 10 W.u. for both isotopes. The value of $B(E3;0_1^+ \rightarrow 3_1^-)$ for ^{194}Pt has also been determined by Baktash *et al.* (Ba78) using Coulomb excitation and found to be 7.1(6) W.u. All published $B(E3;0_1^+ \rightarrow 3_1^-)$ values for the two heaviest Pt isotopes (^{196}Pt and ^{198}Pt) prior to those determined in this thesis have been measured using

model-dependent analyses - firstly by Boeglin *et al.* (Bo88) for ^{194,196}Pt using electron scattering and more recently by Cottle *et al.* (Co88a) for ^{194,196,198}Pt using DWBA fits to (p,p′) data of Deason *et al.* (De81). Their results for ^{194}Pt were consistent with those of Ro77 and Ba78.

$B(E3;0_1^+ \rightarrow 3_1^-)$ values for the stable even-A Pb nuclei are well-known to be in the range 34-38 W.u. These values have been determined by Spear *et al.* (Sp83, Sp78) using Coulomb excitation. On the lower Z side of the Pt and Hg nuclei are the Os nuclei. The only published study of E3 transition strengths in these nuclei is the electron scattering experiment of Boeglin *et al.* (Bo88), in which they find that $B(E3;0_1^+ \rightarrow 3_1^-)$ values for the Os nuclei are very similar to those of the Pt nuclei, namely, 8.5-10.3 W.u. for the Os nuclei, as compared with 5.2-11.1 W.u. for the Pt nuclei.

Model-independent measurements of $B(E3;0_1^+ \rightarrow 3_1^-)$ for the heavier Pt isotopes and the Hg isotopes are fundamental to the understanding of octupole phenomena in this region, in particular the $E_x(3_1^-)$ discontinuity at A=198; one technique for making such measurements is Coulomb excitation. This method is especially suitable as it preferentially selects collective quadrupole and octupole excitation (Cl86).

5.4 Experimental Procedures

5.4.1 Pt Measurements

The particle singles spectroscopy technique (§ 3.3.1) was used to study ^{194,196,198}Pt. Beams of ^{4}He, ^{7}Li and ^{12}C projectiles, at a range of bombarding energies, were backscattered from ^{194}Pt and ^{196}Pt and detected with an annular silicon surface-barrier detector; the data obtained are the same as those discussed in § 4.5. In addition, data taken for ^{198}Pt in another experiment (Gy86) were re-analysed. This data consisted of a spectrum taken with an annular silicon surface-barrier detector for scattered ^{4}He projectiles with an initial bombarding energy of 15.6 MeV. The thicknesses of these targets, as determined by Rutherford scattering, and isotopic compositions of the target material are given in table 5.2. The bombarding energies and scattering angles employed are listed in table 5.3.

Table 5.2: Percentage isotopic composition of Pt target material, as provided by supplier (Oak Ridge National Laboratory) and target thicknesses as measured by Rutherford scattering.

	Target		
Isotope	^{194}Pt	^{196}Pt	^{198}Pt
192	0.04 ± 0.01	–	0.01 ± 0.01
194	95.06 ± 0.15	0.78 ± 0.02	0.79 ± 0.01
195	3.78 ± 0.10	2.39 ± 0.05	1.18 ± 0.01
196	0.97 ± 0.05	96.54 ± 0.10	2.18 ± 0.02
198	0.15 ± 0.02	0.29 ± 0.02	94.85 ± 0.05

Projectile	Thickness (μg cm^{-2})		
^{4}He	20–25	69,89	15
^{7}Li	–	51	–
^{12}C	2–3	1,6	–

Table 5.3: Experimental details and measured excitation probabilities P_{exp} for ^{194,196,198}Pt.

Projectile	Target	E_p [a] (MeV)	θ_{lab} [b]	s [c] (fm)	$P_{exp}(3_1^-)$ ($\times 10^{-4}$)
^{4}He	^{194}Pt	14.0	174.8°	7.18	0.47(9)
		14.8		6.29	0.48(8)
		15.0		6.09	0.72(13)
		15.4		5.69	0.50(17)
		15.6		5.50	0.84(8)
		15.8		5.31	1.06(13)
		16.0		5.13	1.12(7)
		14.4	171.3°	6.74	0.35(3)
		14.6		6.52	0.42(4)
		15.2	169.9°	5.91	0.62(7)
^{4}He	^{196}Pt	14.2	168.7°	6.95	0.32(5)
		15.8		5.31	0.68(8)
		15.0	174.8°	6.06	0.398(17)
		15.2		5.86	0.45(3)
		15.4		5.66	0.60(3)
		15.8		5.28	0.71(6)
^{4}He	^{198}Pt	15.6	174.8°	5.44	0.32(7)

Table 5.3 (cont.)

Projectile	Target	E_p[a] (MeV)	θ_{lab}[b]	s[c] (fm)	$P_{exp}(3_1^-)$ ($\times 10^{-4}$)
^{7}Li	^{196}Pt	22.5	164.0°	5.94	0.87(16)
			168.7°	5.91	0.81(6)
			169.9°	5.90	0.79(12)
^{12}C	^{194}Pt	42.0	171.3°	6.98	3.0(6)
		43.0		6.58	4.2(4)
		44.0	175.0°	6.19	6.6(1.1)
		44.0	169.9°	6.21	4.6(8)
		45.0		5.85	5.9(4)
		46.0		5.50	4.8(5)
^{12}C	^{196}Pt	42.0	171.3°	6.98	3.0(6)
		43.0		6.55	2.5(3)
		44.0	170.0°	6.17	3.14(15)
		45.0		5.81	3.67(19)
		46.0		5.47	3.6(3)
		44.0	175.0°	6.15	3.0(5)

[a]) bombarding energy
[b]) mean scattering angle in the laboratory system
[c]) distance of closest approach of the nuclear surfaces

5.4.2 Hg Measurements

As the probability of excitation for a state decreases with increasing excitation energy, the excitation cross-sections of the 3_1^- states in Hg were expected to be far lower than those in Pt. This rendered the use of ^{4}He projectiles impractical due to the long running times that would have been necessary. Instead, scattered ^{12}C projectiles were detected at a mean laboratory angle of 90° using a gas-filled proportional counter in the focal plane of an Enge split-pole magnetic spectrometer. Two bombarding energies were used for each isotope with the exception of ^{198}Hg; these energies and the corresponding separation of nuclear surfaces are given in table 5.4.

Mercury targets are difficult to produce and must be handled with the greatest care. The targets were made using the method described in Es77a. Enriched isotopes were obtained in the form of HgO (isotopic compositions in table 5.5). The oxide was dissolved in HCl, and then H_2S was bubbled through the solution, thus precipitating β-HgS. After washing in distilled water and alcohol, the precipitate was dried under an infra-red lamp and evaporated onto a layer of carbon. The partial thickness of the Hg was between 1 and 7 μg cm^{-2} as measured by elastic scattering at 15° and 90°; the thickness of each target is given in table 5.5. Each of the targets had a carbon flash of $\sim$ 1 μg cm^{-2} evaporated onto the HgS layer to reduce deterioration under bombardment.

The acceptance angles of the spectrometer, which were determined by a set of horizontal and vertical slits, are also listed in table 5.4. The detector (Op78) was a doubly-gridded gas ionization counter with three resistive wires and two anodes, as shown in fig. 5.3. The detector was oriented at an angle of 45° to the beam direction rather than at 90° as done in the ^{192}Os experiment (§ 3.3.1). The detector was filled with isobutane at pressures between 180 and 200 Torr. The following signals were collected : (a) total energy (E), (b) energy losses (ΔE1, ΔE2), (c) position at wire 1 along the focal plane (P1), (d) position at wire 2 (P2), and (e) veto signal at wire 3, where very few counts were recorded. The angle of entry is obtained from the difference of P1 and P2. The total energy E and energy losses ΔE1 and ΔE2 were corrected for variation of entrance angle using this difference.

Table 5.4: Experimental details and measured excitation probabilities for the Hg isotopes; the mean scattering angle in the laboratory system was 90° for all measurements.

Target	E_p[a] (MeV)	s[b] (fm)	Aperture[c]	$P_{exp}(2_1^+)$ ($\times 10^{-2}$)	$P_{exp}(2_2^+)$ ($\times 10^{-3}$)	$P_{exp}(4_1^+)$ ($\times 10^{-4}$)	$P_{exp}(3_1^-)$ ($\times 10^{-4}$)
^{198}Hg	54	5.57	4.5° × 2.5°	5.5(4)	–	7.7(2.6)	6.1(17)
^{200}Hg	54	5.54	4.5° × 2.5°	5.0(6)	5.0(1.0)	4.6(19)	5.0(5)
^{200}Hg	55	5.26	4.5° × 2.5°	5.55(12)	4.6(1.0)	7.4(1.3)	6.2(9)
^{202}Hg	54	5.51	4.5° × 2.5°	3.60(13)	2.2(4.1)	4.0(6)	4.7(5)
^{202}Hg	55	5.23	4.5° × 2.5°	3.84(6)	1.8(2.3)	3.4(1.9)	5.3(4)
^{204}Hg	54	5.48	6.0° × 2.5°	2.96(6)	3.9(7)	1.7(4)	4.5(7)
^{204}Hg	55	5.20	6.0° × 2.5°	3.14(7)	2.8(5)	1.9(4)	5.3(7)

[a]) ^{12}C bombarding energy
[b]) distance of closest approach of the nuclear surfaces
[c]) horizontal × vertical aperture settings on entry to Enge spectrometer

Table 5.5: Percentage isotopic composition of Hg target material, as provided by supplier (Oak Ridge National Laboratory) and target thicknesses as measured by Rutherford scattering.

	Target			
Isotope	^{198}Hg	^{200}Hg	^{202}Hg	^{204}Hg
198	92.69 ± 0.10	1.2 ± 0.05	0.06 ± 0.02	0.28 ± 0.05
199	5.18 ± 0.05	2.85 ± 0.05	0.17 ± 0.02	0.56 ± 0.05
200	1.10 ± 0.03	88.92 ± 0.05	0.53 ± 0.05	0.90 ± 0.05
201	0.40 ± 0.03	2.51 ± 0.05	1.38 ± 0.05	0.76 ± 0.05
202	0.54 ± 0.03	3.76 ± 0.05	97.58 ± 0.05	4.85 ± 0.10
204	0.09 ± 0.03	0.76 ± 0.05	0.28 ± 0.05	92.64 ± 0.10
Thickness (μg cm^{-2})	1.5(3)	4.1(8)	4.0(8)	6.7(13)

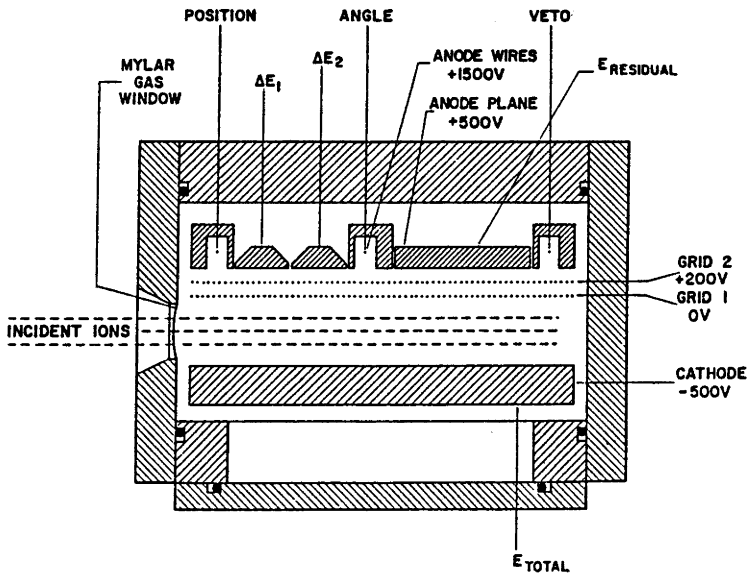

Figure 5.3: Focal plane detector used in conjunction with the Enge mass spectrometer (Op78).

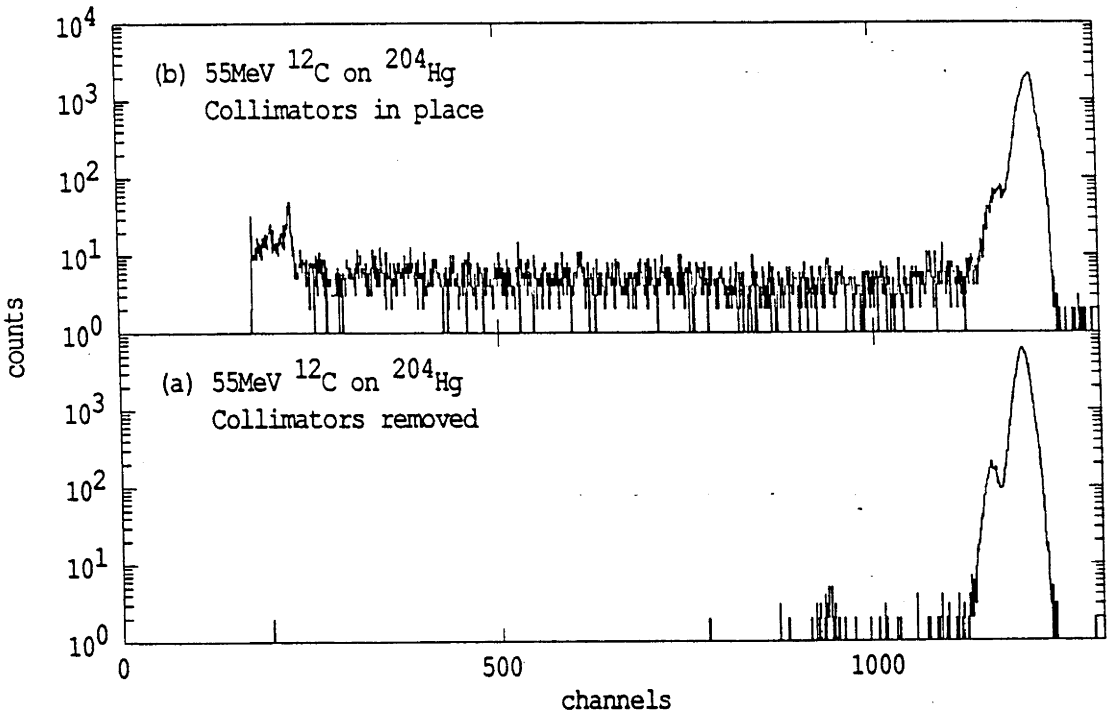

Figure 5.4: Spectra taken with ^{12}C beam on a ^{204}Hg target using an Enge spectrometer (a)with and (b)without collimators in place.

A series of four variable collimators lies upstream of the target chamber of the Enge spectrometer (cf. fig. 3.3). In this experiment it was found that scattering from these collimators resulted in an unacceptably high background so they were inserted while the beam was being focussed and removed before data collection began. Fig. 5.4 shows the effect of removing the collimators on the background levels in the Pt spectrum. Removal of collimators meant that beam stability was of the utmost importance. To ensure that the beam did not move by a significant amount over a long period of time, data collection was periodically halted while the collimators were replaced and the focussing of the beam checked. The target was oriented at an angle of 45° to the incident beams so that scattered ions entering the detector were scattered from the HgS layer without passing through the carbon backings. In order to monitor the condition of the target during the experiment, the count rate of the Hg elastic peak was checked at regular intervals. Significant reduction of the count rate was taken to indicate target degradation and the target was moved so that the beam hit a new position.

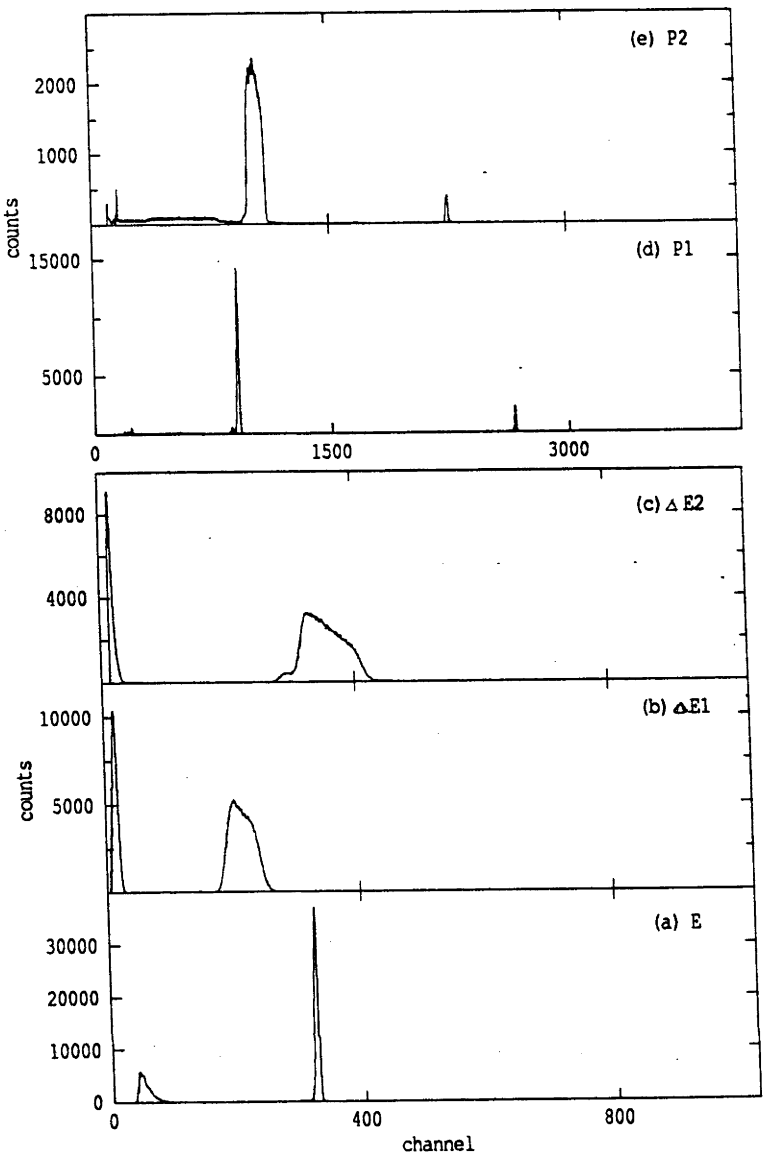

Figure 5.5: Representative spectra taken with ^{12}C beam on a ^{200}Hg target showing each parameter of the focal plane detector of the Enge spectrometer (E, ΔE1, ΔE2, P1, P2).

5.5 Analysis and Results

5.5.1 Sorting and Fitting

Analysis of the Pt data was carried out using the procedures described in § 3.3.1 for data obtained with a surface-barrier detector. Analysis of the Hg data was a little more complex. As mentioned in the previous section, six parameters (E, ΔE1, ΔE2, P1, P2, veto) were recorded in event-by-event mode. Typical spectra for each of these is shown in fig. 5.5, with the exception of the veto signal, for which virtually no counts were recorded. By placing a gate on the Hg peak in the E spectrum, most of the background

in the P1 spectrum was removed (cf. fig. 5.6). Similarly, gates were also set using the ΔE spectrum. The peaks from Hg can be seen clearly in the final sorted P1 spectrum (fig. 5.6), which was then fitted using the same procedures and lineshape as for the Pt data. Allowances did not have to be made for variation of peak width in this experiment (cf. § 3.3.1) due to the 45° orientation of the Enge detector and the relatively poor statistics of the spectra. Charge state fractionation was treated as described in § 3.3.1.

Peaks in each spectrum were identified firstly by an overall energy calibration, obtained by noting the position of the elastic peak at a range of bombarding energies, and, secondly, by an internal calibration, in which the positions of the 0_1^+ and 2_1^+ peaks in a spectrum were used to deduce the energies of other peaks in that spectrum. This is of especial importance in the Hg spectra, where the values of $E_x(3_1^-)$ proposed by Baxter *et al.* had not been confirmed previously.

A typical spectrum for each target is shown in fig. 5.6. The peaks were fitted with the usual lineshape (§ 3.3.1). In the case of the Hg spectra, it was necessary to use the fitted widths to determine the channel limits of peaks having poorer statistics, corresponding to scattering by target nuclei which have been excited to a state higher in excitation energy than the 2_1^+ state. Excitation probabilities $P_{exp}(J_n^\pi)$ were determined from the peak areas. Values of $P_{exp}(3_1^-)$ for ^{194,196,198}Pt are given in table 5.3. Excitation probabilities for the 2_1^+, 4_1^+ and 3_1^- states in ^{198,200,202,204}Hg were obtained; excitation probabilities were also measured for the 2_2^+ states in ^{200,202,204}Hg. The results for the Hg data are listed in table 5.4. Values measured for the positive-parity states were less precise than, but consistent with, previous measurements, with the exception of the 2_2^+ state in ^{204}Hg for which no B(E2) values have yet been published.

The spectra shown in fig. 5.6 are of differing quality. A larger horizontal acceptance angle was used to collect the ^{204}Hg data in an attempt to increase detection efficiency; unfortunately, this resulted in significantly poorer resolution and an asymmetric peak shape due to variation of the gain at the extremities of the aperture. The use of ray-tracing techniques to correct the peak shape was attempted : this was performed by manually correcting the data so that the centroids of the 0_1^+ and 2_1^+ peaks in the P1 spectrum were moved to the positions obtained at the centre of the aperture. Although

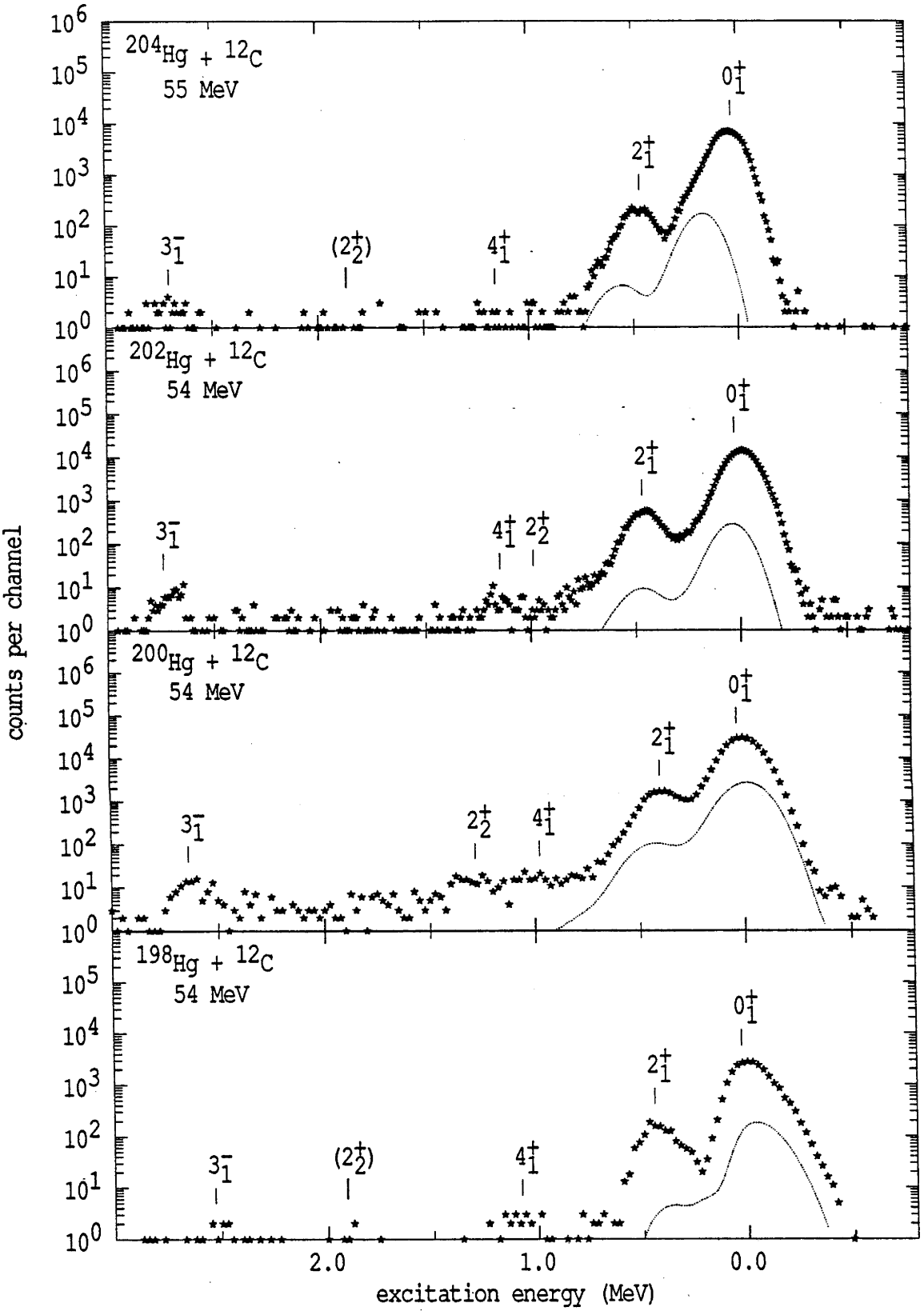

Figure 5.6: Representative spectra for the Hg isotopes, labelled as for figs. 4.6 and 4.11. Positions of the adopted excitation energies are marked.

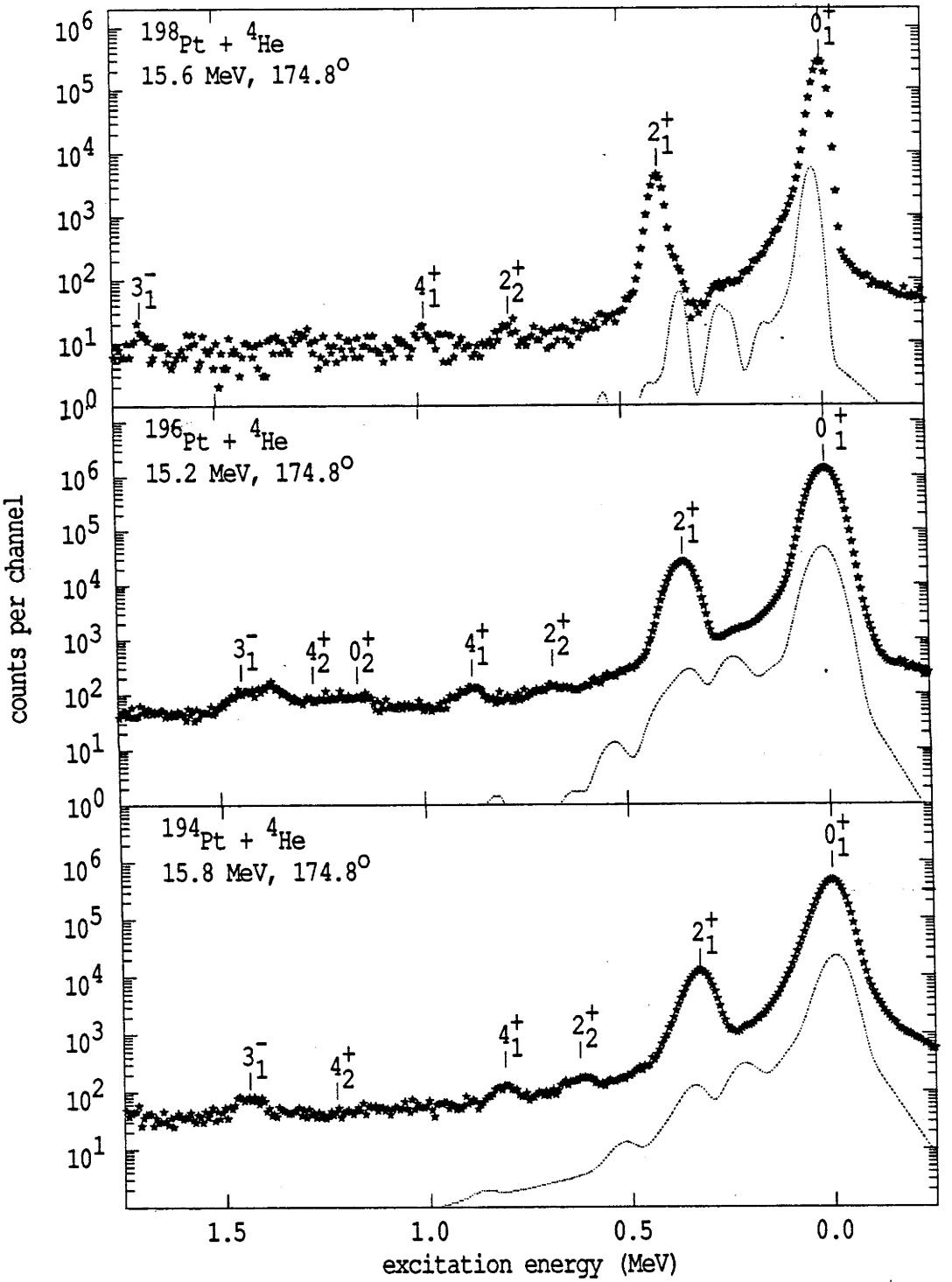

Figure 5.6: Representative spectra for the Pt isotopes, labelled as for figs. 4.6 and 4.11. Positions of the adopted excitation energies are marked.

these corrections produced some visual improvement, they were rejected as the possibility of distorting the results could not be excluded. In the case of ^{198}Hg, the focal plane position signal was digitised using a factor of two smaller conversion gain and collected with a multichannel analyser, as the computer system was unavailable at the time. Hardware gating was employed to reduce low-energy noise due to projectiles which had been scattered from ^{12}C and other light nuclei present in the target.

Contributions from isotopes of the target nucleus other than the one of interest were calculated using the supplier's assay and matrix elements obtained from the literature (cf. § 3.3.1). The matrix elements used for the Pt isotopes are given in tables 4.5, 4.7 and 4.15; those used for analysis of the Hg targets are listed in table 5.6. These contributions are shown in fig. 5.6 by the dotted lines. Checks for contributions from other elements were carried out for ^{194,196}Pt by bombarding the target with 8.0 and 10.5 MeV ^{4}He and 12.0 MeV ^{12}C. The presence of nuclei with A = 85-89 and 165-173 would have affected the values of $P_{exp}(3_1^-)$ obtained for ^{194}Pt; significant amounts of nuclei with A=85-89, 128-134 and 166-174 would have affected the results for $P_{exp}(3_1^-)$ for ^{196}Pt. The upper limits on these contaminants were ascertained to be 3% and 5% of the intensity of the 3_1^- peak of ^{194}Pt and ^{196}Pt respectively and are clearly smaller than the 10% statistical uncertainty typically obtained for $P_{exp}(3_1^-)$ for these nuclei. The measured value of $P_{exp}(3_1^-)$ for ^{198}Pt would have been affected by the presence of contaminants of mass 78-82 in the target at a level which was comparable to the 20% statistical uncertainty obtained; however, an upper limit of 10% could be set for these contaminants. In the case of ^{198}Hg, a significant amount of ^{208}Pb was present in the target. As the 3_1^- peak for ^{208}Pb [$E_x(3_1^-)$ = 2.6 MeV] could not be easily resolved from the 3_1^- peak for ^{198}Hg, the position and intensity of the ^{208}Pb peak was calculated using published values for $B(E3;0_1^+ \rightarrow 3_1^-)$ (Sp89) so that the resultant correction (of the order of 2% of $P_{exp}(3_1^-)$) could be applied. Elastic scattering from nuclei with A=138-141 would have affected the measurements of $P_{exp}(3_1^-)$ for all the Hg targets. Upper limits on these nuclei were found to be no more than 25% of $P_{exp}(3_1^-)$; if any contaminant were present at a level greater than this, it would have been clearly visible in at least one of the spectra taken for each target.

Table 5.6: Magnitudes of E2 matrix elements, $< J_f^\pi \| \mathcal{M}(E2) \| J_i^\pi >$ (in e b), for the Hg isotopes.

J_i^π	J_f^π	^{198}Hg[a])	^{200}Hg[b])	^{202}Hg[c])	^{204}Hg[d])
0_1^+	2_1^+	0.992	0.924	0.778	0.650
2_1^+	2_1^+[e])	1.08	1.41	1.33	0.53
2_1^+	4_1^+	1.64	1.54	1.31	1.05
0_1^+	2_2^+	0.117	0.089	0.059	
2_1^+	2_2^+	0.59	0.274	0.424	

J_i^π	J_f^π	^{199}Hg[f])	J_i^π	J_f^π	^{201}Hg[g])
$1/2_1^-$	$5/2_1^-$	0.851	$3/2_1^-$	$5/2_1^-$	0.529
$1/2_1^-$	$3/2_1^-$	0.69	$3/2_1^-$	$3/2_2^-$	0.75
$1/2_1^-$	$3/2_2^-$	0.57	$3/2_1^-$	$1/2_1^-$	0.26
$1/2_1^-$	$5/2_2^-$	0.44	$3/2_1^-$	$5/2_2^-$	0.58
			$3/2_1^-$	$7/2_1^-$	0.78
			$3/2_1^-$	$5/2_3^-$	0.91
			$3/2_1^-$	$3/2_3^-$	0.37

[a]) Es77, Au83
[b]) Sp80, Sc87b
[c]) Sp80, Es81, Sc87
[d]) Es81, Sc87a
[e]) assumes destructive interference for 2_2^+ state
[f]) Sc88
[g]) Sc86

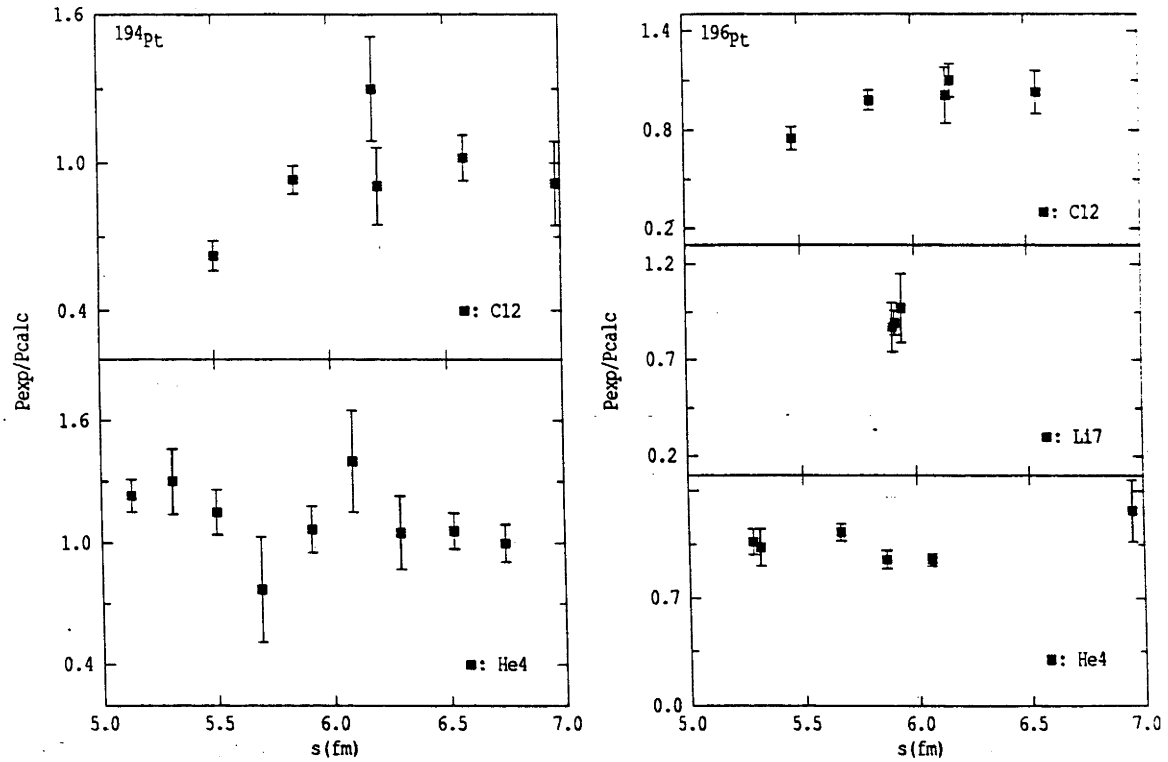

Figure 5.7: Safe-energy plots for ^{194}Pt and ^{196}Pt.

The identification of lower-lying 3^- states in the Hg isotopes would be of theoretical significance. The semi-decoupled calculations of Toki *et al.* predict that the 3_1^- state should lie at $E_x \sim 1.8$MeV for ^{198,200}Hg. The limits on E3 transition strength for any 3^- state with excitation energy in the range 1.6-2.0 MeV were determined to be less than 5.5 W.u. for ^{198}Hg and less than 2.5 W.u. for ^{200,202,204}Hg. The importance of these limits is explained later.

5.5.2 Safe Bombarding Energies

As stressed in earlier chapters, it is essential that the data used to obtain $B(E3;0_1^+ \rightarrow 3_1^-)$ values should be free from significant Coulomb-nuclear interference. The safe-energy plots for ^{194}Pt and ^{196}Pt are shown in fig. 5.7. In the case of the Hg nuclei, it was necessary to compromise between the number of bombarding energies employed for each target and the statistical accuracy of the data at each energy due to the low count rates involved.

Hence, data were taken only at one or two bombarding energies rather than at a range of energies. More stringent checks were considered unnecessary, provided a reasonably large nuclear separation was maintained, because the relatively large statistical uncertainty in $P_{exp}(3_1^-)$, typically of the order of 10%, would obscure any Coulomb-nuclear interference. The measurements of $P_{exp}(2_1^+)$ for ^{194,196}Pt described in chapter 4, and earlier measurements of $P_{exp}(2_1^+)$ for ^{198}Pt (Gy86) and ^{198,200,202,204}Hg (Es77, Sp80, Es81) indicate that nuclear effects are not significant at the distances used (> 5 fm). Whilst this is not proof that these distances are 'safe' for measurements of $P_{exp}(3_1^-)$, it is consistent with the assumption that Coulomb-nuclear interference is negligible. Furthermore, the values of B(E3;$0_1^+ \rightarrow 3_1^-$) deduced for each isotope for the different experimental configurations agree with each other, thus providing additional support for this assumption.

5.5.3 Results

The Winther-de Boer code (Wi66) was used to deduce values for B(E3;$0_1^+ \rightarrow 3_1^-$) from the excitation probabilities. For ^{194}Pt and ^{196}Pt, matrix elements involving transitions between the positive-parity states were taken from results presented in tables 4.7 and 4.15. Matrix elements involving the positive-parity states in ^{198}Pt and the Hg isotopes were taken from the literature (Au83, Gy86, Sc86, Sc87, Sc87a, Sc87b, Sc88) as the excitation probabilities measured in the present work were less precise than the published values. In general, the matrix elements involving the higher positive-parity states (i.e. above the 2_1^+ state) had little effect on the predicted excitation probability for the 3_1^- state. The magnitude of $< 2_1^+ \| \mathcal{M}(E1) \| 3_1^- >$ was assumed to be 0.0(1) e $b^{1/2}$ for all nuclei as the only experimental value for an E1 matrix element for an even-even nucleus in this region was deduced to be 0.0075 e $b^{1/2}$ (Jo78) from a lifetime measurement (Hä72) for ^{206}Pb. The conservative estimate of the uncertainty in this matrix element contributed less than 1% to the total uncertainty.

The values deduced for B(E3;$0_1^+ \rightarrow 3_1^-$) of ^{194,196,198}Pt and ^{198,200,202,204}Hg are listed in table 5.7, together with the equivalent E3 transition strengths, denoted by $|\mathcal{M}(E3)|^2$.

Table 5.7: Values of $B(E3;0_1^+ \rightarrow 3_1^-)$ in e^2b^3 as measured by Coulomb excitation for $^{192,194,196,198}Pt$, $^{198,200,202,204}Hg$ and $^{204,206,208}Pb$. The values in square brackets denote the corresponding E3 transition strengths, $|\mathcal{M}(E3)|^2$, in W.u. Unless otherwise indicated, values are from the present work.

N	Z=78 (Pt)	Z=80 (Hg)	Z=82 (Pb)
114	0.173(31)[a]) [11.1(2.0)]		
116	0.125(8) [8.0(5)]		
118	0.102(4) [6.38(25)]	0.44(14) [27(9)]	
120	0.084(18) [5.2(1.1)]	0.41(4) [25(2)]	
122		0.42(4) [25(3)]	0.66(4)[b]) [38.1(2.3)]
124		0.37(5) [22(3)]	0.65(4)[b]) [36.8(2.3)]
126			0.611(9)[c]) [34.0(5)]

[a]) Ro77
[b]) Sp78
[c]) Sp83

5.5.4 Corrections and Uncertainties

The effect of virtual excitation of the GDR was simulated by including a 1^- state at 14.0 MeV in the calculation of $P_{exp}(3_1^-)$ with the Winther-de Boer program. This state was assumed to be connected to the ground state by an E1 transition strength of 10 W.u. and to the 3_1^- state by an E2 transition strength of 0.1 W.u. Inclusion of the 14.0 MeV state was found to have a negligible effect on the values of $B(E3;0_1^+ \rightarrow 3_1^-)$ obtained. An additional correction was also made in the case of the Hg spectra for the variation of excitation probability across the angular acceptance of the spectrometer, as the angular dependence of the cross-section is quite large at 90°; hence, the values of P_{calc} used in the analysis of the Hg data were weighted according to the Rutherford angular distribution.

The primary sources of uncertainty in the values of $B(E3;0_1^+ \rightarrow 3_1^-)$ obtained are statistics and lineshape analysis. Uncertainties in matrix element values assumed in the analysis were insignificant, as were uncertainties in the beam energy and mean laboratory angle (±0.05% and ±0.1° respectively).

5.5.5 Comparison with Prior Experimental Work

Prior to the present work, 3^- states had been only observed in the stable even-mass Hg isotopes by Baxter *et al.* (Ba81) and possibly in ^{204}Hg by Gatenby *et al.* (Ga89). From their inelastic alpha scattering data, Baxter *et al.* proposed that the lowest 3^- states which are strongly coupled to the ground state lie at excitation energies of around 2.6 MeV. They also measured β_3 to be 0.073 for ^{204}Hg, a value which has been interpreted to be equivalent to an E3 transition strength of 14 W.u. by Cottle *et al.* (Co88a) and 21(10) W.u. by Spear (Sp89). Gatenby *et al.* observed a state in ^{204}Hg at 2.675 MeV with behaviour consistent with a 3^- assignment. Fig. 5.6 shows that clear peaks were present in the Hg spectra with excitation energies consistent with those proposed by Baxter *et al.* (Ba81) for the 3_1^- states, viz, 2.674 MeV for ^{204}Hg, 2.709 MeV for ^{202}Hg, 2.609 MeV for ^{200}Hg and 2.486 and 2.525 MeV for ^{198}Hg. This observation supports the proposed excitation energies of Baxter *et al.* and hence the claim that a discontinuity in $E_x(3_1^-)$ exists between ^{198}Pt and ^{198}Hg. This discontinuity in $E_x(3_1^-)$ is emphasized by the more gradual mass-variation of the energies of other low-lying states, in particular the

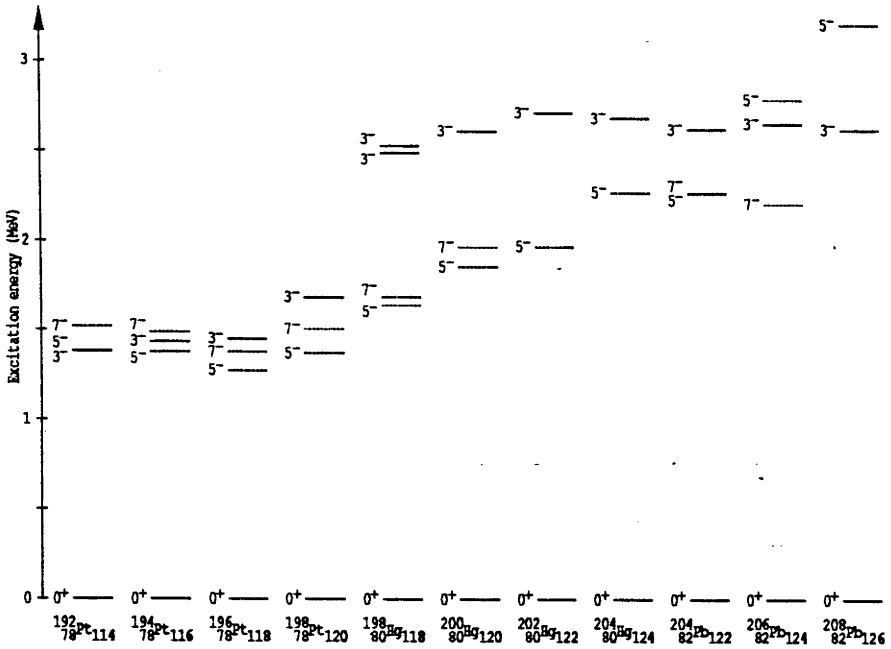

Figure 5.8: Excitation energies in keV of the 3_1^-, 5_1^- and 7_1^- states for all the stable even-A Pt, Hg and Pb isotopes up to ^{208}Pb (Ha79, We79, Au83, Sh83, Ma86, Sc87, Sc87a, Sc87b, Si89). For purposes of presentation, the 3_1^- states are emphasized.

5_1^- and 7_1^- states (fig. 5.8). It should be noted that, as the members of the 3^- 'doublet' observed by Baxter *et al.* for ^{198}Hg were not resolved in the present analysis, the E3 transition strength measured is the combined strength for the two states, assuming that they are both 3^- states. The prior values of $E_x(3_1^-)$ (Ba81) are tentatively confirmed but the data obtained for this thesis lack the resolution necessary to improve on their result. There have been no previous measurements of $B(E3;0_1^+ \rightarrow 3_1^-)$ for any of the Hg isotopes. The estimate of $\sim$ 21(10) W.u. by Spear (Sp89) for the E3 transition strength of ^{204}Hg based on the value of β_3 of Baxter *et al.* (Ba81) is confirmed in contrast to that of 14 W.u. assigned by Cottle *et al.* (Co88a). In fact, all the stable even-A Hg isotopes are found to have $|\mathcal{M}(E3)|^2$ for the 3_1^- state of about the same magnitude.

The values obtained for $B(E3;0_1^+ \rightarrow 3_1^-)$ and $|\mathcal{M}(E3)|^2$ for ^{194}Pt, ^{196}Pt and ^{198}Pt are compared with the earlier measurements of Ronningen *et al.*, Baktash *et al.*, Boeglin *et al.* and Cottle *et al.* in table 5.8. Although a variety of techniques have been used, the agreement between the various experiments is excellent; of the eleven values, only one

Table 5.8: Values of $B(E3;0_1^+ \rightarrow 3_1^-)$ (in e^2b^3) for even-mass isotopes of Pt. The numbers in square brackets give E3 transition strengths in W.u.

Authors	Procedure	^{192}Pt	^{194}Pt	^{196}Pt	^{198}Pt
Ronningen *et al.*(Ro77)	Coulomb excitation	0.17(3)	0.14(3)		
		[11.1(2.0)]	[8.9(1.9)]		
Baktash *et al.*(Ba78)	Coulomb excitation		0.111(9)		
			[7.1(6)]		
Boeglin *et al.*(Bo88)	(e,e′)		0.157(13)	0.103(18)	
			[10.0(1.0)]	[6.4(1.1)]	
Cottle *et al.*(Co88a)	(p,p′) DWBA		0.136(9)	0.099(10)	0.100(10)
			[8.7(6)]	[6.2(6)]	[6.2(6)]
Present work	Coulomb excitation		0.125(8)	0.102(4)	0.084(18)
			[8.0(5)]	[6.38(25)]	[5.2(1.1)]

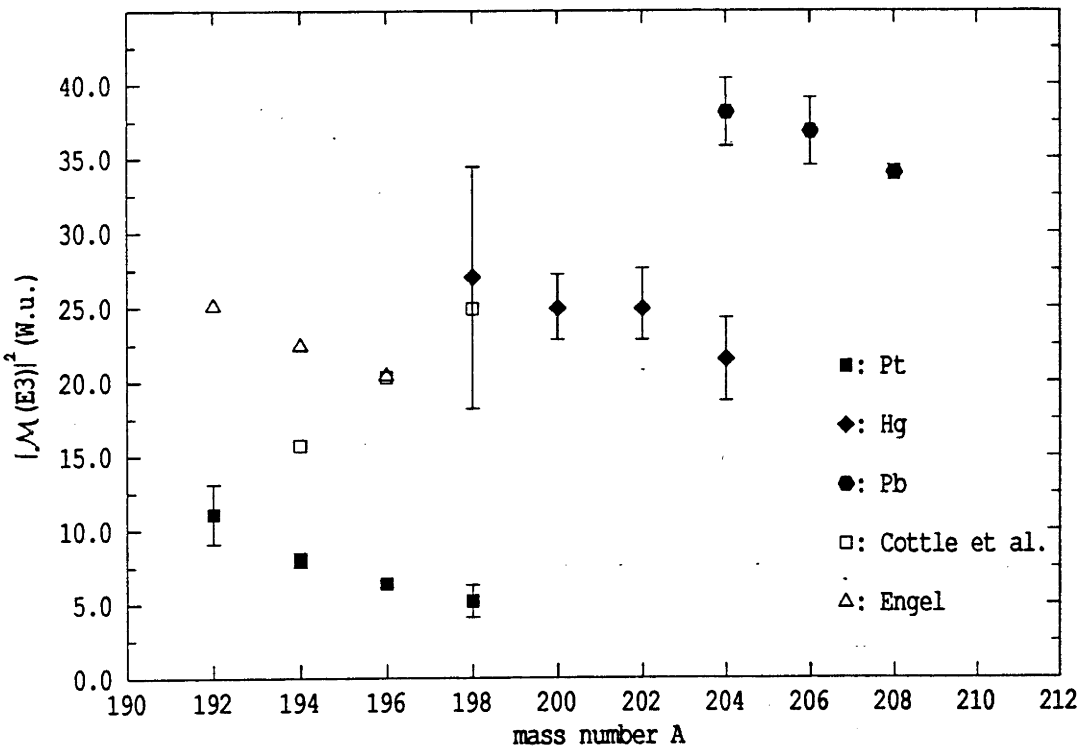

Figure 5.9: Experimental values (table 5.7) of the E3 transition strengths in W.u. for the 3_1^- states, $|\mathcal{M}(E3)|^2$, for all the stable even-mass Pt, Hg and Pb isotopes up to ^{208}Pb. The total transition strengths deduced by Cottle *et al.* (Co88b) from analysis of (p,p') data, and those calculated by Engel (En86), are also shown by open squares and open triangles, respectively.

is not within one standard deviation of the appropriate weighted mean. This confirms that the values of $|\mathcal{M}(E3)|^2$ for all the stable even-mass Pt nuclei are about 10 W.u. or slightly smaller, significantly lower than the values for the Hg nuclei, which, in turn, are about 10–15 W.u. less than $|\mathcal{M}(E3)|^2$ for the Pb isotopes.

5.6 Discussion

Measured values of $|\mathcal{M}(E3)|^2$ are plotted in fig. 5.9 as a function of mass number. A significant change in $|\mathcal{M}(E3)|^2$ is seen as Z is changed in steps of two protons from 78(Pt) to 80(Hg) and finally to 82(Pb). The new data for the Hg nuclei confute the suggestion of Cottle *et al.* (Co88a) that the Pt and Hg isotopes have similar E3 transition strengths for the first 3^- state. The large difference seen between $|\mathcal{M}(E3)|^2$ for Hg and Pb is particularly surprising, given the consistency in $E_x(3_1^-)$ for those nuclei. The observed increase in $|\mathcal{M}(E3)|^2$ with Z is dramatic when compared with the almost constant values for each set of isotopes. Only in the case of the platinum isotopes is

there any definite variation with N; the $|\mathcal{M}(E3)|^2$ values are seen to decrease as N approaches the N=126 shell closure. This insensitivity to change in N is also observed in the $|\mathcal{M}(E3)|^2$ values for the Ba isotopes (Bu85) as N increases to the N=82 shell closure. The variation with neutron number is easy to explain in terms of a simple shell-model picture. Firstly, neutrons, being electrically neutral, have much less effect than protons and, secondly, as the number of valence particles (holes) decreases to zero, the probability of intrashell excitation decreases (Bo69). However, this approach offers no explanation for the observed sharp increase of $|\mathcal{M}(E3)|^2$ with Z.

The observations noted above suggest that octupole collective behaviour in the transitional region is far more strongly affected by a variation in proton number than by a similar change in neutron number. It is interesting to compare this with the conclusion by Tanaka and Sheline (Ta77) that there is a sudden increase in the collectivity of the γ-degree of freedom as one moves from the Hg isotopes to the Au (Z=79) isotopes, and with the B(E2) measurements of Agarwal *et al.* (Ag85) which similarly reflect the reduced sensitivity of quadrupole collectivity in the Hg isotopes to change in neutron number.

The apparent disparity between the E3 transition strengths of the Pt, Hg and Pb nuclei as a function of Z is important as a means of testing the validity of the two hypotheses put forward to explain the apparent discontinuity in $E_x(3_1^-)$ at A=198. The idea that collective octupole strength in the Pt nuclei is shared between several 3^- states has been predicted by Engel (En86) and further developed by Cottle *et al.* (Co88b). Engel's calculations of E3 transition strength are subject to an arbitrary normalization but serve to demonstrate that application of the IBM-1 incorporating an f-boson and assuming an O(6) structure for ^{190,192,194,196}Pt nuclei results in the prediction of three collective 3^- states at excitation energies of $\sim$ 1.4, 2.1 and 2.3 MeV in each isotope. As yet, there are no definite 3^- assignments for states above the 3_1^- state. Engel's results also appear to suggest that the total E3 transition strength should decrease with increasing neutron number (fig. 5.9). It would be interesting to see whether similar predictions of fragmentation are also obtained for the Hg isotopes if an O(6) structure is assumed.

Cottle *et al.* base their proposal of significant fragmentation of the octupole strength

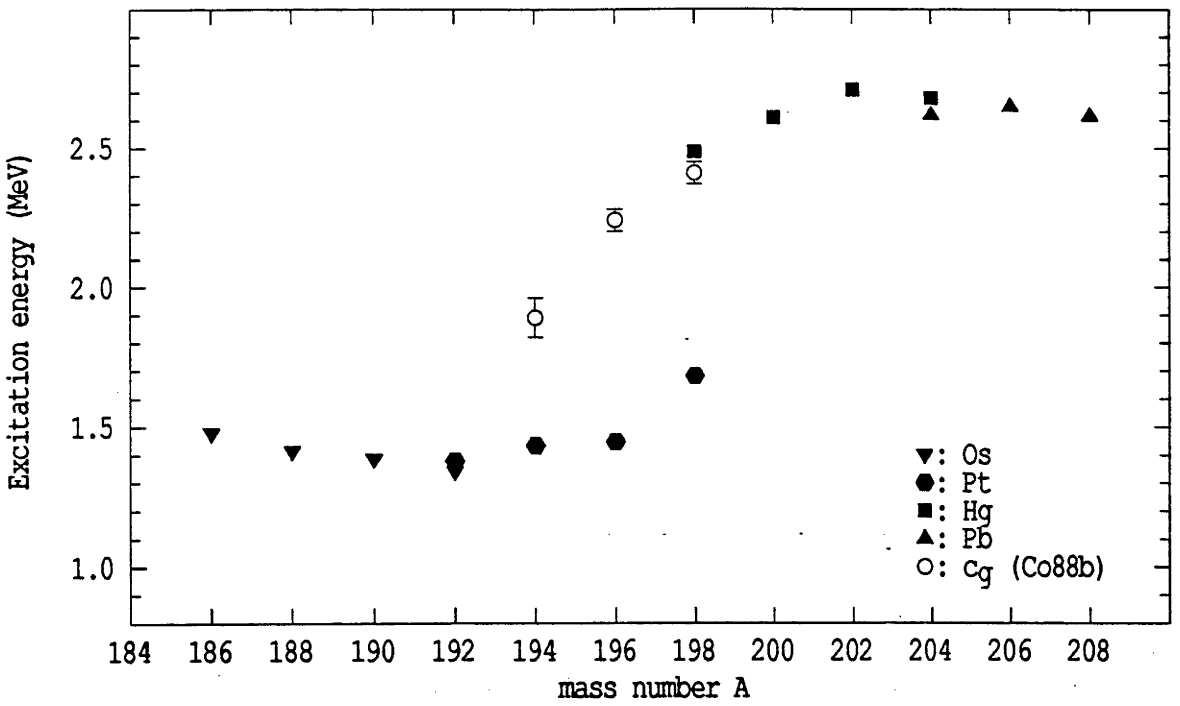

Figure 5.10: Excitation energies of the 3_1^- state for all the stable even-mass Os, Pt, Hg and Pb isotopes up to ^{208}Pb (Sp89) and centres of gravity c_g for the Pt nuclei as calculated by Cottle *et al.* (Co88b) using equation (5.6). Experimental values are denoted by filled triangles, hexagons and squares; the open circles correspond to the calculations of Cottle *et al.*

in the platinum isotopes (Co88b) on their interpretation of angular distributions for certain states in ^{194,196,198}Pt measured by Deason *et al.* (De81) from 35 MeV proton scattering data. They make spin assignments of 3^- to these states from DWBA fits to the data. However, these states are described in the original paper of Deason *et al.* as having unique angular distributions that are unlike those for the known 2_1^+, 3_1^- and 4_1^+ states. These somewhat uncertain spin assignments form the basis of the analysis by Cottle *et al.* They find that the 'centres of gravity', c_g, defined as

$$c_g = \frac{\sum_i E_i B(E3; 0_1^+ \rightarrow 3_i^-)}{\sum_i B(E3; 0_1^+ \rightarrow 3_i^-)}, \tag{5.6}$$

form a smooth curve with $E_x(3_1^-)$ of the mercury and lead nuclei as shown in fig. 5.10. If one assumes that the unconfirmed 3^- assignments of Cottle *et al.* are correct, then it is instructive to consider the total E3 strengths obtained from their analysis (15.7, 20.3 and 24.9 W.u. for ^{194}Pt, ^{196}Pt and ^{198}Pt respectively). This result would remove

the discontinuity in both $E_x(3_1^-)$ and E3 strength between Pt and Hg. However, this does not explain the large increase in $|\mathcal{M}(E3)|^2$ that is encountered when going from Hg to Pb (see fig. 5.9) unless the proposal of fragmentation by Cottle *et al.* is extended to postulate the existence of other 3^- states in both the Pt and Hg nuclei giving an additional E3 transition strength of 10–15 W.u. for each isotope; these hypothetical states must also have a centre of gravity close to 2.6 MeV in order to maintain the continuity of $E_x(3_1^-)$ or c_g with mass number. Furthermore, Cottle *et al.* do not consider the question of the Os nuclei, which have $E_x(3_1^-)$ and $|\mathcal{M}(E3)|^2$ very similar to that of the Pt nuclei. Obviously, there is a need for more data on other 3^- states in the Pt and Hg nuclei to either confirm or refute the proposal of fragmentation.

Yates *et al.* (Ya88) proposed that the 3_1^- states in the Pt nuclei are best described by the semi-decoupled model calculations of Toki *et al.* (To77) while higher-lying 3^- states may be of the same collective octupole character as the 3_1^- states of the Hg and Pb nuclei. This suggestion was made on the following grounds : (a) the 3_1^- state in ^{198}Pt at 1.681 MeV is connected to the 5_1^- state at 1.367 MeV by a strong transition (Ya83) as would be expected from members of a semi-decoupled band, and (b) a state in ^{198}Pt at 2.603 MeV is argued to be a 3^- state because it appears to decay only to the 3_1^- state and seems to be the primary state deexciting to the 3_1^- level (Ya88); this state may correspond to a strongly populated 2.611 MeV state seen by Deason *et al.* (De81). It should be noted that the assignment of 3^- to the 2.603 MeV state is tentative at best; in fact, as mentioned above, there is no conclusive evidence for a strongly excited 3^- state with excitation energy above the 3_1^- state in any of the stable even-mass Pt isotopes. In addition, the only indication that the 3_1^- states of Pt may be different in nature to those of Hg is the discontinuity in $E_x(3_1^-)$. All other experimental evidence is consistent with a collective octupole interpretation for both elements. For example, the values of $|\mathcal{M}(E3)|^2$ measured in the present work for ^{194,196,198}Pt are significantly greater than the single-particle estimate, which is the basic signature of a collective state.

However, serious consideration of the semi-decoupled model as an alternative explanation for observed octupole behaviour in this region is warranted, if only because Toki *et al.* obtained good agreement for the excitation energies of the Pt isotopes (cf. table

5.1). The main difficulty is that of reconciling the calculated $E_x(3_1^-)$ of Toki *et al.* for the Hg isotopes (about 1.8 MeV in ^{198,200}Hg) with experiment. Toki *et al.* included their results for the wavefunctions for various negative-parity states in ^{190}Pt and ^{192}Hg. The wavefunctions for the 3_1^- states in those nuclei can be combined with the equations for matrix elements given by Faessler and Sheline (Fa66) to calculate ratios of $B(E3;0_1^+ \rightarrow 3_1^-)$ for ^{190}Pt to that for ^{192}Hg in this model. If the proton and neutron effective charges are assumed to be equal, the ratio of $B(E3;0_1^+ \rightarrow 3_1^-)_{^{190}Pt}$ to $B(E3;0_1^+ \rightarrow 3_1^-)_{^{192}Hg}$ is about 1.5; if the proton effective charge is assumed to be three times the effective charge of the neutron (e.g. 1.5 as compared to 0.5), this ratio becomes about 1.2. Provided the mixing amplitudes for the different components of the wavefunctions do not change greatly with increasing neutron number, these calculations indicate that the semi-decoupled model predicts $B(E3;0_1^+ \rightarrow 3_1^-)$ to be $\sim 0.068 - 0.085$ e^2b^3 (4.2–5.2 W.u.) for ^{198}Hg and $\sim 0.056 - 0.070$ e^2b^3 (3.4–4.3 W.u.) for ^{200}Hg, if the $B(E3;0_1^+ \rightarrow 3_1^-)$ values obtained for ^{196}Pt and ^{198}Pt in the present work are assumed. The Hg data shown in fig. 5.6 provide upper limits on the E3 transition strength of any 3^- states with excitation energy of 1.6–2.0 MeV to be 5.5 W.u. for ^{198}Hg and 2.5 W.u. for ^{200}Hg; there is no evidence for any putative 3^- states at the energies predicted by Toki *ef al.* .

One possible explanation for the difference between experimental and predicted $E_x(3_1^-)$ in Hg is that Toki *et al.* assumed unrealistic values for the quadrupole deformation parameters defined by Bohr and Mottelson (Bo75), β_2 and γ. Experimental measurements of $Q(2_1^+)$ for Hg (Es77, Sp80, Es81) published after To77 indicate significant oblate deformation in these nuclei rather than the moderate deformation ($|\beta_2| < 0.1$) assumed previously. The values of γ used by Toki *et al.* for the Hg isotopes were $\sim 60°$ whereas Peker and Hamilton (Pe79) argued that the energy level systematics of ^{192,194,196,198,200}Hg point to values of γ of between 30° and 40° for these nuclei. However, changes in β_2 and γ are unlikely to remove the discrepancy in $E_x(3_1^-)$ without altering the predicted values of $E_x(5_1^-)$ and $E_x(7_1^-)$, which are presently in good agreement with experiment. The calculations of Toki *et al.* show that variations in γ move all the excitation energies by the same amount, as seen in fig. 5.11. Nevertheless, it is interesting to note that Nilsson model calculations predict that the energies of the $3s_{1/2}$ and $3d_{3/2}$ orbitals will increase

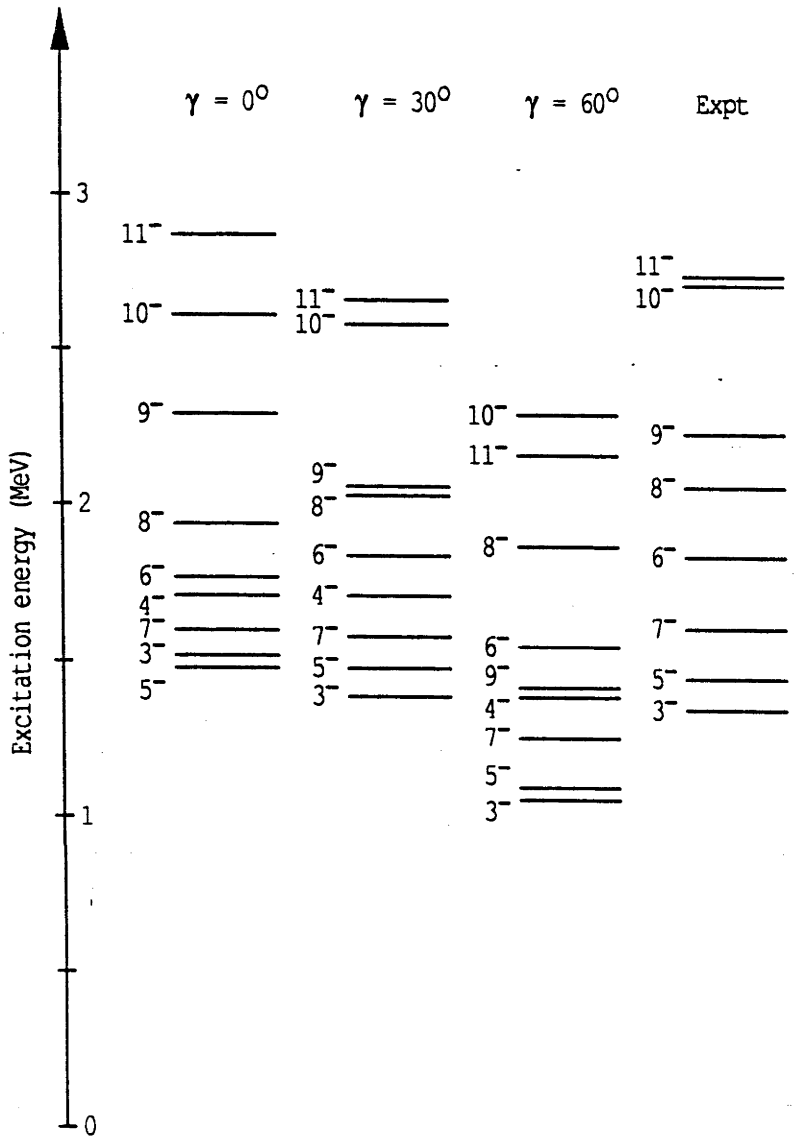

Figure 5.11: Effect of the deformation parameter γ on excitation energies predicted using the semi-decoupled model (taken from To77).

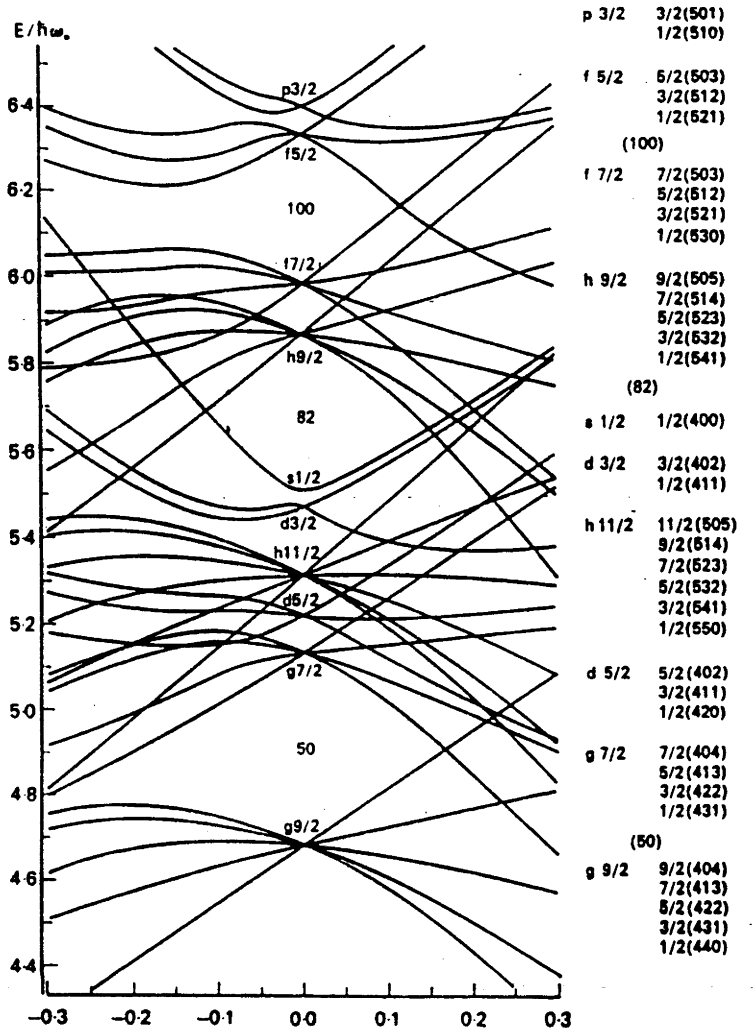

Figure 5.12: Nilsson model calculations of single-particle orbital energies for nuclei with Z≤82, N≤126 (from Ir72).

for negative values of β_2 (corresponding to oblate deformation) while the energy of the $1h_{9/2}$ orbital decreases, as seen in fig. 5.12. These orbitals are expected to provide a substantial component of the 3^- strength in the shell model. Changes in quadrupole deformation which occur as the number of protons increases from 78 in Pt to 80 in Hg, and finally to 82 in the near-spherical Pb nuclei, are likely to result in significant alterations in the single-particle orbital energies (cf. fig. 5.12), which would affect $E_x(3_1^-)$ in turn.

Another possible explanation is suggested by the result of Toki *et al.* that neutron excitation dominates in the Hg nuclei, whereas proton and neutron excitations contribute roughly the same amount in the Pt nuclei. If collectivity in this region is associated with proton excitation, then it would be quite conceivable that collective octupole strength

from a higher-lying 3^- state could be shared with a lower-lying 3^- state which was produced by the semi-decoupled mechanism in such a way that the extent of sharing would be dependent on the relative contribution of proton and neutron excitation to the lower state. This would mean that the predominantly neutron-excited 2qp 3^- state of the Hg nuclei would be much weaker than the equivalent states in the Pt nuclei, assuming the 'true' collective 3^- state to lie at $\sim$ 2.6 MeV in both Pt and Hg.

5.7 Conclusions

Measurements of $B(E3;0_1^+ \rightarrow 3_1^-)$ for ^{194,196,198}Pt and ^{198,200,202,204}Hg have shown that the E3 transition strength to the first 3^- state is between 5 and 11 W.u. for the Pt isotopes but about 20–25 W.u. for each of the Hg isotopes. The absolute difference of 10–15 W.u. between these values is similar to that between the E3 transition strengths for the Hg and Pb isotopes. None of the existing theories provide a quantitative and satisfactory explanation for the observed rapid increase of $|\mathcal{M}(E3)|^2$ with Z. New calculations for the Hg isotopes which incorporate the improved knowledge of the behaviour of these nuclei would be helpful, for instance, it would be useful to know whether the prediction of fragmented octupole strength is a characteristic feature of the O(6) limit of the IBM. In addition, further experimental studies of higher 3^- states in the Pt and Hg nuclei would be of great assistance.

Chapter 6

Summary

The measurements reported in this thesis have employed Coulomb excitation under a number of different experimental conditions to determine electric moments in the Os-Pt-Hg transitional region. The theoretical basis of Coulomb excitation has been outlined, and a discussion has been presented concerning the corrections and uncertainties that should be included in a rigorous treatment of Coulomb excitation data. It was found that an adequate treatment of these corrections and uncertainties is essential if incorrect results are to be avoided.

An apparent discrepancy between the results of reorientation effect measurements and muonic X-ray experiments for the spectroscopic quadrupole moment of the 2_1^+ state in ^{192}Os provided the motivation for a particle singles spectroscopy measurement of the static and transitional electric quadrupole moments for the 2_1^+ state of that nucleus. In particular, the determination of $Q(2_1^+)$ was used as a means of investigating the extent to which quadrupole moment measurements are influenced by the method used. Results obtained in the present Coulomb excitation experiment were found to be in good agreement with those from muonic X-ray data. It was shown that the discrepancy between the muonic X-ray result and earlier reorientation effect measurements may have been due to neglect of various higher-order effects in Coulomb excitation theory. The significance of $Q(2_1^+)$ of ^{192}Os with respect to the overall trend of changing deformation in the Os nuclei was also discussed; its negative sign was contrasted with the positive sign of ^{192}Pt, illustrating the change in shape from prolate (^{192}Os) to oblate (^{192}Pt) deformation

occurring with the interchange of two protons for two neutrons in these nuclei.

The particle singles and particle-γ coincidence techniques were employed to measure excitation probabilities for ^{194}Pt and ^{196}Pt under bombardment with ^{4}He, ^{7}Li, ^{12}C and ^{58}Ni projectiles. E2 and E4 transition matrix elements for many low-lying positive-parity states in those nuclei were extracted from the data. The relatively large values determined for the static quadrupole moments of the 2_1^+, 2_2^+ and 4_1^+ states for ^{194}Pt and ^{196}Pt were discussed in the context of the transition from prolate to oblate deformation in the Os and Pt nuclei. The overall shapes of the nuclear charge distributions of ^{194}Pt and ^{196}Pt were deduced to be oblate and γ-soft. Comparison of various model predictions with the data obtained indicated that phenomenological descriptions of ^{196}Pt which assumed a γ-unstable structure in which the overall nuclear deformation is neither prolate nor oblate, were inferior to microscopic models which proposed a tendency to oblate deformation. It was noted that, with the exception of the U(5) limit of the IBM and, to a lesser extent, the GCM and BET, none of the theoretical calculations were able to fit both the large magnitudes of the quadrupole moments of ^{196}Pt as well as the vanishing crossover transition probability for the 2_2^+ state of that nucleus. The Interacting Boson Model was shown to be unable to describe details of the complex electric quadrupole structure of ^{194}Pt and ^{196}Pt; a more satisfactory overall description was given by the Boson Expansion Theory.

The particle singles spectroscopy technique was used in conjunction with Coulomb excitation to obtain model-independent measurements of E3 transition strengths between the 3_1^- and ground states in ^{194,196,198}Pt and ^{198,200,202,204}Hg as part of an investigation into a discontinuity in $E_x(3_1^-)$ between ^{198}Pt and ^{198}Hg which apparently reflects changes in collective octupole behaviour in this region. The difference of $\sim$ 1 MeV between $E_x(3_1^-)$ of the Pt and Hg isotopes, as well as the observed sudden increase of 10–15 W.u. in $\mid \mathcal{M}(E3) \mid^2$ when going from Z=78(Pt) to Z=80(Hg) and also from Z=80 to Z=82(Pb) revealed that the nature of octupole collectivity in the Pt and Hg nuclei is more intricate than previously suspected.

The work considered in this thesis has pointed to several unanswered questions. The experimental evidence presently available on the exact location of the prolate-to-oblate

transition in the Os and Pt isotopes is still ambiguous in some respects; in particular, a determination of the magnitude and sign of the static quadrupole moment of the 2_1^+ state in ^{190}Pt would show whether that nucleus is prolate like the Os nuclei, as predicted by the BET, or oblate like the other stable even-mass Pt isotopes. Further investigations of the excitation energies and E3 transition strengths of 3^- states in the stable even-mass Os, Pt and Hg isotopes should be valuable in providing information on octupole collectivity. More work could also be carried out on the development of theoretical descriptions of octupole structure in these nuclei, e.g. IBM calculations which employ the O(6) dynamical symmetry for the Hg isotopes.

Appendix A

Volume 200, number 3 PHYSICS LETTERS B 14 January 1988

ENERGY DEPENDENCE OF THE ^{16}O–^{208}Pb EFFECTIVE INTERACTION

C.S. LIM, M.D. REBGETZ [1], R.H. SPEAR, W.J. VERMEER, M.P. FEWELL [2]
Department of Nuclear Physics, Research School of Physical Sciences, The Australian National University, Canberra, ACT 2601, Australia

B.A. ROBSON and R. SMITH [3]
Department of Theoretical Physics, Research School of Physical Sciences, The Australian National University, Canberra, ACT 2601, Australia

Received 31 August 1987

The Coulomb-nuclear interference in the excitation probability of the 2.615 MeV (3^-) state of ^{208}Pb by ^{16}O at $\theta_{CM}=172°$ for bombarding energies 57 MeV $\leqslant E_{lab} \leqslant$ 79 MeV has been studied. The data are described by an effective interaction which has a behaviour similar to that expected from the dispersion relation connecting the real and imaginary parts of the generalized optical potential.

The energy dependences of the effective interactions between heavy ions have been studied in several elastic scattering analyses [1–3]. Such investigations have indicated that, as the bombarding energy is lowered near the Coulomb barrier, the depth of the real part of the optical potential shows firstly a marked increase and then a decrease. This behaviour is expected [4,5] from the dispersion relation which connects the real and imaginary parts of the generalized optical potential. It arises as a result of the sharp decrease in the magnitude of the imaginary potential, corresponding to the effective closure of the non-elastic channels, as the bombarding energy decreases near the Coulomb barrier.

Recently Landowne et al. [6] have extended the above studies to inelastic scattering. Using the conventional distorted-wave Born approximation and a collective model, they have analyzed the Coulomb-nuclear interference in the excitation probability (P) of the 2.615 MeV (3^-) state of ^{208}Pb by ^{16}O at sub-barrier energies, $58 \leqslant E_{lab} \leqslant 69$ MeV. It was found that the calculations were sensitive mainly to the nuclear coupling strength, which was required to be about twice as large as its value above the barrier. Since the nuclear coupling strength was taken to be proportional to the magnitude of the real part of the optical potential, which was assumed to vary linearly with energy, this increase in coupling strength corresponds to a doubling of the depth of the real optical potential.

In the present paper new data for P, defined as the ratio of the inelastic scattering cross section to the elastic-plus-inelastic cross sections, for the 2.615 MeV (3^-) state of ^{208}Pb when bombarded by ^{16}O, are presented. These measurements, which were made using the Australian National University 14 UD pelletron accelerator and experimental arrangements as described previously [7], extend the earlier results to higher bombarding energies, 66 MeV $\leqslant E_{lab} \leqslant$ 79 MeV. The results are listed in table 1. The new data, which cover the interesting energy region around the Coulomb-nuclear interference minimum near 74 MeV, are expected to be more sensitive to the optical potential than the earlier measurements at lower bombarding energies. Comparison of these data with the predictions of ref. [6] shows a signif-

[1] ANU Vacation Scholar.
[2] Present address: Department of Physics, University of New England, Armidale, NSW 2351, Australia.
[3] Present address: Analytical Studies Branch, Central Studies Establishment, Department of Defence, P.O. Box 105, Campbell, ACT 2601, Australia.

0370-2693/88/$ 03.50

Table 1
Excitation probabilities for 2.615 MeV (3^-) state of ^{208}Pb by ^{16}O at 172° (CM).

E_{lab}(MeV)	$P(\times 10^4)$
66.0	4.94± 0.17
68.0	6.06± 0.19
69.0	5.99± 0.21
	6.54± 0.23
70.0	6.32± 0.43
	6.40± 0.29
71.0	5.64± 0.29
72.0	4.55± 0.23
	4.27± 0.27
73.0	2.65± 0.28
74.0	2.05± 0.15
75.0	3.13± 0.22
75.5	6.97± 0.62
76.0	14.9 ± 2.1
77.0	63.0 ± 1.5
78.0	184 ± 5
79.0	412 ±14

icant discrepancy for bombarding energies $\gtrsim 70$ MeV.

We have analysed the complete set of measurements using a similar model to ref. [6]. Coupled-channels calculations have been carried out with the computer code ECIS [8] for a first-order one-phonon vibrational model involving the ground (0^+) and 2.615 MeV (3^-) states of ^{208}Pb. The optical potential was taken to have Woods–Saxon form factors with energy-dependent real and imaginary parts

$$U(E)=V(E)f_V(r)+iW(E)f_W(r)\,, \tag{1}$$

where

$$f_i(r)=\{1+\exp[(r-R)/a_i]\}^{-1}\,, \tag{2}$$

and

$$R=r_0[(16)^{1/3}+(208)^{1/3}]\,. \tag{3}$$

The strength of the imaginary potential (in MeV) was assumed to increase linearly with bombarding energy, as in ref. [6],

$$W(E)=-39-0.85(E_{lab}-104)\,. \tag{4}$$

In order to describe approximately the expected variation with energy, the magnitude of the real part of the optical potential was taken to vary quadratically with energy,

$$V(E)=-68.4+\alpha(E_{lab}-104)+\alpha'(E_{lab}-104)^2\,, \tag{5}$$

with the value of -68.4 MeV at $E_{lab}=104$ MeV from ref. [9]. As in ref. [6], $a_V=0.658$ fm, $a_W=0.565$ fm, $r_0=1.178$ fm and the nuclear coupling strength $\beta_n=0.1227$ were assumed. The Coulomb interaction parameters were $r_c=1.178$ fm and $\beta_c=0.1120$, the latter being chosen to optimise the predictions for P at the lowest bombarding energies.

It should be noted that as a result of the approach taken to optimising predictions at the lowest bombarding energies by detailed consideration of the computation of the Coulomb interaction, with a consequent adjustment of parameters from those adopted in ref. [6], and the different reaction formulation used [i.e. coupled channels as in ref. [8] compared with DWBA [6]], it is not valid to compare directly values of the linear parameter α obtained herein with the values of α quoted in ref. [6].

Initially, for simplicity, α' in eq. (5) was set equal to zero and the linear parameter α was adjusted to obtain optimum fits to P for each of the energy regions 65 MeV$\leqslant E_{lab}\leqslant$74 MeV and 75 MeV $\leqslant E_{lab}\leqslant$ 79 MeV. It was found that the required values of α were close to 0.80 and 1.80, respectively. It is noted that such positive values of α confirm the trend established by the linear potential models of ref. [6] that the value of the real potential depth is greater at energies close to the Coulomb barrier than the value obtained previously at $E_{lab}=104$ MeV [9]. However, a detailed comparison of the predictions for potentials L1 ($\alpha=0.80$) and L2 ($\alpha=1.80$) with data, as given in fig. 1a, demonstrates that no overall fit to the data is possible with a fixed value of α and $\alpha'=0$. To address this problem, the full quadratic form of eq. (5) was considered. Fig. 1b shows the result for a quadratic energy dependence of $V(E)$, potential Q ($\alpha=5.31$, $\alpha'=0.135$), which gives satisfactory agreement over the whole energy range except near 74 MeV. This small discrepancy can be attributed to the simple quadratic form assumed for the magnitude of the real part of the optical potential $|V|$. The angular distribution for the reaction ^{208}Pb(^{16}O, ^{16}O′)^{208}Pb (3^-, 2.615 MeV) at $E_{lab}=78$ MeV as shown in ref. [6] is also well described by potential Q.

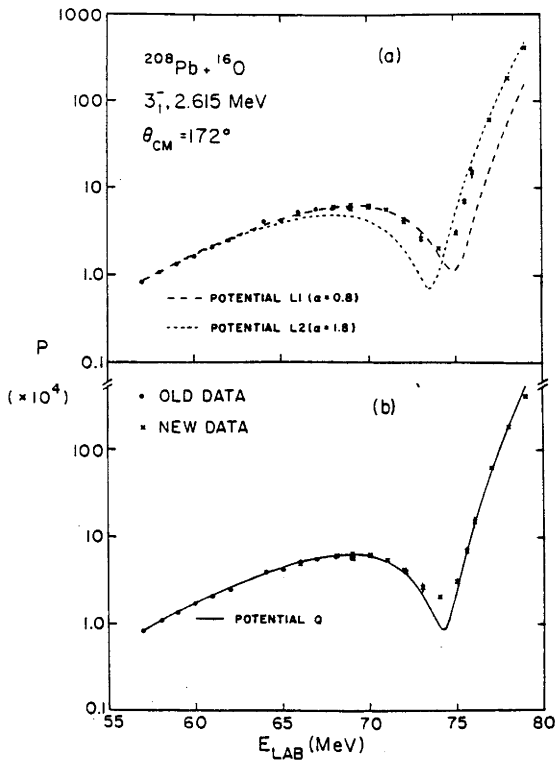

Fig. 1. Excitation probability of the 2.615 MeV (3^-) state of ^{208}Pb by ^{16}O at 172° (CM) as a function of bombarding energy. The old and new data are from ref. [7] and table 1, respectively. Calculations using potentials L1, L2 and Q (see text) are given.

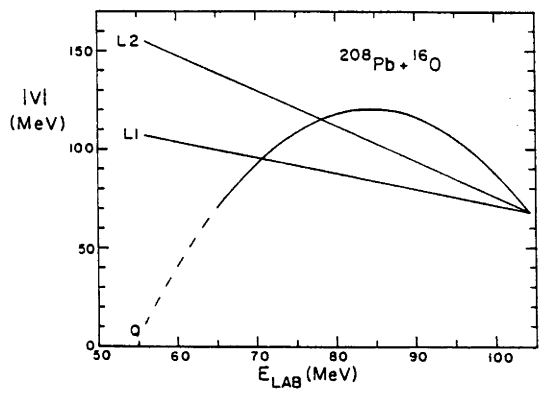

Fig. 2. Magnitude of real part of effective interaction for ^{208}Pb + ^{16}O system as a function of bombarding energy. The curves correspond to potentials L1, L2 and Q, respectively.

Fig. 2 shows the variations in $|V|$ as a function of bombarding energy for the three potentials L1, L2 and Q. For $E_{lab} \lesssim 65$ MeV, the predictions for P are essentially insensitive to the value of $|V|$ and the dashed curve associated with potential Q is not considered physically meaningful. At energies $\lesssim 60$ MeV, the departure from pure Coulomb excitation is less than the experimental uncertainties. In order to describe the observed minimum in P near 74 MeV in fig.1, the value of $|V|$ would need to increase from the line L1 to the line L2 within the smaller energy interval 73–75 MeV rather than the larger energy interval 71–78 MeV given by potential Q. This behaviour is similar to that expected from the dispersion relation connecting the real and imaginary parts of the optical potential.

Summarizing, analysis of the Coulomb-nuclear interference in the excitation probability of the 2.615 MeV (3^-) state of ^{208}Pb by ^{16}O at $\theta_{CM} = 172°$ over the energy range 57 MeV $\leqslant E_{lab} \leqslant$ 79 MeV shows that the magnitude of the real part of the effective interaction firstly increases and then decreases in magnitude with decreasing bombarding energy. This is consistent with the behaviour expected from the optical model dispersion relation. Analysis of new data covering the Coulomb-nuclear interference minimum shows that the magnitude of the real optical potential cannot be described by a *linear* energy dependence.

References

[1] A. Baeza, B. Bilwes, R. Bilwes, J. Diaz and J.L. Ferrero, Nucl. Phys. A 419 (1984) 412.
[2] J.S. Lilley, B.R. Fulton, M.A. Nagarajan, I.J. Thompson and D.W. Banes, Phys. Lett. B 151 (1985) 181.
[3] B.R. Fulton, D.W. Banes, J.S. Lilley, M.A. Nagarajan and I.J. Thompson, Phys Lett. B 162 (1986) 55.
[4] M.A. Nagarajan, C.C. Mahaux and G.R. Satchler, Phys. Rev. Lett. 54 (1985) 1136.
[5] C. Mahaux, H. Ngô and G.R. Satchler, Nucl. Phys. A 449 (1986) 354.
[6] S. Landowne, C.H. Dasso and G. Pollarolo, Phys. Lett. B 178 (1986) 336.
[7] W.J. Vermeer, M.T. Esat, J.A. Kuehner, R.H. Spear, A.M. Baxter and S. Hinds, Aust. J. Phys. 37 (1984) 123.
[8] J. Raynal, Computing as a language of physics (IAEA, Vienna, 1972) p. 281.
[9] G. Pollarolo, R.A. Broglia and A. Winther, Nucl. Phys. A 406 (1983) 307.

Appendix B

Extraction of Matrix Elements

The simultaneous extraction of a large number of matrix elements from measured Coulomb excitation probabilities was carried out in this thesis by incorporating the Winther-de Boer multiple Coulomb excitation program (Wi66) as a subroutine in the minimization program MINUIT (Ja75). Input data consists of up to 30 matrix elements, of which no more than 15 can be varied simultaneously, the measured values for the excitation probabilities P_{exp} and their associated uncertainties ΔP_{exp}. Uncertainties can also be given by the user for those matrix elements which are assumed. The chisquare function F_{chisq} is defined as

$$F_{chisq} = [(P_{exp} - P_{calc})/\Delta P_{exp}]^2 \tag{B.1}$$

where P_{calc} is the excitation probability calculated using a version of the Winther-de Boer program which has been modified to include integration over energy loss in the target and particle detector angle, as well as corrections for vacuum polarization, nuclear polarization and electron screening. The matrix elements which have been designated to be variables are then varied to minimize the value of F_{chisq}. The final step is the calculation of uncertainties in the variable matrix elements.

The program MINUIT offers three different search techniques which complement each other : a Monte Carlo method, the simplex method of Nelder and Mead (Ne65), and the variable metric method of Fletcher (Fl70). The simplex method involves the formation of a simplex (the smallest $n-$dimensional figure with $n+1$ vertices) from the chisquare

function. The initial simplex is formed from the starting values given for the matrix elements. The program then searches for a local minimum along each coordinate axis. A rough estimate of the errors is provided by the size of the simplex and the distance to the minimum. The variable metric method requires starting values for the parameters, their first derivatives and the covariance matrix. These are supplied by the user or, in the case of the derivatives, calculated by the program. The product of the covariance matrix and the matrix of derivatives is taken to be the step size for the minimization search. Optimum performance was obtained by utilizing the Monte Carlo and simplex methods to obtain a quick convergence to the approximate minimum then employing the variable metric method to find the exact minimum.

An order of magnitude estimate of the uncertainties in each variable x_i can be obtained by varying the value of each of the other variables x_j and adding the resultant changes Δx_i in quadrature. Alternatively, the program MINUIT can be used to calculate both the correlation coefficients (which describe the correlation between various parameters) and the confidence intervals (i.e. the region in which a parameter has a given probability of being found) for each variable. The results of these two latter options were found to be mutually consistent in the present work.

Bibliography

[AG85] : Y.K. Agarwal, C. Günther, K. Hardt, P. Schüler, J. Stachel, H.J. Wollersheim, H. Emling, E. Grosse, R. Kulessa and W. Spreng, *Z. Phys.* **A320** (1985) 295

[AL56] : K. Alder, A. Bohr, T. Huus, B. Mottelson and A. Winther, *Rev. Mod. Phys.* **28** (1956) 432, reprinted in K. Alder and A. Winther, "Coulomb excitation" (Academic Press, New York, 1966)

[AL60] : K. Alder and A. Winther, *Mat.-Fys. Medd. Dan. Vid. Selsk.* **32** (1960) no. 8, reprinted in K. Alder and A. Winther, "Coulomb excitation" (Academic Press, New York, 1966)

[AL72] : K. Alder, F. Roesel and R. Morf, *Nucl. Phys.* **A186** (1972) 449

[AL75] : K. Alder and A. Winther, "Electromagnetic excitation" (North-Holland, Amsterdam, 1975)

[AL77] : K. Alder, F. Roesel and R. Morf, *Nucl. Phys.* **A284** (1977) 145

[AL78] : T.K. Alexander and J.S. Forster, *Adv. Nucl. Phys.* **10** (1978) 197

[AN88] : A. Ansari, *Phys. Rev.* **C38** (1988) 953

[AR76] : A. Arima and F. Iachello, *Ann. of Phys.* **99** (1976) 253

[AR78] : A. Arima and F. Iachello, *Ann. of Phys.* **111** (1978) 201

[AR79] : A. Arima and F. Iachello, *Ann. of Phys.* **123** (1979) 468

[AR81] : A. Arima and F. Iachello, *Ann. Rev. Nucl. Part. Sci.* **31** (1981) 75

[AU83] : R.L. Auble, *Nucl. Data Sheets* **40** (1983) 301

[BA57] : R. Barloutaud, P. Lehmann and A. Leveque, *Compt. Rend. Acad. Sci.* **245** (1957) 523

[BA76] : F.T. Baker, A. Scott, T.H. Kruse, W. Hartwig, E. Ventura and W. Savin, *Nucl. Phys.* **A266** (1976) 337

[BA76a] : F.T. Baker, T.H. Kruse, W. Hartwig, I.Y. Lee and J.X. Saladin, *Nucl. Phys.* **A258** (1976) 43

[BA76b] : F.T. Baker, A. Scott, T.H. Kruse, W. Hartwig, E. Ventura and W. Savin, *Phys. Rev. Lett.* **37** (1976) 193

[BA78] : C. Baktash, J.X. Saladin, J.J. O'Brien and J.G. Alessi, *Phys. Rev.* **C18** (1978) 131

[BA79] : F.T. Baker, A. Scott, T.P. Cleary, J.L.C. Ford, E.E. Gross and D.C. Hensley, *Nucl. Phys.* **A321** (1979) 222

[BA80] : C. Baktash, J.X. Saladin, J.J. O'Brien and J.G. Alessi, *Phys. Rev.* **C22** (1980) 2383

[BA81] : A.M. Baxter, S. Hinds, R.H. Spear, T.H. Zabel and R. Smith, *Nucl. Phys.* **A369** (1981) 25

[BA81a] : F.T. Baker, M.A. Grimm, Jr., A. Scott, R.C. Styles, T.H. Kruse, K. Jones and R. Suchannek, *Nucl. Phys.* **A371** (1981) 68

[BA85] : F.T. Baker, A. Sethi, V. Penumetcha, G.T. Emery, W.P. Jones, M.A. Grimm and M.L. Whiten, *Phys. Rev.* **C32** (1985) 2212

[BE53] : H.A. Bethe and J. Ashkin, in "Experimental Nuclear Physics", vol. 1, ed. E. Segre (J. Wiley and Sons, New York, 1953)

[BE69] : A.M. Bernstein, *Adv. Nucl. Phys.* **3** (1969) 325

[BE72] : I. Berkes, R. Rougny, M. Meyer-Lévy, R. Chéry, J. Danière, G. Lhersonneau and A. Troncy, *Phys. Rev.* **C6** (1972) 1098

[BI65] : L.C. Biedenharn and P.J. Brussaard, "Coulomb excitation" (Clarendon Press, Oxford, 1965)

[BI80] : R. Bijker, A.E.L. Dieperink, O. Scholten and R. Spanhoff, *Nucl. Phys.* **A344** (1980) 207

[BO52] : A. Bohr and B.R. Mottelson, *Mat.-Fys. Medd. Dan. Vid. Selsk.* **26** (1952) 14

[BO53] : A. Bohr and B.R. Mottelson, *Mat.-Fys. Medd. Dan. Vid. Selsk.* **27** (1953) 16

[BO68] : J. de Boer and J. Eichler, *Adv. Nucl. Phys.* **1** (1968) 1

[BO69] : A. Bohr and B. Mottelson, "Nuclear Structure" vol. 1 (Benjamin, Reading Mass., 1969)

[BO75] : A. Bohr and B. Mottelson, "Nuclear Structure" vol. 2 (Benjamin, Reading Mass., 1975)

[BO81] : H.H. Bolotin, A.E. Stuchbery, I. Morrison, D.L. Kennedy, C.G. Ryan and S.H. Sie, *Nucl. Phys.* **A370** (1981) 146

[BO83] : P.D. Bond, R.F. Casten, D.D. Warner and D. Horn, *Phys. Lett.* **130B** (1983) 167

[BO84] : J. de Boer, "Inelastic Scattering - Coulomb excitation", in "Treatise on Heavy-Ion Science" vol. 1, ed. D.A. Bromley (Plenum Press, New York, 1984)

[BO85] : W.T.A. Borghols, N. Blasi, R. Bijker, M.N. Harakeh, C.W. de Jager, J.B. van der Laan, H. de Vries and S.Y. van der Werf, *Phys. Lett.* **152B** (1985) 330

[BO88] : W. Boeglin, P. Egelhof, I. Sick, J.M. Cavedon, B. Frois, D. Goutte, V. Méot, P. Leconte, X.H. Phan, S.K. Platchkov, S. Williamson and M. Girod, *Nucl. Phys.* **A477** (1988) 399

[BO88a] : D. Bonatsos, "Interacting Boson Models of Nuclear Structure" (Clarendon Press, Oxford, 1988)

[BR56] : G. Breit, R.L. Gluckstern and J.E. Russell, *Phys. Rev.* **103** (1956) 727

[BR70] : E.J. Bruton, J.A. Cameron, A.W. Gibb, D.B. Kenyon and L. Keszthelyi, *Nucl. Phys.* **A152** (1970) 495

[BU85] : S.M. Burnett, A.M. Baxter, S. Hinds, F. Pribac, R.H. Spear and W.J. Vermeer, *Nucl. Phys.* **A432** (1985) 514

[CA67] : R.F. Casten, J.S. Greenberg, G.A. Burginyon and D.A. Bromley, *Phys. Rev. Lett.* **18** (1967) 912

[CA69] : R.F. Casten, J.S. Greenberg, S.H. Sie, G.A. Burginyon and D.A. Bromley, *Phys. Rev.* **187** (1969) 1532

[CA78] : R.F. Casten and J.A. Cizewski, *Nucl. Phys.* **A309** (1978) 477

[CA78a] : R.F. Casten, A.I. Namenson, W.F. Davidson, D.D. Warner and H.G. Börner, *Phys. Lett.* **76B** (1978) 280

[CA87] : R.F. Casten and J.A. Cizewski, *Phys. Lett.* **185B** (1987) 293

[CH73] : R.C. Chopra, P.N. Tandom, S.H. Devare and H.G. Devare, *Nucl. Phys.* **A209** (1973) 461

[CH83] : C.Y. Chen, J.X. Saladin and A.A. Hussein, *Phys. Rev.* **C28** (1983) 1570

[CH85] : H.C. Chiang, S.T. Hsieh, M.M. King Yen and C.S. Han, *Nucl. Phys.* **A435** (1985) 54

[CI78] : J.A. Cizewski, R.F. Casten, G.J. Smith, M.L. Stelts, W.R. Kane, H.G. Börner and W.F. Davidson, *Phys. Rev. Lett.* **40** (1978) 167

[CI79] : J.A. Cizewski, R.F. Casten, G.J. Smith, M.R. MacPhail, M.L. Stelts, W.R. Kane, H.G. Börner and W.F. Davidson, *Nucl. Phys.* **A323** (1979) 349

[CL78] : D. Cline, "Nuclear structure inferred from heavy-ion Coulomb excitation", in "International Conference on Nuclear Structure" ed. B.A. Robson (Springer-Verlag, Berlin, 1978)

[CL86] : D. Cline, *Ann. Rev. Nucl. Part. Sci.* **36** (1986) 683

[CO70] : A. Covello and G. Sartoris, *Nucl. Phys.* **A149** (1970) 41

[CO88] : P.D. Cottle, K.A. Stuckey and K.W. Kemper, *Phys. Rev.* **C38** (1988) 365

[CO88a] : P.D. Cottle, V. Hnizdo, R.J. Philpott, K.A. Stuckey, K.W. Kemper and J.A. Carr, *Phys. Rev.* **C38** (1988) 1619

[CO88b] : P.D. Cottle, K.A. Stuckey and K.W. Kemper, *Phys. Rev.* **C38** (1988) 2843

[CZ83] : T. Czosnyka, D. Cline and C.Y. Wu, *Bull. Amer. Phys. Soc.* **28** (1983) 745

[DE81] : P.T. Deason, C.H. King, R.M. Ronningen, T.L. Khoo, F.M. Bernthal and J.A. Nolen, Jr., *Phys. Rev.* **C23** (1981) 1414

[DR87] : C.H. Druce, S. Pittel, B.R. Barrett and P.D. Duval, *Ann. of Phys.* **176** (1987) 114

[ED88] : R. Eder, C.J. Ashworth, I. Berkes, D.E. Brown, U. Daemmrich, I.S. Grant, A.G. Griffiths, E. Hagn, R. Hassani, P. Herzog, S. Ohya, M. Massaq, C. Richard-Serre, J. Rikovska, K. Schloesser, N. Severijns, N.J Stone, W. Vanderpoorten, J. Vanhaverbeke, L. Vanneste, T. Woelfle, E. Zech and the ISOLDE collaboration, *Hyp. Int.* **43** (1988) 469

[EN74] : J.B. England, "Techniques in Nuclear Structure Physics" (Macmillan, London, 1974)

[EN86] : J. Engel, *Phys. Lett.* **171B** (1986) 148

[EN88] : J. Engel, priv. comm. to R.H. Spear, 1988

[ES77] : M.T. Esat, D.C. Kean, R.H. Spear, M.P. Fewell and A.M. Baxter, *Phys. Lett.* **72B** (1977) 49

[ES77a] : M.T. Esat, D.C. Kean and R.H. Spear, *Nucl. Inst. Meth.* **141** (1977) 405

[ES81] : M.T. Esat, M.P. Fewell, R.H. Spear, T.H. Zabel, A.M. Baxter and S.Hinds, *Nucl. Phys.* **A362** (1981) 227

[FA66] : A. Faessler and R.K. Sheline, *Phys. Rev.* **148** (1966) 1003

[FE78t] : M.P. Fewell, PhD thesis, Australian National University, 1978 (unpublished)

[FE79] : P. Federman and S. Pittel, *Phys. Rev.* **C20** (1979) 820

[FE84] : M.P. Fewell, *Nucl. Phys.* **A425** (1984) 373

[FE85] : M.P. Fewell, G.J. Gyapong, R.H. Spear, M.T. Esat, A.M. Baxter and S.M. Burnett, *Phys. Lett.* **157B** (1985) 353

[FE86] : M.P. Fewell, *Phys. Lett.* **167B** (1986) 6; and M.P. Fewell, priv. comm.

[FE87] : M.P. Fewell, *Phys. Lett.* **192B** (1987) 9

[FE88] : M.P. Fewell, G.J. Gyapong and R.H. Spear, *Aust. J. Phys.* **41** (1988) 37

[FI81] : A.J. Filo, S.W. Yates, D.F. Coope, J.L. Weil and M.T. McEllistrem, *Phys. Rev.* **C23** (1981) 1938

[FL70] : R. Fletcher, *Comput.* **J13** (1970) 317

[FO65] : H.W. Fowler, "A Dictionary of Modern English Usage", 2nd edition (Clarendon Press, Oxford, 1965)

[GA89] : R.A. Gatenby, E.W. Kleppinger and S.W. Yates, *Nucl. Phys.* **A492** (1989) 45

[GI67] : P. Gilad, G. Goldring, R. Herber and R. Kalish, *Nucl. Phys.* **A91** (1967) 85

[GL69] : J.E. Glenn, R.J. Pryor and J.X. Saladin, *Phys. Rev.* **188** (1969) 1905

[GN71] : G. Gneuss and W. Greiner, *Nucl. Phys.* **171** (1971) 449

[GR66] : L. Grodzins, R.R. Borchers and G.B. Hagemann, *Nucl. Phys.* **88** (1966) 474

[GR84] : H. Grein, H. Emling and J. Stachel, GSI annual Report 1983, (1984) 272

[GY86] : G.J. Gyapong, R.H. Spear, M.T. Esat, M.P. Fewell, A.M. Baxter and S.M. Burnett, *Nucl. Phys.* **A458** (1986) 165

[GY87] : G.J. Gyapong, R.H. Spear, M.P. Fewell, A.M. Baxter and S.M. Burnett, *Nucl. Phys.* **A470** (1987) 415

[GY87t] : G.J. Gyapong, PhD thesis, Australian National University, 1987 (unpublished)

[HÄ72] : O. Häusser, F.C. Khanna and D. Ward, *Nucl. Phys.* **A194** (1972) 113

[HÄ74] : O. Häusser, in "Nuclear Spectroscopy and Reactions" Part C, ed. J. Cerny (Academic Press, New York, 1974)

[HA77] : I. Hamamoto, in "Elementary modes of excitation in nuclei", Proc. Scuola Int. di Fisica "Enrico Fermi" Course LXIX, ed A. Bohr and R.A. Broglia (North-Holland, Amsterdam, 1977)

[HA78] : B. Harwatz, *Nucl. Data Sheets* **23** (1978) 607

[HA79] : J. Halperin, *Nucl. Data Sheets* **28** (1979) 485

[HE74] : K. Heilig and A. Stendel, *At. Data and Nucl. Data Tables* **14** (1974) 613

[HE81] : P.O. Hess, J. Maruhn and W. Greiner, *J. Phys. G.* **7** (1981) 737

[HO77] : M.V. Hoehn, E.B. Shera, Y. Yamazaki and R.M. Steffen, *Phys. Rev. Lett.* **39** (1977) 1313

[HO81] : M.V. Hoehn, E.B. Shera, H.D. Wohlfahrt, Y. Yamazaki, R.M. Steffen and R.K. Sheline, *Phys. Rev.* **C24** (1981) 1667

[IC77] : M. Ichimura, M. Igarashi, S. Landowne, C.H. Dasso, B.S. Nilsson, R.A. Broglia and A. Winther, *Phys. Lett.* **67B** (1977) 129

[IR72] : J.M. Irvine, "Nuclear Structure Theory" (Pergamon Press, Oxford, 1972)

[IS87] : P. Van Isacker, *Nucl. Phys.* **A465** (1987) 497

[JA75] : F. James and M. Roos, *Comp. Phys. Comm.* **10** (1975) 343

[JO77] : N.R. Johnson, P.P. Hubert, E. Eichler, D.G. Sarantites, J. Urbon, S.W. Yates and T. Lindblad, *Phys. Rev.* **C15** (1977) 1325

[JO78] : A.M.R. Joye, A.M. Baxter, S. Hinds, D.C. Kean and R.H. Spear, *Phys. Lett.* **72B** (1978) 307

[KH84] : A. Khan and S.W. Yates, *Phys. Rev.* **C29** (1984) 1081

[KR72] : K.S. Krane, *Nucl. Inst. Meth.* **98** (1972) 205

[KU68] : K. Kumar and M. Baranger, *Nucl. Phys.* **A110** (1968) 529

[KU68a] : K. Kumar and M. Baranger, *Nucl. Phys.* **A122** (1968) 273

[KU72] : K. Kumar, *Phys. Scripta* **6** (1972) 270

[KU82] : A. Kumar and M.R. Gunye, *Pramana* **19** (1982) 189

[LA72] : S.A. Lane and J.X. Saladin, *Phys. Rev.* **C6** (1972) 613

[LE57] : J.S. Levinger, *Phys. Rev.* **107** (1957) 554

[LE77] : I.Y. Lee, D. Cline, P.A. Butler, R.M. Diamond, J.O. Newton, R.S. Simon and F.S. Stephens, *Phys. Rev. Lett.* **39** (1977) 684

[LI78] : R.M. Lieder and H. Ryde, *Adv. Nucl. Phys.* **10** (1978) 1

[LI89] : C.S. Lim, R.H. Spear, W.J. Vermeer and M.P. Fewell, *Phys. Rev.* **C39** (1989) 1142

[MA86] : M.J. Martin, *Nucl. Data Sheets* **47** (1986) 797

[MA86t] : A. Mauthofer, PhD thesis, Johann Wolfgang Goethe-University, Frankfurt, 1986 (unpublished)

[MC58] : F.K. McGowan and P.H. Stelson, *Phys. Rev.* **109** (1958) 901

[MC61] : F.K. McGowan and P.H. Stelson, *Phys. Rev.* **122** (1961) 1274

[MI71] : W.T. Milner, F.K. McGowan, R.L. Robinson, P.H. Stelson and R.O. Sayer, *Nucl. Phys.* **A177** (1971) 1

[MI86] : V.M. Mikhailov, V.O. Sergeev and T.A. Tulina, *Bull. Acad. Sci. USSR Phys. Ser.* **50** (1986) 87

[MO81] : I. Morrison and R.H. Spear, *Phys. Rev.* **C23** (1981) 932

[MU84] : S.J. Mundy, J. Lukasiak and W.R. Phillips, *Nucl. Phys.* **A426** (1984) 144

[NE65] : J.A. Nelder and R. Mead, *Comput.* **J7** (1965) 308

[NE75] : K. Neergård, P. Vogel and M. Radomski, *Nucl. Phys.* **A238** (1975) 199

[NO70] : L.C. Northcliffe and R.F. Schilling, *Nucl. Data Tables* **A7** (1970) 233

[NO86] : A. Novoselsky and I. Talmi, *Phys. Lett.* **172B** (1986) 139

[OP78] : T.R. Ophel and A. Johnston, *Nucl. Inst. Meth.* **157** (1978) 461

[OP88] : T.R. Ophel, L.K Fifield, W.N. Catford, N.A. Orr, C.L. Woods, A. Harding and G.P. Clarkson, *Nucl. Inst. Meth.* **A272** (1988) 734

[OT78] : T. Otsuka, A. Arima, F. Iachello and I. Talmi, *Phys. Lett.* **76B** (1978) 139

[PE79] : L.K. Peker and J.H. Hamilton, *Phys. Rev.* **C20** (1979) 855

[PR70] : R.J. Pryor and J.X. Saladin, *Phys. Rev.* **C1** (1970) 1573

[RA74] : I. Ragnarsson, A. Sobiczewski, R.K. Sheline, S.E. Larsson, B. Nerlo-Pomorska, *Nucl. Phys.* **A233** (1974) 329

[RA87] : S. Raman, C.H. Malarkey, W.T. Milner, C.W. Nestor, Jr. and P.H. Stelson, *At. Data and Nucl. Data Tables* **36** (1987) 1

[RE61] : D.H. Rester, M.S. Moore, F.E. Durham and C.M. Class, *Nucl. Phys.* **22** (1961) 104

[RE84] : W. Reuter, E.B. Shera, M.V. Hoehn, F.W. Hersman, T. Milliman, J.M. Finn, C. Hyde-Wright, R. Lourie, B. Pugh and W. Bertozzi, *Phys. Rev.* **C30** (1984) 1465

[RO74] : F. Roesel, J.X. Saladin and K. Alder, *Comp. Phys. Comm.* **8** (1974) 35

[RO77] : R.M. Ronningen, R.B. Piercey, A.V. Ramayya, J.H. Hamilton, S. Raman, P.H. Stelson and W.K. Dagenhart, *Phys. Rev.* **C16** (1977) 571

[RO88] : B. Roussiére, F. le Blanc, G. Savard, H.T. Duong, J. Pinard, S. Liberman, J.K.P. Lee, J.E. Crawford, G. Thekkadath, P. Kilcher, J. Obert, J. Oms, J.C. Putaux, J. Sauvage and the ISOCELE collaboration, *Hyp. Int.* **43** (1988) 473

[RU78] : P. Russo, J.K. Sprinkle, D. Cline, P.B. Vold and R.P. Scharenberg, University of Rochester Nuclear Structure Research Laboratory, Annual Report (1978) p.79

[SA84] : R. Sahu, *Phys. Rev.* **C29** (1984) 1486

[SC78] : O. Scholten, F, Iachello and A. Arima, *Ann. of Phys.* **115** (1978) 325

[SC86] : M.R. Schmorak, *Nucl. Data Sheets* **49** (1986) 733

[SC87] : M.R. Schmorak, *Nucl. Data Sheets* **50** (1987) 669

[SC87a] : M.R. Schmorak, *Nucl. Data Sheets* **50** (1987) 719

[SC87b] : M.R. Schmorak, *Nucl. Data Sheets* **51** (1987) 689

[SC88] : M.R. Schmorak, *Nucl. Data Sheets* **53** (1988) 331

[SE74] : R. Sedlmayr, M. Sedlmayr and W. Greiner, *Nucl. Phys.* **A232** (1974) 465

[SE87] : P.B. Semmes, A.F. Barfield, B.R. Barrett and J.L. Wood, *Phys. Rev.* **C35** (1987) 844

[SH83] : V.S. Shirley and J.M. Dairiki, *Nucl. Data Sheets* **40** (1983) 425

[SH87] : E.B. Shera, priv. comm., October 1987

[SI89] : B. Singh, *Nucl. Data Sheets* **56** (1989) 75

[SP67] : J.E. Spencer and H.A. Enge, *Nucl. Inst. Meth.* **49** (1967) 181

[SP78] : R.H. Spear, T.H. Zabel, A.M. Baxter, M.P. Fewell, S. Hinds, A.M.R. Joye and D.C. Kean, *Aust. J. Phys.* **31** (1978) 377

[SP80] : R.H. Spear, M.T. Esat, M.P. Fewell, D.C. Kean, T.H. Zabel, A.M. Baxter and S. Hinds, *Nucl. Phys.* **A345** (1980) 252

[SP83] : R.H. Spear, W.J. Vermeer, M.T.Esat, J.A Kuehner, A.M. Baxter and S. Hinds, *Phys. Lett.* **128B** (1983) 29

[SP89] : R.H. Spear, *Atomic Data and Nuclear Data Tables* **42** (1989) 55

[ST72] : F.S. Stephens and R.S. Simon, *Nucl. Phys.* **A183** (1972) 257

[ST77] : K. Stelzer, F. Rauch, T.W. Elze, C.E. Gould, J. Idzko, G.E. Mitchell, H.P. Nottrodt, R. Zoller, H.J. Wollersheim and H. Emling, *Phys. Lett.* **70B** (1977) 297

[TA77] : Y. Tanaka and R.K. Sheline, *Nucl. Phys.* **A276** (1977) 101

[TA86] : T. Tamura, "Boson Expansion Theory", in "International Spring Seminar on Nuclear Physics : Microscopic approaches to nuclear structure calculations", Sorrento May 1986, ed. A. Covello (Italian Physical Society, Bologne, 1986)

[TA87] : T. Tamura, priv. comm. to R.H. Spear, 1987

[TO77] : H. Toki, K. Neergård, P. Vogel and A. Faessler, *Nucl. Phys.* **A279** (1977) 1

[TO79] : L.D. Tolsma, *Phys. Rev.* **C20** (1979) 592

[VE84t] : W.J. Vermeer, PhD thesis, Australian National University, 1987 (unpublished)

[WA72] : F.E. Wagner, H. Spieler, D. Kucheida, P. Kienle and R. Wäppling, *Z. Phys.* **254** (1972) 112

[WA77] : L.K. Wagner, E.B. Shera, G.A. Rinker and R.K. Sheline, *Phys. Rev.* **C16** (1977) 1549

[WA85] : E. van Walle, J. Wouters, D. Vandeplassche, N. Severijns and L. Vanneste, *Hyp. Int.* **22** (1985) 207

[WE79] : M.P. Webb, *Nucl. Data Sheets* **26** (1979) 145

[WE80] : K.J. Weeks and T. Tamura, *Phys. Rev.* **C22** (1980) 1323

[WI56] : L. Wilets and M. Jean, *Phys. Rev.* **102** (1956) 788

[WI66] : A. Winther and J. de Boer, "A computer program for multiple Coulomb excitation", reprinted in K. Alder and A. Winther, "Coulomb excitation" (Academic Press, New York, 1966) p. 303

[WU83t] : C.Y. Wu, PhD thesis, University of Rochester, Nuclear Structure Laboratory, 1983 (unpublished)

[WU85] : C.Y. Wu, priv. comm. to S. Raman *et al.*, from Ra87

[WU87] : C.Y. Wu, priv. comm. to M.P. Fewell

[YA67] : T. Yamazaki, *Nucl. Data Tables* **A3** (1967) 1

[YA79] : Y. Yamazaki, E.B. Shera, M.V. Hoehn, H.D. Wohlfahrt and R.M. Steffen, *J. Phys. Soc. Jap.* **47** (1979) 695

[YA83] : S.W. Yates, A. Khan, A.J. Filo, M.C. Mirzaa, J.L. Weil and M.T. McEllistrem, *Nucl. Phys.* **A406** (1983) 519

[YA88] : S.W. Yates, R. Julin, J. Kumpulainen and E. Verho, *Phys. Rev.* **C37** (1988) 2877

[ZI80] : J.F. Ziegler, "Handbook of stopping cross-sections for energetic ions in all elements" (Pergamon Press, New York, 1980)